# Radar MIMO utilisant des antennes colocalisées : étude théorique, simulations et développement d'une plateforme expérimentale

Oscar Gómez

**UNIVERSITÉ PARIS-EST**
**DOCTORAL SCHOOL MSTIC**
**MATHEMATIQUES, SCIENCES ET TECHNOLOGIES DE L'INFORMATION ET DE LA COMMUNICATION**


# P H D  T H E S I S

To obtain the title of

**Ph.D. of Science**

of the Université Paris-Est

**Specialty: Electronics, Optronics and Systems**


*Author:*

ZAHID OSCAR GÓMEZ URRUTIA


# MIMO Radar with Colocated Antennas: Theoretical Investigation, Simulations and Development of an Experimental Platform

Thesis directed by Geneviève Baudoin and supervised by Florence Nadal, Pascale Jardin, and Benoît Poussot

Defended on June 16th, 2014

**Jury:**

| | | |
|---|---|---|
| *Reviewer:* | Prof. Marc Lesturgie | ONERA - SONDRA - Supélec |
| *Reviewer:* | Prof. Christophe Craeye | Université Catholique de Louvain |
| *Examiner:* | Prof. Daniel Roviras | CEDRIC - CNAM |
| *Examiner:* | Prof. Bernard Huyart | LTCI - Télécom ParisTech |
| *Supervisor:* | Dr. Florence Nadal | ESYCOM - ESIEE Paris |
| *Supervisor:* | Dr. Pascale Jardin | ESIEE Paris |
| *Supervisor:* | Dr. Benoît Poussot | ESYCOM - Université Paris-Est |
| *Thesis director:* | Prof. Geneviève Baudoin | ESYCOM - ESIEE Paris |
| *Invited member:* | Mr. Philippe Eudeline | Thales Air Systems |

# Abstract

**Title: "MIMO Radar with Colocated Antennas: Theoretical Investigation, Simulations and Development of an Experimental Platform".**

A Multiple-Input Multiple-Output (MIMO) radar is a system employing multiple transmitters and receivers in which the waveforms to be transmitted can be totally independent. Compared to standard phased-array radar systems, MIMO radars offer more degrees of freedom which leads to improved angular resolution and parameter identifiability, and provides more flexibility for transmit beampattern design. The main issues of interest in the context of MIMO radar are the estimation of several target parameters (which include range, Doppler, and Direction-of-Arrival (DOA), among others). Since the information on the targets is obtained from the echoes of the transmitted signals, it is straightforward that the design of the waveforms plays an important role in the system accuracy.

This document addresses the investigation of DOA estimation of non-moving targets and waveform design techniques for MIMO radar with colocated antennas. Although narrowband MIMO radars have been deeply studied in the literature, the existing DOA estimation techniques have been usually proposed and analyzed from a theoretical point of view, often assuming ideal conditions. This thesis analyzes existing signal processing algorithms and proposes new ones in order to improve the DOA estimation performance in the case of narrowband and wideband signals. The proposed techniques are studied under ideal and non-ideal conditions considering punctual targets. Additionally, we study the influence of mutual coupling on the performance of the proposed techniques and we establish a more realistic signal model which takes this phenomenon into account. We then show how to improve the DOA estimation performance in the presence of distorted radiation patterns and we propose a crosstalk reduction technique, which makes possible an efficient estimation of the target DOAs. Finally, we present an experimental platform for MIMO radar with colocated antennas which has been developed in order to evaluate the performance of the proposed techniques under more realistic conditions. The proposed platform, which employs only one transmitter and one receiver architectures, relies on the superposition principle to simulate a real MIMO system.

# Acknowledgements

First, I would like to thank all the members of my thesis jury, Marc Lesturgie, Christophe Craeye, Daniel Roviras, Bernard Huyart, and Philippe Eudeline, for the interest they gave to my research and for participating in my defence. Their feedback, discussion and suggestions have been of great advice and constructive for my future carreer.

I would like to thank my thesis advisors Florence Nadal, Pascale Jardin, and Benoît Poussot who gave me the opportunity to work on this interesting topic and who followed me during these three and a half years of Ph.D. I am grateful for the invaluable time you spent with me to guide me and to look closely at every detail of these thesis. Thank you for supporting me and for giving me the freedom to do what I found interesting to do.

I would also like to express my gratitude to my thesis director Geneviève Baudoin for her guidance and enthusiastic encouragement throughout my research. Besides providing helpful advice, she also stimulated me in publishing papers, attending international conferences and working abroad, which have been great experiences for me.

I would like to thank the laboratory engineers of Université Paris-Est for all the help and facilities they provided me during the development of the experimental part of this project. A special thanks to David Delcroix, whose involvement and invaluable help in the development of the experimental platform were essential in the success of this project.

I also want to thank Prof. Vincent Fusco, the Queen's University Belfast and the Institute of Electronics, Communications and Information Technology (ECIT) who hosted me for three months. Under the guidance of Prof. Fusco I investigated the influence of mutual coupling on the performance of MIMO radar which allowed me to establish a link between signal processing and electromagnetics. The results obtained during this collaboration represent a relevant part of this thesis.

A special thanks to Sarah Middleton, whose previous work on MIMO techniques was a basis for me during my first months of thesis.

Thanks to all my colleagues for their support and the great moments we spent together. I enjoyed all the intellectual and not so intellectual discussions we had and those moments are another unforgettable part of this experience.

Finally, I would like to thank my family for all their support. You are my inspiration in everything I do.

# Contents

# List of Figures

# Abbreviations

| | |
|---|---|
| ADC | Analog-to-Digital Converter |
| AWG | Arbitrary Waveform Generator |
| CW | Continuous Wave |
| CSSM | Coherent Signal Subspace Method |
| dB | Decibel |
| DFT | Discrete Fourier Transform |
| DOA | Direction-Of-Arrival |
| DOD | Direction-Of-Departure |
| EMC | ElectroMagnetic Compatibility |
| FM | Frequency Modulated |
| GLR | Generalized Likelihood Ratio |
| GLRT | Generalized Likelihood Ratio Test |
| GPIB | General Purpose Interface Bus |
| GPS | Global Positioning System |
| HFSWR | High Frequency Surface Waves Radar |
| IDFT | Inverse Discrete Fourier Transform |
| i.i.d. | Independent and identically distributed |
| LNA | Low Noise Amplifier |
| LS | Least Squares |
| max | Maximum |
| MC | Mutual Coupling |
| MIMO | Multiple Input Multiple Output |
| min | Minimum |
| ML | Maximum Likelihood |
| MSE | Mean Square Error |

| | |
|---|---|
| M-SFBT | Multiband Spectral Density Focusing Beampattern synthesis Technique |
| M-TOPS | Multiband Test of Orthogonality of Projected Subspaces |
| MUSIC | MUltiple SIgnal Classification |
| PA | Power Amplifier |
| PAPR | Peak-to-Average Power Ratio |
| PC | External Computer |
| PDF | Probability Density Function |
| QPSK | Quadrature Phase Shift Keying |
| RCS | Radar Cross Section |
| RF | Radio Frequency |
| Rx | Receiver |
| SFBT | Spectral Density Focusing Beampattern synthesis Technique |
| SNR | Signal-to-Noise Ratio |
| SPDT | Single Pole Double Throw |
| s.t. | Subject to |
| TCP | Transmission Control Protocol |
| TOPS | Test of Orthogonality of Projected Subspaces |
| Tx | Transmitter |
| ULA | Uniform Linear Array |
| UWB | Ultra-WideBand |
| VSA | Vector Signal Analyzer |
| WBFIT | Wideband Beampattern Formation via Iterative Techniques |
| WiFi | Wireless Fidelity |

# Symbols

**Scalars**

| | |
|---|---|
| $\beta$ | Reflection coefficient of a target |
| $\lambda$ | Wavelength [m] |
| $\Delta$ | The largest dimension of an antenna [m] |
| $\varepsilon_r$ | Dielectric constant |
| $\mu_0$ | Permeability constant of free space [T·m/A] |
| $\rho$ | GLR |
| $\varrho$ | A PAPR threshold |
| $\sigma$ | Standard deviation of the noise |
| $\tau$ | Time delay [s] |
| $\theta$ | DOA of a wave [°] |
| $B$ | Bandwidth of a signal [Hz] |
| $c$ | Complex envelope of a transmitted signal [V] |
| $D$ | $x$-component of a target position vector [m] |
| $d_r$ | Inter-element spacing of the receiver array [m] |
| $d_t$ | Inter-element spacing of the transmitter array [m] |
| $E$ | Electric field [V/m] |
| $e$ | Euler's number |
| $E_r$ | Electric field reflected by a target [V/m] |
| $E_t$ | Total electric field at a target location [V/m] |
| $f$ | Frequency [Hz] |
| $f_c$ | Carrier frequency [Hz] |
| $g_{r,l}$ | Radiation pattern of the $l^{\text{th}}$ receiver antenna element |
| $g_{t,i}$ | Radiation pattern of the $i^{\text{th}}$ transmitter antenna element |
| $H$ | $y$-component of a target position vector [m] |

| | |
|---|---|
| $j$ | Imaginary unit |
| $K$ | Number of targets |
| $L_r$ | Number of antenna elements of a receiving array |
| $L_t$ | Number of antenna elements of a transmitting array |
| $m_{l,i}$ | Transmission coefficient between the $i^{\text{th}}$ transmitter element and the $l^{\text{th}}$ receiver elements |
| $n$ | Discrete-time index |
| $N$ | Number of temporal samples of a signal |
| $N_s$ | Total number of temporal samples of a transmitted frame |
| $p$ | Discrete-frequency index |
| $P_{cap}$ | Capon's spatial spectrum |
| $P_{MUSIC}$ | MUSIC spatial spectrum |
| $R$ | Radial distance between the origin of the Cartesian coordinate system and a target position [m] |
| $s$ | Source signal to be detected |
| $t$ | Time [s] |
| $v$ | Wave propagation speed [m/s] |

**Vectors**

| | |
|---|---|
| $\boldsymbol{\alpha}_r$ | General phase-only receive steering vector |
| $\boldsymbol{\alpha}_t$ | General phase-only transmit steering vector |
| $\mathbf{a}_r$ | Standard receive steering vector |
| $\mathbf{a}_t$ | Standard transmit steering vector |
| $\tilde{\mathbf{a}}_t$ | General transmit steering vector |
| $\tilde{\mathbf{a}}_r$ | General receive steering vector |
| $\mathbf{c}$ | Vector of complex envelopes of the transmitted signals [V] |
| $\mathbf{E}_r$ | Vector of electric fields measured by a receiver array [V/m] |
| $\mathbf{p}$ | Position vector [m] |
| $\mathbf{k}$ | Two-dimensional wave vector [rad/m] |
| $\mathbf{r}$ | Vector linking one element of an antenna array with a target position [m] |
| $\mathbf{s}$ | Set of source signals to be detected |
| $\mathbf{x}$ | Vector of received signals |

| | |
|---|---|
| $\mathbf{z}$ | Vector of noise and interference |

**Matrices**

| | |
|---|---|
| $\mathbf{C}$ | Matrix of complex envelopes of the transmitted signals |
| $\mathbf{I}$ | Identity matrix |
| $\mathbf{M}$ | Crosstalk matrix |
| $\mathbf{R}_c$ | Auto-covariance matrix of the transmitted signals |
| $\mathbf{R}_x$ | Auto-covariance matrix of the received signals |
| $\mathbf{R}_{xc}$ | Cross-covariance matrix between the received and the transmitted signals |
| $\mathbf{R}_z$ | Auto-covariance matrix of noise |
| $\mathbf{X}$ | Matrix of received signals |
| $\mathbf{Z}$ | Matrix of noise and interference |

**Mathematical Operators**

| | |
|---|---|
| $(\cdot)^*$ | Complex conjugate |
| $(\cdot)^T$ | Transpose |
| $(\cdot)^H$ | Hermitian transpose |
| $\lvert\cdot\rvert$ | Determinant of a matrix or absolute value of a scalar number |
| $\lVert\cdot\rVert$ | Euclidean norm of a vector |
| $\lVert\cdot\rVert_F$ | Frobenius norm of a matrix |
| $\lfloor x \rfloor$ | Largest integer less than or equal to $x$ |
| $\arg\{\cdot\}$ | Argument of a complex number |
| $\mathrm{diag}(\mathbf{v})$ | Diagonal matrix with the elements of vector $\mathbf{v}$ on the main diagonal |
| $\mathrm{E}[\cdot]$ | Mathematical expectation |
| $\mathrm{Im}[\cdot]$ | Imaginary part |
| $\mathrm{Re}[\cdot]$ | Real part |
| $\mathrm{tr}[\cdot]$ | Trace of a matrix |
| $\frac{\partial}{\partial}$ | Partial derivative |
| $*$ | Temporal convolution |

# Chapter 1

# Introduction

## 1.1 Principle and Interest of MIMO Radar

Multi-antenna based radar systems are widely used in both military and civilian applications. One of the most implemented radar configurations is the phased-array radar system. Phased-arrays employ multiple transmitter and multiple receiver antenna elements which are usually colocated. The multiple transmitter elements are capable of cohering and steering the transmitted energy toward a desired direction by transmitting scaled and delayed versions of a single waveform. At the receiver array, the received signals can be steered in a given direction in order to maximize the probability of detection or the Signal-to-Noise Ratio (SNR). This can be done in two different ways: By performing analog beamforming via the use of phase shifters in the different receiver architectures, or by performing digital beamforming via adaptive processing. Digital beamforming offers several advantages over its analog counterpart, including the capability to steer multiple simultaneous beams [1][2] and the possibility to implement single and multiple sidelobe cancelers [3].

Another type of multi-antenna radar system is the Multiple-Input Multiple-Output (MIMO) radar. A MIMO radar also employs multiple transmitter and multiple receiver elements, but unlike the phased-array systems, the different waveforms transmitted by a MIMO radar can be correlated or uncorrelated with each other [4]. Compared to phased-array radars, MIMO radars offer more degrees of freedom which lead to improved angular resolution [5][6], improved parameter identifiability, and more flexibility for transmit beampattern design [4]. Additionally, MIMO radars can synthesize larger virtual arrays which increases resolution and the number of targets that can be detected [6][7].

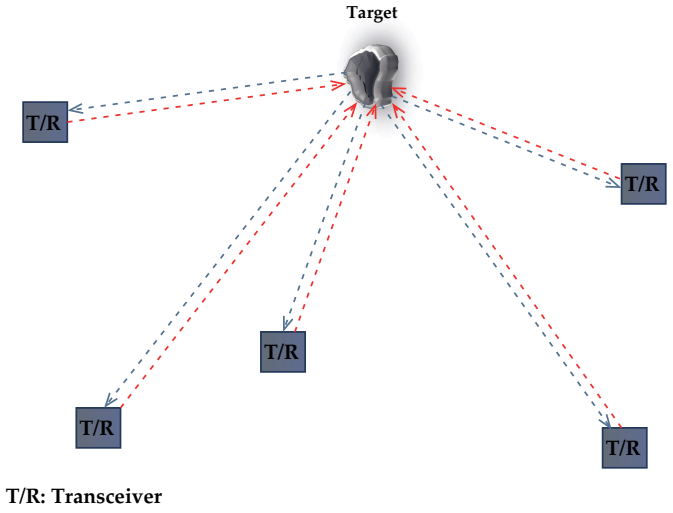


FIGURE 1.1: MIMO radar with widely separated antennas.

There are several configurations of MIMO radar depending on the location of the transmitting and the receiving elements. One of them is the MIMO radar with widely separated antennas (or statistical MIMO radar) [8][9]. The separation between the different transceivers must be large enough (several wavelenghts) to receive uncorrelated echoes from the targets. This configuration allows exploiting the spatial diversity of the targets' Radar Cross Section (RCS) to improve the radar performance by addressing the problem similarly to a MIMO communications problem. Actually, by combining the different target echoes coming from different directions (see Figure 1.1) by non-coherent (or statistical) processing, a diversity gain is achieved, similarly to the diversity gain obtained in MIMO communications when data is transmitted over independent channels [8].

Another type of MIMO radar, known as MIMO radar with colocated antennas, employs transmit and receive antenna arrays containing elements which are closely spaced relatively to the working wavelength (e.g. spaced by half the wavelength). In a receiver array of colocated antennas, the signals reflected by the targets have similar amplitude at each receive antenna element and the targets are usually modeled as punctual. While this configuration does not provide spatial diversity, spatial resolution can be increased by combining the information from all of the transmitting and receiving paths. This is done by coherent processing: By exploiting the different time delays and/or phase shifts, the received signals are coherently combined to form multiple beams. This configuration also has other benefits such as a good interference rejection and a good flexibility for transmitting a desired beampattern [4]. MIMO radars with colocated antennas can be further classified into bistatic MIMO radars if the transmitter array is widely separated from the receiver array [10] (see Figure 1.2);

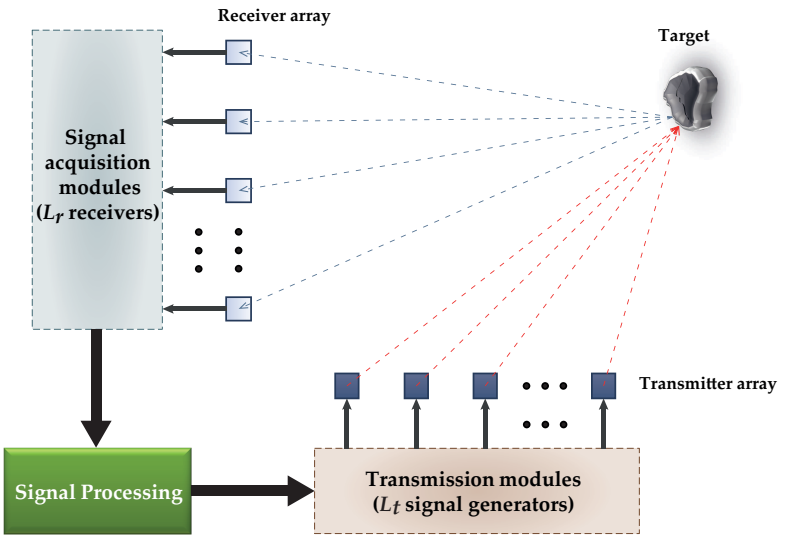


FIGURE 1.2: Bistatic MIMO radar with colocated antennas.

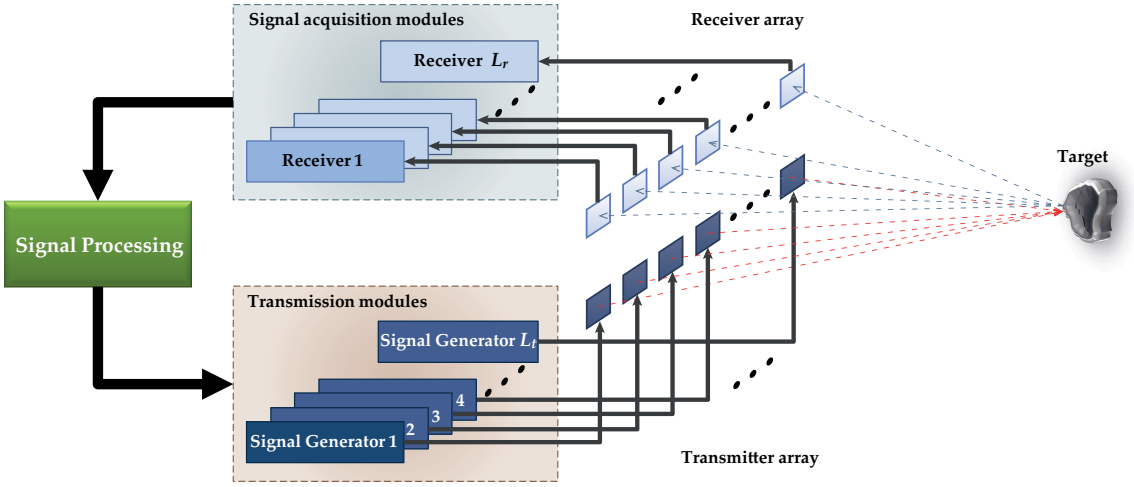


FIGURE 1.3: Monostatic MIMO radar with colocated antennas.

or monostatic MIMO radars if the transmitter and receiver arrays are closely spaced or colocated [11] (see Figure 1.3).

One of the main issues of interest in the context of MIMO radar is the estimation of several target parameters which include range, Doppler, Direction-of-Arrival (DOA), and reflection coefficients, among others. Another main topic which attracts the interest of researchers is waveform design. In fact, the capability of transmitting different arbitrary waveforms by every element of the array allows having great flexibility when trying to transmit a desired beampattern. This capability can be exploited to improve the target parameter identification, to maximize the SNR, to improve angular and range resolution or to achieve interference rejection, among others. Moreover, additional improvement in resolution and interference rejection can be obtained by the use of wideband signals to synthesize the transmit beampatterns.

## 1.2 MIMO Radar Applications

Radar systems have been used in many fields of application in the last decades, including military and civilian areas, and the need of more sophisticated and accurate radar functions have been constantly increasing. Thanks to its improved capabilities in resolution, target parameter identification, and waveform design among others, MIMO radars might be widely used in the future and make possible the development of additional features such as communication by radar or intelligent signal coding [12].

Today, MIMO radars can be used in many of the applications where other multi-antenna based radars are employed. Such applications include ground surveillance [13][14], automotive [15][16] and interferometry [17] applications. Other interesting applications might be possible such as the detection of anti-personnel mines by ground penetrating radar measurements [18], the detection of tsunami waves [19] and maritime surveillance by employing a MIMO configuration of High Frequency Surface Waves Radar (HFSWR) [13][20], or through-the-wall radar imaging applications for urban sensing [21]. MIMO radars also find applications in the medical area, e.g. for breast cancer detection [22] or to monitor the water accumulation in the human body [23].

## 1.3 Problem Statement

This document addresses the investigation of DOA estimation of non-moving targets and waveform design techniques for monostatic MIMO radar with colocated antennas. Although narrowband MIMO radars have been deeply studied in the literature, the existing DOA estimation techniques have been usually proposed and analyzed from a theoretical point of view, often assuming ideal conditions. Moreover, in the case of wideband signals, the assumptions done in the signal model no longer hold and narrowband detection techniques cannot be directly applied. The objective of this thesis is to study the existing DOA estimation and waveform design techniques and to develop new signal processing algorithms in order to improve the DOA estimation performance in the wideband case. The proposed techniques will be studied under ideal and non-ideal conditions considering punctual and non-moving targets. They will be validated by experimental results.

The thesis is divided into a theoretical and an experimental part which are described thereafter.

### 1.3.1 Theoretical Investigation

The thesis starts with the introduction of the signal model of MIMO radar with colocated antennas. Then, a review of the existing narrowband DOA estimation techniques is done. Since the use of wideband signals is gaining in importance, we investigate DOA estimation and waveform design in the wideband case. We propose new wideband DOA estimation techniques mainly based on a literature review on wideband array processing. We also propose new waveform design algorithms.

Additionally, we study the electromagnetic interactions between the antenna elements in order to analyze their influence on the performance of the proposed techniques and to create a more realistic signal model. We then propose methods to overcome the undesired effects of mutual coupling such as the radiation pattern distortion and crosstalk.

### 1.3.2 Experimental Implementation

An experimental platform for MIMO radar with colocated antennas is developed in order to evaluate the performance of the proposed techniques under more realistic conditions. Since a real large MIMO system is particularly expensive and complex to develop, synchronize and calibrate, the proposed platform contains only one transmitting and one receiving Radio Frequency (RF) architectures. An automated mechanical system is used to simulate a real MIMO radar. By applying the superposition principle, the received signals are combined to construct the received signal matrix of the MIMO system.

Finally, a set of experimental results is presented which allows us to evaluate the real performance of some narrowband DOA estimation techniques.

## 1.4 Thesis Outline

The thesis is organized as follows. In Chapter 2, the narrowband far-field signal model is presented, followed by a review of some existing narrowband DOA estimation techniques. Once the relevant theory has been introduced, the different techniques are compared via simulation results in order to highlight their strengths and weaknesses, including spatial resolution and robustness against noise and jammers. Moreover, the limit between the spherical-wave and plane-wave regions of the far field is also studied, showing when a target can really be assumed to be in the plane-wave region.

In Chapter 3, the signal model is extended to the case of wideband signals. Then, a review and comparison of two existing wideband waveform design techniques is performed. Based on these existing techniques, we propose a new multiband waveform design technique which allows decorrelating the signals reflected by the targets. Moreover, we propose an adaptation of the previously reviewed narrowband DOA estimation techniques to the wideband context. Additionally, a wideband array processing technique is adapted to the context of wideband MIMO radar. The performance of the studied techniques is analyzed and compared through simulation.

In Chapter 4, the electromagnetic interactions between the different elements of the antenna arrays are taken into account in order to establish a more realistic signal model. The influence of mutual coupling on the DOA estimation performance is then studied by combining signal processing with electromagnetic simulations. Moreover, we show how to improve the DOA estimation performance in the presence of distorted radiation patterns and propose a crosstalk reduction technique, which makes possible an efficient estimation of the target DOAs.

Finally, the developed experimental platform is fully described in Chapter 5, including the synchronization and calibration procedures. Then, experimental results are presented in order to analyze the real performance of the discussed narrowband algorithms, including the DOA estimation and crosstalk reduction techniques.

Additional mathematical developments regarding the reviewed algorithms are provided in Appendices A and B.

An extended summary in French is given in Appendix C.

The different notations are defined at their first appearance and are common to the entire document.

## 1.5 Publications

The work carried out in this thesis led to several publications, which are listed below.

**International conferences with proceedings**

- O. Gómez, P. Jardin, F. Nadal, B. Poussot, and G. Baudoin. “Multiband waveform synthesis and detection for a wideband MIMO radar”. In *2011 IEEE International Conference on Microwaves, Communications, Antennas and Electronics Systems (COMCAS)*, pages 1-5, 2011.

- O. Gómez, F. Nadal, P. Jardin, G. Baudoin, and B. Poussot. "On wideband MIMO radar: Detection techniques based on a DFT signal model and performance comparison". In *2012 IEEE Radar Conference (RADAR)*, pages 0608-0612, 2012.

- O. Gómez, B. Poussot, F. Nadal, P. Jardin, and G. Baudoin. "An Experimental Platform for MIMO Radar with Colocated Antennas". In *2012 IEEE Asia-Pacific Microwave Conference Proceedings (APMC)*, pages 1085-1087, 2012.

**National conference with proceedings**

- O. Gómez, B. Poussot, F. Nadal, P. Jardin, and G. Baudoin. "Radar MIMO cohérent : développement d'une plateforme expérimentale". In *18$^{èmes}$ Journées Nationales Micro-ondes (JNM)*, 2013.

**Paper presented at a workshop**

- O. Gómez, B. Poussot, F. Nadal, P. Jardin, and G. Baudoin. "A reconfigurable experimental platform for coherent MIMO radar". In *SONDRA Workshop*, 2013.

# Chapter 2

# MIMO Radar with Colocated Antennas

A MIMO radar with colocated antennas has many benefits compared to other MIMO radar architectures, such as a better spatial resolution and a good flexibility for transmitting a desired beampattern, among others [4]. This configuration also allows the direct application of many adaptive array processing techniques for parameter estimation, including the well known Capon beamformer and MUSIC algorithm. In this chapter, the narrowband signal models for both the spherical-wave and plane-wave regions of the far field are described. Next, some existing detection techniques are presented and their performance is analyzed in the narrowband case with different MATLAB simulations. Other simulations are performed in order to establish when a target can be considered in the spherical-wave or in the plane-wave region of a MIMO radar. The obtained condition is compared to the one usually presented in the literature.

## 2.1 Far-Field Signal Model

In electromagnetic theory, the near field and the far field are two regions of the electromagnetic field radiated by a source, which are defined by relations between the distance from the source to the point where the field is measured, the wavelength of the transmitted signal and the aperture of the antenna. In the far-field region, the electric and magnetic components of the field radiated by a given antenna are orthogonal to each other [24], and the field pattern does not change with the distance between the antenna and the point where the field is measured. The far-field condition is very useful to obtain a simple expression of a propagating wave.

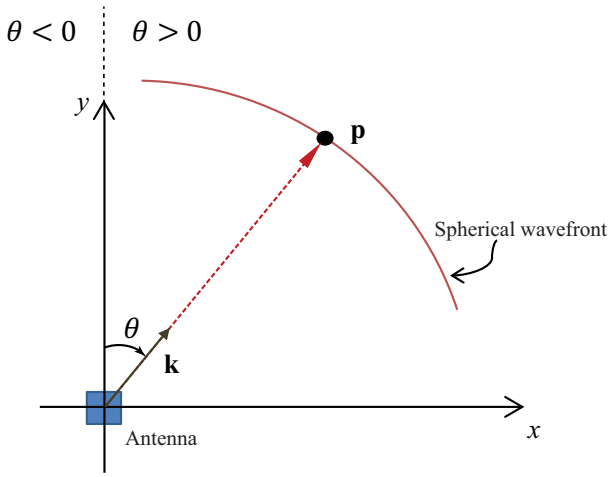


FIGURE 2.1: An antenna transmitting a signal of spherical wavefront.

The condition for a point in the space to be considered in the far-field region of an antenna is given by [24]

$$R \geq \frac{2\Delta^2}{\lambda}, \tag{2.1}$$

where $\Delta$ is the largest dimension of the antenna, $\lambda$ is the wavelength, and $R$ is the distance from the antenna to the point where the field is measured. In the same way, a target is considered to be in the far field of a MIMO radar if it is located in the far-field regions of both the transmitter and the receiver arrays. The far-field assumption is always used throughout this document.

Consider the complex representation of a time-varying current source signal given by

$$I(t) = c(t)e^{j2\pi f_c t} \tag{2.2}$$

where $c(t)$ is the complex envelope and $f_c$ is the carrier frequency. Assuming that the source signal $I(t)$ is incident at the input of a transmitting antenna, the far-field electric field at position $\mathbf{p}$ radiated by such antenna is given by [25]

$$\begin{aligned} \mathbf{E}(\mathbf{p},\mathbf{t}) &= -\frac{\mu_0}{4\pi\|\mathbf{p}\|}\left[\mathbf{h}_t\left(\mathbf{u}_\mathbf{p},t\right) * I(t)\right] * \delta\left(t - \frac{\mathbf{k}^T\mathbf{p}}{2\pi f_c}\right) \\ &= -\frac{\mu_0}{4\pi\|\mathbf{p}\|}\mathbf{h}_t\left(\mathbf{u}_\mathbf{p},t\right) * c\left(t - \frac{\mathbf{k}^T\mathbf{p}}{2\pi f_c}\right) e^{j(2\pi f_c t - \mathbf{k}^T\mathbf{p})}, \end{aligned} \tag{2.3}$$

where $\mathbf{k}$ is the wave vector, $\mathbf{u}_\mathbf{p} = \mathbf{p}/\|\mathbf{p}\|$ is the position unit vector, $\mu_0 = 4\pi 10^{-7}$ T·m/A is the permeability constant of free space, $\delta(t)$ is the Dirac delta function and $\mathbf{h}_t\left(\mathbf{u}_\mathbf{p},t\right)$ is the effective height or far-field impulse response of the transmitting antenna. Operators $\|\cdot\|$ and $*$ denote respectively the vector Euclidean norm and the temporal convolution.

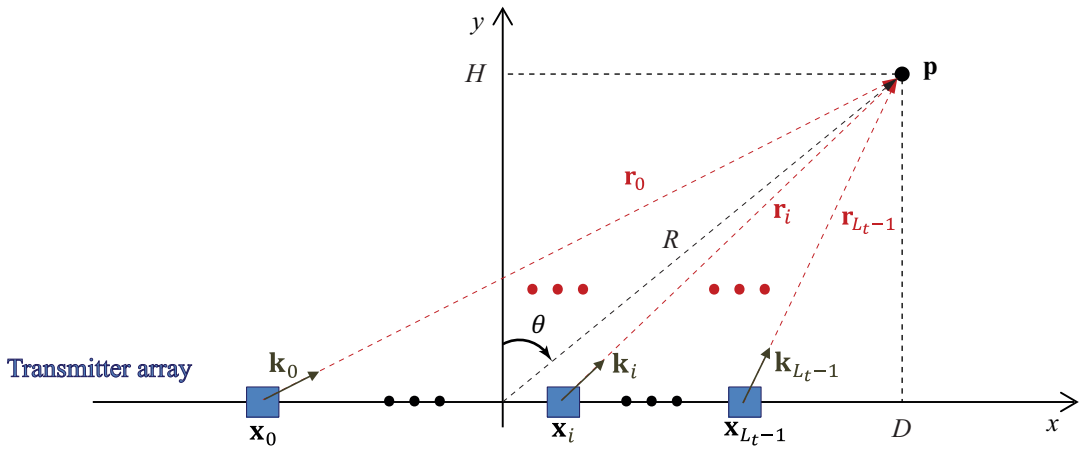


FIGURE 2.2: A transmitter Uniform Linear Array.

Both the position and the wave vectors are in reality three-dimensional, however, they are assumed here to be two-dimensional since the arrays of interest in this work can only detect targets in the $x-y$ plane. The wave vector is defined as

$$\mathbf{k} = \frac{2\pi}{\lambda}\begin{bmatrix}\sin\theta & \cos\theta\end{bmatrix}^T, \tag{2.4}$$

where $\theta \in [-90°, 90°]$ is the direction of propagation of the wave (see Figure 2.1). Equation (2.3) describes the propagation of a spherical wave whose amplitude decreases with the distance $\|\mathbf{p}\|$.

For simplicity, we will consider only the portion of the radiated field which is polarized in the $\mathbf{u}_{\text{pol}}$ direction. Accordingly, the scalar electric field at position $\mathbf{p}$ is given by

$$E(\mathbf{p},t) = -\frac{\mu_0}{4\pi\|\mathbf{p}\|} h_t\left(\mathbf{u}_\mathbf{p}, t\right) * c\left(t - \frac{\mathbf{k}^T\mathbf{p}}{2\pi f_c}\right) e^{j(2\pi f_c t - \mathbf{k}^T\mathbf{p})}, \tag{2.5}$$

where

$$h_t\left(\mathbf{u}_\mathbf{p}, t\right) = \mathbf{h}_t^T\left(\mathbf{u}_\mathbf{p}, t\right)\mathbf{u}_{\text{pol}}. \tag{2.6}$$

Consider now the transmitting Uniform Linear Array (ULA) shown in Figure 2.2. Note that the array is centered at the origin of the Cartesian coordinate system; for an odd number of antenna elements, the central element will be placed at the origin of the $x-y$ plane. Then, the field radiated by the $i^{\text{th}}$ antenna element due to a source signal $c_i(t)$ at an arbitrary target position $\mathbf{p}$ of coordinates $[D, H]$ is given by

$$\begin{gathered} E_i(\mathbf{p},t) = -\frac{\mu_0}{4\pi\|\mathbf{r}_i\|} h_{t,i}\left(\mathbf{u}_{\mathbf{r}_i}, t\right) * c_i\left(t - \tau_i\right) e^{j(2\pi f_c t - \mathbf{k}_i^T\mathbf{r}_i)} \\ i = 0, ..., L_t - 1, \end{gathered} \tag{2.7}$$

where

$$h_{t,i}\left(\mathbf{u}_{\mathbf{r}_i},t\right)=\mathbf{h}_{t,i}^{T}\left(\mathbf{u}_{\mathbf{r}_i},t\right)\mathbf{u}_{\mathrm{pol}}, \tag{2.8}$$

$\mathbf{h}_{t,i}\left(\mathbf{u}_{\mathbf{r}_i},t\right)$ is the effective height of the $i^{\mathrm{th}}$ transmitter antenna element, $\tau_i=\frac{\mathbf{k}_i^T\mathbf{r}_i}{2\pi f_c}$ is the time needed by the signal $c_i(t)$ to travel from the $i^{\mathrm{th}}$ antenna element to the target, $\mathbf{r}_i$ is the vector linking the $i^{\mathrm{th}}$ antenna element with the target position $\mathbf{p}$, $\mathbf{u}_{\mathbf{r}_i}=\mathbf{r}_i/\|\mathbf{r}_i\|$, and $L_t$ is the number of transmitting elements. The total field at the target location can be expressed as the superposition of the fields radiated by every antenna element as

$$E_t(\mathbf{p},t)=-\frac{\mu_0}{4\pi}\sum_{i=0}^{L_t-1}\frac{1}{\|\mathbf{r}_i\|}h_{t,i}\left(\mathbf{u}_{\mathbf{r}_i},t\right)*c_i\left(t-\tau_i\right)e^{j(2\pi f_c t-\mathbf{k}_i^T\mathbf{r}_i)}. \tag{2.9}$$

The field reflected by the target can be measured by a receiver array. Assuming that the transmitting and the receiving arrays are colocated[1], the reflected field measured at the $l^{\mathrm{th}}$ receiving antenna is then given by

$$\begin{aligned}E_r(\mathbf{x}_l,t) &= -\beta\frac{1}{\|\mathbf{r}_l\|}\left[h_{r,l}(\mathbf{u}_{\mathbf{r}_l},t)*E_t(\mathbf{p},t)\right]*\delta\left(t-\tau_l\right)\\ &= \frac{\mu_0\beta}{4\pi\|\mathbf{r}_l\|}e^{-j\mathbf{k}_l^T\mathbf{r}_l}h_{r,l}(\mathbf{u}_{\mathbf{r}_l},t)*\sum_{i=0}^{L_t-1}\frac{1}{\|\mathbf{r}_i\|}h_{t,i}\left(\mathbf{u}_{\mathbf{r}_i},t\right)*c_i\left(t-\tau_i-\tau_l\right)e^{j(2\pi f_c t-\mathbf{k}_i^T\mathbf{r}_i)}\\ &\qquad l=0,...,L_r-1,\end{aligned} \tag{2.10}$$

where

$$h_{r,l}\left(\mathbf{u}_{\mathbf{r}_l},t\right)=\mathbf{h}_{r,l}^{T}\left(\mathbf{u}_{\mathbf{r}_l},t\right)\mathbf{u}_{\mathrm{pol}}, \tag{2.11}$$

$\mathbf{h}_{r,l}\left(\mathbf{u}_{\mathbf{r}_l},t\right)$ and $\mathbf{x}_l$ are respectively the effective height and the position of the $l^{\mathrm{th}}$ receiving antenna element, $\tau_l$ is the time needed by the reflected signal to travel from the target to the $l^{\mathrm{th}}$ element, $\mathbf{u}_{\mathbf{r}_l}=\mathbf{r}_l/\|\mathbf{r}_l\|$, and $\beta$ is the complex reflection coefficient of the target.

### 2.1.1 Narrowband Signals

A signal is said to be narrowband, wideband or ultra-wideband (UWB) depending on how large its bandwidth is. The condition for a bandpass signal to be narrowband is given by

$$B\ll f_c, \tag{2.12}$$

where $B$ is the bandwidth of the signal. The signal can be considered in practice as narrowband if its bandwidth is much smaller (at least ten times) than the median frequency, which is usually the carrier frequency [26]. In array signal processing theory, if the different complex envelopes $c_i(t)$ are narrowband, the baseband signal sampled

[1] Note that Equation (2.10) is general: While the transmitting and receiving arrays are both assumed to be centered at the origin of the $x-y$ plane, the different transmitting elements may not be colocated with the receiving elements, and both arrays may have a different number of elements (i.e. $L_t\neq L_r$).

at two different points in space by a receiving ULA does not change too much in amplitude and the different time delays $\tau_i$ and $\tau_l$ can be neglected. Hence, the set of signals at the receiver array can be approximated as [27]

$$c_i\left(t-\tau_i-\tau_l\right) \approx c_i(t). \tag{2.13}$$

Accordingly, (2.10) can be written as

$$\begin{gathered} E_r(\mathbf{x}_l, t)=\frac{\mu_0 \beta}{4\pi\|\mathbf{r}_l\|} e^{-j\mathbf{k}_l^T \mathbf{r}_l} h_{r,l}(\mathbf{u}_{\mathbf{r}_l}, t) * \sum_{i=0}^{L_t-1} \frac{1}{\|\mathbf{r}_i\|} h_{t,i}\left(\mathbf{u}_{\mathbf{r}_i}, t\right) * c_i\left(t\right) e^{j\left(2\pi f_c t-\mathbf{k}_i^T \mathbf{r}_i\right)} \\ l=0, ..., L_r-1, \end{gathered} \tag{2.14}$$

Moreover, if the system is narrowband, (2.14) can be simplified by expressing the electric field in terms of the antenna radiation patterns, which are parameters measurable in the frequency domain. To see this, consider the received electric field in the frequency domain (i.e. the Fourier transform of (2.14))

$$\begin{gathered} E_r(\mathbf{x}_l, f)=\frac{\mu_0 \beta}{4\pi\|\mathbf{r}_l\|} e^{-j\mathbf{k}_l^T \mathbf{r}_l} H_{r,l}(\mathbf{u}_{\mathbf{r}_l}, f) \sum_{i=0}^{L_t-1} \frac{1}{\|\mathbf{r}_i\|} H_{t,i}\left(\mathbf{u}_{\mathbf{r}_i}, f\right) C_i\left(f-f_c\right) e^{-j\mathbf{k}_i^T \mathbf{r}_i} \\ l=0, ..., L_r-1, \end{gathered} \tag{2.15}$$

where $H_{r,l}(\mathbf{u}_{\mathbf{r}_l}, f)$, $H_{t,i}\left(\mathbf{u}_{\mathbf{r}_i}, f\right)$, and $C_i(f)$ are the Fourier transforms of $h_{r,l}(\mathbf{u}_{\mathbf{r}_l}, t)$, $h_{t,i}\left(\mathbf{u}_{\mathbf{r}_i}, t\right)$, and $c_i(t)$ respectively. The electric field is then proportional to the antenna transfer functions $H_{r,l}(\mathbf{u}_{\mathbf{r}_l}, f)$ and $H_{t,i}\left(\mathbf{u}_{\mathbf{r}_i}, f\right)$, which describe the antenna patterns as a function of the frequency, and the azimuth and elevation angles [28]. Note that if the system is narrowband, the transfer functions can be assumed to be constant within the working frequency band. The electric field radiated and/or received by a given narrowband antenna can then be assumed to be proportional to the antenna radiation pattern measured at the working frequency $f_c$ and at a given polarization. Accordingly, the reflected field (2.14) measured at the receiver array can be written under the narrowband assumption, as

$$\begin{gathered} E_r(\mathbf{x}_l, t)=\alpha\beta e^{j2\pi f_c t} \frac{1}{\|\mathbf{r}_l\|} e^{-j\mathbf{k}_l^T \mathbf{r}_l} g_{r,l}(\theta) \sum_{i=0}^{L_t-1} \frac{1}{\|\mathbf{r}_i\|} g_{t,i}(\theta) c_i\left(t\right) e^{-j\mathbf{k}_i^T \mathbf{r}_i} \\ l=0, ..., L_r-1, \end{gathered} \tag{2.16}$$

where $\alpha$ is a proportionality constant and $g_{t,i}(\theta)$ and $g_{r,l}(\theta)$ are respectively the radiation patterns of the $i^{\text{th}}$ transmitter and the $l^{\text{th}}$ receiver elements, measured at frequency $f_c$, at a given elevation angle, and for a polarization in the direction $\mathbf{u}_{\text{pol}}$.

Finally, the electric field at the receiver array can be written in vector notation as

$$\mathbf{E}_r(t) = \alpha\beta e^{j2\pi f_c t}\mathbf{a}_r^*(\theta, R)\,\mathbf{a}_t^H(\theta, R)\,\mathbf{c}(t), \tag{2.17}$$

where $\mathbf{E}_r(t) = \begin{bmatrix} E_r(\mathbf{x}_0, t) & \cdots & E_r(\mathbf{x}_{L_r-1}, t) \end{bmatrix}^T$ is the set of electric fields measured at the receiver array, $\mathbf{c}(t) = \begin{bmatrix} c_0(t) & \cdots & c_{L_t-1}(t) \end{bmatrix}^T$ is the set of complex envelopes of the transmitted signals,

$$\mathbf{a}_t(\theta, R) = \begin{bmatrix} g_{t,0}^*(\theta)\frac{1}{\|\mathbf{r}_0\|}e^{j\mathbf{k}_0^T\mathbf{r}_0} \\ \vdots \\ g_{t,L_t-1}^*(\theta)\frac{1}{\|\mathbf{r}_{L_t-1}\|}e^{j\mathbf{k}_{L_t-1}^T\mathbf{r}_{L_t-1}} \end{bmatrix}, \tag{2.18}$$

$$\mathbf{a}_r(\theta, R) = \begin{bmatrix} g_{r,0}^*(\theta)\frac{1}{\|\mathbf{r}_0\|}e^{j\mathbf{k}_0^T\mathbf{r}_0} \\ \vdots \\ g_{r,L_r-1}^*(\theta)\frac{1}{\|\mathbf{r}_{L_r-1}\|}e^{j\mathbf{k}_{L_r-1}^T\mathbf{r}_{L_r-1}} \end{bmatrix}, \tag{2.19}$$

$$\begin{aligned} \|\mathbf{r}_i\| &= \sqrt{H^2 + \left[D - \left(i - \tfrac{L_t-1}{2}\right)d_t\right]^2}, \\ \|\mathbf{r}_l\| &= \sqrt{H^2 + \left[D - \left(l - \tfrac{L_r-1}{2}\right)d_r\right]^2}, \\ H &= R\cos\theta, \\ D &= R\sin\theta, \end{aligned} \tag{2.20}$$

and $d_t$ and $d_r$ are the inter-element spacings of the transmitting and the receiving arrays respectively.

The terms $\mathbf{a}_t(\theta, R)$ and $\mathbf{a}_r(\theta, R)$ are known as the transmit and receive steering vectors respectively. One may note that every wave vector $\mathbf{k}_i$ is colinear with the corresponding vector $\mathbf{r}_i$ and hence the dot product $\mathbf{k}_i^T\mathbf{r}_i$ is always $\frac{2\pi}{\lambda}\|\mathbf{r}_i\|$. Accordingly, we can write the transmit steering vector as

$$\mathbf{a}_t(\theta, R) = \begin{bmatrix} g_{t,0}^*(\theta)\frac{1}{\|\mathbf{r}_0\|}e^{j\frac{2\pi}{\lambda}\|\mathbf{r}_0\|} \\ \vdots \\ g_{t,L_t-1}^*(\theta)\frac{1}{\|\mathbf{r}_{L_t-1}\|}e^{j\frac{2\pi}{\lambda}\|\mathbf{r}_{L_t-1}\|} \end{bmatrix}. \tag{2.21}$$

The target location is then defined by parameters $[\theta, R]$ where $R$ is the radial distance between the origin of the Cartesian coordinate system and point $\mathbf{p} = [D, H]$, and $\theta$ is the angle between the radial vector and the $y$-axis.

### 2.1.2 The Plane-Wave Approximation

The electromagnetic theory states that the waves radiated by antennas of finite dimensions are spherical; their amplitudes are inversely proportional to the distance to the antenna [24], which is consistent with the signal model (2.17). However, in many cases, the distance from the antenna to the target is large enough to assume that the wavefronts are locally plane. The far-field region can then be divided into a spherical-wave region and a plane-wave region, which are defined by relations between the distance from the antenna to the target position, the wavelength of the transmitted signal and the aperture of the antenna. The limit between the spherical-wave and plane-wave regions is evaluated in Section 2.3.4.

Although the steering vectors $\mathbf{a}_r(\theta, R)$ and $\mathbf{a}_t(\theta, R)$ in the model (2.17) are general and can always be used in the narrowband case, the plane-wave assumption allows us to do some simplifications in the signal model. First, since a plane wavefront propagates in a single direction, all the wave vectors are parallel as shown in Figure 2.3. Then, the dot product $\mathbf{k}_i^T \mathbf{r}_i$ is given by

$$\mathbf{k}_i^T \mathbf{r}_i = \frac{2\pi}{\lambda}\left(D - \left(i - \frac{L_t - 1}{2}\right) d_t\right) \sin\theta + \frac{2\pi}{\lambda} H \cos\theta \qquad i = 0, \ldots, L_t - 1. \tag{2.22}$$

Secondly, given that the inter-element spacing $d_t$ is much smaller than the distance from the array to the target, all the attenuation terms $1/\|\mathbf{r}_i\|$ are approximately the same, i.e. $1/\|\mathbf{r}_i\| \approx 1/R$. Thus, in the narrowband case, the transmit steering vector depends only on the direction $\theta$ of the wavefront and can be expressed as

$$\mathbf{a}_t(\theta) = \frac{1}{R} e^{j\frac{2\pi}{\lambda}(D\sin\theta + H\cos\theta)} \left[ g_{t,i}^*(\theta) e^{j\frac{2\pi}{\lambda}\left(\frac{L_t-1}{2} - i\right) d_t \sin\theta} \right]_{i=0,\ldots,L_t-1}. \tag{2.23}$$

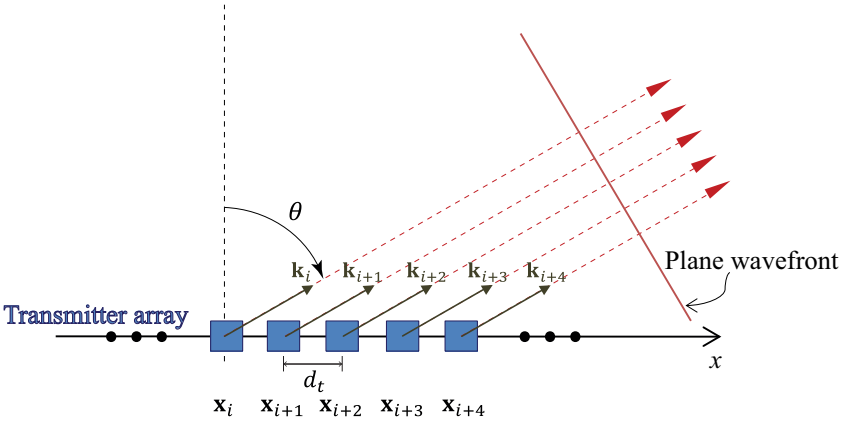


FIGURE 2.3: Far-field plane wavefront transmitted by a ULA.

The term placed outside the vector is common to every element of the array and can be omitted. Therefore, the plane-wave transmit steering vector is finally given by

$$\mathbf{a}_t(\theta) = \left[ g_{t,i}^*(\theta) e^{j\frac{2\pi}{\lambda}(\frac{L_t-1}{2}-i)d_t \sin\theta} \right]_{i=0,\ldots,L_t-1}. \tag{2.24}$$

In the same way, a plane-wave receive steering vector $\mathbf{a}_r(\phi)$ can be defined in terms of the direction $\phi$ of the wavefront traveling from the target to the receiver array. In general, the directions of the transmit and the receive wavefronts are known as Direction-Of-Departure (DOD) and DOA respectively. However, since the architecture of MIMO radar studied in this work has colocated transmitter and receiver arrays, only the term DOA and the angle $\theta$ will be used in the remainder of this document.

### 2.1.3 The Sampled Received Signals in the Narrowband Case

The previously presented signal model was written in terms of the radiated (and received) electric fields which are analog quantities. However, all the signal processing approaches are based on the observed data, obtained after down-conversion and sampling of the received signals. The bandpass signal $x_l^{(\mathrm{mod})}(t)$ received by the $l^{\mathrm{th}}$ antenna element is proportional to the corresponding field $E_r(\mathbf{x}_l, t)$. Thus, letting $x_l(t)$ denote the demodulated version of $x_l^{(\mathrm{mod})}(t)$, the different received discrete-time baseband signals are given by

$$\begin{aligned} x_l(n) &\triangleq x_l\left(t = \tfrac{n}{F_s}\right) \\ n &= 0, \ldots, N-1, \\ l &= 0, \ldots, L_r - 1, \end{aligned} \tag{2.25}$$

where $N$ is the number of samples, and $F_s$ is the sampling frequency which is taken equal to the bandwidth of the signal in the narrowband case. Then, the received signals due to the reflection from $K$ targets in the plane-wave region can be written as

$$\mathbf{x}(n) = \sum_{k=1}^{K} \beta_k \mathbf{a}_r^*(\theta_k)\mathbf{a}_t^H(\theta_k)\mathbf{c}(n) + \mathbf{z}(n), \tag{2.26}$$

where $\mathbf{x}(n) = \begin{bmatrix} x_0(n) & \cdots & x_{L_r-1}(n) \end{bmatrix}^T$, $\mathbf{c}(n) = \begin{bmatrix} c_0(n) & \cdots & c_{L_t-1}(n) \end{bmatrix}^T$ is the set of discrete-time complex envelopes of the transmitted signals, $\mathbf{z}(n) = \begin{bmatrix} z_0(n) & \cdots & z_{L_r-1}(n) \end{bmatrix}^T$ represents the unmodelled interference and noise, and $\theta_k$ and $\beta_k$ are respectively the DOA and the reflection coefficient of the $k^{th}$ target. The radiation patterns of every antenna element of a ULA are usually assumed to be identical, angle-independent and of unity gain, and hence, the plane-wave steering

vectors $\mathbf{a}_t(\theta_k)$ and $\mathbf{a}_r(\theta_k)$ have the following simplified form

$$\mathbf{a}_t(\theta) = \left[e^{j\frac{2\pi}{\lambda}(\frac{L_t-1}{2}-i)d_t\sin\theta}\right]_{i=0,\ldots,L_t-1}, \tag{2.27}$$

$$\mathbf{a}_r(\theta) = \left[e^{j\frac{2\pi}{\lambda}(\frac{L_r-1}{2}-l)d_r\sin\theta}\right]_{l=0,\ldots,L_r-1}. \tag{2.28}$$

The equivalent spherical-wave model can be easily obtained by using the appropriate spherical-wave steering vectors.

Note that in practice the radiation patterns might not be identical from one element to the other and are always angle-dependent. These considerations should be taken into account in the signal model and will be discussed in Chapter 4.

The signal model can be described using matrix notation, by stacking the $N$ received samples in the columns of a matrix $\mathbf{X}$ as

$$\mathbf{X} = \sum_{k=1}^{K} \beta_k \mathbf{a}_r^*(\theta_k)\mathbf{a}_t^H(\theta_k)\mathbf{C} + \mathbf{Z}. \tag{2.29}$$

Both $\mathbf{X}$ and $\mathbf{Z}$ are of dimension $L_r \times N$ while the matrix $\mathbf{C} = \begin{bmatrix}\mathbf{c}(0) & \cdots & \mathbf{c}(N-1)\end{bmatrix}$ is of dimension $L_t \times N$.

## 2.2 Narrowband Direction-of-Arrival Estimation Techniques

Direction-of-Arrival estimation of narrowband sources using arrays of sensors is a topic which has been highly studied in the past years. To date, a variety of DOA estimation techniques have been proposed such as the Maximum Likelihood (ML) technique [29], Capon (also known as Minimum Variance) technique [30], and the MUSIC algorithm [31] among others. Many of those techniques can be directly applied to the radar context considering that the source signals to be detected are the signals reflected by the targets. This section presents two relevant DOA estimation techniques (Capon and MUSIC) and the Generalized Likelihood Ratio Test (GLRT) technique adapted to the context of narrowband MIMO radar.

### 2.2.1 The Capon Beamformer

The Capon beamformer [30] is an array processing technique frequently used for DOA estimation. It uses a spatial filter $\mathbf{w}(\theta)$ constrained to minimize the signal power coming

from all directions but the desired ones. Let $y(n)$ denote the output of the spatial filtering process as

$$y(n) = \mathbf{w}^H(\theta)\mathbf{x}(n). \tag{2.30}$$

The spatial filter $\mathbf{w}(\theta)$ can be obtained by solving the following optimization problem [30][32]

$$\begin{aligned} &\min_{\mathbf{w}} P(\theta) \\ &\text{s.t. } \mathbf{w}^H(\theta)\mathbf{a}_r^*(\theta) = 1, \end{aligned} \tag{2.31}$$

where $P(\theta)$ is the output power defined as

$$P(\theta) = E[|y(n)|^2] = \mathbf{w}^H(\theta)\mathbf{R}_x\mathbf{w}(\theta), \tag{2.32}$$

$E[\cdot]$ denotes the mathematical expectation, and $\mathbf{R}_x = E[\mathbf{x}(n)\mathbf{x}^H(n)]$ is the auto-covariance matrix of the received signals. The optimal vector $\overset{\triangle}{\mathbf{w}}(\theta)$ can be found using the method of Lagrange multipliers. It is given by (see Appendix A)

$$\overset{\triangle}{\mathbf{w}}(\theta) = \frac{\mathbf{R}_x^{-1}\mathbf{a}_r^*(\theta)}{\mathbf{a}_r^T(\theta)\mathbf{R}_x^{-1}\mathbf{a}_r^*(\theta)}. \tag{2.33}$$

By replacing $\mathbf{w}(\theta)$ by $\overset{\triangle}{\mathbf{w}}(\theta)$ in Equation (2.32), we obtain the Capon's spatial spectrum

$$P_{cap}(\theta) = \frac{1}{\mathbf{a}_r^T(\theta)\mathbf{R}_x^{-1}\mathbf{a}_r^*(\theta)}, \tag{2.34}$$

and the DOAs of the targets can be found by searching for the maxima of $P_{cap}(\theta)$.

Note that in practice, the auto-covariance matrix $\mathbf{R}_x$ is estimated using a finite set of $N$ samples of $\mathbf{x}(n)$. This estimate can be found by calculating

$$\hat{\mathbf{R}}_x = \frac{1}{N}\mathbf{X}\mathbf{X}^H. \tag{2.35}$$

### 2.2.2 MUSIC

The MUSIC algorithm is a subspace-based array processing technique originally proposed to estimate the DOAs of uncorrelated narrowband sources [31]. It uses eigenvalue decomposition to separate the auto-covariance matrix of the observed data into a signal and a noise subspace. The orthogonality between both subspaces is then exploited to locate the sources. The MUSIC algorithm is based on the following signal model:

$$\mathbf{x}(n) = \sum_{k=1}^{K} \mathbf{a}_r^*(\theta_k)s_k(n) + \mathbf{z}(n), \tag{2.36}$$

where $\mathbf{x}(n)$ is the $L_r \times 1$ observed data vector, $s_k(n)$ is the $k^{\text{th}}$ source signal to be detected, and $\mathbf{z}(n)$ denotes a white additive noise which is independent from the transmitted signals $\mathbf{s}(n)$ and has a common variance $\sigma^2$ for all sensors. For notation simplicity, the steering vectors can be stacked in the columns of a matrix as $\mathbf{A} = \begin{bmatrix} \mathbf{a}_r^*(\theta_1) & \cdots & \mathbf{a}_r^*(\theta_K) \end{bmatrix}$ and the signal model becomes

$$\mathbf{x}(n) = \mathbf{A}\mathbf{s}(n) + \mathbf{z}(n), \tag{2.37}$$

where $\mathbf{s}(n) = \begin{bmatrix} s_1(n) & \cdots & s_K(n) \end{bmatrix}^T$. The auto-covariance matrix of the received signals $\mathbf{x}(n)$ is given by

$$\mathbf{R}_x = E[\mathbf{x}(n)\mathbf{x}^H(n)] = \mathbf{A}E[\mathbf{s}(n)\mathbf{s}^H(n)]\mathbf{A}^H + E[\mathbf{z}(n)\mathbf{z}^H(n)]. \tag{2.38}$$

Then, denoting $\mathbf{R}_s = E[\mathbf{s}(n)\mathbf{s}^H(n)]$ as the source auto-covariance matrix, the auto-covariance matrix $\mathbf{R}_x$ becomes

$$\mathbf{R}_x = \mathbf{A}\mathbf{R}_s\mathbf{A}^H + \sigma^2\mathbf{I}, \tag{2.39}$$

where $\mathbf{I}$ denotes the $L_r \times L_r$ identity matrix. Using a spectral decomposition, the auto-covariance matrix of the received signals can be expressed as [1]

$$\mathbf{R}_x = \mathbf{U}\mathbf{\Lambda}\mathbf{U}^H, \tag{2.40}$$

where $\mathbf{U} = \begin{bmatrix} \mathbf{u}_1 & \cdots & \mathbf{u}_{L_r} \end{bmatrix}$ is a matrix whose columns are the eigenvectors of $\mathbf{R}_x$, and $\mathbf{\Lambda} = \text{diag}(\lambda_1, \ldots, \lambda_{L_r})$ is a diagonal matrix containing the eigenvalues of $\mathbf{R}_x$ in decreasing order (i.e. $\lambda_1 \geq \cdots \geq \lambda_{L_r} > 0$). The latter spectral decomposition can be written as

$$\mathbf{R}_x = \mathbf{U}_s\mathbf{\Lambda}_s\mathbf{U}_s^H + \mathbf{U}_n\mathbf{\Lambda}_n\mathbf{U}_n^H, \tag{2.41}$$

where $\mathbf{\Lambda}_s = \text{diag}(\lambda_1, \ldots, \lambda_K)$ and $\mathbf{\Lambda}_n = \text{diag}(\lambda_{K+1}, \ldots, \lambda_{L_r})$, and $\mathbf{U}_s$ and $\mathbf{U}_n$ are matrices composed by the eigenvectors of the signal-plus-noise subspace and the noise-only subspace respectively. The largest $K$ eigenvalues $\lambda_i$ of $\mathbf{R}_x$ correspond to the signal-plus-noise subspace and the $L_r - K$ smallest eigenvalues are equal to $\sigma^2$.

Every eigenvector of the noise-only subspace is orthogonal to the signal-plus-noise subspace, and hence orthogonal to $\mathbf{A}$. This can be seen from the eigenvalue equation of $\mathbf{R}_x$

$$\begin{aligned} (\mathbf{R}_x - \lambda_i\mathbf{I})\,\mathbf{u}_i &= \mathbf{0} \\ i &= 1, 2, \ldots, L_r. \end{aligned} \tag{2.42}$$

Then, using only the noise subspace eigenvectors and replacing $\mathbf{R}_x$ by its expression (2.39), the latter equation becomes

$$\begin{aligned} \mathbf{A}\mathbf{R}_s\mathbf{A}^H\mathbf{u}_i &= \mathbf{0} \\ i &= K+1,\ldots,L_r. \end{aligned} \tag{2.43}$$

Since the matrices $\mathbf{A}$ and $\mathbf{R}_s$ are full rank (assuming that the source signals are non coherent), the matrix $\mathbf{A}\mathbf{R}_s\mathbf{A}^H$ is also full rank and the noise eigenvectors must be orthogonal to $\mathbf{A}$, i.e. $\mathbf{A}^H\mathbf{u}_i = \mathbf{0}$. Then we have

$$\begin{aligned} \mathbf{a}_r^T(\theta)\mathbf{u}_i &= 0 \\ i &= K+1,\ldots,L_r. \end{aligned} \tag{2.44}$$

Note that $\{\theta_1,\ldots,\theta_K\}$ are the only possible solutions to Equation (2.44). Based on this orthogonality, a MUSIC spatial spectrum can be defined as

$$P_{MUSIC}(\theta) = \frac{1}{\mathbf{a}_r^T(\theta)\mathbf{U}_n\mathbf{U}_n^H\mathbf{a}_r^*(\theta)}. \tag{2.45}$$

In the case of MIMO radar, the model described in Equation (2.26) is equivalent to (2.36) where the source signals $s_k(n)$ are the signals reflected by the targets, i.e.

$$\mathbf{s}(n) = \begin{bmatrix} s_1(n) \\ \vdots \\ s_K(n) \end{bmatrix} = \begin{bmatrix} \beta_1\mathbf{a}_t^H(\theta_1)\mathbf{c}(n) \\ \vdots \\ \beta_K\mathbf{a}_t^H(\theta_K)\mathbf{c}(n) \end{bmatrix}. \tag{2.46}$$

Then, Equation (2.44) holds only if the equivalent of $\mathbf{R}_s$ is still full rank. By defining

$$\mathbf{B} = \begin{bmatrix} \beta_1\mathbf{a}_t^H(\theta_1) \\ \vdots \\ \beta_K\mathbf{a}_t^H(\theta_K) \end{bmatrix}, \tag{2.47}$$

Equation (2.46) can be written as

$$\mathbf{s}(n) = \mathbf{B}\mathbf{c}(n). \tag{2.48}$$

Then, the auto-covariance matrix $\mathbf{R}_s$ is given by

$$\begin{aligned} \mathbf{R}_s &= E\left[\mathbf{B}\mathbf{c}(n)\mathbf{c}^H(n)\mathbf{B}^H\right] \\ &= \mathbf{B}\mathbf{R}_c\mathbf{B}^H. \end{aligned} \tag{2.49}$$

Given that $\mathbf{B}$ is full rank, $\mathbf{R}_s$ will be full rank only if $\mathbf{R}_c$ is also full rank, which is usually

the case. Under this condition, the MUSIC algorithm can be applied to the MIMO radar signal model.

### 2.2.3 The Generalized Likelihood Ratio Test (GLRT)

The GLRT detection technique for narrowband MIMO radar was derived in [32] assuming that the columns of the noise term $\mathbf{Z}$ of Equation (2.29) are i.i.d. circularly symmetric complex Gaussian random vectors with zero mean and unknown covariance matrix $\mathbf{R}_z$. The GLR is given by [32][33]

$$\rho(\theta) = 1 - \left[\frac{\max_{\mathbf{R}_z} f(\mathbf{X}|\beta = 0, \mathbf{R}_z)}{\max_{\beta,\mathbf{R}_z} f(\mathbf{X}|\beta, \mathbf{R}_z)}\right]^{\frac{1}{N}}, \tag{2.50}$$

where

$$f(\mathbf{X}|\beta, \mathbf{R}_z) = \pi^{-NL_r}|\mathbf{R}_z|^{-N} e^{-\mathrm{tr}[\mathbf{R}_z^{-1}(\mathbf{X}-\beta\mathbf{a}_r^*(\theta)\mathbf{a}_t^H(\theta)\mathbf{C})(\mathbf{X}-\beta\mathbf{a}_r^*(\theta)\mathbf{a}_t^H(\theta)\mathbf{C})^H]} \tag{2.51}$$

is the probability density function (PDF) of the received signals given the parameters $\beta$ (i.e. the target reflexion coefficient) and $\mathbf{R}_z$, and $\mathrm{tr}[\cdot]$ and $|\cdot|$ denote the trace and the determinant of a matrix, respectively. The fractional part of Equation (2.50) is the ratio between two likelihood functions; the first one under the noise-alone hypothesis (without any target) and the second one under signal-plus-noise hypothesis (with a target in direction $\theta$). If there is a target in a direction $\theta$ of interest, the denominator $\max_{\beta,\mathbf{R}_z} f(\mathbf{X}|\beta, \mathbf{R}_z)$ will be much greater than $\max_{\mathbf{R}_z} f(\mathbf{X}|\beta = 0, \mathbf{R}_z)$ and then the value of $\rho(\theta)$ will be close to one. Otherwise, if there is no target at $\theta$, the value of $\rho(\theta)$ will approach zero. After some derivations (see Appendix A), (2.50) can be written as

$$\rho(\theta) = 1 - \frac{\mathbf{a}_r^T(\theta)\hat{\mathbf{R}}_x^{-1}\mathbf{a}_r^*(\theta)}{\mathbf{a}_r^T(\theta)\hat{\mathbf{Q}}^{-1}\mathbf{a}_r^*(\theta)}, \tag{2.52}$$

where $\hat{\mathbf{Q}}$ is defined as

$$\hat{\mathbf{Q}} = \hat{\mathbf{R}}_x - \frac{\hat{\mathbf{R}}_{xc}\mathbf{a}_t(\theta)\mathbf{a}_t^H(\theta)\hat{\mathbf{R}}_{xc}^H}{\mathbf{a}_t^H(\theta)\hat{\mathbf{R}}_c\mathbf{a}_t(\theta)}, \tag{2.53}$$

$\hat{\mathbf{R}}_c$ is the estimated auto-covariance matrix of the received and the transmitted signals, and $\hat{\mathbf{R}}_{xc}$ is the estimated cross-covariance matrix between the received and the transmitted signals. The covariance matrices are estimated as

$$\begin{aligned} \hat{\mathbf{R}}_c &= \tfrac{1}{N}\mathbf{C}\mathbf{C}^H, \\ \hat{\mathbf{R}}_{xc} &= \tfrac{1}{N}\mathbf{X}\mathbf{C}^H. \end{aligned} \tag{2.54}$$

The use of the GLRT to detect the target DOAs is of particular interest since it is able to reject interference or jammers which are uncorrelated with the transmitted signals.

## 2.3 Narrowband Simulations

The previously described DOA estimation techniques for MIMO radar are investigated in this section using MATLAB simulations. The different strengths and weaknesses of each one are discussed, including spatial resolution and robustness against noise and jammers. Moreover, the limit between the spherical-wave and the plane-wave regions is also studied, showing when a target can really be assumed to be in the plane-wave region and avoid the errors which may occur due to a wrong use of the plane-wave approximation.

### 2.3.1 Simulation Parameters

Consider a MIMO radar with colocated antennas whose transmitter and receiver arrays are two ULA of $L_t = L_r = L = 10$ elements, and the inter-element spacings are set to $d_t = d_r = d = \lambda/2$. The transmitted signals $\{c_i(n)\}_{i=0}^{L_t-1}$ are independent sequences of $N = 512$ Quadrature Phase Shift Keying (QPSK) symbols. Each symbol has a mean power of $P_s = 0.1$. The carrier frequency is set to $f_c = 5.8$ GHz. In the following simulations, the radiation patterns of the transmitting and receiving elements are assumed to be identical, angle-independent and of unity gain.

### 2.3.2 Target Detection

#### 2.3.2.1 Detection in the Plane-Wave Region

Consider $K = 3$ targets located in the plane-wave region at $\theta_1 = -60°$, $\theta_2 = 0°$, $\theta_3 = 40°$ with reflection coefficients $\beta_1 = \beta_2 = \beta_3 = \beta = 1$. The received signals are constructed using the plane-wave narrowband signal model (2.29) where the noise term is modeled as white Gaussian noise such that the SNR equals to 10 dB. Here the SNR is defined as the ratio between the mean power of the signals reflected by the targets (measured by the receiver array) and the mean power of the noise term. By denoting the signals reflected by the targets as

$$\begin{aligned} \breve{\mathbf{x}}(n) &= \sum_{k=1}^{K} \beta_k \mathbf{a}_r^*(\theta_k)\mathbf{a}_t^H(\theta_k)\mathbf{c}(n), \\ \breve{\mathbf{x}}(n) &= \begin{bmatrix} \breve{x}_0(n) & \cdots & \breve{x}_{L_r-1}(n) \end{bmatrix}^T, \end{aligned} \tag{2.55}$$

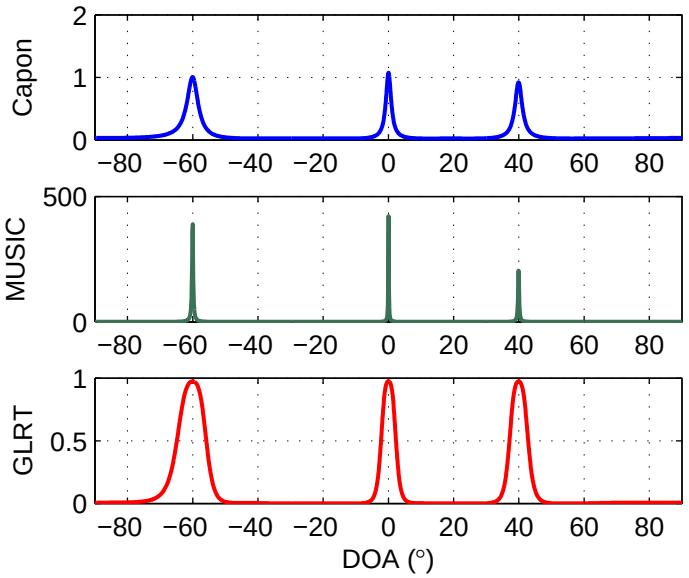


FIGURE 2.4: Capon, MUSIC, and GLRT spectra for three targets located in the plane-wave region at $\theta_1 = -60°$, $\theta_2 = 0°$, and $\theta_3 = 40°$, and an SNR of 10 dB.

the SNR (in dB) is then given by

$$\text{SNR} = 10\log_{10}\left[\frac{\sum_{n=0}^{N-1}\sum_{l=0}^{L_r-1}|\breve{x}_l(n)|^2}{\sum_{n=0}^{N-1}\sum_{l=0}^{L_r-1}|z_l(n)|^2}\right]. \tag{2.56}$$

Figure 2.4 shows the Capon, MUSIC and GLRT spectra constructed using a grid of angles $\theta \in [-90°, 90°]$ with a mesh grid size of 0.1°. The MUSIC spectrum has the best resolution, showing the sharpest peaks, followed by Capon. Since the SNR is relatively good (10 dB), the three techniques can clearly identify the DOAs of the targets.

However, in the case of a low SNR, such as -10 dB, the target DOAs can hardly be found in both Capon and MUSIC spectra as shown in Figure 2.5, and some peaks can appear as noise in this particular example. On the other hand, even though the values of the GLR are far from 1, the GLRT seems more robust to noise since the peaks corresponding to the targets can still be clearly seen.

Consider now the three targets ($\theta_1 = -60°$, $\theta_2 = 0°$, $\theta_3 = 40°$) with different reflection coefficients $\beta_1 = 1$, $\beta_2 = 0.5$, and $\beta_3 = 0.2$. Figure 2.6 shows the spatial spectra of Capon, MUSIC, and GLRT for an SNR of 10 dB. As we can see, both Capon and MUSIC are very sensitive to the $\beta_k$ coefficients: The peaks corresponding to targets of $\beta_2 = 0.5$ (at $\theta_2 = 0°$) and $\beta_3 = 0.2$ (at $\theta_3 = 40°$) can hardly be seen. On the other hand, the three

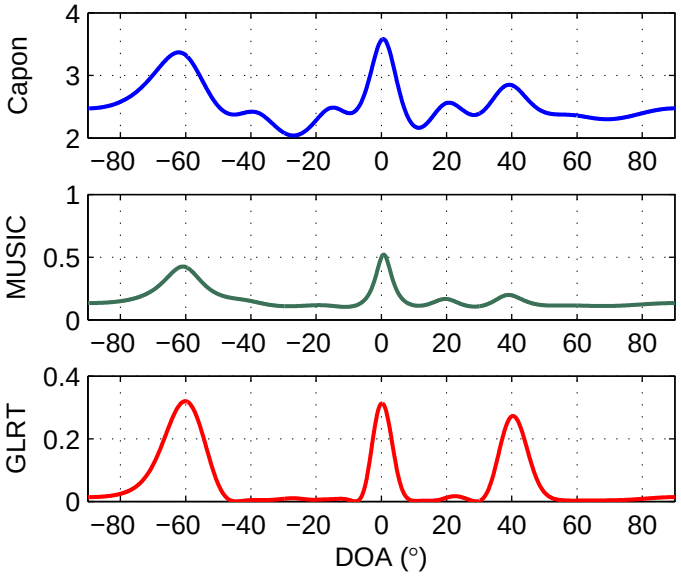


FIGURE 2.5: Capon, MUSIC, and GLRT spectra for three targets located in the plane-wave region at $\theta_1 = -60°$, $\theta_2 = 0°$, and $\theta_3 = 40°$, and an SNR of -10 dB.

peaks clearly appear in the GLRT spectrum. Even for a low reflection coefficient, the values of the GLR are very close to 1 in the target directions.

The high resolution of MUSIC can be useful to detect targets which are closely spaced to each other. This is illustrated by Figure 2.7 where two targets located at $\theta_1 = 17°$ and $\theta_2 = 22°$ are considered and the SNR is set to 10 dB. As shown, while the Capon and GLRT techniques are unable to resolve the targets, the MUSIC spectrum has two sharp peaks corresponding to the two DOAs. In this particular example the DOAs estimated by MUSIC were $[\hat{\theta}_1, \hat{\theta}_2]_{\text{MUSIC}} = [17.3°, 21.8°]$.

However, it is difficult to determine the minimum angular spacing between two targets that a given technique is able to detect since it depends on several parameters, including the number of antenna elements, the target positions, the SNR and the orthogonality of the transmitted waveforms.

As a conclusion, the MUSIC algorithm offers the best resolution among the three studied detection techniques and it is useful to detect closely spaced targets. As for the GLRT, even though it is not able to resolve two closely spaced targets, it is the most robust against noise and the least sensitive to the target reflection coefficients.

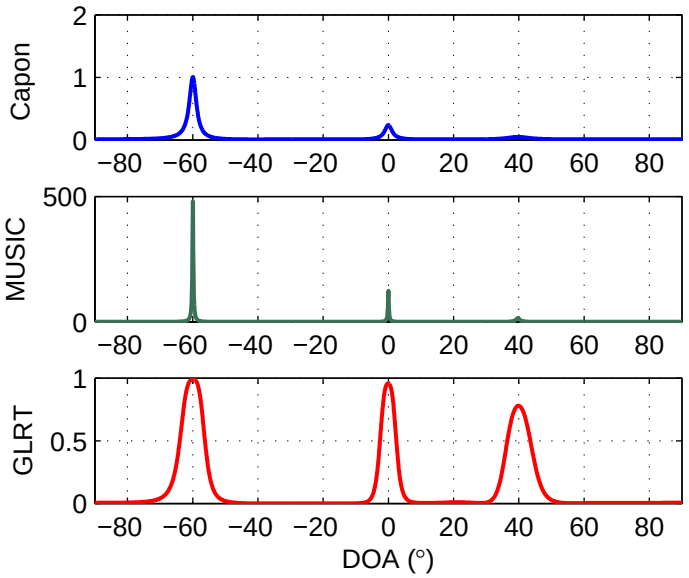


FIGURE 2.6: Capon, MUSIC, and GLRT spectra for three targets located in the plane-wave region ($\theta_1 = -60°$, $\theta_2 = 0°$, $\theta_3 = 40°$) with different reflection coefficients ($\beta_1 = 1$, $\beta_2 = 0.5$, $\beta_3 = 0.2$).

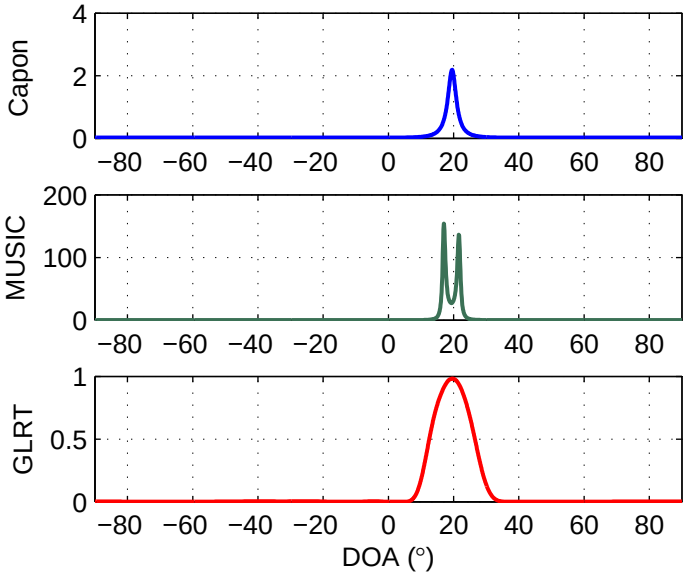


FIGURE 2.7: Capon, MUSIC, and GLRT spectra for two closely spaced targets located in the plane-wave region ($\theta_1 = 17°$, $\theta_2 = 22°$).

#### 2.3.2.2 Detection in the Spherical-Wave Region

The signal model (2.29) is also applicable for a detection in the spherical-wave region by using the appropriate steering vectors, which are defined as (see Section 2.1.1)

$$\mathbf{a}_t(\theta, R) = \begin{bmatrix} \frac{1}{\|\mathbf{r}_0\|} e^{j\frac{2\pi}{\lambda}\|\mathbf{r}_0\|} \\ \vdots \\ \frac{1}{\|\mathbf{r}_{L_t-1}\|} e^{j\frac{2\pi}{\lambda}\|\mathbf{r}_{L_t-1}\|} \end{bmatrix}, \tag{2.57}$$

$$\mathbf{a}_r(\theta, R) = \begin{bmatrix} \frac{1}{\|\mathbf{r}_0\|} e^{j\frac{2\pi}{\lambda}\|\mathbf{r}_0\|} \\ \vdots \\ \frac{1}{\|\mathbf{r}_{L_r-1}\|} e^{j\frac{2\pi}{\lambda}\|\mathbf{r}_{L_r-1}\|} \end{bmatrix}. \tag{2.58}$$

Since such steering vectors depend on the direction $\theta_k$ and the distance $R_k$ from the center of the array to the $k^{\text{th}}$ target (see Figure 2.8), the DOA estimation techniques must be performed along with a two-dimensional search. The target DOAs are then found by searching for the maxima of the three dimensional spatial spectra ($P_{cap}(\theta, R)$, $P_{MUSIC}(\theta, R)$, and $\rho(\theta, R)$).

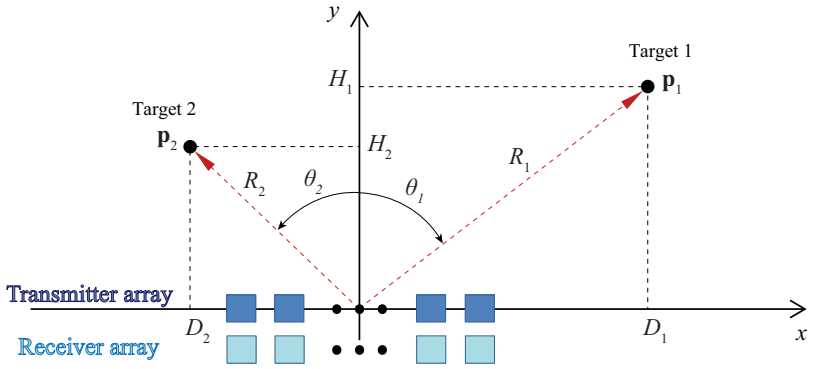


FIGURE 2.8: MIMO radar with colocated transmitter and receiver arrays, and two targets.

Consider $K = 3$ targets located in the spherical-wave region of the transmitter and receiver arrays, with $\beta_1 = \beta_2 = \beta_3 = \beta = 1$ and with parameters $[\theta_1, R_1] = [-65°, 0.35 \text{ m}]$, $[\theta_2, R_2] = [5°, 0.45 \text{ m}]$ and $[\theta_3, R_3] = [45°, 0.55 \text{ m}]$ respectively. Figure 2.9 shows the spatial spectra of Capon, MUSIC, and GLRT, constructed using a grid of angles $\theta \in [-90°, 90°]$ with a mesh grid size of 0.1° and a grid of distances $R \in [0.1 \text{ m}, 1.1 \text{ m}]$ with a step of 0.01 m. The SNR was set to 10 dB. As shown, the high resolution of MUSIC allows an easy estimation of the parameters $[\theta_k, R_k]$ of the targets; however, the lobes become larger as the distance $R_k$ increases. The GLRT can also be used to estimate both parameters by searching for the maxima in angular and

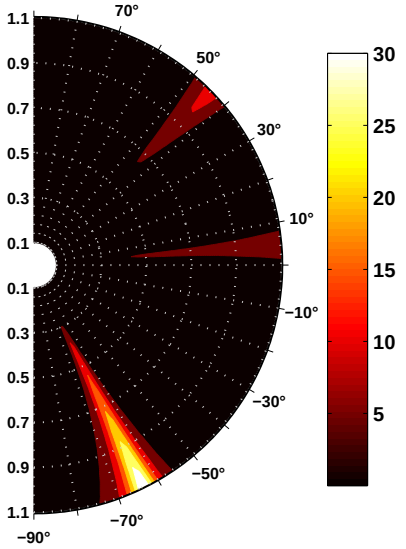


(a)

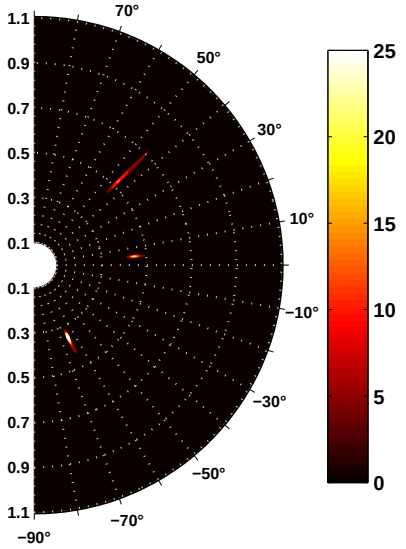


(b)

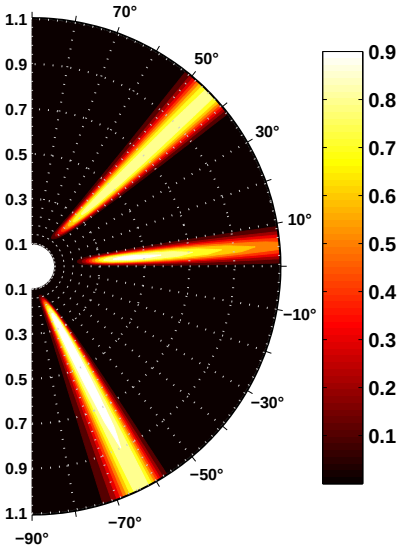


(c)

FIGURE 2.9: (a) Capon, (b) MUSIC, and (c) GLRT spectra. (Targets located in the spherical-wave region at $[\theta_1, R_1] = [-65°, 0.35 \text{ m}]$, $[\theta_2, R_2] = [5°, 0.45 \text{ m}]$ and $[\theta_3, R_3] = [45°, 0.55 \text{ m}]$)

radial senses. However, the lobes of GLRT are much wider than those of MUSIC. On the other hand, Capon does not allow estimating the distances from the arrays to the targets since there is no maximum at positions $[\theta_k, R_k]$. It can only be used to estimate the parameters $\theta_k$ for known distances $R_k$ by searching for the maxima in an angular sense only.

### 2.3.3 Jammer Rejection

In real world environments, the signals received by a radar might be mixed with several undesired waves coming from sources external to the radar, such as communication signals (satellite, GPS, WiFi, ...), signals coming from other radars, or jammers. To observe the influence of this kind of interferences on the DOA estimation techniques let us consider $K = 3$ targets located in the plane-wave region at $\theta_1 = -60°$, $\theta_2 = 0°$, $\theta_3 = 40°$ with $\beta = 1$. A strong jammer located in the plane-wave region at 20° transmits an unknown QPSK modulated signal of magnitude 1000, i.e. 70 dB above the transmitted signal power $P_s$. The SNR is set to 10 dB as defined in (2.56), where the noise terms $z_l(n)$ do not include the jamming signal.

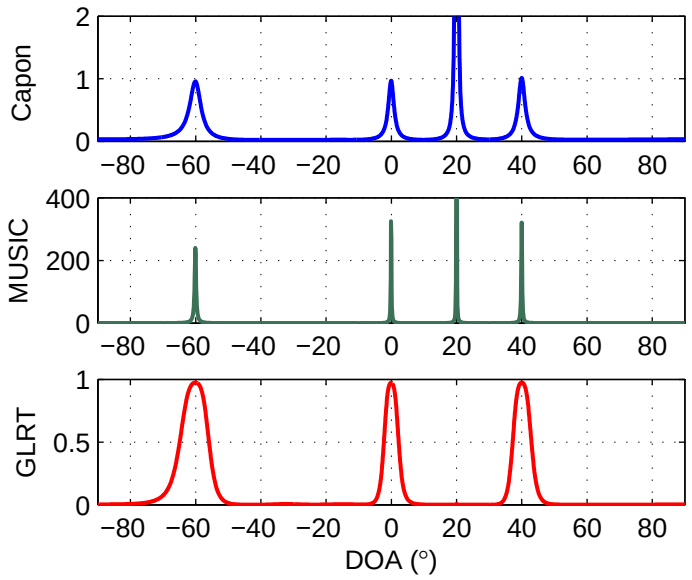


FIGURE 2.10: Capon, MUSIC, and GLRT spectra in the presence of a jammer at 20°.

As shown in Figure 2.10, both Capon and MUSIC spectra show a high peak due to the jammer at 20°, which could lead to a wrong detection. On the other hand, the GLRT totally rejects the strong jammer by showing only the peaks corresponding to the targets. Despite its lower resolution compared to MUSIC and Capon, the GLRT is very robust against interference and jammers and can be used to estimate the number of targets.

### 2.3.4 Limit Between the Spherical-Wave and Plane-Wave Regions

The use of the general form of the steering vectors (2.57) and (2.58) (which takes into account the spherical shape of the wavefronts) may allow in theory the estimation of both parameters $[\theta_k, R_k]$ of the targets even if they are located in the plane-wave

region. However, this processing requires a bidimensional search and therefore a much higher processing time. Moreover, as the distance between the targets and the arrays increases, more distances should be included in the grid of distances $R$, making the processing even heavier. Hence, the use of the plane-wave approximation may be more appropriate in some cases to reduce the processing time at the expense of estimating only the directions $\theta_k$. The question is to determine when a target can be considered to be in the spherical-wave or in the plane-wave region of a MIMO radar. Even though the far-field condition (2.1) given by antenna theory is often used in signal processing as a plane-wave condition, the approximation done in the signal model might be inaccurate in a particular zone of the far-field region and the real plane-wave condition might differ from $R > 2\Delta^2/\lambda$ (where $\Delta$ is the largest dimension of the antenna). The limit between spherical-wave and plane-wave regions is studied herein from a signal processing point of view.

To evaluate the limit between spherical-wave and plane-wave regions, the Mean Square Error (MSE) of the estimated DOA (in degrees) has been computed for a target at 60° located at different distances, using a grid of values of $R$ going from 0.2 m to 10 m by a step of 0.05 m. For every distance, 100 different Monte Carlo trials have been performed. The signal model used to simulate the signals going toward and coming from the target is

$$\mathbf{X} = \sum_{k=1}^{K} \beta_k \mathbf{a}_r^*(\theta_k, R)\mathbf{a}_t^H(\theta_k, R)\mathbf{C} + \mathbf{Z}, \tag{2.59}$$

considering the spherical shape of the wavefronts. Then, the Capon, MUSIC, and GLRT techniques were performed to estimate the DOA using always the plane-wave steering vectors $\mathbf{a}_t(\theta)$ and $\mathbf{a}_r(\theta)$ defined by (2.27) and (2.28) respectively. This allows us to see the error generated by using the plane-wave approximation for different distances $R$.

The first simulation was performed for three different SNR levels (-10, 0, and 10 dB) considering a transmitter and a receiver antenna arrays of $L_t = L_r = L = 10$ elements. The results are shown in Figure 2.11. As expected, the error is high for short distances $R$ since the target is in the spherical-wave region, and it decreases as the distance becomes larger. We will consider that the target is in the plane-wave region once the MSE becomes stable, which means that the error introduced by the plane-wave approximation is no longer visible. From the MSE curves obtained with an SNR of 10 dB, the frequently used condition $R = 2\Delta^2/\lambda$ does not hold for any of the three DOA estimation techniques, and the error actually stabilizes at $R \approx 5\Delta^2/\lambda$, with $\Delta = (L-1)d$. However, for the case of lower SNR values the transition between the spherical-wave and plane-wave regions is less visible and the condition $R > 2\Delta^2/\lambda$ is acceptable. If the DOA estimation techniques are performed using the spherical-wave steering vectors instead, the MSE should be relatively constant for all distances $R$ (for a fixed SNR). This is illustrated by

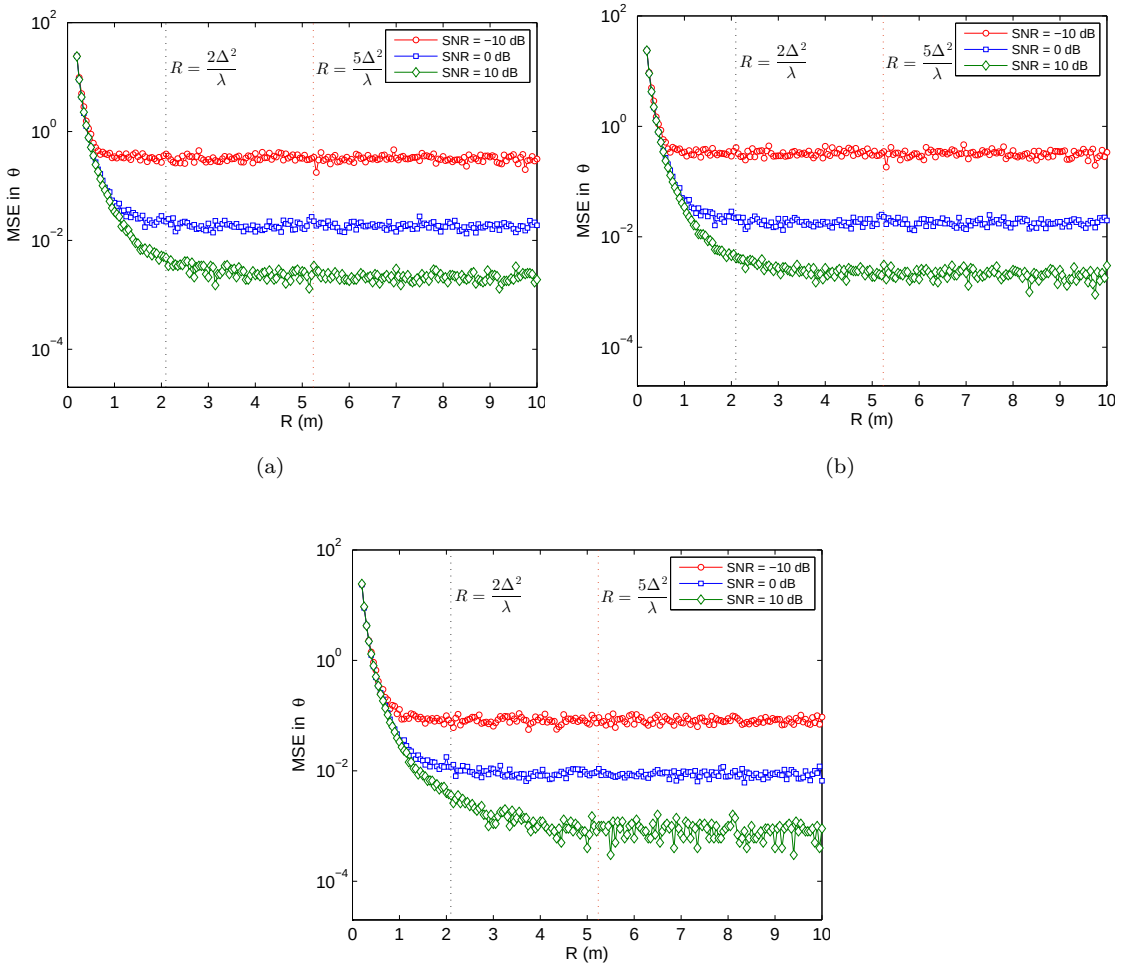


FIGURE 2.11: MSE in $\theta$ for (a) Capon, (b) MUSIC, and (c) GLRT, for different SNR (plane-wave processing).

Figure 2.12, where the MSEs of the DOA estimated by the GLRT using spherical-wave and plane-wave processing are compared in the case of an SNR of 10 dB. Note that both MSEs have approximately the same values after the plane-wave condition $R > 5\Delta^2/\lambda$, proving that the error due to the plane-wave approximation can be neglected.

A second simulation was performed to observe the evolution of the plane-wave condition as a function of the size of the antenna arrays. The simulation was done for a fixed SNR of 10 dB and three different antenna sizes (5, 10, and 15 elements). The results are shown in Figure 2.13. We can clearly verify that the plane-wave condition is dependent of the size of the antenna arrays. To consider that a target is located in the plane-wave region, the distance between the target and the center of the array must be all the more important as the arrays are large.

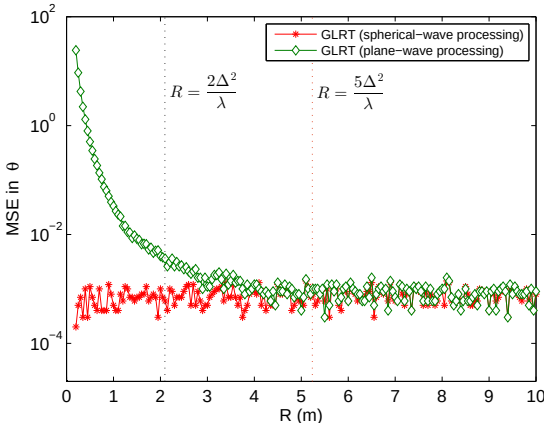


FIGURE 2.12: MSE in $\theta$ for GLRT after spherical-wave or plane-wave processing (SNR = 10 dB).

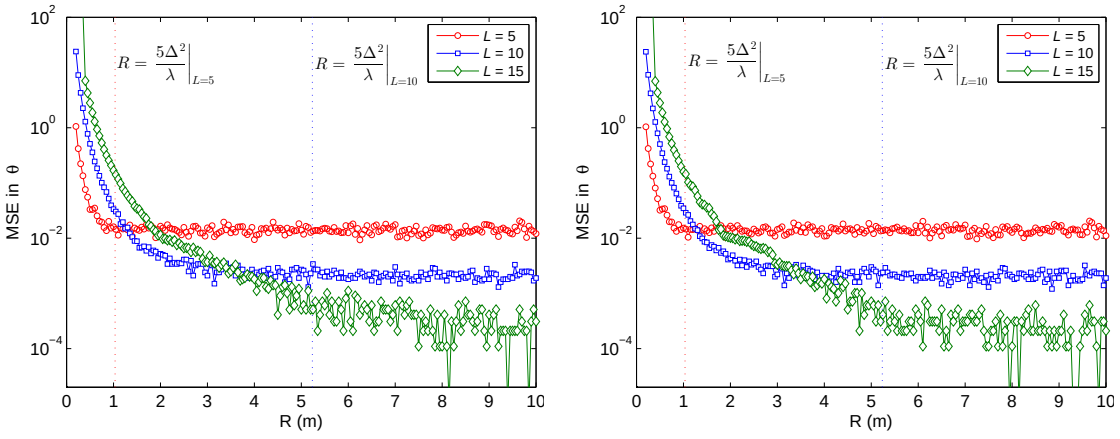


(a) (b)

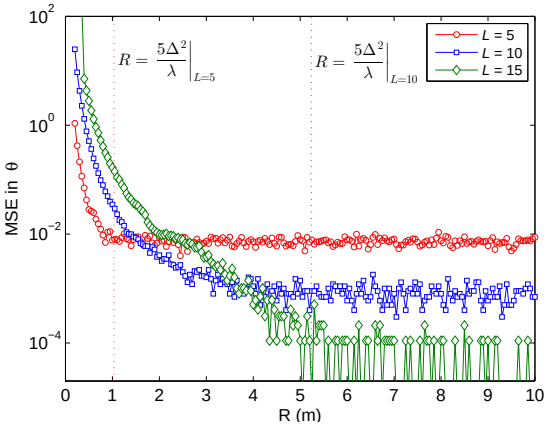


(c)

FIGURE 2.13: MSE in $\theta$ for (a) Capon, (b) MUSIC, and (c) GLRT, for different antenna array sizes (plane-wave processing).

## 2.4 Summary

The signal model of narrowband MIMO radar with colocated antennas was presented, followed by the description of the Capon, MUSIC, and GLRT methods as DOA estimation techniques of non-moving targets. The simulations showed that MUSIC offers the best angular resolution followed by Capon and GLRT. Because of its high resolution, MUSIC is able to resolve closely spaced targets. As for the GLRT, even though it is not able to detect closely spaced targets, it is the most robust against noise and the less sensitive to the target reflection coefficients among the three techniques. Moreover, the GLRT has the capability of rejecting strong interference or jammers which are uncorrelated with the transmitted signals.

Also, we investigated the limit between the spherical-wave and plane-wave regions from a signal processing point of view in order to determine when a target can be considered to be in the spherical-wave or in the plane-wave region of a MIMO radar. Even though the plane-wave condition $R > 2\Delta^2/\lambda$ is acceptable in low SNR cases, the plane-wave region is actually farther away and some error might be introduced by a wrong use of the plane-wave approximation. Moreover, the actual SNR is often difficult to determine, so the plane-wave condition $R > 5\Delta^2/\lambda$ seems to be more appropriate since it applies for low and high SNR levels, and for the three tested antenna sizes (5, 10, and 15 elements). For other antenna sizes, the same study should be done in order to determine the right plane-wave condition.

# Chapter 3

# Wideband MIMO Radar with Colocated Antennas

The use of wideband signals for radar systems has shown to provide many benefits. According to radar theory, the radar range resolution is inversely proportional to the bandwidth of the transmitted signal [34], which means that the range resolution can be improved by the use of wideband and UWB signals. Unlike the narrowband case, where the target dimensions are smaller than the range resolution, in the wideband case the target dimensions can be larger than the range resolution and the targets can be modeled as multi-point targets. Then, target recognition can be achieved by exploiting the different short-time target echoes [35][36]. This feature is also useful for detecting several closely spaced targets. Additionally, wideband signals can increase the immunity of radar systems to external narrowband jammers and noise [37].

Wideband signals can be generated in several ways. The simplest wideband waveform is a pulse whose width is chosen to achieve a desired range resolution. Although reducing the pulse width allows increasing the range resolution, the average power is reduced (for a fixed pulse amplitude) making the targets harder to be detected. This problem might be solved by transmitting high peak-power pulses but this is in general expensive and difficult to achieve in practice. Nevertheless, high range resolution using low peak-power pulses is still attainable through the use of modern pulse compression techniques [38].

Another type of wideband waveforms is the Continuous Wave (CW) signal (which contains many frequency components), such as linear Frequency Modulated (FM) chirps, stepped-frequency waveforms, and random (or pseudo-random) signals [36]. The use of random signals for radar has many advantages. Indeed, they allow transmitting a convenient average power while having a very high range resolution. Additionally, random signals are suitable for military applications since they are

difficult to detect by other radar systems, and offer good interference suppression capabilities if correlation processing is done at the receiver. Moreover, random signals are also very appropriate for civilian applications since they provide excellent electromagnetic compatibility (EMC) performance [36][39]. In this chapter, only the random-based wideband signals are taken into account.

Even though narrowband MIMO radars have been deeply investigated in recent years, the assumptions done in the signal model no longer hold in the case of wideband signals, and narrowband detection techniques cannot be directly applied. The chapter is organized as follows: The wideband signal model of MIMO radar is described in Section 3.1, followed by the description of the simulation procedure in Section 3.2. Next, two existing wideband waveform design techniques are investigated in Section 3.3. In Section 3.4, we propose a multiband waveform design technique aiming at decorrelating the signals reflected by the targets, which allows applying many wideband array processing detection techniques in the context of MIMO radar. Moreover, the adaptation of some DOA estimation techniques is presented in Section 3.5 along with a performance comparison.

## 3.1 Wideband Signal Model

In the narrowband case, the time delays in the signal can be neglected (as in (2.13)) and only the phase shifts in the propagating waves are taken into account. This approximation no longer holds in the case of wideband signals, and therefore a new signal model must be introduced. Consider a MIMO system configuration where the $L_t$ transmitting and $L_r$ receiving antennas are colocated (see Figure 2.2). In the case of one target located at $(\theta, R)$, the received baseband signal at the $l^{\text{th}}$ antenna element of the receiver array, derived from the electric-field model (2.10), is given by

$$x_l(t) = \frac{\mu_0 \beta e^{-j\mathbf{k}_l^T \mathbf{r}_l}}{4\pi \|\mathbf{r}_l\|} \left[ h_{r,l}(\mathbf{u}_{\mathbf{r}_l}, t) * \sum_{i=0}^{L_t-1} \frac{h_{t,i}\left(\mathbf{u}_{\mathbf{r}_i}, t\right)}{\|\mathbf{r}_i\|} * c_i\left(t - \tau_i - \tau_l\right) e^{j(2\pi f_c t - \mathbf{k}_i^T \mathbf{r}_i)} \right] e^{-j2\pi f_c t} + z_l(t) \quad l = 0, ..., L_r - 1, \tag{3.1}$$

where $z(t)$ is the unmodelled interference and noise received by the $l^{\text{th}}$ antenna element. Given that $\tau_i = \frac{\mathbf{k}_i^T \mathbf{r}_i}{2\pi f_c}$ and $\tau_l = \frac{\mathbf{k}_l^T \mathbf{r}_l}{2\pi f_c}$, Equation (3.1) can be written as

$$x_l(t) = \frac{\mu_0 \beta e^{-j\mathbf{k}_l^T \mathbf{r}_l}}{4\pi \|\mathbf{r}_l\|} \left[ h_{r,l}(\mathbf{u}_{\mathbf{r}_l}, t) * \sum_{i=0}^{L_t-1} \frac{h_{t,i}\left(\mathbf{u}_{\mathbf{r}_i}, t\right)}{\|\mathbf{r}_i\|} * c_i \left( t - \frac{\mathbf{k}_i^T \mathbf{r}_i}{2\pi f_c} - \frac{\mathbf{k}_l^T \mathbf{r}_l}{2\pi f_c} \right) e^{j(2\pi f_c t - \mathbf{k}_i^T \mathbf{r}_i)} \right] \times e^{-j2\pi f_c t} + z_l(t)$$
$$l = 0, ..., L_r - 1. \tag{3.2}$$

Assume that the signals $c_i(t)$ are wideband with a spectral support included in the interval $\left[-\frac{B}{2}, \frac{B}{2}\right]$. Then, Equation (3.2) can be written in frequency domain, after applying the Fourier transform, as

$$X_l(f) = \frac{\mu_0 \beta e^{-j\mathbf{k}_l^T \mathbf{r}_l \left(1+\frac{f}{f_c}\right)}}{4\pi \|\mathbf{r}_l\|} H_{r,l}(\mathbf{u}_{\mathbf{r}_l}, f_c + f) \sum_{i=0}^{L_t-1} \frac{1}{\|\mathbf{r}_i\|} H_{t,i}\left(\mathbf{u}_{\mathbf{r}_i}, f_c + f\right) e^{-j\mathbf{k}_i^T \mathbf{r}_i \left(1+\frac{f}{f_c}\right)} C_i(f) + Z_l(f), \tag{3.3}$$

where $C_i(f)$, $X_l(f)$, $Z_l(f)$, $H_{r,l}(\mathbf{u}_{\mathbf{r}_l}, f)$, and $H_{t,i}\left(\mathbf{u}_{\mathbf{r}_i}, f\right)$ are the Fourier Transforms of $c_i(t)$, $x_l(t)$, $z_l(f)$, $h_{r,l}(\mathbf{u}_{\mathbf{r}_l}, t)$, and $h_{t,i}\left(\mathbf{u}_{\mathbf{r}_i}, t\right)$ respectively, e.g.

$$C_i(f) = \int_{-\infty}^{\infty} c_i(t) e^{-j2\pi f t} dt. \tag{3.4}$$

Given than the transfer functions $H_{r,l}(\mathbf{u}_{\mathbf{r}_l}, f)$ and $H_{t,i}\left(\mathbf{u}_{\mathbf{r}_i}, f\right)$ are proportional to the antenna radiation patterns [28], (3.3) can be expressed as

$$X_l(f) = \alpha\beta \frac{1}{\|\mathbf{r}_l\|} e^{-j\mathbf{k}_l^T \mathbf{r}_l \left(1+\frac{f}{f_c}\right)} g_{r,l}(\theta, f_c + f) \sum_{i=0}^{L_t-1} \frac{1}{\|\mathbf{r}_i\|} g_{t,i}\left(\theta, f_c + f\right) e^{-j\mathbf{k}_i^T \mathbf{r}_i \left(1+\frac{f}{f_c}\right)} C_i(f) + Z_l(f), \tag{3.5}$$

where $\alpha$ is a proportionality constant and $g_{r,l}(\theta, f_c + f)$ and $g_{t,i}(\theta, f_c + f)$ are respectively the frequency-dependent radiation patterns of the $l^{\text{th}}$ receiver and the $i^{\text{th}}$ transmitter antenna elements.

The baseband signal model at frequency $f$ can then be written in vector notation as

$$\mathbf{X}(f) = \alpha\beta \mathbf{a}_r^*\left(\theta, R, f\right) \mathbf{a}_t^H\left(\theta, R, f\right) \mathbf{C}(f) + \mathbf{Z}(f), \tag{3.6}$$

where $\mathbf{X}(f) = \begin{bmatrix} X_0(f) & \cdots & X_{L_r-1}(f) \end{bmatrix}^T$, $\mathbf{C}(f) = \begin{bmatrix} C_0(f) & \cdots & C_{L_t-1}(f) \end{bmatrix}^T$, $\mathbf{Z}(f) = \begin{bmatrix} Z_0(f) & \cdots & Z_{L_r-1}(f) \end{bmatrix}^T$, and

$$\mathbf{a}_t(\theta, R, f) = \begin{bmatrix} g^*_{t,0}(\theta, f_c+f)\dfrac{1}{\|\mathbf{r}_0\|}e^{j\mathbf{k}_0^T\mathbf{r}_0\left(1+\frac{f}{f_c}\right)} \\ \vdots \\ g^*_{t,L_t-1}(\theta, f_c+f)\dfrac{1}{\|\mathbf{r}_{L_t-1}\|}e^{j\mathbf{k}_{L_t-1}^T\mathbf{r}_{L_t-1}\left(1+\frac{f}{f_c}\right)} \end{bmatrix} \tag{3.7}$$

and

$$\mathbf{a}_r(\theta, R, f) = \begin{bmatrix} g^*_{r,0}(\theta, f_c+f)\dfrac{1}{\|\mathbf{r}_0\|}e^{j\mathbf{k}_0^T\mathbf{r}_0\left(1+\frac{f}{f_c}\right)} \\ \vdots \\ g^*_{r,L_r-1}(\theta, f_c+f)\dfrac{1}{\|\mathbf{r}_{L_r-1}\|}e^{j\mathbf{k}_{L_r-1}^T\mathbf{r}_{L_r-1}\left(1+\frac{f}{f_c}\right)} \end{bmatrix} \tag{3.8}$$

are the wideband transmit and receive steering vectors respectively. Note that these steering vectors are frequency-dependent. Hence, in the spherical-wave case, the DOA estimation techniques should be performed using a three-dimensional grid of parameters $[\theta, R, f]$ which would require an important processing time. In this chapter, we will only consider the plane-wave case and the DOA estimation techniques will be performed by a two-dimensional search over parameters $[\theta, f]$.

In the plane-wave case, the dot product $\mathbf{k}_i^T\mathbf{r}_i$ is given by (see Section 2.1.2)

$$\mathbf{k}_i^T\mathbf{r}_i = \frac{2\pi f_c}{v}\left(D - \left(i - \frac{L_t-1}{2}\right)d_t\right)\sin\theta + \frac{2\pi f_c}{v}H\cos\theta \qquad i = 0, \ldots, L_t-1, \tag{3.9}$$

where $v$ is the wave propagation speed. A similar expression can be obtained for the dot product $\mathbf{k}_l^T\mathbf{r}_l$. Hence, by developing the dot products in (3.7) and (3.8), the plane-wave wideband steering vectors can be expressed as

$$\mathbf{a}_t(\theta, f) = \frac{1}{R}e^{j\frac{2\pi(f_c+f)}{v}(D\sin\theta + H\cos\theta)}\left[g^*_{t,i}(\theta, f_c+f)e^{j2\pi(f_c+f)(\frac{L_t-1}{2}-i)\frac{d_t\sin\theta}{v}}\right]_{i=0,\ldots,L_t-1}, \tag{3.10}$$

$$\mathbf{a}_r(\theta, f) = \frac{1}{R}e^{j\frac{2\pi(f_c+f)}{v}(D\sin\theta + H\cos\theta)}\left[g^*_{r,l}(\theta, f_c+f)e^{j2\pi(f_c+f)(\frac{L_r-1}{2}-l)\frac{d_r\sin\theta}{v}}\right]_{l=0,\ldots,L_r-1}. \tag{3.11}$$

Then, omitting what is common to every element of the arrays, the plane-wave wideband steering vectors are given by

$$\mathbf{a}_t(\theta, f) = \left[g^*_{t,i}(\theta, f_c+f)e^{j2\pi(f_c+f)(\frac{L_t-1}{2}-i)\frac{d_t\sin\theta}{v}}\right]_{i=0,\ldots,L_t-1}, \tag{3.12}$$

and

$$\mathbf{a}_r(\theta, f) = \left[ g_{r,l}^*(\theta, f_c + f) e^{j2\pi(f_c+f)(\frac{L_r-1}{2}-l)\frac{d_r \sin\theta}{v}} \right]_{l=0,\ldots,L_r-1}. \tag{3.13}$$

The wideband signal model in the case of $K$ targets located in the plane-wave region is then expressed in frequency domain as

$$\mathbf{X}(f) = \sum_{k=1}^{K} \beta_k \mathbf{a}_r^*(\theta_k, f)\mathbf{a}_t^H(\theta_k, f)\mathbf{C}(f) + \mathbf{Z}(f). \tag{3.14}$$

Note that the constant $\alpha$ has been omitted for notational simplicity.

Before applying digital signal processing to the received signals, it is convenient to consider the sampled baseband signals

$$\begin{aligned} x_l(n) &\triangleq x_l\left(t = \tfrac{n}{F_s}\right) \\ n &= 0, \ldots, N-1, \\ l &= 0, \ldots, L_r - 1. \end{aligned} \tag{3.15}$$

Also, the DOA estimation techniques must be performed over the whole frequency band using in practice a grid of discrete frequencies. Hence, it is suitable to consider the Discrete Fourier Transform (DFT) of $\{x_l(n)\}_{n=0}^{N-1}$

$$\begin{aligned} X_l(p) &= \sum_{n=0}^{N-1} x_l(n) e^{-j2\pi \frac{n}{N}\left(p-\frac{N}{2}\right)} \\ p &= 0, \ldots, N-1. \end{aligned} \tag{3.16}$$

Accordingly, Equation (3.14) can be written in discrete-frequency domain as

$$\begin{aligned} \mathbf{X}(p) &\approx \sum_{k=1}^{K} \beta_k \mathbf{a}_r^*(\theta_k, p)\mathbf{a}_t^H(\theta_k, p)\mathbf{C}(p) + \mathbf{Z}(p) \\ p &= 0, \ldots, N-1, \end{aligned} \tag{3.17}$$

with

$$\mathbf{a}_t(\theta_k, p) = \left[ g_{t,i}^*(\theta_k, f_c + f_p) e^{j2\pi(f_c+f_p)(\frac{L_t-1}{2}-i)\frac{d_t \sin\theta_k}{v}} \right]_{i=0,\ldots,L_t-1} \tag{3.18}$$

and

$$\mathbf{a}_r(\theta_k, p) = \left[ g_{r,l}^*(\theta_k, f_c + f_p) e^{j2\pi(f_c+f_p)(\frac{L_r-1}{2}-l)\frac{d_r \sin\theta_k}{v}} \right]_{l=0,\ldots,L_r-1}, \tag{3.19}$$

where

$$f_p = \frac{pF_s}{N} - \frac{F_s}{2}, \tag{3.20}$$

and $\mathbf{X}(p) = \begin{bmatrix} X_0(p) & \cdots & X_{L_r-1}(p) \end{bmatrix}^T$, $\mathbf{C}(p) = \begin{bmatrix} C_0(p) & \cdots & C_{L_t-1}(p) \end{bmatrix}^T$, and $\mathbf{Z}(p) = \begin{bmatrix} Z_0(p) & \cdots & Z_{L_r-1}(p) \end{bmatrix}^T$ are the DFT (element-wise) of $\mathbf{x}(n)$, $\mathbf{c}(n)$, and $\mathbf{z}(n)$ respectively. Note that the use of the DFT makes (3.14) and (3.17) only approximately equivalent.

In this chapter, the radiation patterns of the antenna elements are assumed to be identical, angle-independent and of unity gain within the working frequency band. Accordingly, the plane-wave steering vectors are finally given by

$$\mathbf{a}_t(\theta_k, p) = \left[ e^{j2\pi(f_c+f_p)(\frac{L_t-1}{2}-i)\frac{d_t \sin\theta_k}{v}} \right]_{i=0,\ldots,L_t-1} \tag{3.21}$$

and

$$\mathbf{a}_r(\theta_k, p) = \left[ e^{j2\pi(f_c+f_p)(\frac{L_r-1}{2}-l)\frac{d_r \sin\theta_k}{v}} \right]_{l=0,\ldots,L_r-1}. \tag{3.22}$$

## 3.2 Simulation Method of Signal Transmission and Reception

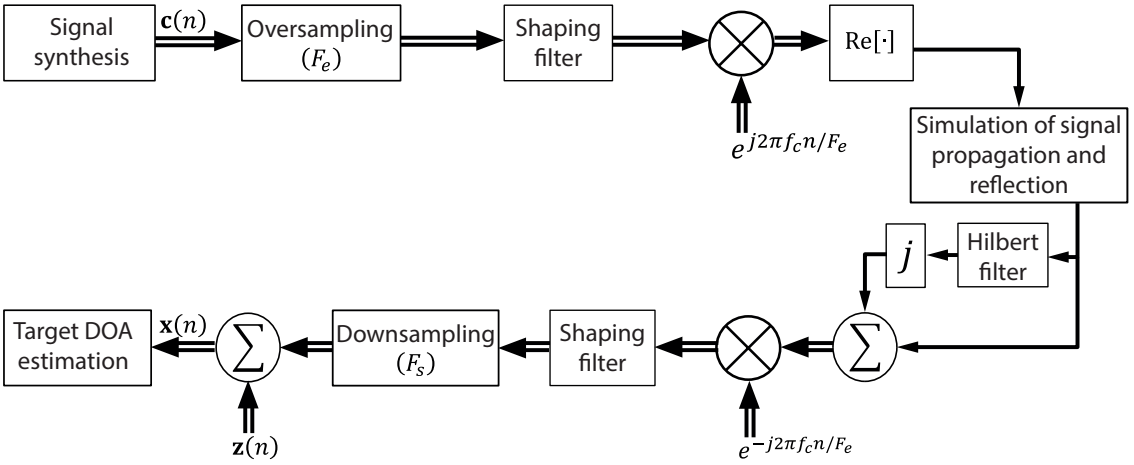


FIGURE 3.1: Flow diagram of the wideband simulations.

The flow of the simulation method is shown in Figure 3.1. First, the set of discrete-time complex envelopes $\{\mathbf{c}(n)\}_{n=0}^{N-1}$ of the signals to be transmitted is synthesized by MATLAB. The $\{\mathbf{c}(n)\}_{n=0}^{N-1}$ are either chosen to be independent sequences of QPSK symbols or are synthesized using one of the waveform design techniques presented in Sections 3.3 and 3.4 in order to match a desired beampattern. The symbol frequency $F_s$ is chosen to be larger than $\frac{f_c}{10}$ (and less than $2f_c$) so that the signals can be considered to be wideband. The $\{\mathbf{c}(n)\}_{n=0}^{N-1}$ are then oversampled at $F_e = 5f_c$ in order to prevent aliasing. Before modulation, the signals are filtered by a root-raised-cosine filter.

The signal propagation between the antenna arrays and the targets is simulated taking into account the different delays due to the different propagation paths: The signals are first oversampled by a factor of 32 so that we can distinguish between two paths corresponding to targets at DOAs separated by 1°; once the different delays have been applied, the signals are downsampled by the same factor of 32.

At the receivers, the "reflected" signals are demodulated. Next, the baseband received signals are filtered by a root-raised-cosine filter. Finally, the signals are downsampled to the symbol frequency $F_s$ before adding complex white Gaussian noise vectors $\mathbf{z}(n)$.

In all the simulations presented in this chapter, we consider a wideband MIMO radar with colocated antennas whose transmitter and receiver arrays are two ULA of $L_t = L_r = L = 10$ elements, and the inter-element spacings are set to half the minimum wavelength, i.e. $d_t = d_r = d = v/(2(f_c + F_s/2))$. Both arrays operate at a carrier frequency $f_c = 1$ GHz. The signals $\{\mathbf{c}(n)\}_{n=0}^{N-1}$ of $N = 512$ symbols, are normalized such that

$$\begin{aligned} \left[\hat{\mathbf{R}}_c\right]_{i,i} &= \frac{1}{L} \\ i &= 0, \ldots, L-1, \end{aligned} \tag{3.23}$$

where $\left[\hat{\mathbf{R}}_c\right]_{i,i}$ denotes the $(i,i)^{\text{th}}$ element of $\hat{\mathbf{R}}_c$. Note that the normalization implies that the mean power of the signal transmitted by every antenna element equals $1/L$.

## 3.3 Existing Waveform Design Techniques

Waveform design is one of the most attractive research topics about MIMO radars. In fact, the capability of transmitting different arbitrary waveforms by every element of the array allows having great flexibility when trying to transmit a desired beampattern. The waveform design problem can be addressed in several ways: The set of waveforms can be chosen in order to obtain a desirable MIMO ambiguity function to improve the angular and range resolution [40]; alternatively, by having previous knowledge on the target and clutter statistics, the waveforms can be adapted to the target signatures to improve the detection and/or interference rejection performance [41]; also, the waveforms can be synthesized by designing a covariance matrix such that the power is transmitted to a desired range of angles, which has shown to improve the DOA estimation performance in the narrowband case [42].

In this section, two recently proposed wideband waveform design techniques are described followed by the proposition of a multiband waveform design which satisfies a low Peak-to-Average Power Ratio (PAPR) constraint.

### 3.3.1 Wideband Beampattern Formation via Iterative Techniques (WBFIT)

The Wideband Beampattern Formation via Iterative Techniques (WBFIT) algorithm was proposed in [43] to design low PAPR sequences for transmit beampattern synthesis in wideband MIMO systems. The signals to be transmitted are designed such that their DFT are the solution of a beampattern matching problem.

Considering that the transmitted signals at angle $\theta$ are given, in discrete-frequency domain, by

$$\begin{aligned} \breve{C}(\theta, p) &= \mathbf{a}_t^H(\theta, p)\mathbf{C}(p) \\ p &= 0, \ldots, N-1, \end{aligned} \tag{3.24}$$

the spatial power distribution at frequency $f_p + f_c$ is given by

$$P\left(\theta, f_p + f_c\right) = |\breve{C}(\theta, p)|^2 = |\mathbf{a}_t^H(\theta, p)\mathbf{C}(p)|^2. \tag{3.25}$$

A waveform design problem can then be formulated with the goal of designing a set of signals $\{\mathbf{c}(n)\}_{n=0}^{N-1}$ such that the power distribution $\{P\left(\theta, f_p + f_c\right)\}_{p=0}^{N-1}$ matches a desired beampattern. Letting $\delta(\theta_h, p)$ denote the desired beampattern, where $\{\theta_h\}_{h=1}^{H}$ represents a grid of angles covering the interval $[-90°, 90°]$, the beampattern matching problem can be formulated as

$$\begin{aligned} \min_{\{\mathbf{c}(n)\}} & \sum_{h=1}^{H}\sum_{p=0}^{N-1}\left[\delta(\theta_h, p) - \left|\mathbf{a}_t^H(\theta_h, p)\mathbf{C}(p)\right|\right]^2 \\ & \text{s.t. PAPR}\left(\{c_i(n)\}_{n=0}^{N-1}\right) \leq \varrho, \\ & i = 0, \ldots, L_t - 1, \end{aligned} \tag{3.26}$$

where the PAPR of the $i^{\text{th}}$ signal $\{c_i(n)\}_{n=0}^{N-1}$ is defined as

$$\text{PAPR}\left(\{c_i(n)\}_{n=0}^{N-1}\right) = \frac{\max_n |c_i(n)|^2}{\frac{1}{N}\sum_{n=0}^{N-1}|c_i(n)|^2}, \tag{3.27}$$

and $\varrho \geq 1$ is a predefined threshold.

The authors propose in [43] a two-stage design approach to solve the optimization problem (3.26). In stage 1, the problem is solved with respect to $\{\mathbf{C}(p)\}_{p=0}^{N-1}$, which are considered to be general complex vectors. In stage 2, the DFT of $\{\mathbf{c}(n)\}_{n=0}^{N-1}$ is fitted to the obtained $\{\mathbf{C}(p)\}_{p=0}^{N-1}$ subject to the PAPR constraint. Both stages are described in Appendix B.

### 3.3.2 Spectral Density Focusing Beampattern Synthesis Technique (SFBT)

The Spectral Density Focusing Beampattern Synthesis Technique (SFBT) is an approach proposed in [44] to transmit the power directly to the targets of interest. It follows from (3.25) that we can transmit the power in a direction $\theta_0$ by choosing a signal whose DFT is

$$\begin{aligned} \mathbf{C}(p) &= \mathbf{a}_t(\theta_0, p) \\ p &= 0, \ldots, N-1. \end{aligned} \tag{3.28}$$

Then, the beampattern is given by

$$P\left(\theta, f_p + f_c\right) = \left|\mathbf{a}_t^H(\theta, p)\mathbf{a}_t(\theta_0, p)\right|^2 = \left|\sum_{i=0}^{L_t-1} e^{j2\pi(f_c+f_p)(\frac{L_t-1}{2}-i)\frac{d_t(\sin\theta_0-\sin\theta)}{v}}\right|^2. \tag{3.29}$$

It can be noted that the beampattern will have a maximum for $\theta = \theta_0$. Then, the signals to be transmitted can be obtained by performing the Inverse Discrete Fourier Transform (IDFT) of $\{\mathbf{C}(p)\}_{p=0}^{N-1}$, i.e.

$$\begin{aligned} c_i(n) &= \frac{1}{N}\sum_{p=0}^{N-1} C_i(p) e^{j2\pi\frac{n}{N}\left(p-\frac{N}{2}\right)} \\ n &= 0, \ldots, N-1, \\ i &= 0, \ldots, L_t-1. \end{aligned} \tag{3.30}$$

The signals resulting from (3.30) are given by

$$\begin{aligned} c_i(n) &= \frac{1}{N} e^{j2\pi f_c u_i} e^{-j\frac{\pi}{N}(u_i F_s+n)} \frac{\sin\left(\pi(u_i F_s+n)\right)}{\sin\left(\frac{\pi}{N}(u_i F_s+n)\right)} \\ n &= 0, \ldots, N-1, \\ i &= 0, \ldots, L_t-1, \end{aligned} \tag{3.31}$$

where

$$u_i = \left(\frac{L_t-1}{2} - i\right)\frac{d_t \sin\theta_0}{v}. \tag{3.32}$$

Note that each signal $\{c_i(n)\}_{n=0}^{N-1}$ is a phase-shifted version of the other ones, which leads to a set of correlated signals and a rank deficient auto-covariance matrix $\mathbf{R}_c$. However, the use of uncorrelated signals is usually desired before applying adaptive processing algorithms. In order to get a full-rank auto-covariance matrix, a random phase $\{\phi(p)\}_{p=0}^{N-1}$ can be included in the design of the $\{\mathbf{C}(p)\}_{p=0}^{N-1}$. Indeed, $\{\mathbf{C}(p)\}_{p=0}^{N-1}$ and $\{\mathbf{C}(p)e^{j\phi(p)}\}_{p=0}^{N-1}$ lead to the same value of $P\left(\theta, f_p + f_c\right)$ in the mono-target case.

The idea of the SFBT is then to construct the signals in discrete-frequency domain $\{\mathbf{C}(p)\}_{p=0}^{N-1}$, in the case of multiple targets, as

$$\begin{gathered}\mathbf{C}(p)=\sum_{k=1}^{K}\mathbf{a}_t(\hat{\theta}_k,p)e^{j\phi_k(p)}\\ p=0,\ldots,N-1,\end{gathered} \tag{3.33}$$

where $\{\hat{\theta}_k\}_{k=1}^{K}$ are initial estimates of the target DOAs, and $\{\phi_k(p)\}$ take random values in $[0,2\pi]$. Finally, the signals to be transmitted are obtained by performing the IDFT of $\{\mathbf{C}(p)\}_{p=0}^{N-1}$. This method is not optimal since it is not the solution of an optimization problem such as (3.26). However, the beampattern created by the signals obtained in (3.33) will present maxima around the directions $\{\hat{\theta}_k\}_{k=1}^{K}$.

### 3.3.3 Comparison Between WBFIT and SFBT

The previously described waveform design techniques, WBFIT and SFBT, are compared in this section via several MATLAB simulations.

#### 3.3.3.1 Mono-Target Case

Consider that we have an initial DOA estimate $\hat{\theta}=40°$ of one target ($K=1$) located in the plane-wave region. The WBFIT is used to synthesize a set of signals $\{\mathbf{c}(n)\}_{n=0}^{N-1}$ such that the power is directly transmitted to the target by defining the following desired beampattern:

$$\begin{gathered}\delta(\theta,p)=\begin{cases}1, & \theta=\hat{\theta}\\ 0, & \text{other } \theta\end{cases}\\ p=0,\ldots,N-1.\end{gathered} \tag{3.34}$$

Note that the beampattern is aimed to have a main lobe at 40° over the whole range of discrete frequencies $\left[f_c-\frac{F_s}{2},f_c+\frac{F_s}{2}-\frac{F_s}{N}\right]$.

Figure 3.2 shows the beampattern (calculated as (3.25)) synthesized by WBFIT with $\varrho=2$. The beampattern is designed for a symbol frequency $F_s=f_c/5=200$ MHz and using a grid of angles $\theta\in[-90°,90°]$ with a mesh grid size of 0.1°. We can see that the beampattern has a mainlobe in the direction $\hat{\theta}=40°$. The mainlobe has approximately the same amplitude and width over the whole range of frequencies. As shown in Figure 3.3, the signals synthesized by WBFIT satisfy the PAPR constraint: The PAPR of every sequence $\{c_i(n)\}_{n=0}^{N-1}$ is equal to 2.

If a very low PAPR constraint is used instead, the beampattern may be degraded. As shown in Figure 3.4, the beampattern synthesized for $\varrho=1$ becomes uneven.

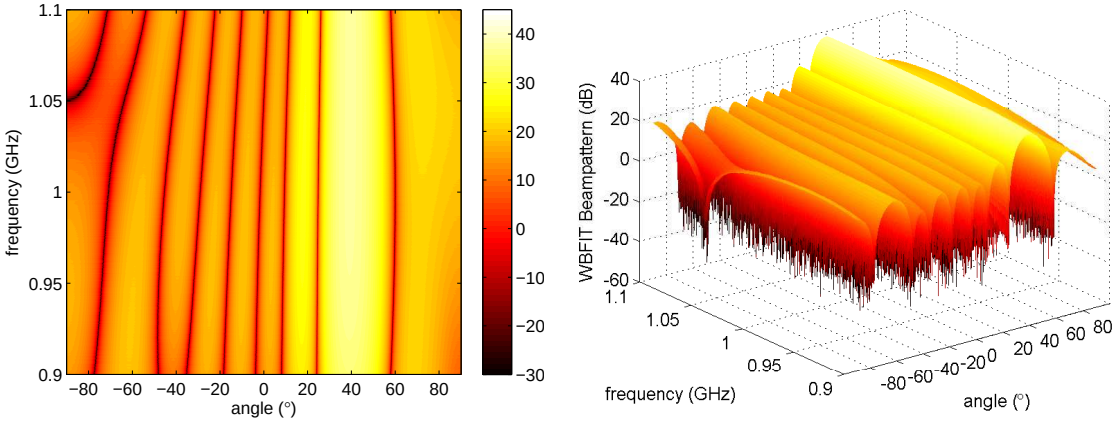


(a) (b)

FIGURE 3.2: The WBFIT beampattern in dB with $\varrho = 2$ and $F_s = f_c/5 = 200$ MHz (1 target at $\hat{\theta} = 40°$). (a) 2D plot, (b) 3D plot.

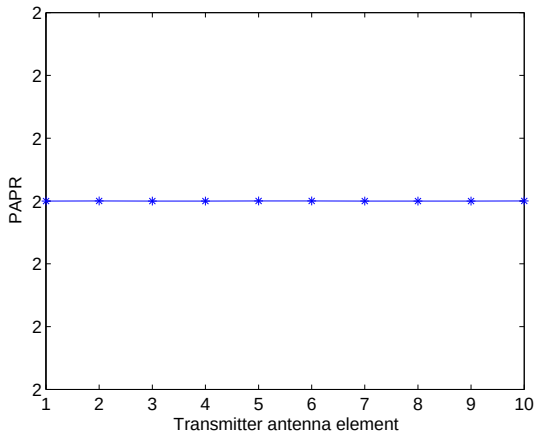


FIGURE 3.3: PAPR of every $\{c_i(n)\}_{n=0}^{N-1}$ synthesized by WBFIT ($\varrho = 2$).

Nevertheless, a maximum of power is still transmitted in the desired direction $\hat{\theta}$ while every sequence $\{c_i(n)\}_{n=0}^{N-1}$ perfectly meets the PAPR constraint (see Figure 3.5).

A transmit beampattern is also synthesized by the SFBT. The set of signals $\{\mathbf{c}(n)\}_{n=0}^{N-1}$ is choosen such that the power is transmitted in the direction $\hat{\theta}$ by calculating the IDFT (element-wise) of (3.33). As shown in Figure 3.6, the beampattern synthesized by the SFBT is very smooth, similar to the WBFIT beampattern of Figure 3.2. However, we must note that the mainlobe is wider at low frequencies. Actually, in the case of one target at $\hat{\theta}$, the SFBT beampattern is given by

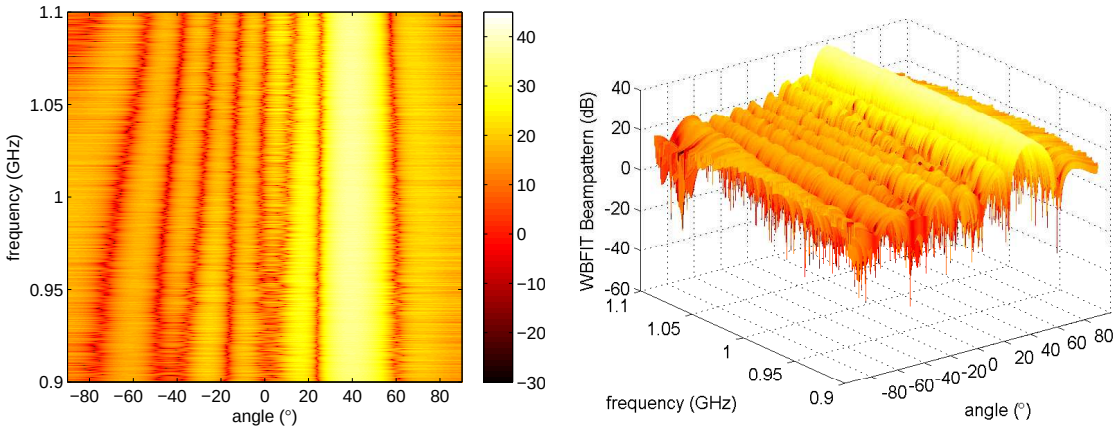


(a) (b)

FIGURE 3.4: The WBFIT beampattern in dB with $\varrho = 1$ and $F_s = f_c/5 = 200$ MHz (1 target at $\hat{\theta} = 40°$). (a) 2D plot, (b) 3D plot.

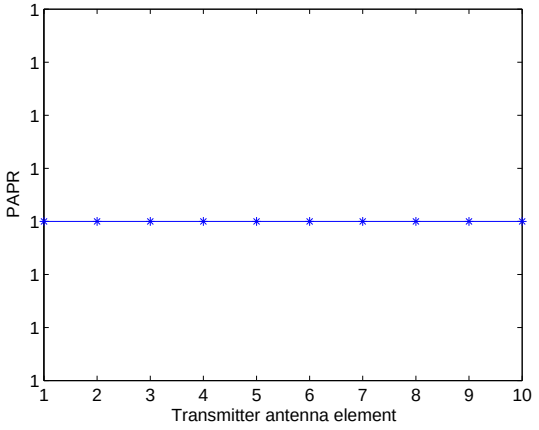


FIGURE 3.5: PAPR of every $\{c_i(n)\}_{n=0}^{N-1}$ synthesized by WBFIT ($\varrho = 1$).

$$P(\theta, f_p + f_c) = \left|\mathbf{a}_t^H(\theta, p)\mathbf{a}_t(\hat{\theta}, p)e^{j\phi(p)}\right|^2 = \left(\frac{\sin\left(\pi L_t(f_c + f_p)\frac{d_t(\sin\hat{\theta} - \sin\theta)}{v}\right)}{\sin\left(\pi(f_c + f_p)\frac{d_t(\sin\hat{\theta} - \sin\theta)}{v}\right)}\right)^2 \tag{3.35}$$
$$p = 0, \ldots, N-1,$$

which implies that the mainlobe will be wider as $f_p$ decreases. On the other hand, the design of the $\{\mathbf{c}(n)\}_{n=0}^{N-1}$ by the SFBT can lead to high PAPR signals, as shown in Figure 3.7, which are usually undesirable since either they require a large range of dynamic linearity of the circuits resulting in high power consumption or they generate spectral regrowth in adjacent channels.

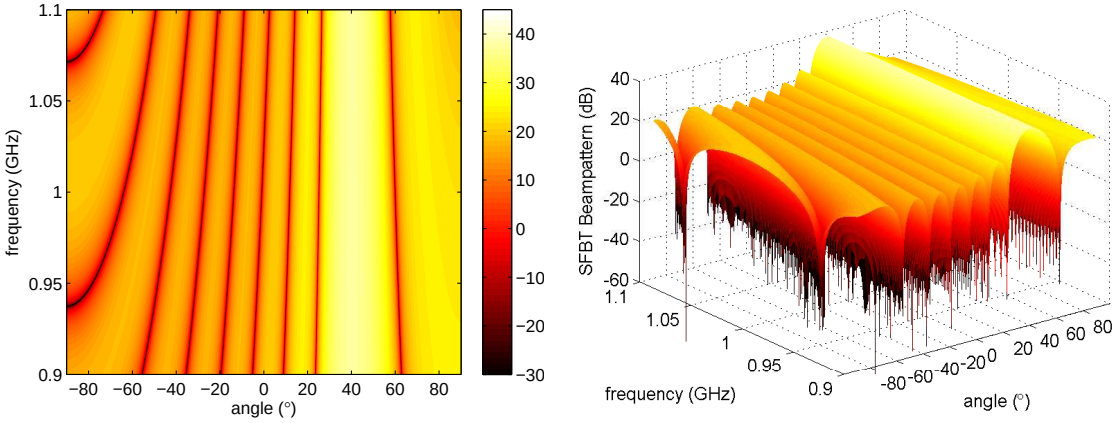


(a) (b)

FIGURE 3.6: The SFBT beampattern in dB with $F_s = f_c/5 = 200$ MHz (1 target at $\hat{\theta} = 40°$). (a) 2D plot, (b) 3D plot.

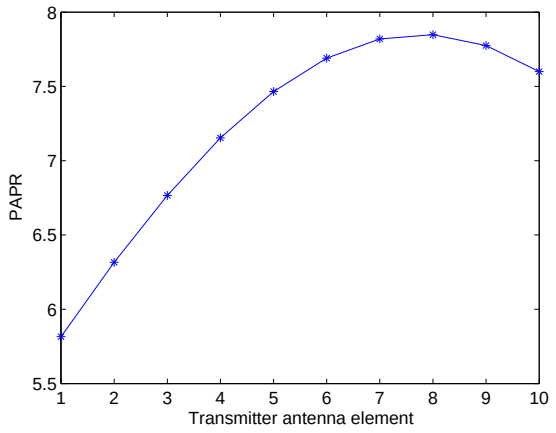


FIGURE 3.7: PAPR of every $\{c_i(n)\}_{n=0}^{N-1}$ synthesized by SFBT.

Consider now the case of a larger bandwidth. Figures 3.8 and 3.10 show respectively the WBFIT ($\varrho = 2$) and the SFBT beampatterns synthesized with a symbol frequency $F_s = f_c/2 = 500$ MHz. We observe that the WBFIT is degraded as the bandwidth becomes large: The mainlobe is centered at $\hat{\theta}$ at high frequencies and is deviated at low frequencies. Moreover, even though a maximum of power can be transmitted around $\hat{\theta}$, comparable amount of power is transmitted in other directions as shown in Figure 3.9, where we have plotted the WBFIT beampattern at frequency $f_c$ (i.e. $P(\theta, f_c)$). Indeed, the mainlobe level is only around 1.7 and 3.6 dB higher than the greatest sidelobes. On the other hand, the SFBT works relatively well: The mainlobe has an approximately constant amplitude at $\hat{\theta}$ over the whole range of frequencies. However, the mainlobe becomes wider as the frequency decreases, which is coherent with (3.35). In contrast to WBFIT, SFBT allows transmitting much more power to direction $\hat{\theta}$ than to other directions as shown in Figure 3.11: The mainlobe level is at least 10 dB higher than

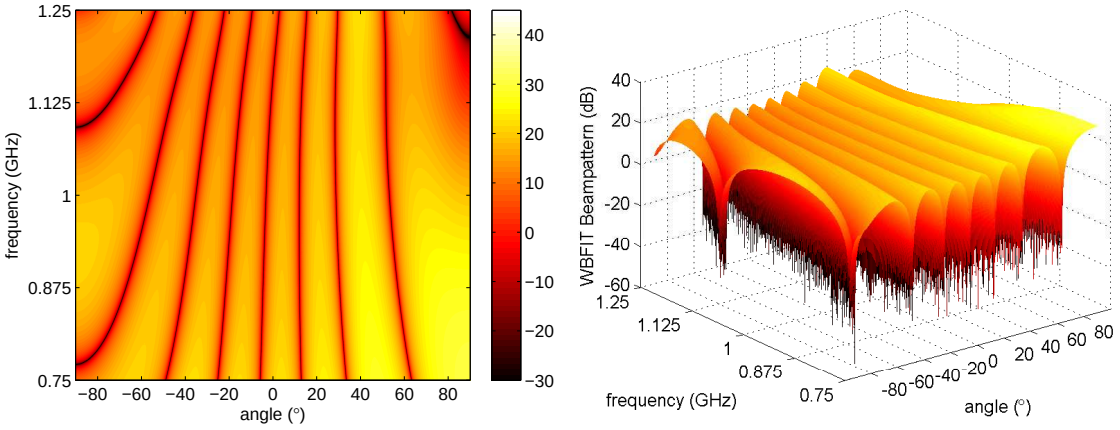


(a) (b)

FIGURE 3.8: The WBFIT beampattern in dB with $\varrho = 2$ and $F_s = f_c/2 = 500$ MHz (1 target at $\hat{\theta} = 40°$). (a) 2D plot, (b) 3D plot.

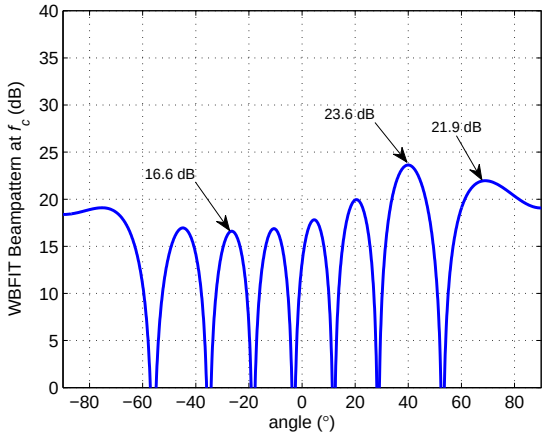


FIGURE 3.9: The WBFIT beampattern in dB at $f_c$ ($\varrho = 2$).

the sidelobe levels.

#### 3.3.3.2 Multi-Target Case

Suppose that we have initial estimates of $K = 3$ target DOAs: $\hat{\theta}_1 = -60°$, $\hat{\theta}_2 = 0°$, and $\hat{\theta}_3 = 40°$.

The desired beampattern used in the WBFIT design is given by

$$\delta(\theta, p) = \begin{cases} 1, & \theta = \hat{\theta}_k, \quad k = 1, \ldots, K \\ 0, & \text{other } \theta \end{cases} \qquad (3.36)$$
$$p = 0, \ldots, N-1.$$

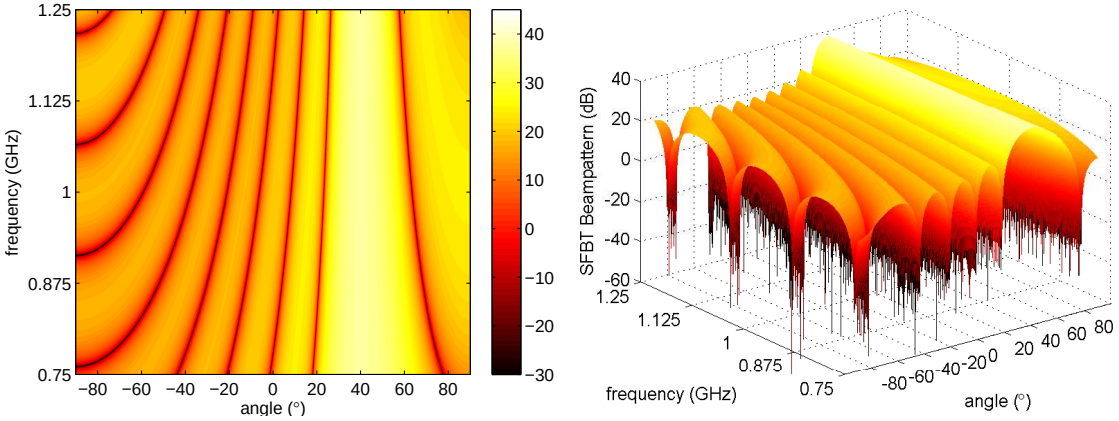


(a) (b)

FIGURE 3.10: The SFBT beampattern in dB with $F_s = f_c/2 = 500$ MHz (1 target at $\hat{\theta} = 40°$). (a) 2D plot, (b) 3D plot.

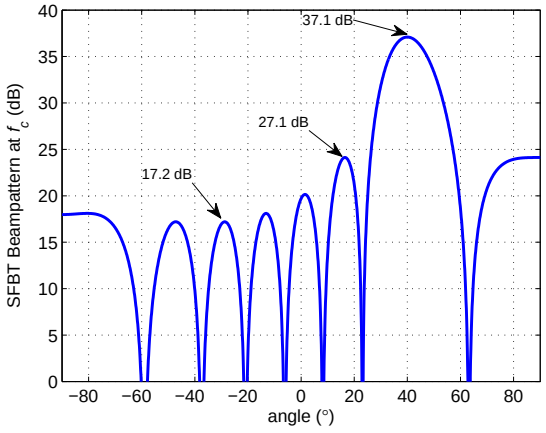


FIGURE 3.11: The SFBT beampattern in dB at $f_c$.

The WBFIT ($\varrho = 2$) and the SFBT beampatterns for $F_s = f_c/5 = 200$ MHz are illustrated by Figures 3.12 and 3.13 respectively. We can see that both beampatterns have three high lobes around the targets directions. While the WBFIT beampattern has a smooth shape in almost the whole range of frequencies, the SBFT beampattern is more irregular due to the different random phase associated to every target in (3.33).

However, if the bandwidth is increased, the WBFIT may be highly deteriorated. This is the case for $F_s = f_c/2 = 500$ MHz, as shown in Figure 3.14. We can see that the lobes are deformed as $|\theta|$ becomes large; moreover, a parasite lobe appears around $-40°$. As for the SFBT, the beampattern shown in Figure 3.15 is not deformed and allows transmitting the power directly to the three targets. As expected, the lobes are wider at low frequencies.

The WBFIT allows designing low PAPR sequences while matching a desired beampattern. As discussed before, the WBFIT works very well for relatively small

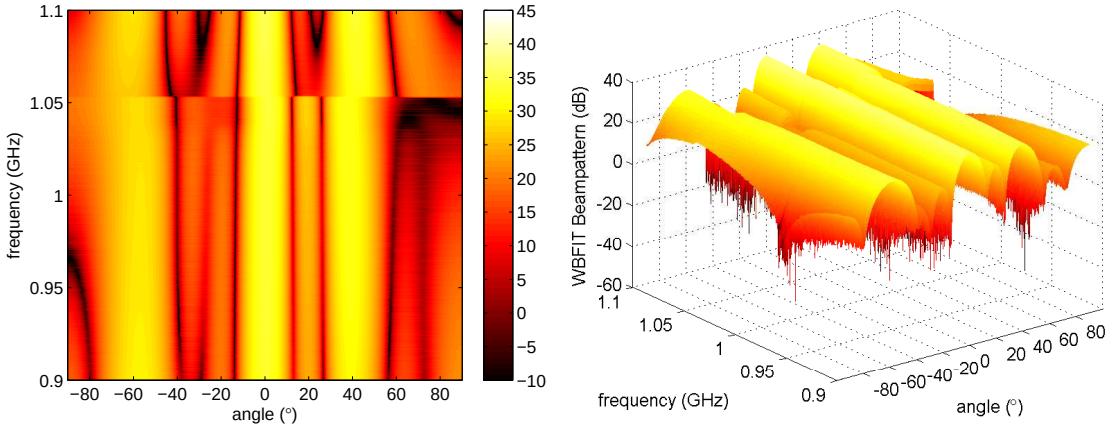


(a) (b)

FIGURE 3.12: The WBFIT beampattern in dB with $\varrho = 2$ and $F_s = f_c/5 = 200$ MHz ($\hat{\theta}_1 = -60°$, $\hat{\theta}_2 = 0°$, $\hat{\theta}_3 = 40°$). (a) 2D plot, (b) 3D plot.

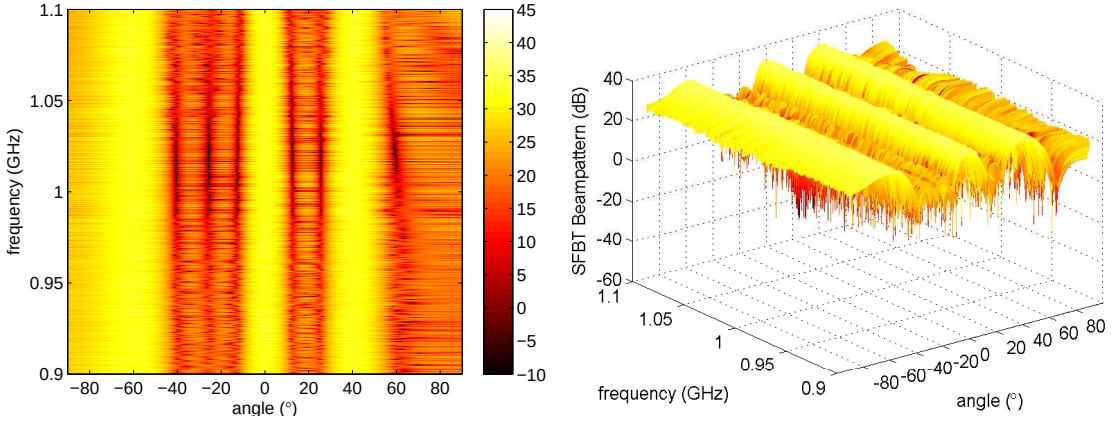


(a) (b)

FIGURE 3.13: The SFBT beampattern in dB with $F_s = f_c/5 = 200$ MHz ($\hat{\theta}_1 = -60°$, $\hat{\theta}_2 = 0°$, $\hat{\theta}_3 = 40°$). (a) 2D plot, (b) 3D plot.

bandwidths, such as $F_s = f_c/5$, but its performance is seriously degraded as the bandwidth increases. On the other hand, even though the SFBT does not provide low PAPR signals, it works relatively well in both small and large bandwidth cases. Moreover, since the SFBT is not an iterative process, it is much faster to compute than WBFIT and hence more suitable for real-time applications. In the previous simulations, the SFBT was at least 2000 times faster than WBFIT.

## 3.4 Proposition of a Multiband Waveform Design

In the MIMO radar context, every target reflects the superposition of all of the transmitted signals, and hence some correlation may exist between the reflected

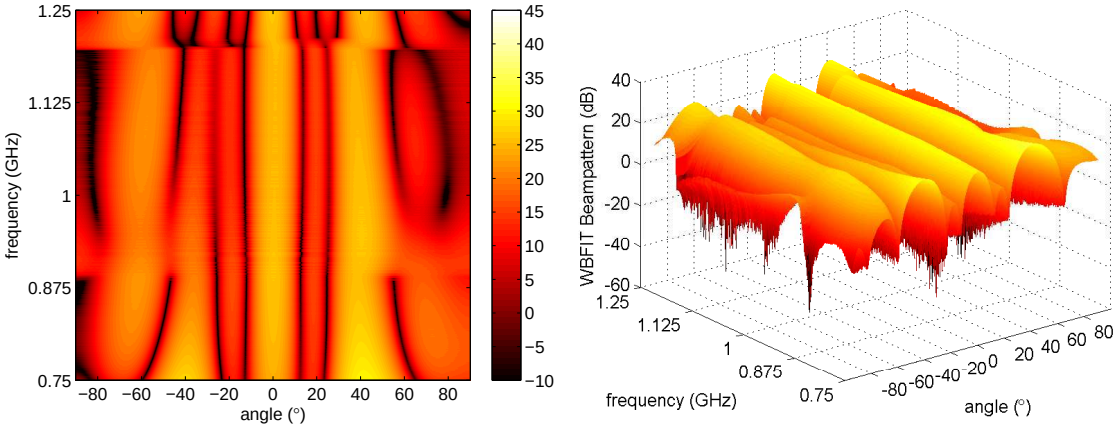


(a) (b)

FIGURE 3.14: The WBFIT beampattern in dB with $\varrho = 2$ and $F_s = f_c/2 = 500$ MHz ($\hat{\theta}_1 = -60°$, $\hat{\theta}_2 = 0°$, $\hat{\theta}_3 = 40°$). (a) 2D plot, (b) 3D plot.

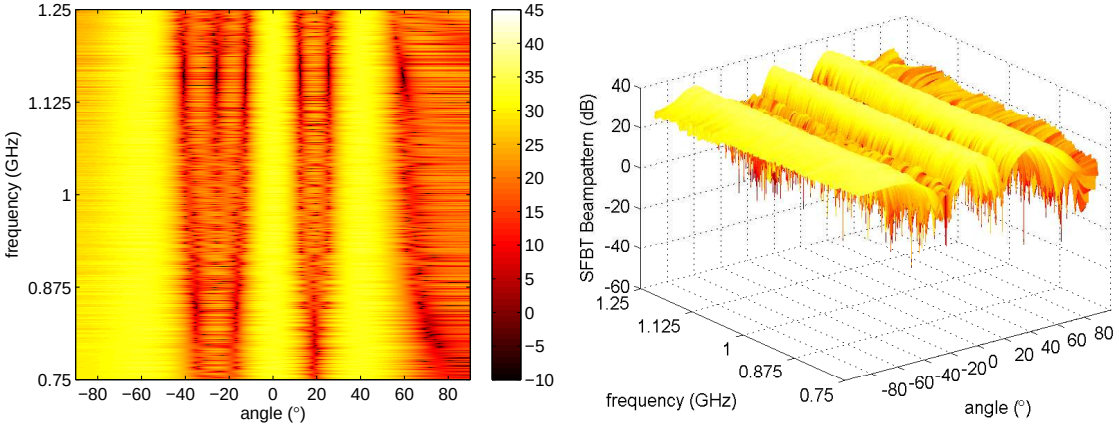


(a) (b)

FIGURE 3.15: The SFBT beampattern in dB with $F_s = f_c/2 = 500$ MHz ($\hat{\theta}_1 = -60°$, $\hat{\theta}_2 = 0°$, $\hat{\theta}_3 = 40°$). (a) 2D plot, (b) 3D plot.

signals. However, the reception of uncorrelated echoes is sometimes desirable before applying DOA estimation techniques as it will be discussed in Section 3.5. Nonetheless, the signals to be transmitted can be designed such that the received signals are uncorrelated.

### 3.4.1 Principle of the Multiband Spectral Focusing Beampattern Synthesis Technique (M-SFBT)

So far SFBT allows transmitting the power directly to the targets of interest in the whole range of frequencies. However, we could exploit the frequency diversity to have more flexible beampatterns using several frequency bands. The use of multiple bands has other benefits, such as the reception of uncorrelated target echoes.

In order to make the signals reflected by the targets uncorrelated, we proposed in [45] the Multiband Spectral Focusing Beampattern synthesis Technique (M-SFBT) which is a modified version of the original SFBT. The M-SFBT consists in allocating one or more non-overlapping frequency bands to each target. Letting $\delta_k(p)$ denote the desired power distribution allocated to the $k^{\text{th}}$ target, the set of signals to be transmitted can be constructed in frequency domain as

$$\begin{aligned} \mathbf{C}(p) &= \sum_{k=1}^{K} \mathbf{a}_t(\hat{\theta}_k, p)\delta_k(p)e^{j\phi_k(p)} \\ & p = 0, \ldots, N-1. \end{aligned} \tag{3.37}$$

Then, the signals in time domain $\{\mathbf{c}(n)\}_{n=0}^{N-1}$ can be found by performing the IDFT (element-wise) of (3.37). Note that such signals may have a relatively high PAPR (as shown in Section 3.3.3 in the case of SFBT) which is usually undesirable.

A low PAPR can be achieved by adding a constraint in the design of the waveforms, following the same idea as WBFIT. The set of signals $\{\mathbf{c}'(n)\}_{n=0}^{N-1}$ of low PAPR can then be designed by solving the following minimization problem:

$$\begin{aligned} &\min_{\{c_i'(n)\}_{n=0}^{N-1}} \left\| c_i'(n) - c_i(n) \right\|^2 \\ &\text{s.t. PAPR}\left(\{c_i'(n)\}_{n=0}^{N-1}\right) \leq \varrho \\ &i = 0, \ldots, L_t - 1. \end{aligned} \tag{3.38}$$

This problem can be easily solved by performing the "nearest-vector" algorithm described in [46] and recalled in Appendix B.

### 3.4.2 Numerical Examples

Assume that there are $K = 3$ targets located in the plane-wave region and that we have initial DOA estimates $\hat{\theta}_1 = -60°$, $\hat{\theta}_2 = 0°$, and $\hat{\theta}_3 = 40°$. Then, the signals to be transmitted can be synthesized via M-SFBT with a suitable choice of $\{\delta_k(p)\}$ in order to generate a multiband beampattern. A simple choice of $\{\delta_k(p)\}$ is to allocate a single frequency band to each target as

$$\begin{aligned} \delta_k(p) &= \begin{cases} 1 & \text{for } f_{ck} - \frac{B_k}{2} \leq f_p \leq f_{ck} + \frac{B_k}{2} \\ 0 & \text{otherwise} \end{cases} \\ & p = 0, \ldots, N-1 \\ & k = 1, \ldots, K, \end{aligned} \tag{3.39}$$

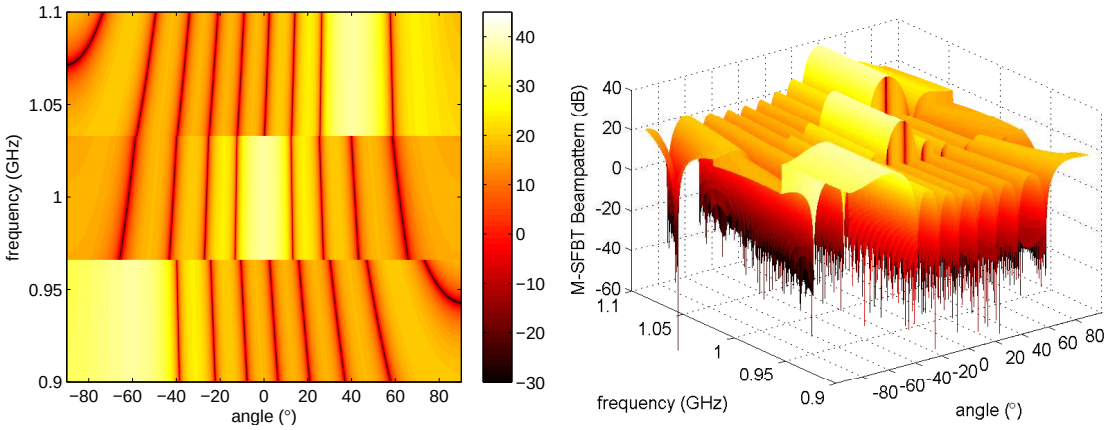


(a) (b)

FIGURE 3.16: The M-SFBT beampattern in dB with $F_s = f_c/5 = 200$ MHz ($\hat{\theta}_1 = -60°$, $\hat{\theta}_2 = 0°$, $\hat{\theta}_3 = 40°$). (a) 2D plot, (b) 3D plot.

where $f_{ck}$ and $B_k$ are respectively the center frequency and the bandwidth of the band allocated to the $k^{\text{th}}$ target. In this example we use non-overlapping frequency bands so that the signals reflected by the targets are uncorrelated. In the following simulations, the $\{\delta_k(p)\}$ are chosen as

$$\delta_k(p) = \begin{cases} 1 & \text{for } (k-1)\left\lfloor \frac{N}{K} \right\rfloor \leq p \leq k\left\lfloor \frac{N}{K} \right\rfloor - 1 \\ 0 & \text{otherwise} \end{cases} \qquad \begin{array}{l} p = 0, \ldots, N-1 \\ k = 1, \ldots, K, \end{array} \tag{3.40}$$

where $\lfloor x \rfloor$ denotes the largest integer less or equal to $x$.

The signals $\{\mathbf{C}(p)\}_{p=0}^{N-1}$ are then generated in frequency domain using (3.37) and the corresponding beampattern $P(\theta, f_p + f_c) = \left|\mathbf{a}_t^H(\theta, p)\mathbf{C}(p)\right|^2$ is shown in Figure 3.16 for $F_s = f_c/5 = 200$ MHz. We can see that the power is directly transmitted to the targets using a different frequency band for each one. As expected, the signals $\{\mathbf{c}(n)\}_{n=0}^{N-1}$ have relatively high PAPR with values varying from 5.8 to 9.2 (see Figure 3.17).

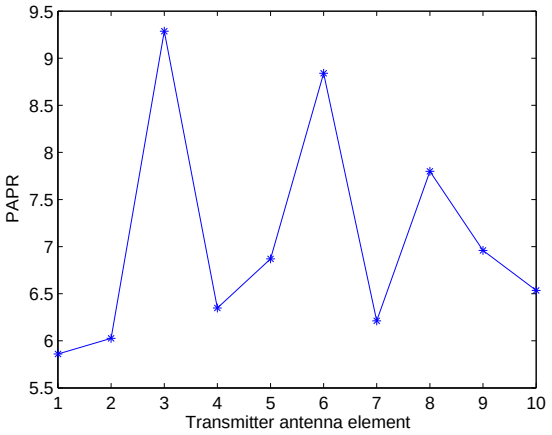


FIGURE 3.17: PAPR of every $\{c_i(n)\}_{n=0}^{N-1}$ synthesized by M-SFBT.

Let us impose the PAPR constraint $\varrho = 2$. The set of signals $\{\mathbf{c}'(n)\}_{n=0}^{N-1}$ satisfying the PAPR constraint is then found by solving the problem (3.38). The new beampattern is given by $P(\theta, f_p + f_c) = \left|\mathbf{a}_t^H(\theta, p)\mathbf{C}'(p)\right|^2$, where $\{\mathbf{C}'(p)\}_{n=0}^{N-1}$ is the DFT (element-wise) of $\{\mathbf{c}'(n)\}_{n=0}^{N-1}$. As shown in Figure 3.18 the beampattern now has an uneven aspect but the spectral and spatial distribution of the new waveforms $\{\mathbf{c}'(n)\}_{n=0}^{N-1}$ are close to those of the initial $\{\mathbf{c}(n)\}_{n=0}^{N-1}$, i.e. the power is transmitted to the targets while keeping the desired frequency allocation. Moreover, the new waveforms perfectly meet the PAPR constraint as shown in Figure 3.19.

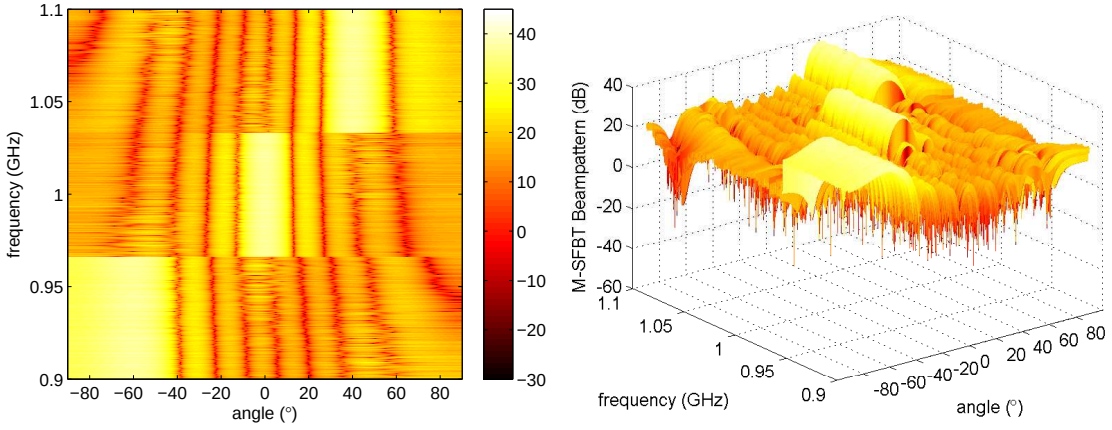


(a) (b)

FIGURE 3.18: The M-SFBT beampattern in dB with $\varrho = 2$ and $F_s = f_c/5 = 200$ MHz ($\hat{\theta}_1 = -60°$, $\hat{\theta}_2 = 0°$, $\hat{\theta}_3 = 40°$). (a) 2D plot, (b) 3D plot.

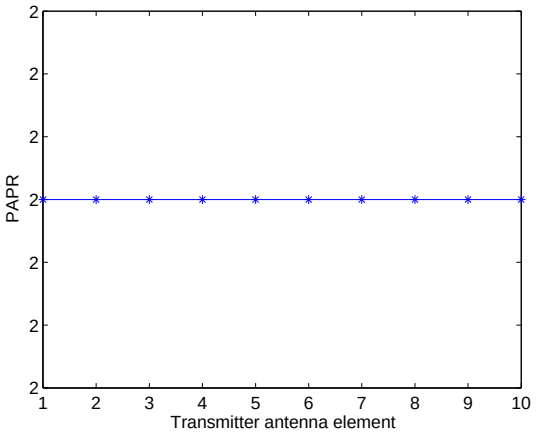


FIGURE 3.19: PAPR of every $\{c_i(n)\}_{n=0}^{N-1}$ synthesized by M-SFBT with $\varrho = 2$.

We must note that a multiband beampattern can also be synthesized by WBFIT. Similar to (3.40), the WBFIT desired beampattern is chosen as

$$\delta(\theta, p) = \begin{cases} 1 & \text{for } (k-1)\left\lfloor \frac{N}{K} \right\rfloor \leq p \leq k\left\lfloor \frac{N}{K} \right\rfloor - 1 \text{ and } \theta = \hat{\theta}_k, \quad k = 1, \ldots, K \\ 0 & \text{otherwise} \end{cases}$$
$$p = 0, \ldots, N-1, \tag{3.41}$$

Figure 3.20 shows the WBFIT multiband beampattern under the PAPR constraint $\varrho = 2$. As expected, the WBFIT beampattern is smoother than the M-SFBT's counterpart. It also has a narrower lobe at $-60°$. However, WBFIT is much more computationally expensive than M-SFBT.

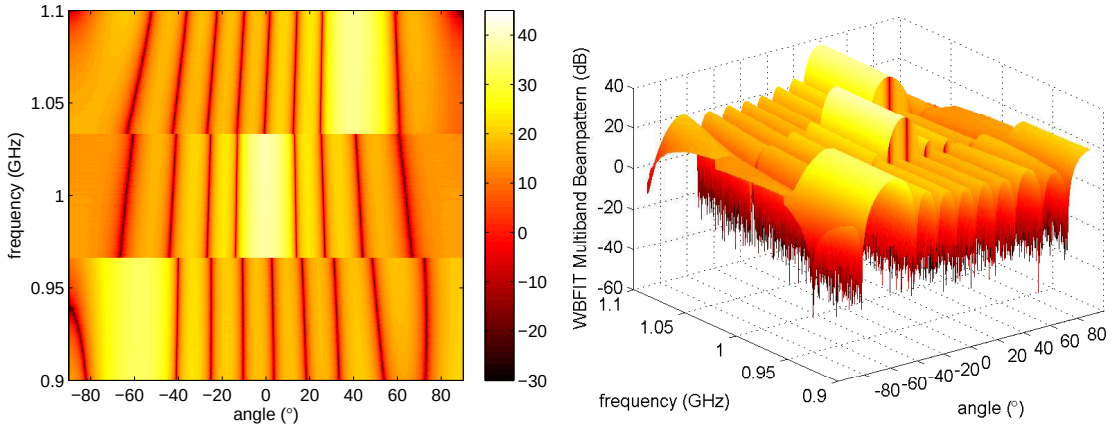


(a) (b)

FIGURE 3.20: The WBFIT multiband beampattern in dB with $\varrho = 2$ and $F_s = f_c/5 = 200$ MHz ($\hat{\theta}_1 = -60°$, $\hat{\theta}_2 = 0°$, $\hat{\theta}_3 = 40°$). (a) 2D plot, (b) 3D plot.

## 3.5 Wideband Direction-of-Arrival Estimation Techniques

To date, most of the DOA estimation techniques for MIMO radar have been proposed in the case of narrowband signals as described in Chapter 2. However, given that the approximations done in the narrowband model no longer hold with wideband signals, those techniques cannot be directly applied in the wideband context. In this section we propose the adaptation of some wideband array processing techniques to the context of wideband MIMO radar.

### 3.5.1 Wideband Array Processing Techniques

In wideband array processing, a variety of techniques have been proposed in the literature to estimate the DOAs of wideband sources. In most of the cases, the received signals are decomposed in several narrowband components using the DFT, leading to the following signal model:

$$\begin{aligned} \mathbf{X}(p) \approx \sum_{k=1}^{K} \mathbf{a}_r^*(\theta_k, p) S_k(p) + \mathbf{Z}(p) \\ p = 0, \ldots, N-1, \end{aligned} \tag{3.42}$$

where $\{S_k(p)\}_{p=0}^{N-1}$ is the DFT of the $k^{\text{th}}$ source signal. Note that taking $S_k(p) = \beta_k \mathbf{a}_t^H(\theta_k, p)\mathbf{C}(p)$, the signal model (3.42) becomes equivalent to the MIMO radar signal model (3.17), which means that, in a MIMO radar context, the sources to be detected are the targets reflecting the signals to the receiver array. Thus, many source DOA estimation techniques can be applied in the context of MIMO radar. Some of these techniques are described thereafter.

#### 3.5.1.1 Incoherent Methods

A low-complexity method consists in applying narrowband DOA estimation techniques, such as Capon or MUSIC, at every frequency component of the signal model (3.42). Some form of averaging procedure is then used to combine the individual results and obtain the final DOA estimates [47][48]. These methods are said to be incoherent since they do not combine the results obtained at every frequency bin in a coherent way. Although the incoherent methods are simple to implement and effective in high SNR cases, their performance is deteriorated in low SNR cases or when the SNR is not constant in the whole frequency band of interest. Indeed, the DOA estimates can be very bad at some frequencies, and the averaging procedure can also lead to inaccurate estimates.

#### 3.5.1.2 Coherent Methods

A more sophisticated method, called Coherent Signal Subspace Method (CSSM), exploits the fact that the signal subspace at a given frequency is different from that at another frequency [49]. Actually, the signal-plus-noise subspaces at different frequencies can be coherently combined to form a single signal subspace which can be used to estimate the DOAs of wideband sources. This is achieved by using a focusing procedure: The covariance matrices of the received signals at several frequency bins are transformed into a general covariance matrix at a reference frequency $f_{ref}$ by using different transformation (or focusing) matrices. The reference frequency, which is often chosen to be equal to the center frequency, can be optimally selected by the method presented in [50]. The general covariance matrix at frequency $f_{ref}$ is then given by [49]

$$\mathbf{R}(f_{ref}) = \sum_{p=0}^{N-1} \alpha_p \mathbf{\Phi}(f_p) \hat{\mathbf{R}}_x(f_p) \mathbf{\Phi}^H(f_p), \tag{3.43}$$

where $\alpha_p$ is a weighting coefficient proportional to the SNR in the $p^{\text{th}}$ frequency bin, $\hat{\mathbf{R}}_x(f_p)$ is the estimated covariance matrix of the received signals at frequency $f_p$, and $\mathbf{\Phi}(f_p)$ is the focusing matrix which is able to transform the signal-plus-noise subspace at frequency $f_p$ to the corresponding subspace at frequency $f_{ref}$. The so-obtained $\mathbf{R}(f_{ref})$ can then be used along with subspace-based methods, such as MUSIC, to estimate the source DOAs. A method to estimate the covariance matrices is presented in Appendix B.

The focusing matrices can be found by solving the following optimization problems [51]:

$$\begin{gathered} \min_{\mathbf{\Phi}(f_p)} \left\| \hat{\mathbf{A}}(f_{ref}) - \mathbf{\Phi}(f_p) \hat{\mathbf{A}}(f_p) \right\|_F \\ \text{s.t. } \mathbf{\Phi}(f_p)^H \mathbf{\Phi}(f_p) = \mathbf{I} \\ p = 0, \ldots, N-1 \end{gathered} \tag{3.44}$$

with

$$\hat{\mathbf{A}}(f_p) = \left[ \mathbf{a}_r^*(\hat{\theta}_1, p) \quad \cdots \quad \mathbf{a}_r^*(\hat{\theta}_K, p) \right], \tag{3.45}$$

where the $\{\hat{\theta}_k\}_{k=1}^K$ are initial estimates of the source DOAs (also called focusing angles), $\mathbf{I}$ is the $L_r \times L_r$ identity matrix, and $\|\cdot\|_F$ denotes the Frobenius norm [52] defined as $\|\mathbf{A}\|_F = \left(\text{tr}\left[\mathbf{A}^H \mathbf{A}\right]\right)^{1/2}$.

The CSSM has shown to have better performance than the incoherent methods in low SNR cases [47][48]. However, it requires initial focusing angles which must be very close to the true DOAs to form the focusing matrices, and its estimation performance is sensitive to those initial values even in high SNR cases [53].

#### 3.5.1.3 Test of Orthogonality of Projected Subspaces (TOPS)

The Test of Orthogonality of Projected Subspaces (TOPS) was proposed in [54] as an alternative to the CSSM to estimate the DOAs of uncorrelated sources. TOPS does not suffer from bias at high SNR and it has an improved performance at low SNR compared to the incoherent methods. Even though TOPS also uses transformation matrices to exploit multiple frequency components, it does not require the use of initial focusing angles. In fact, the signal subspace at a reference frequency $f_{ref}$ is transformed over all of the other frequencies for every hypothesized angle $\theta$. Then, an orthogonality test between the transformed signal-plus-noise subspaces and the noise subspaces is performed at every frequency component. The orthogonality will be preserved only when an hypothesized angle $\theta$ corresponds to a true DOA.

TOPS uses diagonal transformation matrices of the form

$$\mathbf{\Phi}(\Delta f_p, \theta) = \text{diag}\left(\left[e^{j2\pi(f_c+\Delta f_p)(\frac{L_r-1}{2}-l)\frac{d_r \sin\theta}{v}}\right]_{l=0,\ldots,L_r-1}\right) \tag{3.46}$$

where

$$\Delta f_p = f_p - f_{ref}. \tag{3.47}$$

It is easy to see that the matrix $\mathbf{\Phi}(\Delta f_p, \theta)$ allows transforming the steering vector $\mathbf{a}_r(\theta, ref)$ at the reference frequency $f_{ref}$ into the corresponding steering vector at any other frequency $f_p$, i.e.

$$\begin{aligned}\mathbf{\Phi}(\Delta f_p, \theta)\mathbf{a}_r(\theta, ref) &= \left[e^{j2\pi(f_c+f_{ref}+\Delta f_p)(\frac{L_r-1}{2}-l)\frac{d_r \sin\theta}{v}}\right]_{l=0,\ldots,L_r-1} \\ &= \left[e^{j2\pi(f_c+f_p)(\frac{L_r-1}{2}-l)\frac{d_r \sin\theta}{v}}\right]_{l=0,\ldots,L_r-1} \\ &= \mathbf{a}_r(\theta, p).\end{aligned} \tag{3.48}$$

Similarly, the transformation matrix can be used to transform the signal-plus-noise subspace at the reference frequency $\mathbf{U}_s(f_{ref})$ into the signal-plus-noise subspace at any other frequency by performing the following operation [54]:

$$\begin{aligned}\mathbf{F}_s(f_p) &= \mathbf{\Phi}(\Delta f_p, \theta)\mathbf{U}_s(f_{ref}) \\ p &= 0, \ldots, N-1,\end{aligned} \tag{3.49}$$

where $\mathbf{F}_s(f_p)$ is the transformed signal-plus-noise subspace at frequency $f_p$. Note that the different signal-plus-noise and noise subspaces at every frequency can be obtained by eigenvalue decomposition of the covariance matrices of the received signals $\{\hat{\mathbf{R}}_x(f_p)\}_{p=0}^{N-1}$. The quality of the estimated subspaces depends on the estimation of the covariance matrices, which is linked to the SNR and the number of samples. However, it is possible

to reduce some errors by projecting the transformed signal-plus-noise subspaces onto the null space of $\mathbf{a}_r(\theta, p)$ (see [54] for details). By defining the projection matrix $\mathbf{P}(\theta, f_p)$ as

$$\begin{gathered}\mathbf{P}(\theta, f_p) = \mathbf{I} - \left(\mathbf{a}_r^T(\theta, p)\mathbf{a}_r^*(\theta, p)\right)^{-1} \mathbf{a}_r^*(\theta, p)\mathbf{a}_r^T(\theta, p) \\ p = 0, \ldots, N-1,\end{gathered} \tag{3.50}$$

the projected signal-plus-noise subspaces are given by

$$\begin{gathered}\mathbf{F}'_s(\theta, f_p) = \mathbf{P}(\theta, f_p)\mathbf{F}_s(f_p) \\ p = 0, \ldots, N-1.\end{gathered} \tag{3.51}$$

Given that the signal-plus-noise and the noise subspaces are in theory orthogonal (as described in Section 2.2.2), an orthogonality test can be performed at every hypothesized angle $\theta$ for every frequency $f_p$. This is done by defining a matrix $\mathbf{D}(\theta)$ as

$$\mathbf{D}(\theta) = \left[\mathbf{F}_s'^H(\theta, f_0)\mathbf{U}_n(f_0) \quad \cdots \quad \mathbf{F}_s'^H(\theta, f_{N-1})\mathbf{U}_n(f_{N-1})\right], \tag{3.52}$$

where $\mathbf{U}_n(f_p)$ is the noise subspace at frequency $f_p$. Note that the matrix $\mathbf{D}(\theta)$ should become rank deficient when $\theta$ corresponds to a true DOA. In practice, the matrix $\mathbf{D}(\theta)$ might not be rank deficient but close to singular. Hence, the source DOAs can be found by searching for the maxima of the TOPS spatial spectrum

$$P_{TOPS}(\theta) = \frac{1}{\sigma_{\min}(\theta)}, \tag{3.53}$$

where $\sigma_{\min}$ is the smallest singular value of $\mathbf{D}(\theta)$.

### 3.5.2 Incoherent Techniques for MIMO Radar

Similar to the incoherent methods used in wideband array processing, many narrowband detection techniques can be performed to estimate the target DOAs in the context of wideband MIMO radar. Indeed, since the signal model (3.17) uses the DFT to decompose the signals into several narrowband components, the narrowband Capon, MUSIC, and GLRT techniques described in Section 2.2 can be applied in every frequency bin. The individual spatial spectra can then be averaged to obtain the DOA estimates as we proposed in [55].

#### 3.5.2.1 The Wideband Capon Beamformer

In the case of wideband signals, Capon spatial filters can be obtained at every frequency component by solving $N$ optimization problems

$$\begin{aligned} \min_{\mathbf{w}} \mathbf{w}^H(\theta, f_p)\mathbf{R}_x(f_p)\mathbf{w}(\theta, f_p) \\ \text{s.t. } \mathbf{w}^H(\theta, f_p)\mathbf{a}_r^*(\theta, p) = 1 \\ p = 0, \ldots, N-1, \end{aligned} \tag{3.54}$$

where $\mathbf{R}_x(f_p)$ is the covariance matrix of the received signals at frequency $f_p$.

As presented in Section 2.2.1 (see also Appendix A), the resolution of every problem in (3.54) leads to the following narrowband Capon spatial spectra

$$\begin{aligned} P_{cap}(\theta, f_p) = \frac{1}{\mathbf{a}_r^T(\theta, p)\mathbf{R}_x^{-1}(f_p)\mathbf{a}_r^*(\theta, p)} \\ p = 0, \ldots, N-1. \end{aligned} \tag{3.55}$$

In order to have a general Capon spectrum, we propose to average the results obtained in every frequency bin as follows:

$$\bar{P}_{cap}(\theta) = \frac{1}{N}\sum_{p=0}^{N-1} P_{cap}(\theta, f_p). \tag{3.56}$$

The target DOAs can then be estimated by searching for the maxima of $\bar{P}_{cap}(\theta)$.

#### 3.5.2.2 The Wideband MUSIC Algorithm

In Section 2.2.2 we described the narrowband MUSIC algorithm, which exploits the fact that the noise eigenvectors are orthogonal to the receive steering vectors $\mathbf{a}_r(\theta)$ when $\theta$ corresponds to a true DOA (see (2.44)). This orthogonality also holds true in the wideband case, i.e.

$$\begin{aligned} \mathbf{a}_r^T(\theta, p)\mathbf{u}_i(f_p) = 0 \\ i = K+1, \ldots, L_r \\ p = 0, \ldots, N-1, \end{aligned} \tag{3.57}$$

where $\{\mathbf{u}_i(f_p)\}_{i=1}^{L_r}$ are the eigenvectors of $\mathbf{R}_x(f_p)$. Then, a MUSIC spatial spectrum can be calculated at every frequency component as

$$P_{MUSIC}(\theta, f_p) = \frac{1}{\mathbf{a}_r^T(\theta, p)\mathbf{U}_n(f_p)\mathbf{U}_n^H(f_p)\mathbf{a}_r^*(\theta, p)}. \tag{3.58}$$

Finally, a general wideband MUSIC spatial spectrum can be calculated as [54]

$$\bar{P}_{MUSIC}(\theta) = \frac{1}{\sum_{p=0}^{N-1} \mathbf{a}_r^T(\theta,p)\mathbf{U}_n(f_p)\mathbf{U}_n^H(f_p)\mathbf{a}_r^*(\theta,p)}. \tag{3.59}$$

The target DOAs can be found by searching for the maxima of $\bar{P}_{MUSIC}(\theta)$.

#### 3.5.2.3 The Wideband GLRT Technique

The narrowband GLR at every frequency $f_p$ is given by

$$\rho(\theta,f_p) = 1 - \frac{\mathbf{a}_r^T(\theta,p)\hat{\mathbf{R}}_x(f_p)^{-1}\mathbf{a}_r^*(\theta,p)}{\mathbf{a}_r^T(\theta,p)\hat{\mathbf{Q}}^{-1}(f_p)\mathbf{a}_r^*(\theta,p)} \quad p=0,\ldots,N-1, \tag{3.60}$$

where $\hat{\mathbf{Q}}(f_p)$ is defined as

$$\hat{\mathbf{Q}}(f_p) = \hat{\mathbf{R}}_x(f_p) - \frac{\hat{\mathbf{R}}_{xc}(f_p)\mathbf{a}_t(\theta,p)\mathbf{a}_t^H(\theta,p)\hat{\mathbf{R}}_{xc}^H(f_p)}{\mathbf{a}_t^H(\theta,p)\hat{\mathbf{R}}_c(f_p)\mathbf{a}_t(\theta,p)}, \tag{3.61}$$

$\hat{\mathbf{R}}_c(f_p)$ is the estimated auto-covariance matrix of the transmitted signals at frequency $f_p$, and $\hat{\mathbf{R}}_{xc}(f_p)$ is the estimated cross-covariance matrix between the received and the transmitted signals at frequency $f_p$.

The GLR obtained at every frequency can be averaged as

$$\bar{\rho}(\theta) = \frac{1}{N}\sum_{p=0}^{N-1}\rho(\theta,f_p), \tag{3.62}$$

and the target DOAs can be estimated by searching for the maxima of $\bar{\rho}(\theta)$.

#### 3.5.2.4 Numerical Examples

Simulations are performed as described in Section 3.2 for $F_s = f_c/5 = 200$ MHz. The covariance matrices are estimated for $N_f = 65$ frequency components $f_{p'}$ as described in Appendix B.

For all the simulations, $K = 3$ targets located in the plane-wave region at $\theta_1 = -30°$, $\theta_2 = 0°$, and $\theta_3 = 60°$ are considered, and the $\{\beta_k\}_{k=1}^K$ are set to 1.

An initial omnidirectional stage is performed by transmitting independent random sequences $\{\mathbf{c}(n)\}_{n=0}^{N-1}$ of $N = 512$ QPSK symbols. The narrowband Capon, MUSIC,

and GLRT techniques are then applied in every frequency bin. In a second stage, SBFT is used to match a desired beampattern using the DOA estimates obtained in the omnidirectional stage.

In order to evaluate the DOA estimation performance, the MSE for the target at $-30°$ is computed using 500 Monte Carlo trials for both the omnidirectional and the SFBT stage.

**Omnidirectional Stage**

Figure 3.21 shows the Capon, MUSIC, and GLRT angle and frequency dependent spatial spectra ($P_{cap}(\theta, f_{p'})$, $P_{MUSIC}(\theta, f_{p'})$, and $\rho(\theta, f_{p'})$), obtained after the transmission of independent signals. The reciprocal of noise level is set to $-10\log_{10}\sigma^2 = 0$. As expected, MUSIC has the best resolution over the whole bandwidth. The results obtained at every frequency are averaged to calculate the general spectra $\bar{P}_{cap}(\theta)$, $\bar{P}_{MUSIC}(\theta)$, and $\bar{\rho}(\theta)$ according to (3.56), (3.59), and (3.62) respectively. As shown in Figure 3.22, the target DOAs can be found by searching for the maxima in any of the three averaged spectra.

Figure 3.23 shows the MSEs of the estimates obtained using Capon, MUSIC, and GLRT for the target at $-30°$. As we can see, the GLRT, despite its apparent lower resolution, has better performance than Capon and MUSIC in the omnidirectional stage. MUSIC has slightly better performance than Capon in the whole range of noise levels and has even better performance than GLRT at low noise level ($-10\log_{10}\sigma^2 = 15$).

**SFBT Stage**

A new set of signals $\{\mathbf{c}(n)\}_{n=0}^{N-1}$ is synthesized by SFBT using the DOAs previously estimated by the GLRT. The incoherent Capon, MUSIC, and GLRT techniques are performed once again. The corresponding angle and frequency dependent spectra are shown in Figure 3.24 and the resulting averaged angle-dependent spectra are shown in Figure 3.25. Both Capon and MUSIC spectra have narrow beams in the target directions after the SFBT stage. In contrast, the resolution of GLRT is significantly reduced after transmitting the SFBT beampattern, i.e. the lobes are spatially larger. This is due to the non-orthogonality of the signals synthesized by SFBT. Indeed, the best spatial resolution can be obtained after transmitting orthogonal signals [6]. Even though the signals transmitted in the omnidirectional stage are not perfectly orthogonal, the use of independent sequences will always offer the best spatial resolution.

After the SFBT stage, the three techniques have similar DOA estimation performance at high noise levels ($-10\log_{10}\sigma^2 \leq 5$), as shown in Figure 3.26. However, we must notice that MUSIC outperforms both Capon and GLRT at low noise levels ($-10\log_{10}\sigma^2 \geq 10$).

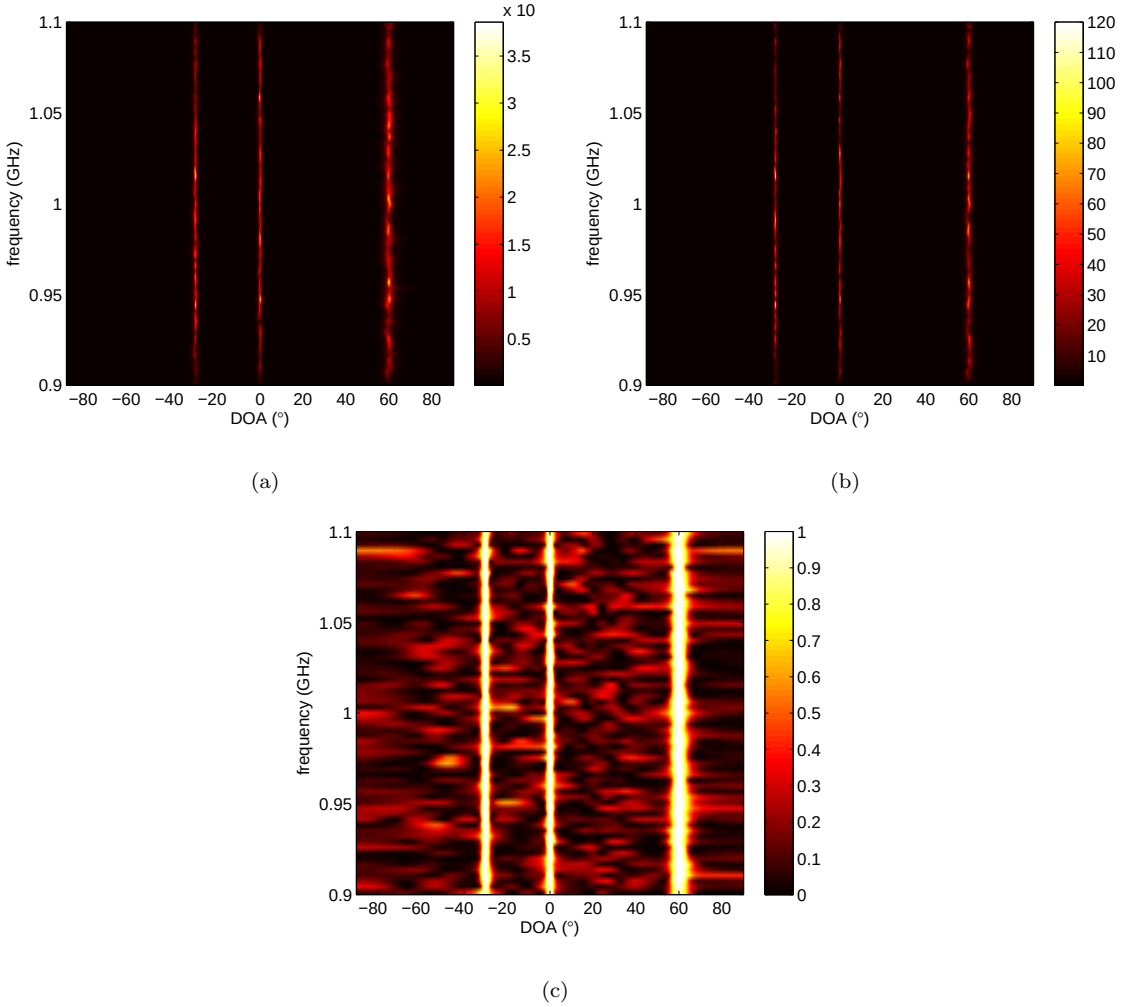


FIGURE 3.21: Stacked narrowband spectra of (a) Capon, (b) MUSIC, and (c) GLRT after the omnidirectional stage ($\theta_1 = -30°$, $\theta_2 = 0°$, $\theta_3 = 60°$, $F_s = f_c/5 = 200$ MHz).

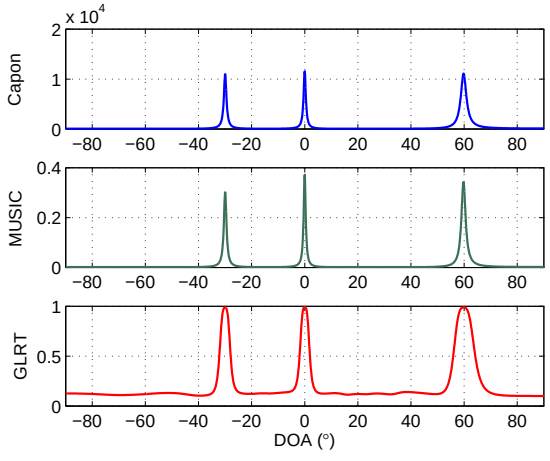


FIGURE 3.22: Incoherent spatial spectra of (a) Capon, (b) MUSIC, and (c) GLRT after the omnidirectional stage ($\theta_1 = -30°$, $\theta_2 = 0°$, $\theta_3 = 60°$, $F_s = f_c/5 = 200$ MHz).

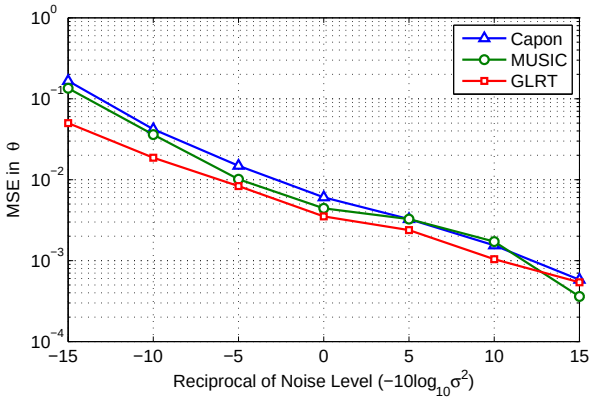


FIGURE 3.23: MSE in $\theta$ for the target at $-30°$ using the Capon, MUSIC, and GLRT estimates after the omnidirectional stage ($F_s = f_c/5 = 200$ MHz).

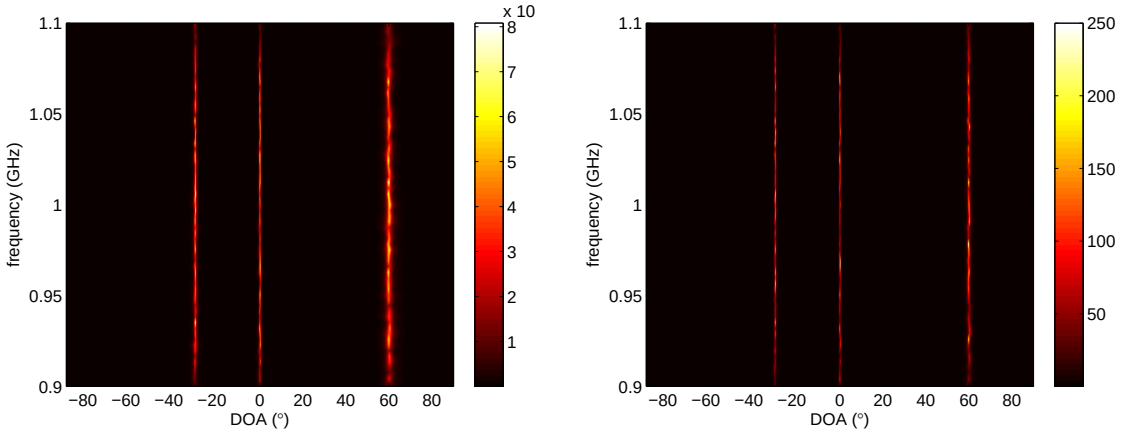


(a) (b)

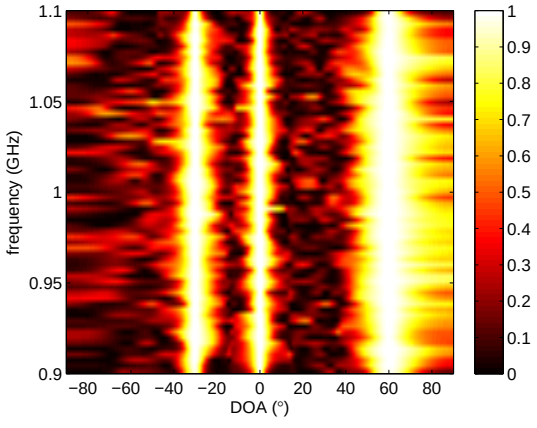


(c)

FIGURE 3.24: Stacked narrowband spectra of (a) Capon, (b) MUSIC, and (c) GLRT after the SBFT stage ($\theta_1 = -30°$, $\theta_2 = 0°$, $\theta_3 = 60°$, $F_s = f_c/5 = 200$ MHz).

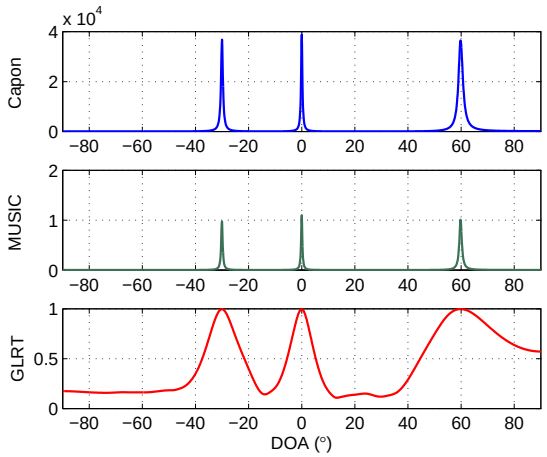


FIGURE 3.25: Incoherent spatial spectra of (a) Capon, (b) MUSIC, and (c) GLRT after the SFBT stage ($\theta_1 = -30°$, $\theta_2 = 0°$, $\theta_3 = 60°$, $F_s = f_c/5 = 200$ MHz).

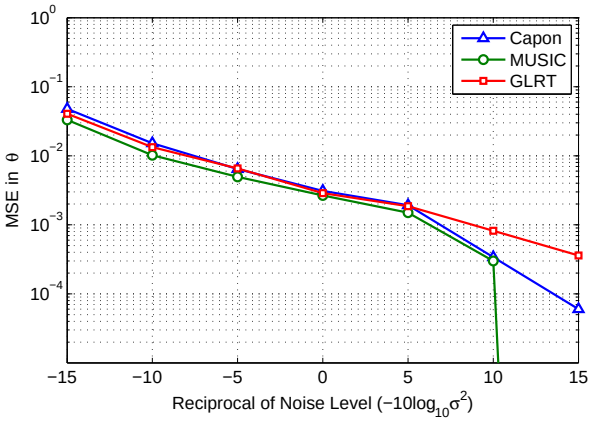


FIGURE 3.26: MSE in $\theta$ for the target at $-30°$ using the Capon, MUSIC, and GLRT estimates after the SFBT stage ($F_s = f_c/5 = 200$ MHz).

#### Comparison of Omnidirectional Probing and SFBT Performance

The concentration of the power in the target directions using SFBT allows improving the DOA estimation performance. This is illustrated by the MSE curves shown in Figure 3.27 for the target at $-30°$. As we can see, the estimation performance of Capon and MUSIC are significantly improved after the SFBT stage. As for GLRT, despite the loss in resolution after the SFBT stage, the DOA estimation performance is slightly improved compared to the omnidirectional stage.

### 3.5.3 Adaptation of TOPS to the MIMO Radar Context

The TOPS technique was originally developed to estimate the DOAs of uncorrelated sources. In the case of MIMO radar, the signals reflected by the targets can be partially correlated, which can degrade the performance of TOPS. This can be

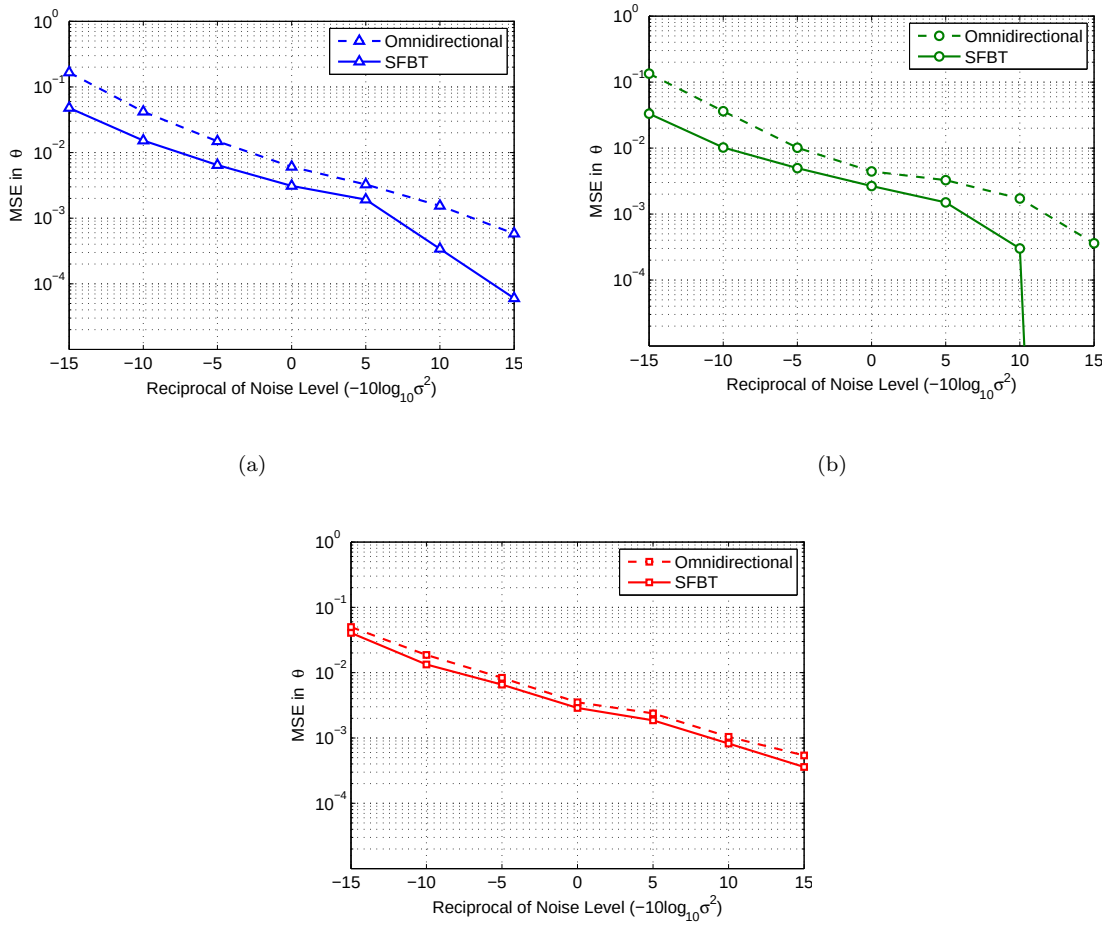


FIGURE 3.27: MSE in $\theta$ for the target at $-30°$ using the estimates given by (a) Capon, (b) MUSIC, and (c) GLRT ($F_s = f_c/5 = 200$ MHz).

observed by applying TOPS as described in Section 3.5.1.3 after transmitting an omnidirectional pattern.

In order to successfully apply TOPS in the context of MIMO radar, the signals to be transmitted can be synthesized using a multiband beampattern as described in Section 3.4. TOPS must then be performed in every frequency band, where in each case the reference frequency will be the center frequency of the corresponding band. Accordingly, we derive thereafter a general expression for the use of TOPS in multiple frequency bands, called M-TOPS.

#### 3.5.3.1 Description of M-TOPS

Let define the transformed signal-plus-noise subspace of the $k^{\text{th}}$ band at frequency $f_p$ as

$$\begin{aligned} \mathbf{F}_{s_k}(f_p) &= \mathbf{\Phi}(\Delta f_{p_k}, \theta)\mathbf{U}_s(f_{ck}) \\ p &= 0, \ldots, N-1, \end{aligned} \tag{3.63}$$

where

$$\Delta f_{p_k} = f_p - f_{ck}, \tag{3.64}$$

and $\mathbf{U}_s(f_{ck})$ is the signal-plus-noise subspace at the center frequency of the $k^{\text{th}}$ band $f_{ck}$. The projected signal-plus-noise subspaces of each frequency band are then given by

$$\begin{aligned} \mathbf{F}'_{s_k}(\theta, f_p) &= \mathbf{P}(\theta, f_p)\mathbf{F}_{s_k}(f_p) \\ p &= 0, \ldots, N-1, \end{aligned} \tag{3.65}$$

with $\mathbf{P}(\theta, f_p)$ defined in (3.50). Then, a test of orthogonality must be performed for every frequency band by defining $K$ matrices $\mathbf{D}_k(\theta)$ as

$$\mathbf{D}_k(\theta) = \left[\mathbf{F}'^H_{s_k}(\theta, f_0)\mathbf{U}_n(f_0) \quad \cdots \quad \mathbf{F}'^H_{s_k}(\theta, f_{N-1})\mathbf{U}_n(f_{N-1})\right]. \tag{3.66}$$

Note that every matrix $\mathbf{D}_k(\theta)$ will be close to singular when the hypothesized $\theta$ corresponds to a true DOA. Therefore, the target DOAs can be estimated by searching for the maxima of

$$P_{M-TOPS}(\theta) = \max \left\{ \frac{1}{\sigma_k(\theta)} \right\}_{k=1}^{K}, \tag{3.67}$$

where $\sigma_k(\theta)$ is the smallest singular value of $\mathbf{D}_k(\theta)$.

#### 3.5.3.2 Numerical Examples

Consider $K = 3$ targets located in the plane-wave region at $\theta_1 = -30°$, $\theta_2 = 0°$, and $\theta_3 = 60°$ with reflection coefficients $\{\beta_k\}_{k=1}^{K}$ equal to 1.

Given that we do not assume any prior knowledge on the target DOAs, an initial omnidirectional stage is performed by transmitting independent sequences $\{\mathbf{c}(n)\}_{n=0}^{N-1}$ of $N = 512$ symbols. The symbol frequency is set to $F_s = f_c/5 = 200$ MHz.

Let us directly apply TOPS to the received signals as described in Section 3.5.1.3. Figure 3.28 shows the TOPS spatial spectrum obtained using (3.53), for a reciprocal of noise level of $-10\log_{10}\sigma^2 = 10$. Since the received signals are not uncorrelated, several false peaks appear around the true DOAs which could lead to a wrong estimation of the target directions.

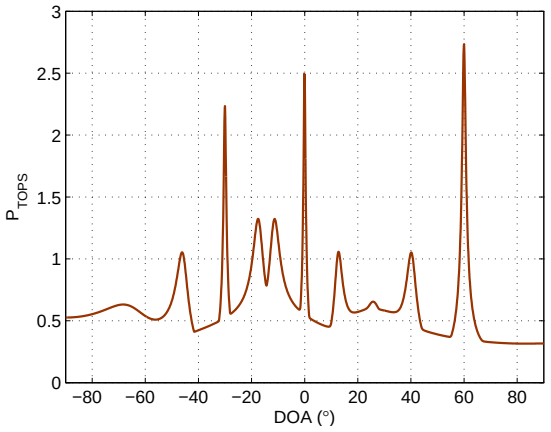


FIGURE 3.28: The TOPS spectrum after the omnidirectional stage ($\theta_1 = -30°$, $\theta_2 = 0°$, $\theta_3 = 60°$, $F_s = f_c/5 = 200$ MHz).

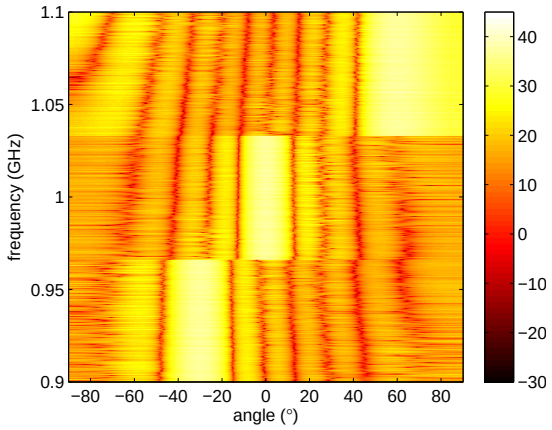


FIGURE 3.29: The M-SFBT beampattern in dB with $\varrho = 2$ and $F_s = f_c/5 = 200$ MHz ($\theta_1 = -30°$, $\theta_2 = 0°$, and $\theta_3 = 60°$).

Let us transmit a multiband beampattern by using M-SFBT in order to receive uncorrelated signals from the targets. The initial DOA estimates required by M-SFBT to synthesize the signals are obtained by applying the incoherent GLRT technique after the omnidirectional stage. One different and non-overlapping frequency band is allocated to each target as shown in Figure 3.29. The PAPR constraint is set to $\varrho = 2$.

Then, M-TOPS can be applied to the received signals, which are now uncorrelated. Figure 3.30 shows the TOPS spatial spectrum $P_{M-TOPS}(\theta)$ calculated from (3.67). We can see that now only the peaks corresponding to the target DOAs appear in the spectrum.

Figure 3.31 shows the MSE of M-TOPS for the target at $-30°$ (computed using 500 Monte Carlo trials) compared with the previously obtained MSE curves of the incoherent Capon, MUSIC, and GLRT techniques after the SFBT stage. As we can see, the incoherent methods have better DOA estimation performance than M-TOPS.

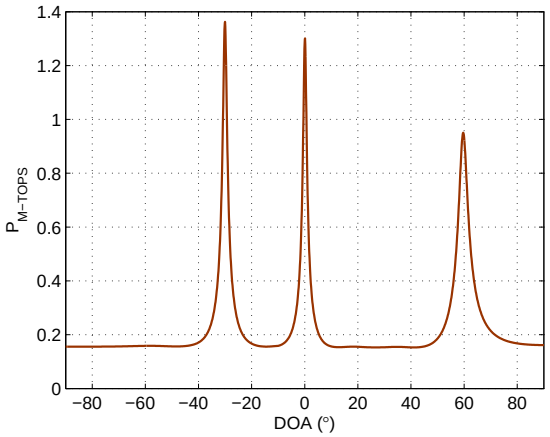


FIGURE 3.30: The TOPS spectrum after the M-SFBT stage ($\theta_1 = -30°$, $\theta_2 = 0°$, $\theta_3 = 60°$, $F_s = f_c/5 = 200$ MHz).

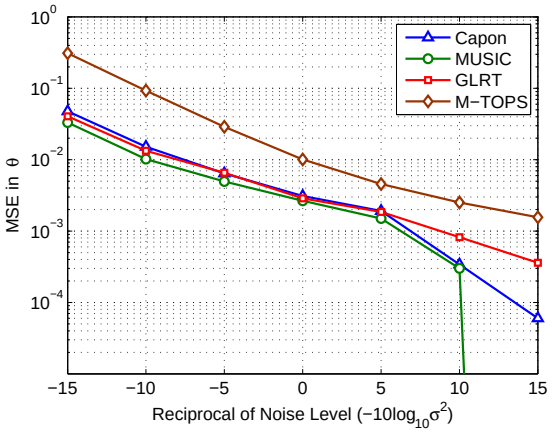


FIGURE 3.31: MSE in $\theta$ for the target at $-30°$ using the Capon, MUSIC, and GLRT estimates after the SFBT stage and the M-TOPS estimates after the M-SFBT stage ($F_s = f_c/5 = 200$ MHz).

However, the incoherent methods fail when the SNR at each frequency varies, as discussed in [54]. In that case, the use of alternative methods such as M-TOPS might be convenient.

## 3.6 Summary

A wideband signal model of MIMO radar was presented in Section 3.1. In this model, the received signals are decomposed into several narrowband components by using the DFT. Next, two recently proposed wideband waveform design techniques, WFBIT and SFBT, were described and compared in Section 3.3. WBFIT can synthesize low PAPR sequences and beampatterns that are usually smoother than those obtained by SFBT. However, the performance of WBFIT is seriously degraded when the bandwidth is

relatively large ($F_s = f_c/2$): The beams are deformed and parasitic lobes might appear around the directions of interest. Moreover, WFBIT is an iterative process that requires a considerable amount of computing time. On the other hand, SFBT works well even in the case of relatively large bandwidths ($F_s = f_c/2$) and is much faster to compute than WFBIT (at least 2000 times). However, the sequences synthesized by SFBT usually have high PAPR. For this reason, a multiband waveform design technique (M-SFBT) based on SFBT was proposed in Section 3.4. The M-SFBT is used to transmit the power directly to the targets while allocating a different non-overlapping frequency band to each one. The use of multiband beampatterns allows receiving uncorrelated signals from the targets. Moreover, the signals synthesized by M-SFBT meet a PAPR constraint similar to WBFIT.

In Section 3.5 some target DOA estimation techniques were presented based on the existing wideband array processing techniques. The incoherent methods consist in applying narrowband techniques (Capon, MUSIC, and GLRT) at each frequency component and averaging the results over frequency to obtain a general spectrum. The simulations showed that the use of SFBT improves the DOA estimation performance of the incoherent techniques compared to an omnidirectional probing. Even though the three incoherent techniques, Capon, MUSIC, and GLRT have similar estimation performance after the omnidirectional stage, the incoherent MUSIC algorithm has the minimum MSE after the SFBT stage.

TOPS is a more sophisticated method which exploits the orthogonality between the signal-plus-noise and the noise subspaces at different frequencies. However, TOPS cannot be successfully applied when the received signals are correlated: Several false peaks appear around the target directions in the TOPS spectrum, which could lead to a wrong detection. As described in Section 3.5.3, after transmitting a multiband beampattern, the received signals are uncorrelated and the target DOAs can be successfully estimated by performing TOPS in each frequency band.

Our contributions presented in this chapter are the proposition of a multiband waveform design technique (M-SFBT) which allows receiving uncorrelated signals from the targets, the adaptation of narrowband DOA estimation techniques to the wideband case, and the adaptation of TOPS to the context of wideband MIMO radar with colocated antennas.

# Chapter 4

# Effects of Mutual Coupling on MIMO Radar Performance

The signal models of MIMO radar for both the narrowband and the wideband cases have been presented in Chapters 2 and 3 respectively. While these models are general, some assumptions were done to simplify the development and simulation of the detection techniques and waveform design algorithms. As it is usually done in the literature, the antenna elements of the ULAs used for transmission and reception were assumed to have identical characteristics, i.e. equal gain, radiation pattern, and bandwidth among others. However, such characteristics can significantly differ from one element to the other in real antenna arrays due to the existence of mutual coupling: The electromagnetic characteristics of every antenna element are influenced by the neighboring elements. Indeed, due to the proximity between the antenna elements, part of the signal radiated by every single element is received by the surrounding elements, even if they are all transmitting elements [56]. Moreover, the coupled signal might be re-radiated or scattered. As for the receiver elements, they might reflect part of the incident waves and thus act like small transmitters even if they are supposed to "receive" only.

The mutual coupling in antenna arrays depends on several factors, including the type of antennas, the inter-element spacings, the antenna orientation, the bandwidth, the directivity, and the feeding network among others. The existence of mutual coupling leads to several negative effects on the array performance. The electromagnetic interactions between different antenna elements cause changes (in magnitude and phase) in the current distributions of every antenna element which leads to an alteration of the different input impedances [57]. This usually produces impedance mismatches at the transmitters, receivers, and transmission lines. Also, in many array

configurations, the change in the current distributions produces distortions in the radiation patterns. Actually, the radiation of every antenna element might totally differ from that of an isolated element. This is non-negligible and can significantly affect the DOA estimation performance [58]-[61].

Another negative effect is the direct coupling between the transmitter and the receiver elements. In fact, part of the transmitted signals can be directly received by the receiver elements depending on the separation between the transmitter and receiver arrays. Herein, this phenomenon will be referred to as "crosstalk".

The effects of mutual coupling (radiation pattern distortion and crosstalk) in the performance of narrowband MIMO radar with colocated antennas are studied in this chapter. In Section 4.1 the different radiation patterns are taken into account in order to improve the DOA estimation performance in the presence of mutual coupling. In Section 4.2 we propose a crosstalk reduction technique based on a signal processing approach.

## 4.1 Radiation Pattern Distortion due to Mutual Coupling

The effects of mutual coupling on the radiation patterns of antenna arrays have been highly studied in the literature. In [33], different array modeling methods are presented and compared in the case of phased array systems. The authors also present a pattern prediction method for small and medium-sized arrays of equally spaced elements.

Various approaches for reducing mutual coupling can be found in the literature. In many cases, parasitic structures are added between the antenna elements to reduce the coupled power [62]-[64]. Other methods based on antenna design are presented in [65]-[68]. Also, instead of modifying the antenna structures, the distortions in the radiation patterns can be compensated by designing compensation networks based on the mutual impedances of the antenna elements [69] or the scattering parameter (S-parameter) matrix [70]. This compensation can also be achieved in post-processing by including S-parameter-based compensation matrices in the array processing algorithms [59][60][61][71].

In this section, we analyze the influence of mutual coupling on the radiation patterns of a narrowband MIMO radar with colocated antennas via electromagnetic simulations. Unlike the approaches mentioned above, we do not try to compensate or reduce mutual coupling. We show that taking into account the radiation pattern of every antenna element allows reducing the DOA estimation errors without need of using compensation matrices or parasitic structures.

The work persented in this section is the result of a collaboration with Prof. Vincent Fusco at Queen's University Belfast and the Institute of Electronics, Communications and Information Technology (ECIT).

### 4.1.1 Radiation Pattern of an Isolated Element

Consider the single linearly polarized patch antenna shown in Figure 4.1. The antenna, designed to resonate at 5.8 GHz, is coaxially fed and has a RT5880 substrate of dielectric constant $\varepsilon_r = 2.2$. The normalized radiation pattern of the patch antenna at 5.8 GHz, obtained by electromagnetic simulations in CST Microwave Studio, is shown in Figure 4.2. We do not see any particular distortion in the radiation pattern since there is no mutual coupling in an isolated element. For simplicity and given that the arrays of interest in this document detect targets only in azimuthal directions ($\theta$), in the following simulations the radiation patterns are assumed to be two-dimensional, but only the component at phi = 0° is of interest.

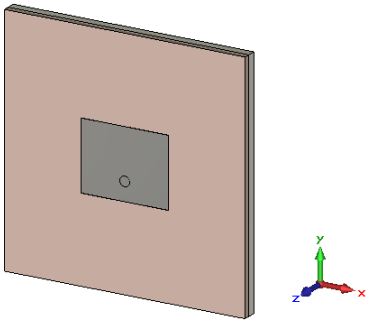


FIGURE 4.1: Linearly polarized patch antenna.

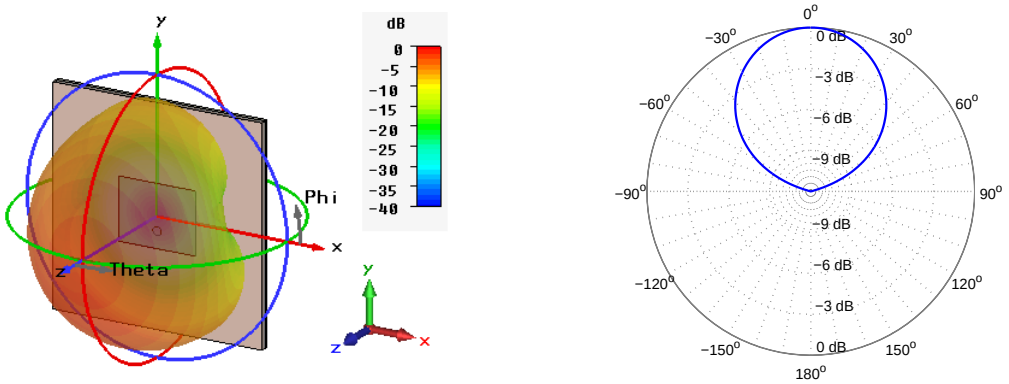


(a) (b)

FIGURE 4.2: Normalized radiation pattern (in magnitude) of an isolated patch antenna at 5.8 GHz in (a) 3D and (b) 2D (cutting plane phi = 0°).

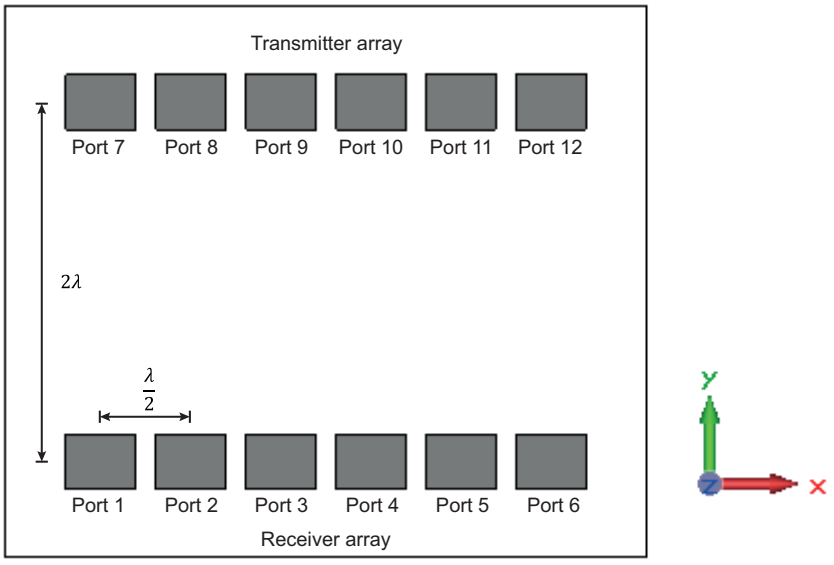


FIGURE 4.3: Transmitter and receiver arrays of patch antennas resonating at 5.8 GHz ($L = L_t = L_r = 6$).

### 4.1.2 Radiation Patterns of the Elements of a Transmitter and a Receiver Array

Consider now the transmitter and receiver arrays of $L = L_t = L_r = 6$ elements shown in Figure 4.3. The elements are identical to the patch antenna of Figure 4.1, the inter-element spacings are $d_t = d_r = \lambda/2$ and the arrays are separated by a distance of $2\lambda$. The receiving elements are placed at ports 1 to 6 while the transmitting elements are at ports 7 to 12.

Figures 4.4 and 4.5 show the radiation patterns at 5.8 GHz of the antenna elements of the receiver and the transmitter arrays respectively. As we can see, all the radiation patterns are deformed and totally differ from that of an isolated element. Moreover, even if the arrays are two ULAs, the radiation patterns are all different. We must however note that the radiation patterns of the elements of a same array are symmetrical because of the geometry of the array. Also, the radiation patterns of the receiving elements are very similar to those of the transmitting elements.

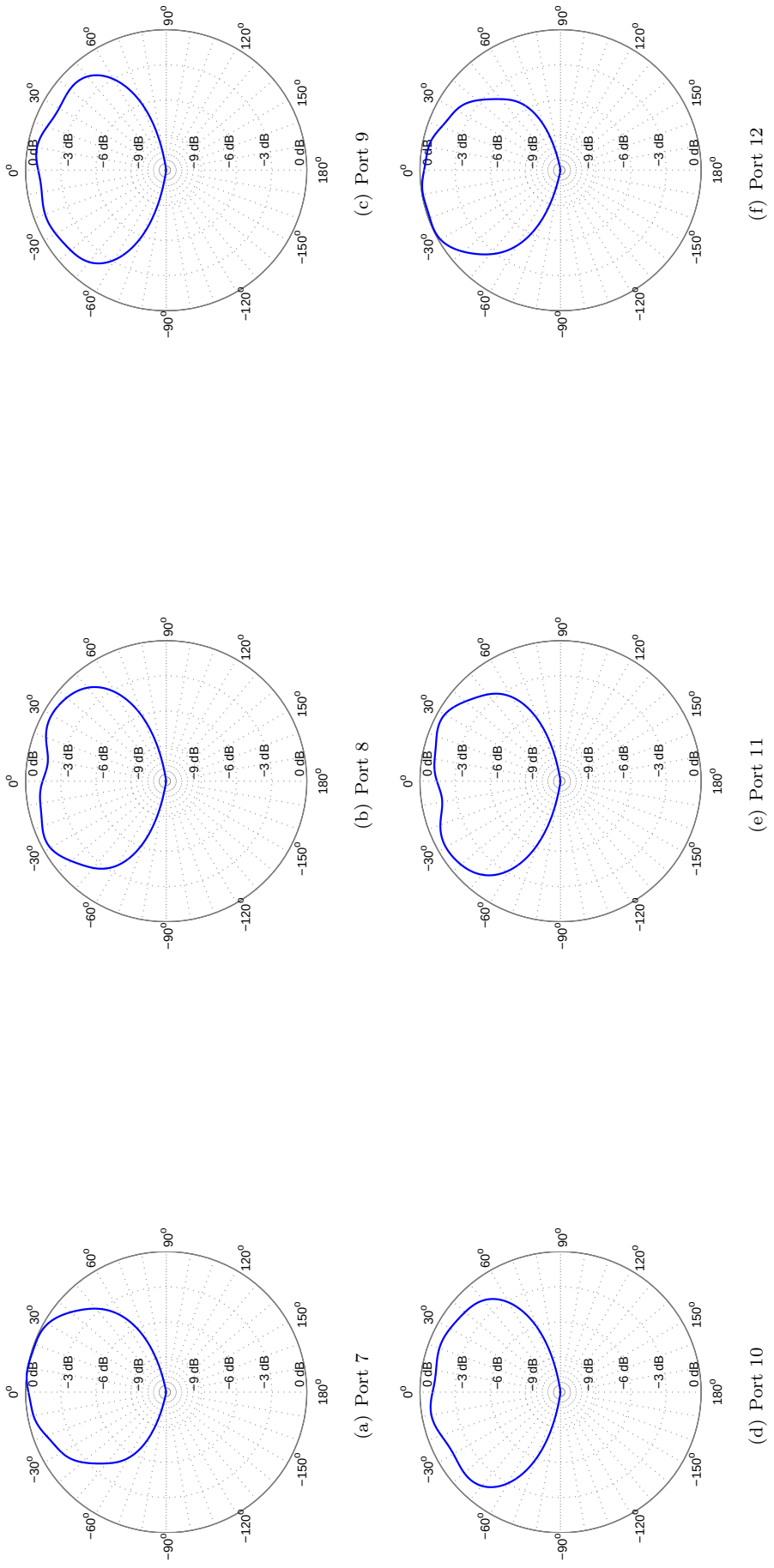


(a) Port 7 (b) Port 8 (c) Port 9

(d) Port 10 (e) Port 11 (f) Port 12

FIGURE 4.4: Normalized radiation patterns (in magnitude) of the receiving elements at 5.8 GHz (ports 1 to 6).

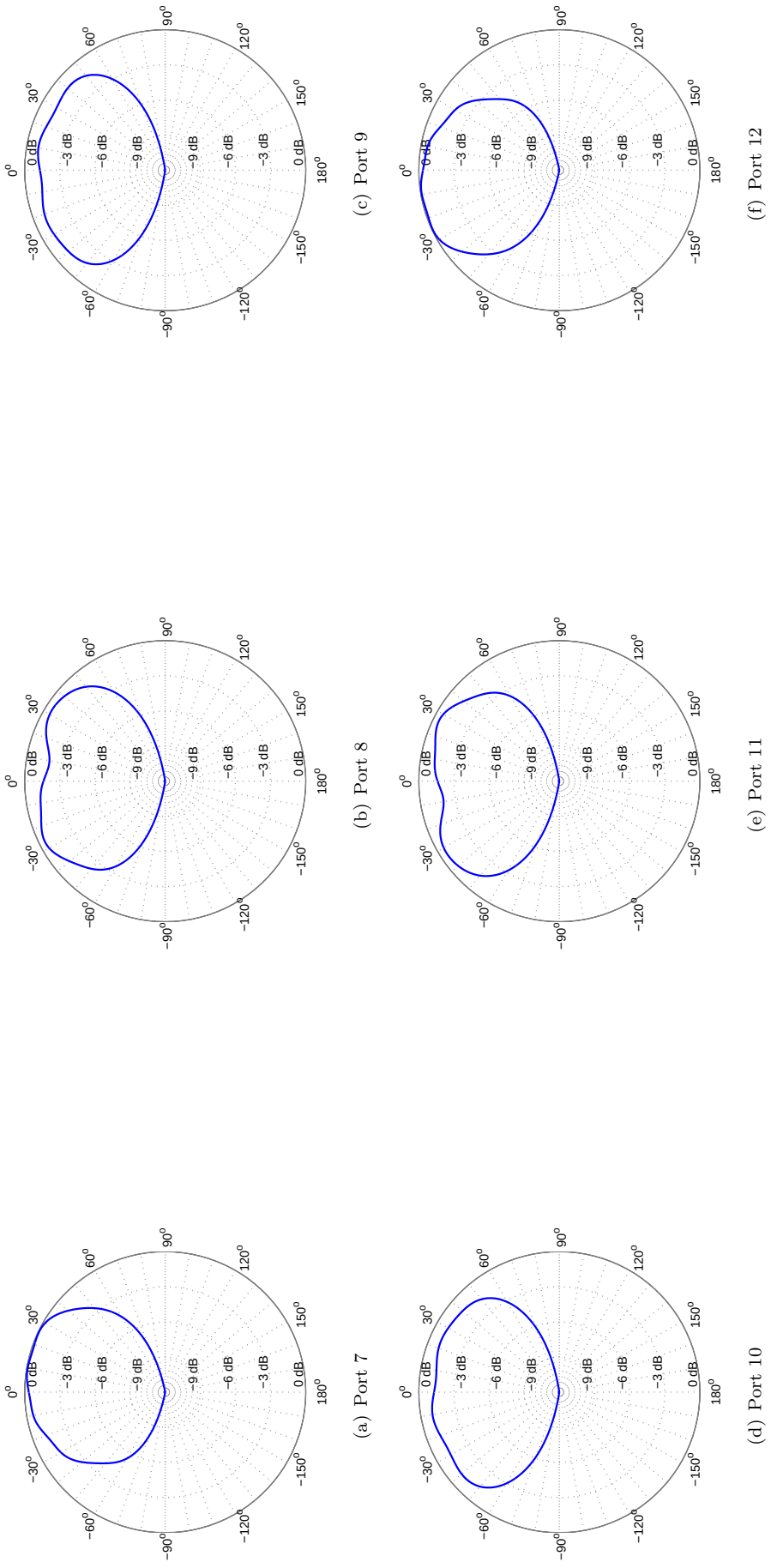


(a) Port 7 (b) Port 8 (c) Port 9

(d) Port 10 (e) Port 11 (f) Port 12

FIGURE 4.5: Normalized radiation patterns (in magnitude) of the transmitting elements at 5.8 GHz (ports 7 to 12).

### 4.1.3 Taking the Radiation Patterns into Account

The simulations presented in Chapter 2 were performed using the standard steering vectors

$$\mathbf{a}_t(\theta) = \left[e^{j\frac{2\pi}{\lambda}(\frac{L_t-1}{2}-i)d_t\sin\theta}\right]_{i=0,\ldots,L_t-1} \tag{4.1}$$

and

$$\mathbf{a}_r(\theta) = \left[e^{j\frac{2\pi}{\lambda}(\frac{L_r-1}{2}-l)d_r\sin\theta}\right]_{l=0,\ldots,L_r-1}, \tag{4.2}$$

which omit the different radiation patterns as it is commonly done in the literature. However, the use of such steering vectors can lead to wrong DOA estimation given that the radiation patterns are actually different because of mutual coupling. To observe this, MATLAB simulations are performed in narrowband considering the antenna arrays of figure 4.3 and using the signal model

$$\mathbf{x}(n) = \sum_{k=1}^{K} \beta_k \tilde{\mathbf{a}}_r^*(\theta_k)\tilde{\mathbf{a}}_t^H(\theta_k)\mathbf{c}(n) + \mathbf{z}(n), \tag{4.3}$$

where

$$\tilde{\mathbf{a}}_t(\theta) = \left[g_{t,i}^*(\theta)e^{j\frac{2\pi}{\lambda}(\frac{L_t-1}{2}-i)d_t\sin\theta}\right]_{i=0,\ldots,L_t-1} \tag{4.4}$$

and

$$\tilde{\mathbf{a}}_r(\theta) = \left[g_{r,l}^*(\theta)e^{j\frac{2\pi}{\lambda}(\frac{L_r-1}{2}-l)d_r\sin\theta}\right]_{l=0,\ldots,L_r-1} \tag{4.5}$$

are the general steering vectors which include the different radiation patterns. The radiation patterns used here are those obtained by electromagnetic simulations and shown in Figures 4.4 and 4.5. In practice, the radiation patterns can be measured or computed using the active element pattern method [57][72].

Consider $K = 3$ targets located in the plane-wave region at $\theta_1 = -40°$, $\theta_2 = 20°$, $\theta_3 = 40°$ with reflection coefficients $\beta_1 = \beta_2 = \beta_3 = \beta = 1$. Let us apply the narrowband Capon, MUSIC, and GLRT techniques neglecting the pattern distortions: The different spatial spectra are computed using the standard steering vectors $\mathbf{a}_t(\theta)$ and $\mathbf{a}_r(\theta)$. The spectra obtained for a reciprocal of noise level of $-10\log_{10}\sigma^2 = 20$ are shown in Figure 4.6. As we can see, the peaks in the spectra are not centered in the target directions in none of the three techniques, which leads to biased DOA estimates. We can also note that the resolution of MUSIC is significantly reduced: The lobes in the MUSIC spectrum are almost as wide as those in the Capon spectrum.

The pattern distortions can be taken into account by using the general form of the steering vectors to compute the spatial spectra. Figure 4.7 shows the Capon, MUSIC, and GLRT spectra obtained using the steering vectors $\tilde{\mathbf{a}}_t(\theta)$ and $\tilde{\mathbf{a}}_r(\theta)$ for the same noise

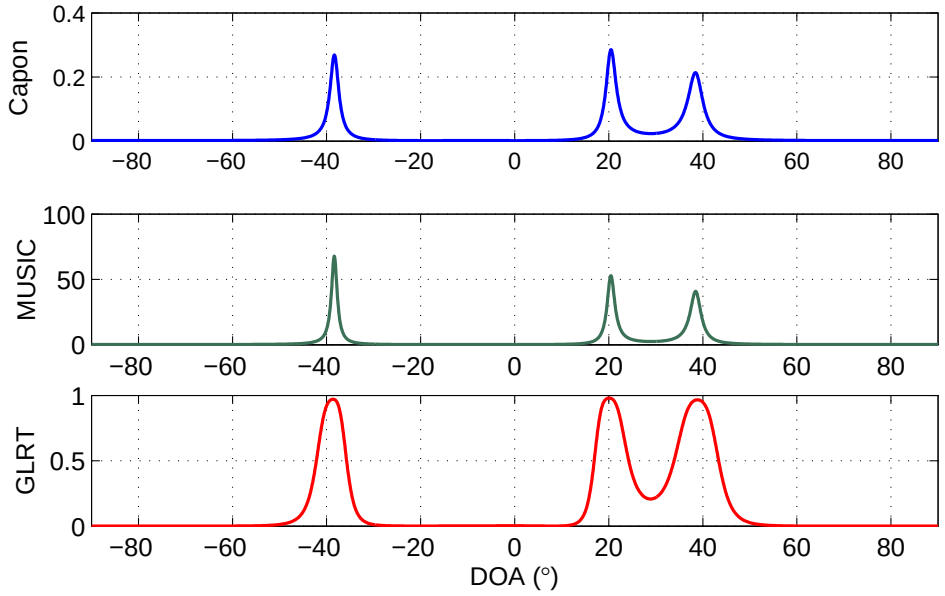


FIGURE 4.6: Capon, MUSIC, and GLRT spectra for three targets at $\theta_1 = -40°$, $\theta_2 = 20°$, and $\theta_3 = 40°$, neglecting the pattern distortions ($-10\log_{10}\sigma^2 = 20$).

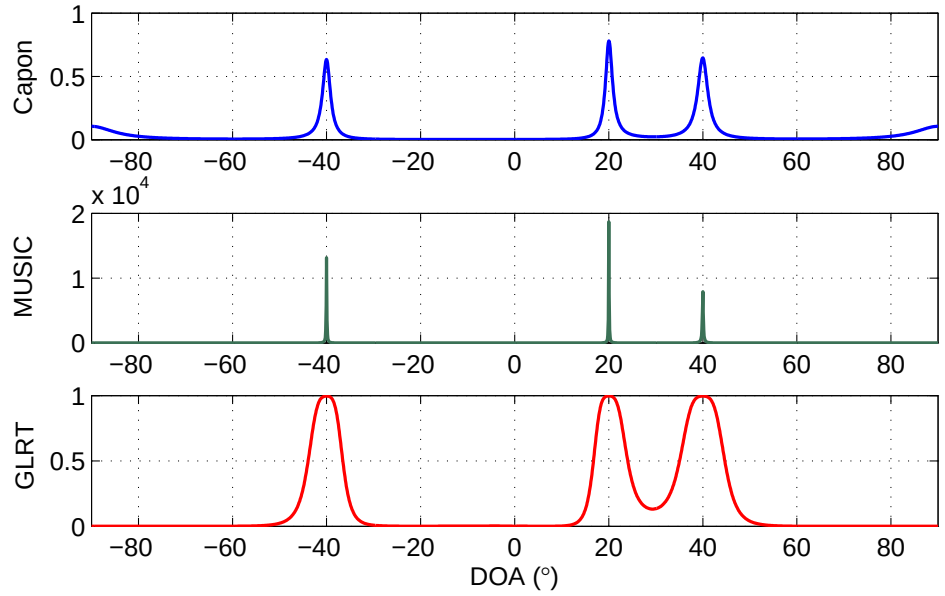


FIGURE 4.7: Capon, MUSIC, and GLRT spectra for three targets at $\theta_1 = -40°$, $\theta_2 = 20°$, and $\theta_3 = 40°$, taking the radiation patterns into account ($-10\log_{10}\sigma^2 = 20$).

level ($-10\log_{10}\sigma^2 = 20$). We can now see that the peaks in the three spatial spectra are centered at the target directions. Moreover, the resolution of MUSIC is significantly improved: Three sharp peaks are present at the target DOAs.

The negative effects of pattern distortion on the DOA estimation performance can be even worse in the case of closely spaced targets. Consider now $K = 3$ targets located in the plane-wave region at $\theta_1 = -40°$, $\theta_2 = -5°$, $\theta_3 = 5°$ with reflection coefficients $\beta_1 = \beta_2 = \beta_3 = \beta = 1$. The Capon, MUSIC, and GLRT spatial spectra obtained for a

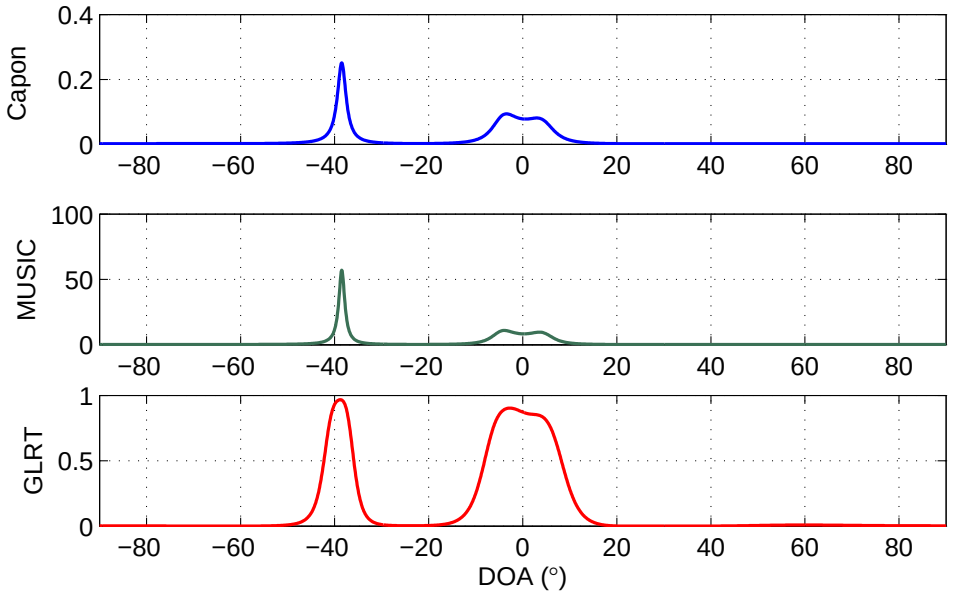


FIGURE 4.8: Capon, MUSIC, and GLRT spectra for three targets at $\theta_1 = -40°$, $\theta_2 = -5°$, and $\theta_3 = 5°$, neglecting the pattern distortions ($-10\log_{10}\sigma^2 = 20$).

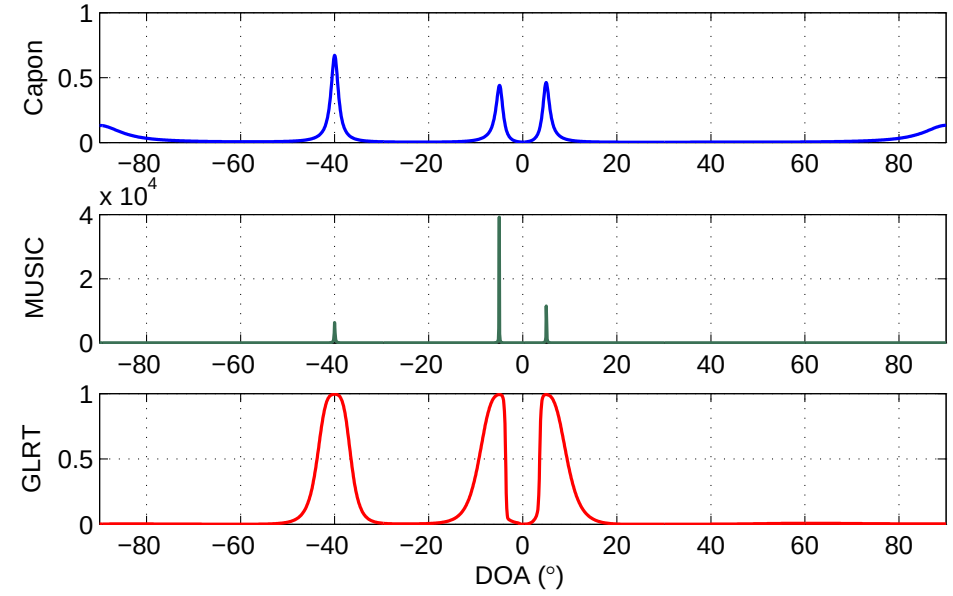


FIGURE 4.9: Capon, MUSIC, and GLRT spectra for three targets at $\theta_1 = -40°$, $\theta_2 = -5°$, and $\theta_3 = 5°$, taking the radiation patterns into account ($-10\log_{10}\sigma^2 = 20$).

reciprocal of noise level of $-10\log_{10}\sigma^2 = 20$ and neglecting the pattern distortions are shown in Figure 4.8. We can clearly see that the three techniques are unable to resolve the closely spaced targets. On the other hand, if we take the radiation patterns into account, all the targets are perfectly detected by Capon, MUSIC, and GLRT, as shown in Figure 4.9.

Let us now analyze the influence of the radiation patterns in the case of a relatively high noise level. Consider one target located in the plane-wave region at $-40°$ with

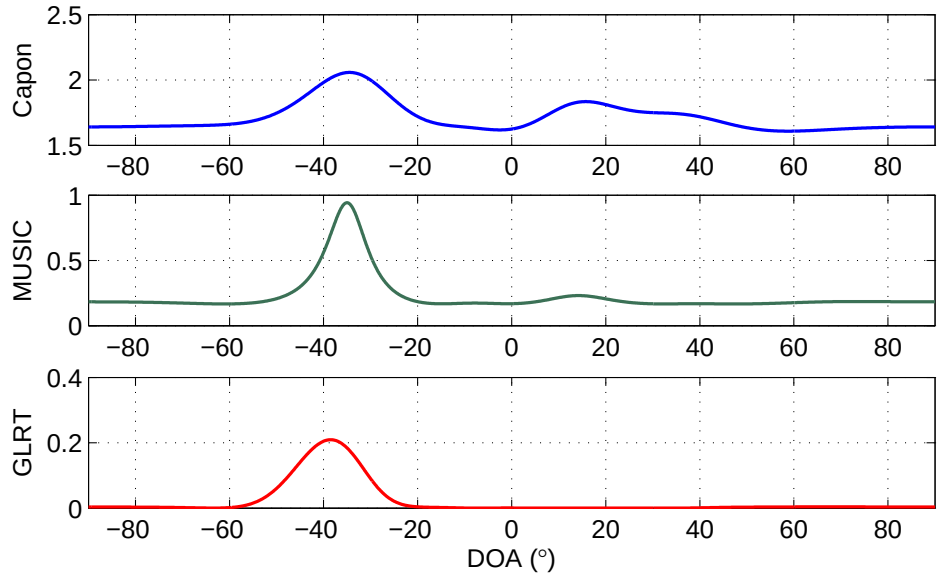


FIGURE 4.10: Capon, MUSIC, and GLRT spectra for one target at $-40°$, neglecting the pattern distortions ($-10\log_{10}\sigma^2 = -10$).

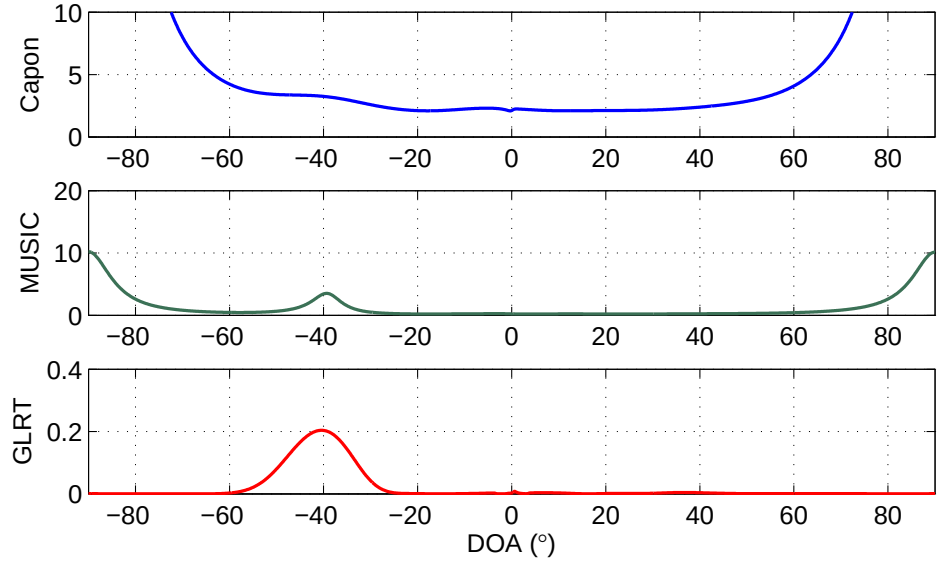


FIGURE 4.11: Capon, MUSIC, and GLRT spectra for one target at $-40°$, taking the radiation patterns into account ($-10\log_{10}\sigma^2 = -10$).

reflection coefficient $\beta = 1$. The Capon, MUSIC, and GLRT spatial spectra obtained for a reciprocal of noise level of $-10\log_{10}\sigma^2 = -10$ and neglecting the pattern distortions are shown in Figure 4.10. As expected, the peaks in the three spectra are not centered at the target DOA which leads to highly biased DOA estimates. As discussed before, the bias should be reduced by taking the radiation patterns into account to compute the spatial spectra. Figure 4.11 shows the Capon, MUSIC, and GLRT spectra obtained using the steering vectors $\tilde{\mathbf{a}}_t(\theta)$ and $\tilde{\mathbf{a}}_r(\theta)$ for the same noise level ($-10\log_{10}\sigma^2 = -10$).

We can see that the lobe in the GLRT and MUSIC spectra is now re-centered at the target DOA. In contrast, a high regrowth appears in the Capon spectrum at angles close to $-90°$ and $90°$. The regrowth is so large that the target lobe can hardly be seen. A similar but less important regrowth also appears in the MUSIC spectrum; however, it does not affect the lobe around $-40°$. This regrowth is related to the definition of the Capon and MUSIC spectra, and the weak magnitudes of the radiation patterns at angles close to $-90°$ and $90°$. Actually, the Capon and MUSIC spectra, computed using the general steering vectors are given by (see Section 2.2)

$$P_{cap}(\theta) = \frac{1}{\tilde{\mathbf{a}}_r^T(\theta)\mathbf{R}_x^{-1}\tilde{\mathbf{a}}_r^*(\theta)} \tag{4.6}$$

and

$$P_{MUSIC}(\theta) = \frac{1}{\tilde{\mathbf{a}}_r^T(\theta)\mathbf{U}_n\mathbf{U}_n^H\tilde{\mathbf{a}}_r^*(\theta)}. \tag{4.7}$$

Given that the magnitudes of the radiation patterns are close to zero for angles close to $-90°$ and $90°$ (see Figures 4.4 and 4.5), $P_{cap}(\theta)$ and $P_{MUSIC}(\theta)$ may have high values when $|\theta|$ tends to $90°$. This regrowth seems to be accentuated at high noise levels.

This problem might be solved by including only the phase of the radiation patterns in the steering vectors. Let us define the general phase-only steering vectors as

$$\boldsymbol{\alpha}_t(\theta) = \left[e^{-j\arg\{g_{t,i}(\theta)\}}e^{j\frac{2\pi}{\lambda}(\frac{L_t-1}{2}-i)d_t\sin\theta}\right]_{i=0,\ldots,L_t-1} \tag{4.8}$$

and

$$\boldsymbol{\alpha}_r(\theta) = \left[e^{-j\arg\{g_{r,l}(\theta)\}}e^{j\frac{2\pi}{\lambda}(\frac{L_r-1}{2}-l)d_r\sin\theta}\right]_{l=0,\ldots,L_r-1}. \tag{4.9}$$

Then, the spatial spectra can be computed using $\boldsymbol{\alpha}_t(\theta)$ and $\boldsymbol{\alpha}_r(\theta)$ instead of $\tilde{\mathbf{a}}_t(\theta)$ and $\tilde{\mathbf{a}}_r(\theta)$ respectively.

Consider the same target at $-40°$ ($\beta = 1$) and the same noise level ($-10\log_{10}\sigma^2 = -10$). The Capon, MUSIC, and GLRT spectra obtained using the general phase-only steering vectors are shown in Figure 4.12. As we can see, there is no regrowth in any of the spectra given that the magnitudes of the radiation patterns are not included in the steering vectors. Moreover, the lobes are still centered close to the target DOAs. The impact of the different steering vectors on the DOA estimation performance is evaluated in Section 4.1.4.

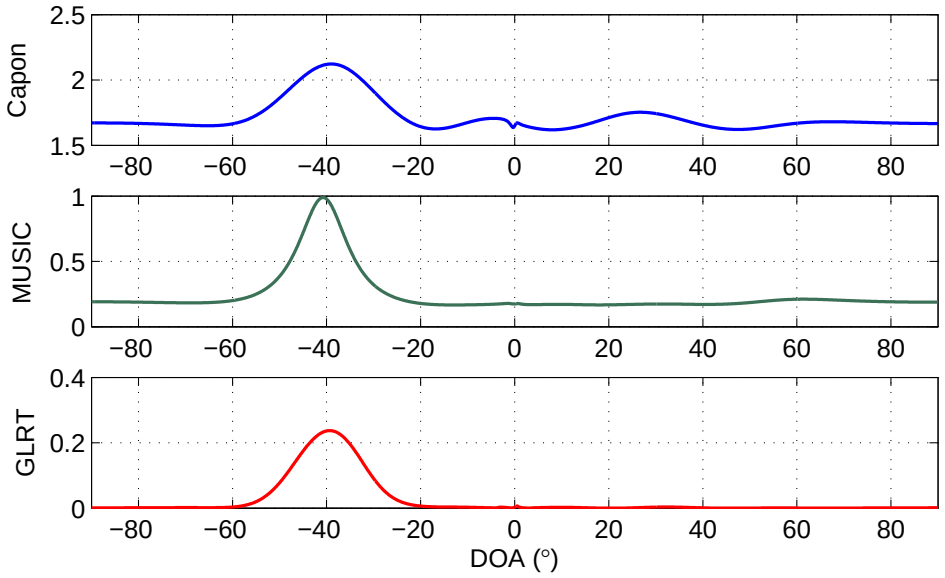


FIGURE 4.12: Capon, MUSIC, and GLRT spectra for one target at $-40°$, taking only the phase of the radiation patterns into account ($-10\log_{10}\sigma^2 = -10$).

### 4.1.4 DOA Estimation Performance in the Presence of Distorted Radiation Patterns

In order to evaluate the DOA estimation performance of narrowband Capon, MUSIC, and GLRT techniques in the presence of distorted radiation patterns, the MSE for one target located at $\theta_1 = -40°$ ($\beta = 1$) is computed using 500 Monte Carlo trials. The MSE in the DOA estimated in degrees is computed for four different cases:

- **Ideal case**: The signal propagation is simulated without pattern distortion by using the signal model $\mathbf{x}(n) = \beta\mathbf{a}_r^*(\theta_1)\mathbf{a}_t^H(\theta_1)\mathbf{c}(n) + \mathbf{z}(n)$, and the Capon, MUSIC, and GLRT spectra are computed using the standard steering vectors $\mathbf{a}_r(\theta)$ and $\mathbf{a}_t(\theta)$.

- **Standard processing case**: The signal propagation is simulated including pattern distortion by using the signal model $\mathbf{x}(n) = \beta\tilde{\mathbf{a}}_r^*(\theta_1)\tilde{\mathbf{a}}_t^H(\theta_1)\mathbf{c}(n) + \mathbf{z}(n)$, but the Capon, MUSIC, and GLRT spectra are computed using the standard steering vectors $\mathbf{a}_r(\theta)$ and $\mathbf{a}_t(\theta)$.

- **Mutual-Coupling (MC) based processing case**: The signal propagation is simulated including pattern distortion by using the signal model $\mathbf{x}(n) = \beta\tilde{\mathbf{a}}_r^*(\theta_1)\tilde{\mathbf{a}}_t^H(\theta_1)\mathbf{c}(n) + \mathbf{z}(n)$, and the Capon, MUSIC, and GLRT spectra are computed using the general steering vectors $\tilde{\mathbf{a}}_r(\theta)$ and $\tilde{\mathbf{a}}_t(\theta)$.

- **Mutual-Coupling (MC) based phase-only processing case**: The signal propagation is simulated including pattern distortion by using the signal model

$\mathbf{x}(n) = \beta\tilde{\mathbf{a}}_r^*(\theta_1)\tilde{\mathbf{a}}_t^H(\theta_1)\mathbf{c}(n) + \mathbf{z}(n)$, and the Capon, MUSIC, and GLRT spectra are computed using the general phase-only steering vectors $\boldsymbol{\alpha}_r(\theta)$ and $\boldsymbol{\alpha}_t(\theta)$.

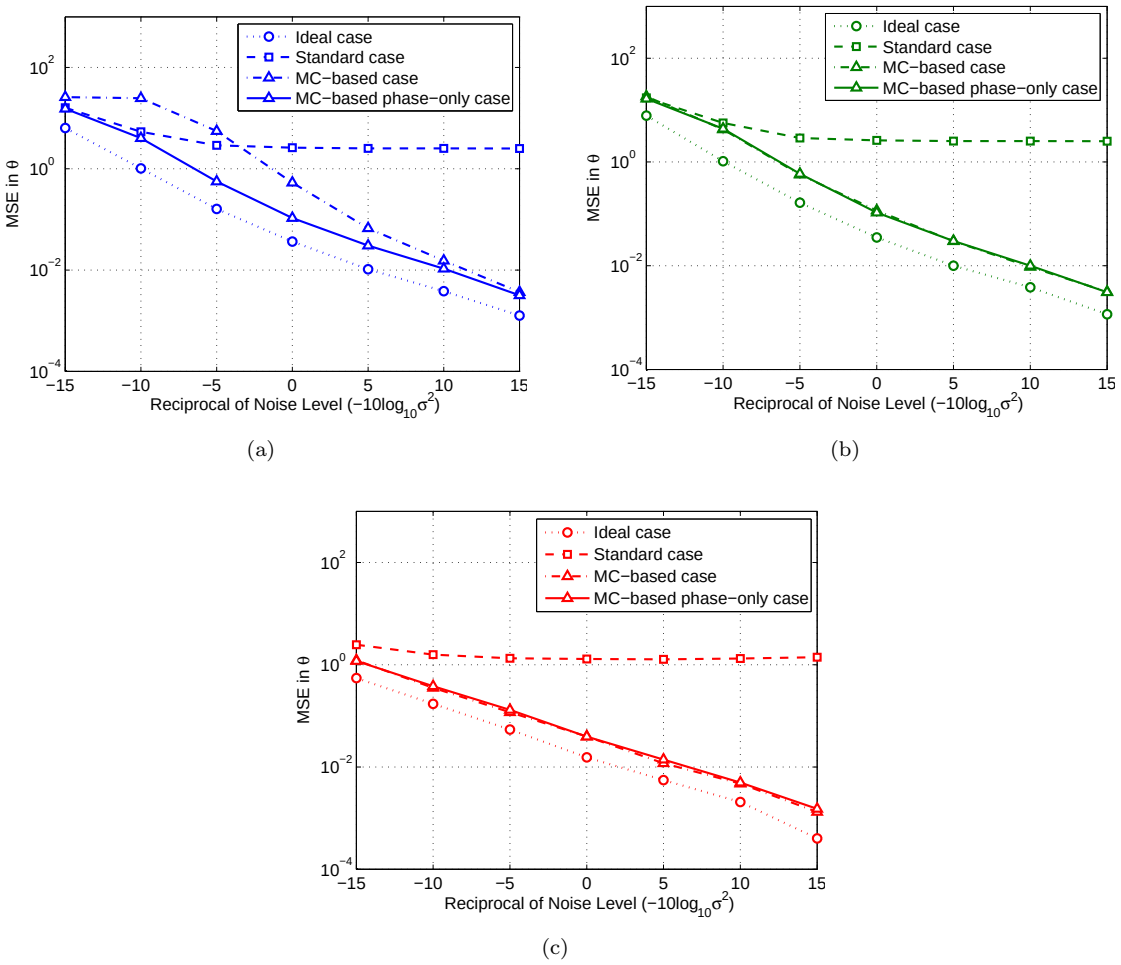


FIGURE 4.13: MSE in $\theta$ for one target at $-40°$ using the estimates given by (a) Capon, (b) MUSIC, and (c) GLRT.

The results are shown in Figure 4.13. We can see that the minimum MSE is obtained in the ideal case, however this is an unrealistic simulation given that the signal propagation is modeled assuming that the radiation patterns are all identical and angle independent. We can also see that important errors are obtained using the standard processing given that pattern distortion is not taken into account in the steering vectors $\mathbf{a}_r(\theta)$ and $\mathbf{a}_t(\theta)$. In contrast, we can clearly see that the use of the MC-based processing allows reducing the errors introduced by the distortions in the radiation patterns: The MSEs in the DOA estimated by Capon, MUSIC, and GLRT are greatly reduced and approach the ideal MSE curves. We must however note that MC-based method increases the MSE in the DOA estimated by Capon at high noise levels ($-10\log_{10}\sigma^2 \leq -5$), which is due to the high regrowth present in the Capon spectrum at high noise levels. Nevertheless, we can see that this problem is solved by using the general phase-only steering vectors

to compute the spatial spectra: The MSE in the DOA estimated by Capon is reduced and is always lower than the MSE of the standard processing case. As for MUSIC and GLRT, there is no visible difference between both MC-based cases (the MSE curves are overlapped), which means that excluding the magnitudes of the radiation patterns does not introduce any significant error.

## 4.2 Crosstalk

Besides the distortion of the radiation patterns, the existence of crosstalk is another negative consequence of the small separation between the antenna arrays. In the case of MIMO radar, the signals reflected by the targets and received by the receiver array are corrupted by a part of every transmitted signal which is directly transferred from the transmitter elements to the receiver ones. This can be seen as noise or interference which is correlated with the transmitted signals and can significantly degrade the DOA estimation performance.

### 4.2.1 Crosstalk Modeling

The signals directly transmitted from the transmitter to the receiver elements can be modeled as a mixture of the set of the transmitted signals. In the case of narrowband signals, the baseband signal received by the $l^{\text{th}}$ receiver element ($l = 0, \ldots, L_r - 1$) due to the signals directly transmitted by the $L_t$ transmitter elements is given by

$$\sum_{i=0}^{L_t-1} m_{l,i} c_i(n), \tag{4.10}$$

where $m_{l,i}$ is a complex transmission coefficient between the $i^{th}$ transmitter element and the $l^{\text{th}}$ receiver element.

By placing the set of transmission coefficients in a $L_r \times L_t$ crosstalk matrix $\mathbf{M}$, the MIMO radar narrowband signal model in the presence of crosstalk is given by

$$\mathbf{x}(n) = \sum_{k=1}^{K} \beta_k \tilde{\mathbf{a}}_r^*(\theta_k) \tilde{\mathbf{a}}_t^H(\theta_k) \mathbf{c}(n) + \mathbf{M}\mathbf{c}(n) + \mathbf{z}(n), \tag{4.11}$$

where

$$\mathbf{M} = \begin{bmatrix} m_{0,0} & \cdots & m_{0,L_t-1} \\ \vdots & \ddots & \vdots \\ m_{L_r-1,0} & \cdots & m_{L_r-1,L_t-1} \end{bmatrix}. \tag{4.12}$$

Note that the signal model (4.11) also includes the different radiation patterns.

### 4.2.2 Crosstalk Reduction

The crosstalk matrix can be estimated from a first transmission in an environment without any target. In that case, the narrowband received signal is

$$\tilde{\mathbf{x}}(n) = \mathbf{M}\mathbf{c}(n) + \mathbf{z}(n). \tag{4.13}$$

We seek to determine the matrix $\mathbf{M}$ which minimizes the MSE criterion

$$J = E\left[\|\tilde{\mathbf{x}}(n) - \mathbf{M}\mathbf{c}(n)\|^2\right]. \tag{4.14}$$

By denoting $\mathbf{m}_l$ the $l^{\text{th}}$ row of $\mathbf{M}$ and $\tilde{x}_l(n)$ the $l^{\text{th}}$ element of $\tilde{\mathbf{x}}(n)$, the criterion (4.14) can be written as

$$J = E\left[\sum_{l=0}^{L_r-1} |\tilde{x}_l(n) - \mathbf{m}_l\mathbf{c}(n)|^2\right]. \tag{4.15}$$

Finally, the optimal $l^{\text{th}}$ row of $\mathbf{M}$ will be the one that minimizes

$$J_l = E\left[|\tilde{x}_l(n) - \mathbf{m}_l\mathbf{c}(n)|^2\right]. \tag{4.16}$$

The solution of (4.16) is that of a classical Wiener filtering:

$$\tilde{\mathbf{m}}_l = E\left[\tilde{x}_l(n)\mathbf{c}^H(n)\right] E\left[\mathbf{c}(n)\mathbf{c}^H(n)\right]^{-1}. \tag{4.17}$$

Consequently, the optimal crosstalk matrix according to the MSE criterion is given by

$$\tilde{\mathbf{M}} = \mathbf{R}_{\tilde{x}c}\mathbf{R}_c^{-1}, \tag{4.18}$$

where $\mathbf{R}_{\tilde{x}c} = E\left[\tilde{\mathbf{x}}(n)\mathbf{c}^H(n)\right]$.

Once this matrix has been estimated, the contribution of crosstalk to the received signals can be reduced by calculating

$$\mathbf{x}_{sc}(n) = \mathbf{x}(n) - \hat{\mathbf{M}}\mathbf{c}(n) \tag{4.19}$$

where $\hat{\mathbf{M}}$ is an estimate of $\tilde{\mathbf{M}}$, computed from the estimated versions of $\mathbf{R}_{\tilde{x}c}$ and $\mathbf{R}_c$.

### 4.2.3 Numerical Examples

In this section, the influence of crosstalk on the MIMO radar performance and the effectiveness of the crosstalk reduction technique are presented via MATLAB simulations. The validity of this technique is illustrated in Chapter 5 by experimental results using real hardware.

Consider a narrowband MIMO radar with colocated antennas whose transmitter and receiver arrays are the two ULAs of $L = L_t = L_r = 6$ elements. The simulations are performed using the signal model (4.11) considering $K = 2$ targets located in the plane-wave region at $\theta_1 = -20°$ and $\theta_2 = 20°$, and a reciprocal of noise level of $-10\log_{10}\sigma^2 = 20$. Both the real and the imaginary parts of the coefficients of the crosstalk matrix $\mathbf{M}$ are randomly generated and uniformly distributed in the open interval $(-1/\sqrt{2}\,, 1/\sqrt{2})$. Although this is not a realistic crosstalk matrix, it is useful to evaluate the system performance in the presence of correlated interference.

A first simulation is done considering the ideal signal model

$$\mathbf{x}(n) = \sum_{k=1}^{K} \beta_k \mathbf{a}_r^*(\theta_k)\mathbf{a}_t^H(\theta_k)\mathbf{c}(n) + \mathbf{M}\mathbf{c}(n) + \mathbf{z}(n), \tag{4.20}$$

which does not take the different radiation patterns into account.

The Capon, MUSIC, and GLRT spatial spectra computed from the received signals $\mathbf{x}(n)$ (using $\mathbf{a}_r(\theta)$ and $\mathbf{a}_t(\theta)$) are shown in Figure 4.14. As we can see, the GLRT spectrum is highly affected by crosstalk as several secondary lobes appear around the true DOAs, which can lead to a wrong detection. Actually, the crosstalk term $\mathbf{M}\mathbf{c}(n)$ can be seen as a noise correlated with the transmitted signals, which is not consistent with the assumptions made in the definition of the GLRT and explains the sensitivity of the latter to crosstalk. In contrast, Capon and MUSIC are less sensitive to this phenomenon given that the crosstalk term $\mathbf{M}\mathbf{c}(n)$ is not expressed in terms of a steering vector and hence it is included in the "noise-only" subspace. However, the resolution of Capon and MUSIC is degraded and the estimated DOAs are actually biased.

The crosstalk matrix is then estimated using (4.18) after simulating a target-free environment. Next, the crosstalk is reduced from the received signals by computing (4.19). Finally, the Capon, MUSIC, and GLRT spatial spectra are computed from $\mathbf{x}_{sc}(n)$. As shown in Figure 4.15, after the crosstalk reduction the resolution of Capon and MUSIC is significantly improved. Moreover, no secondary lobes appear in the GLRT spectrum, which allows an appropriate estimation of the target DOAs.

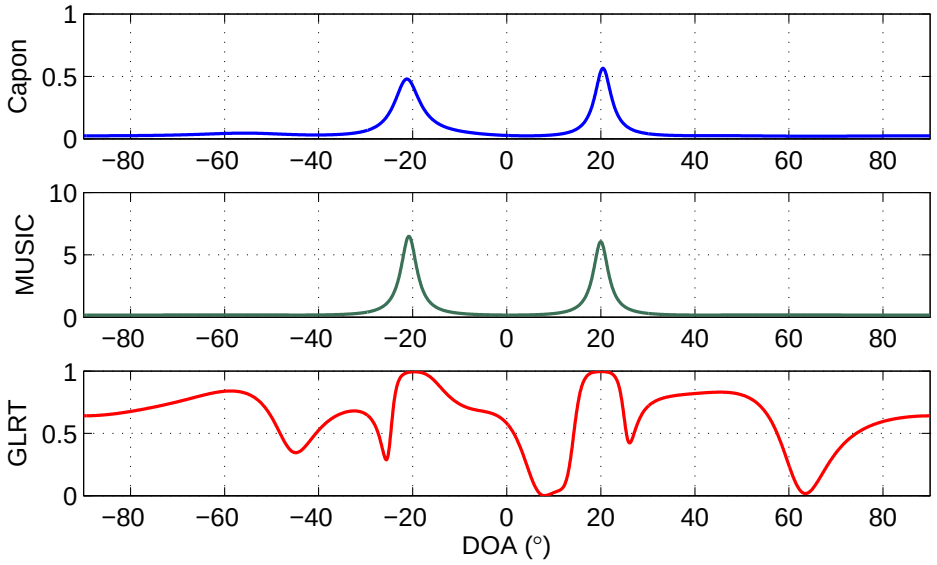


FIGURE 4.14: Capon, MUSIC, and GLRT spectra for two targets at $\theta_1 = -20°$, and $\theta_2 = 20°$ before crosstalk reduction (ideal case).

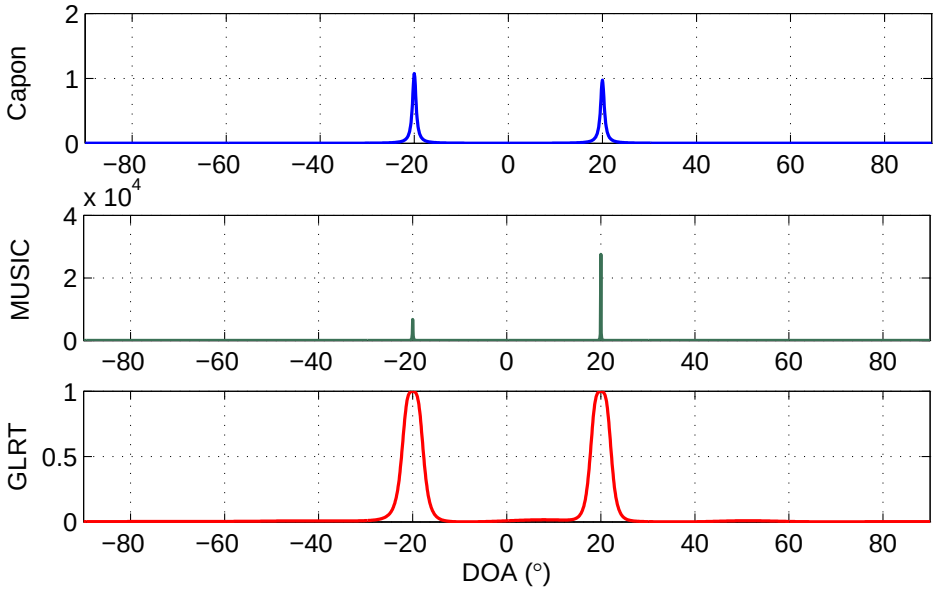


FIGURE 4.15: Capon, MUSIC, and GLRT spectra for two targets at $\theta_1 = -20°$, and $\theta_2 = 20°$ after crosstalk reduction (ideal case).

A second simulation is carried out considering the antenna arrays shown in Figure 4.3. The signal propagation is simulated using the signal model (4.11) which includes the different radiation patterns. The Capon, MUSIC, and GLRT spatial spectra, computed using $\boldsymbol{\alpha}_r(\theta)$ and $\boldsymbol{\alpha}_t(\theta)$ before crosstalk reduction, are shown in Figure 4.16. Similar to the ideal case, several secondary lobes appear around the true DOAs in the GLRT spectrum, while Capon and MUSIC spectra only show the target lobes.

The crosstalk is now reduced from the received signals by computing (4.19) and the

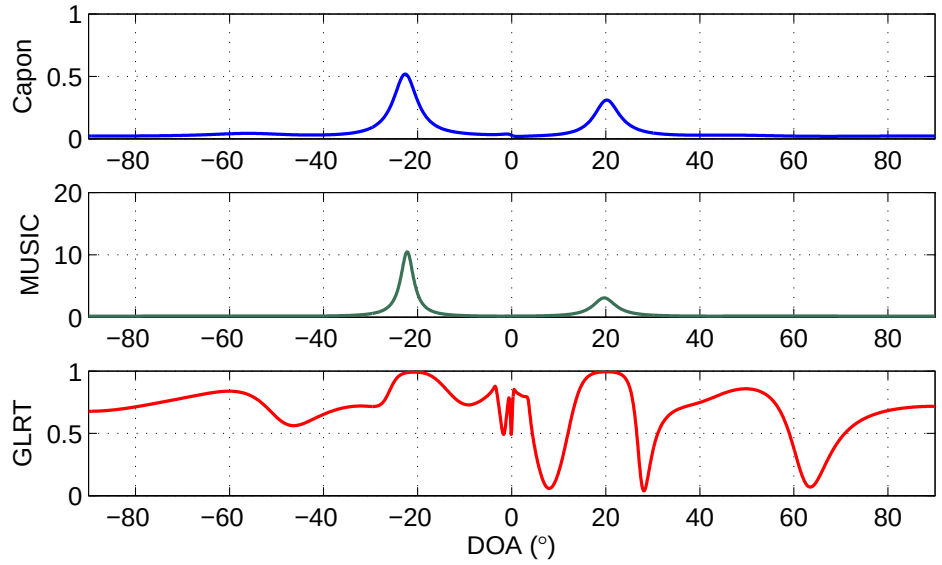


FIGURE 4.16: Capon, MUSIC, and GLRT spectra for two targets at $\theta_1 = -20°$, and $\theta_2 = 20°$ before crosstalk reduction (taking only the phase of the radiation patterns into account).

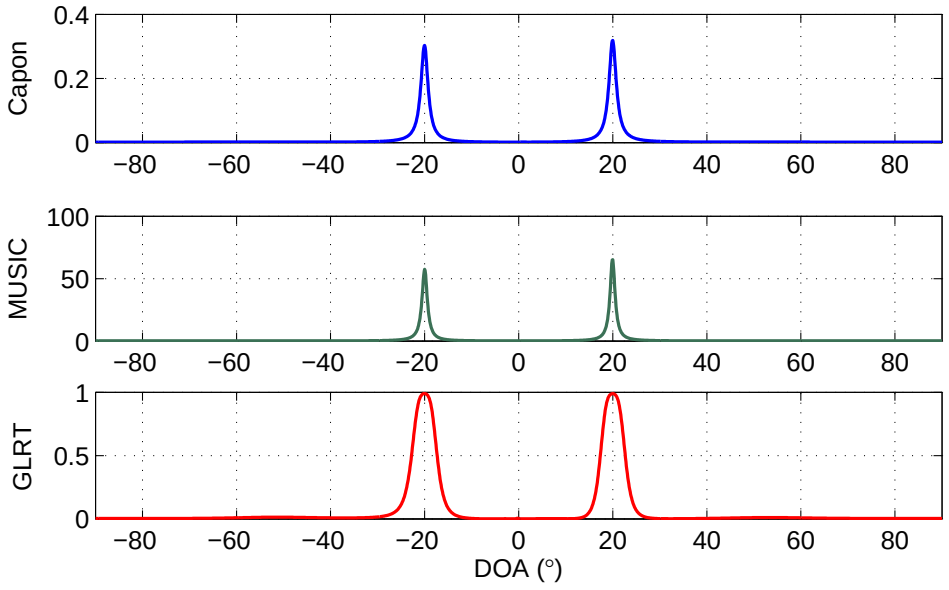


FIGURE 4.17: Capon, MUSIC, and GLRT spectra for two targets at $\theta_1 = -20°$, and $\theta_2 = 20°$ after crosstalk reduction (taking only the phase of the radiation patterns into account).

Capon, MUSIC, and GLRT spectra are re-computed using $\boldsymbol{\alpha}_r(\theta)$ and $\boldsymbol{\alpha}_t(\theta)$. As shown in Figure 4.17, the secondary lobes are once again totally suppressed from the GLRT spectrum, and the lobes in the Capon and MUSIC spectra are re-centered at the target DOAs. We can then see that both crosstalk and pattern distortion can together be taken into account in order to reduce the negative influence of mutual coupling on the MIMO radar performance.

## 4.3 Summary

In this chapter, the influence of mutual coupling on the DOA estimation in a MIMO radar system has been described and studied by combining signal processing with electromagnetic simulations. In Section 4.1, we showed that in antenna arrays, the radiation patterns differ from one element to another. As a consequence, the resolution and the performance of the DOA estimation algorithms are highly degraded. Those problems are caused not only by mutual coupling, but also by the use of the standard steering vectors assuming that the radiation patterns are all identical and angle-independent, as it is commonly done in the literature. We then showed the importance of using a more exact expression of the steering vectors: When the different radiation patterns (which take into account the effects of mutual coupling) are included in the steering vectors, the DOA estimation performance is greatly improved and gets close to the performance obtained in the ideal mutual-coupling-free case. Moreover, we showed that including only the phase of the radiation patterns allows improving the DOA estimation performance of Capon (by suppressing the regrowth at the spectrum edges) without degrading the GLRT and MUSIC performance.

In Section 4.2, we studied the influence of crosstalk in MIMO radar performance. We showed that the resolution of Capon, MUSIC, and GLRT is affected by crosstalk or by interference which is correlated with the transmitted signals. It is clear that the GLRT is much more sensitive to this phenomenon than Capon and MUSIC, and is unable to detect the targets. In order to overcome this problem, we presented a more realistic signal model (4.11) which takes mutual coupling into account and should always be used in the case of narrowband MIMO radars with colocated antennas. We then proposed a crosstalk reduction technique: The crosstalk matrix is first estimated (based on a minimum MSE approach) from a transmission in an environment without any target, and the crosstalk term is finally subtracted from the received signals. The simulation results showed that after crosstalk reduction, there are no longer secondary lobes in the GLRT spectrum and the resolution of Capon and MUSIC is improved, which makes possible an efficient estimation of the target DOAs.

Our contributions presented in this chapter are the proposition of a more realistic signal model which takes mutual coupling into account, the introduction of the phase-only steering vectors which deal with distorted radiation patterns, and the proposition of a crosstalk reduction technique.

# Chapter 5

# Experimental Platform for MIMO Radar with Colocated Antennas

Several DOA estimation techniques for a narrowband MIMO radar with colocated antennas have been studied and compared in Chapters 2 and 4. However, all of these techniques have been developed and simulated from a theoretical point of view assuming ideal conditions, e.g. punctual targets, transmission on an additive white Gaussian noise channel, and absence of multi-path phenomenon. In this chapter, we present an experimental platform for MIMO radar which allows testing the previously proposed DOA estimation techniques in nearly real conditions. The developed measurement platform is described in Section 5.1, while the synchronization and calibration procedures are described in Sections 5.2 and 5.3 respectively. Finally, some measurement results are presented in Section 5.4, which includes a repeatability test of the proposed platform, DOA estimation, and crosstalk reduction.

## 5.1 Hardware Description

An experimental platform has been developed in order to study the actual performance of a narrowband MIMO radar with colocated antennas. In a conventional MIMO system, each antenna element is associated with a separate RF architecture and the overall system has to be synchronized. The requirements for such implementations are difficult to fulfill especially for large MIMO systems and lead to high cost and complex hardware at the RF level.

The proposed platform uses only one transmitter (Tx) and one receiver (Rx) RF architectures. Actually, a single transmitter antenna element is used to transmit a

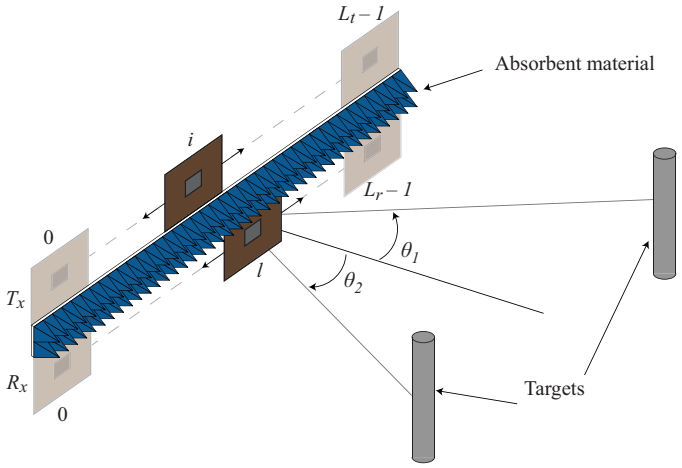


FIGURE 5.1: Scheme of the antenna configuration of the measurement platform.

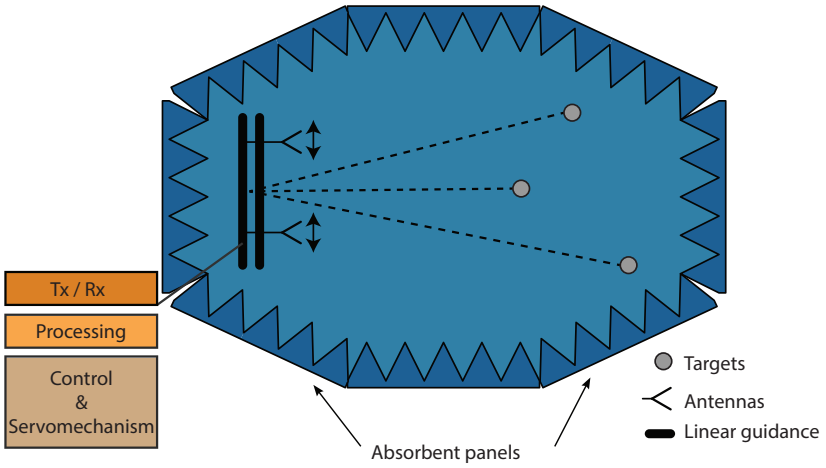


FIGURE 5.2: Experimental measurement configuration.

chosen waveform and a single receiver antenna element is used to receive the signals reflected by the targets. An automated mechanism containing two rails, one for each antenna, places the transmitter and the receiver element in every position of a ULA (see Figure 5.1). A series of measurements is performed for a given position of the transmitter, while the receiver takes the different positions of a ULA. The same procedure is repeated for the different positions of the transmitter antenna. In this way, all possible configurations between the transmitter and the receiver in a MIMO system are covered. By applying the superposition principle, the received signals at each position can be wisely combined to construct the received signals matrix $\mathbf{X}$ of the MIMO system. As the superposition principle is valid provided that the environment is stationary, the measurements are carried out in an anechoic chamber as shown in Figure 5.2. Note that this platform does not allow taking the whole effects of mutual coupling into account since we have the same radiation pattern at every position of the Tx and Rx antennas.

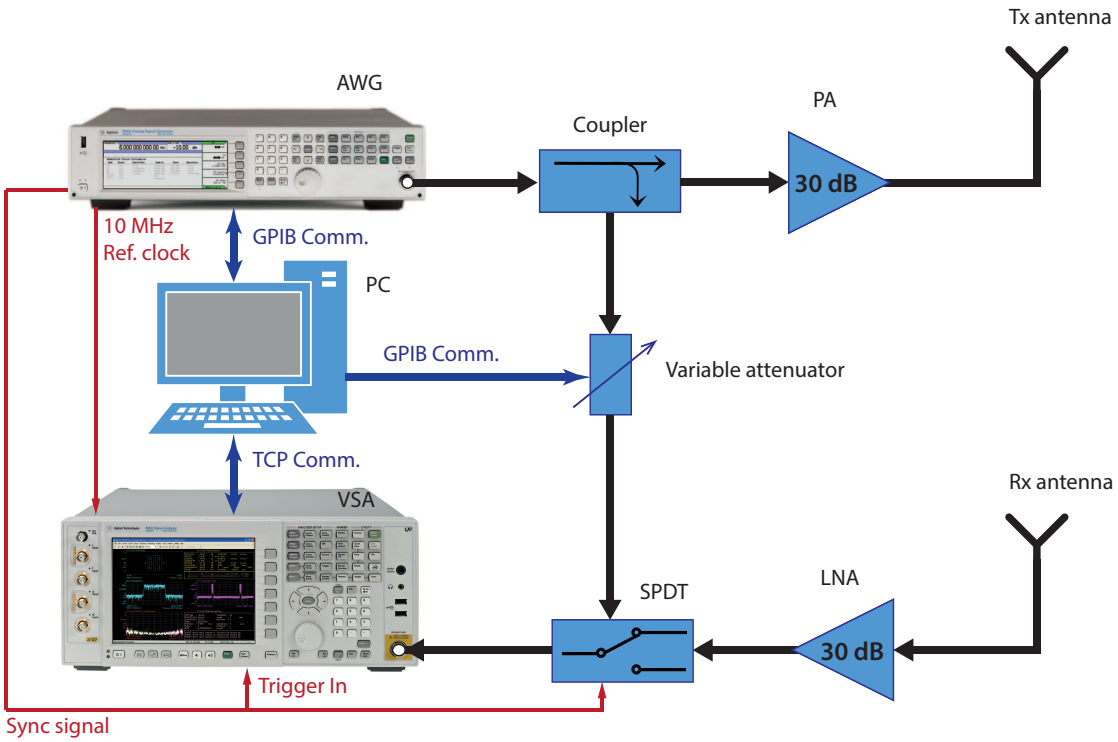


FIGURE 5.3: Tx/Rx RF architecture block diagram.

The block diagram of the RF architecture is shown in Figure 5.3 and the different hardware components are described thereafter.

**Signal Generator**: The transmitted signals are generated from samples provided by MATLAB, and modulated by an Arbitrary Waveform Generator (AWG). The signals are transmitted at a carrier frequency $f_c = 5.88$ GHz (wavelength $\lambda = 51.02$ mm) and the output power is set to $-5$ dBm.

**Signal Analyzer**: The signal acquisition is done by a Vector Signal Analyzer (VSA), which receives the RF reflected signals and demodulates them before recording the data.

**Power Amplifier**: A 30 dB gain Power Amplifier (PA) is used to achieve an output power of 25 dBm at the Tx antenna level.

**Low Noise Amplifier**: A 30 dB gain Low Noise Amplifier (LNA) is used to amplify the weak signals received at the Rx antenna.

**Directional Coupler**: A 10 dB directional coupler is used to directly transmit a reference signal from the AWG to the VSA for synchronization purposes (see Section 5.2).

**Variable attenuator**: A programmable variable attenuator is used for synchronization and calibration purposes (see Sections 5.2 and 5.3). The attenuation is adjustable from 0 to 58 dB by step of 1 dB.

**Switch**: A Single Pole Double Throw (SPDT) is used to switch between the reference signal and the signal reflected by the targets (see Section 5.2).

**Antennas**: The Tx and the Rx antennas are two coaxially-fed linearly polarized patch antennas. The antenna prototypes are printed on RT/Duroid 5880 substrate with a thickness of 1.508 mm, a dielectric constant of $\varepsilon_r = 2.2$ and a loss tangent of 0.0009.

**External Computer**: An external computer (PC) controls both the AWG and the VSA via a General Purpose Interface Bus (GPIB) interface. The PC synthesizes the different waveforms via MATLAB and sends the data to the AWG, which transmits a different waveform for each position of the Tx antenna. The PC also controls both rails to displace the antennas to each pair of positions once the previous signal acquisition has been completed. Additionally, the PC adjusts the attenuator to an appropriate value during a calibration procedure (see Section 5.3).

The distance between the rails is about $8\lambda$. In order to reduce the crosstalk level, the space separating the transmitter and the receiver elements was filled with absorbent material. Actually, the crosstalk reduction technique presented in Section 4.2 should work with any crosstalk level in theory; however, a high crosstalk level might increase the noise floor at the analog-to-digital conversion stage, and in practice, the weak reflected signals might be undetectable or inaccurately converted by the ADC (Analog-to-Digital Converter) which has a resolution of 14 bits. Moreover, a high crosstalk level might saturate the receiver and produce non-linear effects.

Some pictures of the experimental platform are shown in Figure 5.4.

## 5.2 Synchronization

In order to synchronize the transmitter and the receiver architectures, both the AWG and the VSA are first linked by the same 10 MHz reference clock. Then, the signal acquisition done by the VSA is triggered by an external "trigger signal" directly transmitted from the AWG. As shown in Figure 5.5, the trigger signal has the same length as the transmitted signal and has a single pulse: Only the first symbol is set to "1" while all the others are set to "0". The receiver is then triggered by the positive slope of the trigger signal so that the signal acquisition starts at the same instant that the first symbol is transmitted.

However, this synchronization procedure was found to be inaccurate. In fact, the trigger signal provided by the AWG exhibits jitter on the rising and falling edges which leads to phase synchronization errors.

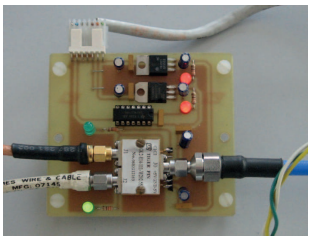

**Directional coupler and SPDT switch for Tx-Rx synchronization**

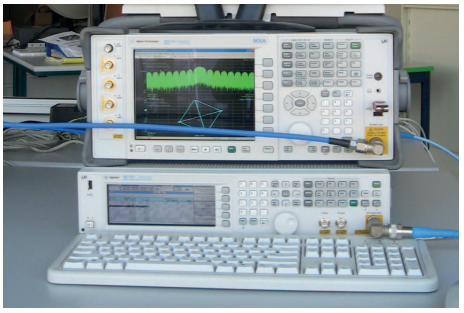

**Generator MXG N5182 & Analyzer MXA N9020A**

**Patch antenna @5.88 GHz**

**Rail**

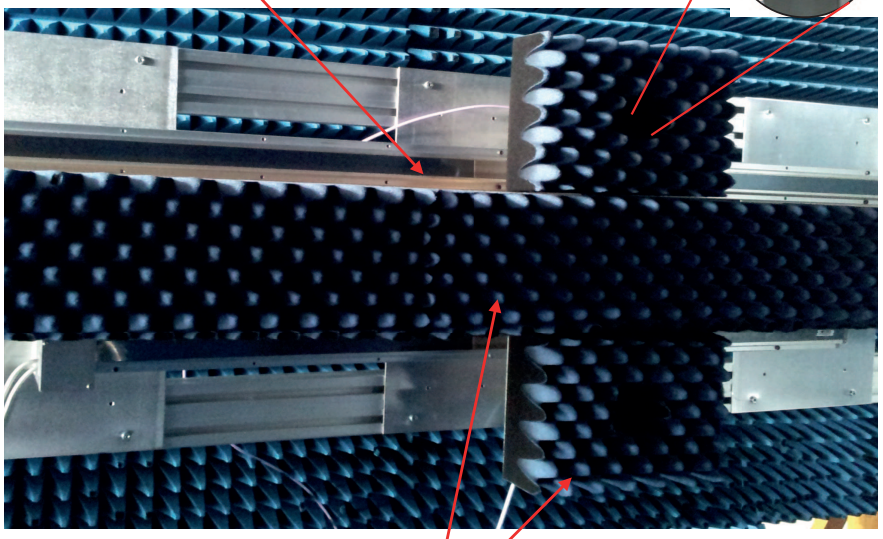

**Absorbent material to reduce Tx-Rx coupling**

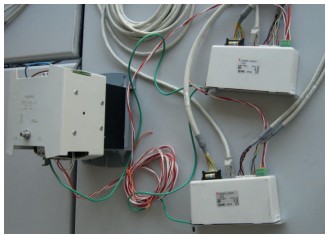

**Motor programming interface**

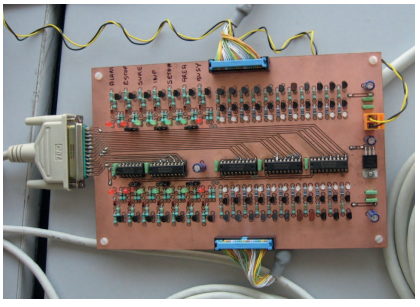

**Displacement control interface**

FIGURE 5.4: System overview.

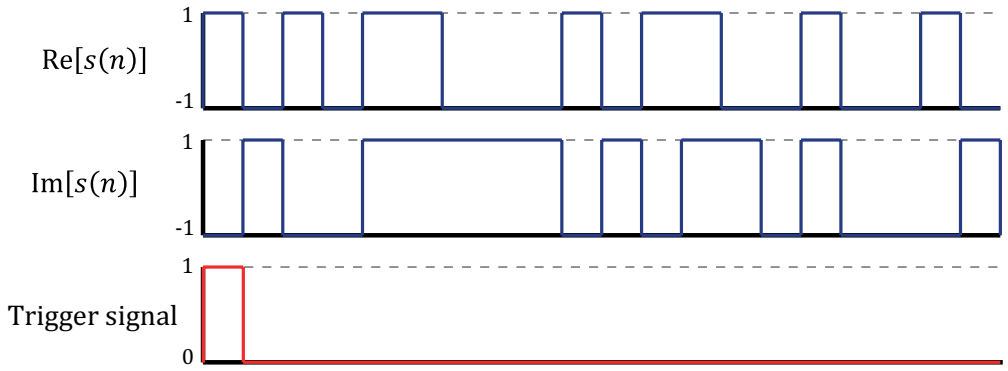


FIGURE 5.5: Example of timing diagram of the baseband transmit signal and the trigger signal (only the first 20 symbols are shown).

### 5.2.1 Evaluation of the phase synchronization error in a wired transmission

To evaluate the phase errors introduced by an inaccurate synchronization we consider the wired transmission shown in Figure 5.6.

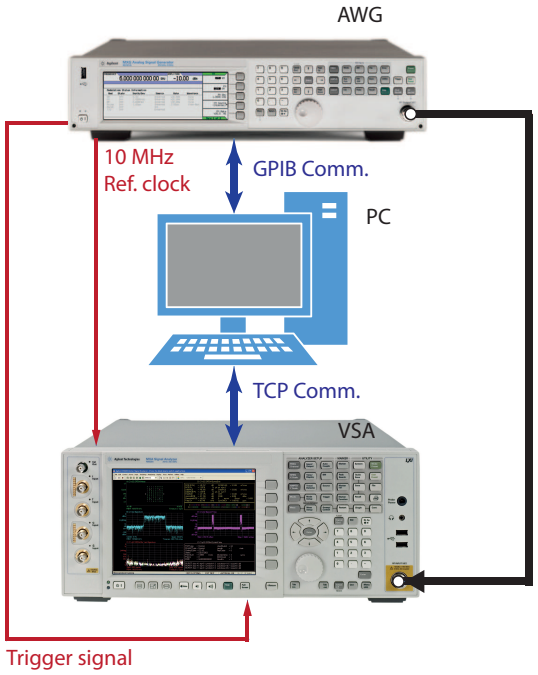


FIGURE 5.6: Configuration of a first synchronization test.

Denoting $\{c(n)\}_{n=0}^{N-1}$ the baseband signal which is directly transmitted (after modulation) from the AWG to the VSA, the baseband signal $\{r(n)\}_{n=0}^{N-1}$ acquired by the VSA is given by

$$\begin{aligned} r(n) &= \alpha c(n) e^{j\phi} \\ n &= 0, \ldots, N-1, \end{aligned} \tag{5.1}$$

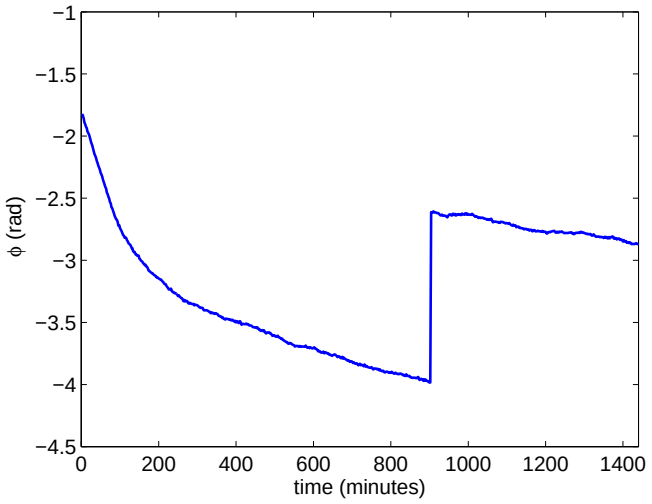


FIGURE 5.7: Phase error computed from 720 acquisitions.

where $\phi$ denotes the phase error term and $\alpha$ is an attenuation constant. The phase error can be estimated by searching for the $\phi$ which minimizes the Least Squares (LS) criterion

$$J = \sum_{n=0}^{N-1} \left| r(n) - \alpha c(n) e^{j\phi} \right|^2 . \tag{5.2}$$

The phase $\phi$ which minimizes the criterion is such that

$$\frac{\partial J}{\partial \phi} = j\alpha \sum_{n=0}^{N-1} \left( r(n) c^*(n) e^{-j\phi} - c(n) r^*(n) e^{j\phi} \right) = 0. \tag{5.3}$$

Finally, the optimal phase according to the LS criterion is given by

$$\phi = \arg \left\{ \sum_{n=0}^{N-1} r(n) c^*(n) \right\} . \tag{5.4}$$

The evolution of the estimated phase error $\phi$ can be observed by performing different acquisitions of the signal $\{r(n)\}_{n=0}^{N-1}$ for a same transmitted signal $\{c(n)\}_{n=0}^{N-1}$. Accordingly, we continuously transmit the signal $\{c(n)\}_{n=0}^{N-1}$, which is a sequence of $N = 512$ QPSK symbols, during 24 hours. The carrier and sampling frequencies are set to $f_c = 5.88$ GHz and $F_s = 1.28$ MHz respectively. The received signal $\{r(n)\}_{n=0}^{N-1}$ is measured every 2 minutes (i.e. 720 times). The different phase errors are calculated using (5.4) and are shown in Figure 5.7. As we can see, important phase errors occur during the whole measurement process. This can highly degrade the DOA estimation performance of MIMO radar with colocated antennas given that the phase of the signals is a critical parameter in the DOA estimation problem. We found that, with this configuration, it is impossible to estimate the target DOAs unless the phase errors are compensated.

### 5.2.2 Adopted synchronization configuration

In order to overcome the phase synchronization problem, we use the directional coupler and the SPDT shown in Figure 5.3. Every transmitted frame $\{s(n)\}_{n=0}^{N_s-1}$ is composed of a reference signal $\{s_{ref}(n)\}_{n=0}^{N-1}$ and the useful signal $\{c(n)\}_{n=0}^{N-1}$ as shown in Figure 5.8. Even if the whole frame is transmitted by the Tx antenna, only the useful part $\{c(n)\}_{n=0}^{N-1}$ is used to estimate the target DOAs. The reference signal, which is directly transmitted from the AWG to the VSA via the directional coupler, is used to estimate the phase synchronization error $\phi$ (according to (5.4)) present at every signal acquisition. The so obtained $\phi$ is then used to compensate the phase error present in the reflected useful signal.

At the receiver, an SPDT is used to switch between the reference signal and the useful signal reflected by the targets. As shown in Figure 5.8, the transmitted frame is composed of two idle symbols at the beginning, followed by the useful signal $\{c(n)\}_{n=0}^{N-1}$, two other idle symbols, and the reference signal $\{s_{ref}(n)\}_{n=0}^{N-1}$ at the end. The idle symbols are used to avoid any switch bouncing that may affect either the useful signal or the reference signal. The "sync" signal has two purposes, its positive slope is used to trigger the signal acquisition and its high and low levels are used to control the states of the switch: When the "sync" signal is at "1" the useful signal will pass through the switch, and when it

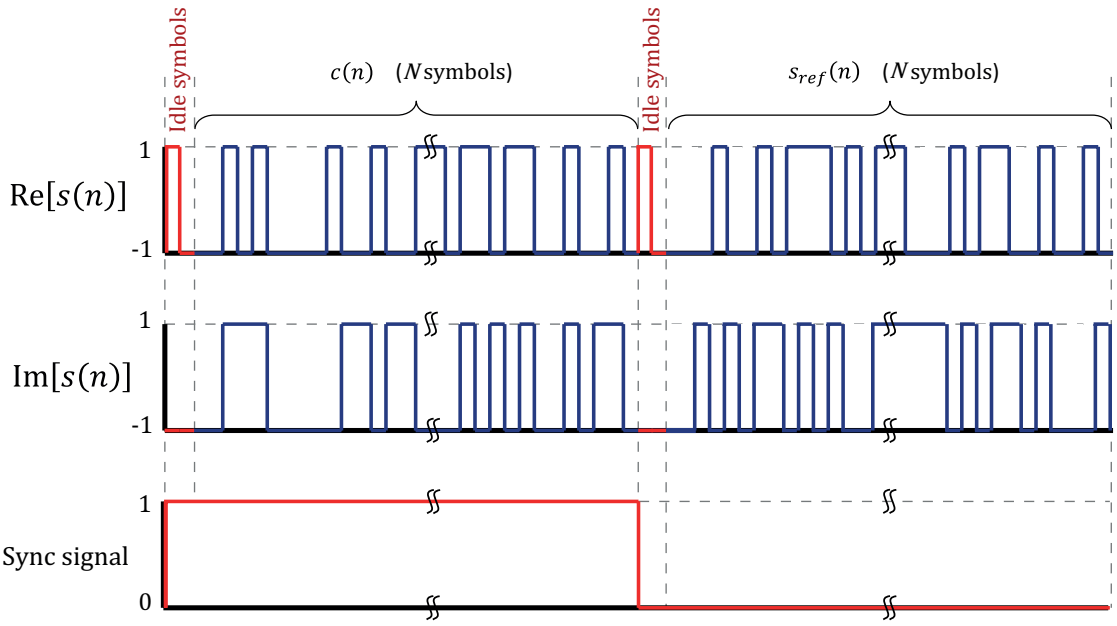


FIGURE 5.8: Example of timing diagram of the baseband transmit signal using a reference signal.

is at "0" the reference signal will pass. At the receiver, the reference and useful signals are found from the received frame by correlation process.

The amplitude of the reference signal is a parameter which must be carefully chosen in order to reduce the quantization errors. A method to optimally adjust the reference signal amplitude is presented in Section 5.3.

## 5.3 System Calibration

The experimental platform is calibrated before and during the measurement process. The AWG and the VSA are automatically calibrated before the measurement process starts.

A parameter which must be adjusted during the measurement process is the reference voltage of the ADC in the VSA. If the reference voltage is set too low, the input signal may overload the ADC circuitry which introduces distortion into the measurements. If the reference voltage is set too high, the conversion accuracy is decreased and the noise floor is increased. The reference voltage should then be set equal to the maximum input signal amplitude in order to have the best possible accuracy in the analog-to-digital conversion stage. This value is also used to configure all the internal amplifiers and attenuators of the VSA to maximize the dynamic range and minimize the signal distortion caused by the non-linearities of the circuits. The flow chart of the developed process for the configuration of the ADC reference voltage $\text{ADC}_{ref}$ is shown in Figure 5.9(a). The reference voltage must be previously set to a value higher than the maximum input signal amplitude. Then, the mean power $P_s$ of the input signal (i.e. the received frame) is measured by the VSA, and the reference voltage $\text{ADC}_{ref}$ is calculated from this value. Note that the so obtained $\text{ADC}_{ref}$ may be lower than the maximum input signal which would overload the system. If the VSA detects an overload warning, the reference voltage is multiplied by $10^{0.1}$ (increase of 2 dB) until the warning disappears.

Another parameter which must be adjusted is the amplitude of the reference signal $\{s_{ref}(n)\}_{n=0}^{N-1}$. This value must be set as close as possible to the amplitude of the reflected useful signal so that they have equal quality of quantization. Indeed, if there is a big difference between the reference and the reflected useful signal amplitudes, the signal of the smallest amplitude might be inaccurately converted or even be under the noise floor. The reference signal amplitude must then be controlled in order to match the reflected signal amplitudes, which can change depending on the target locations. This is done using a variable attenuator which is controlled by the PC following the procedure

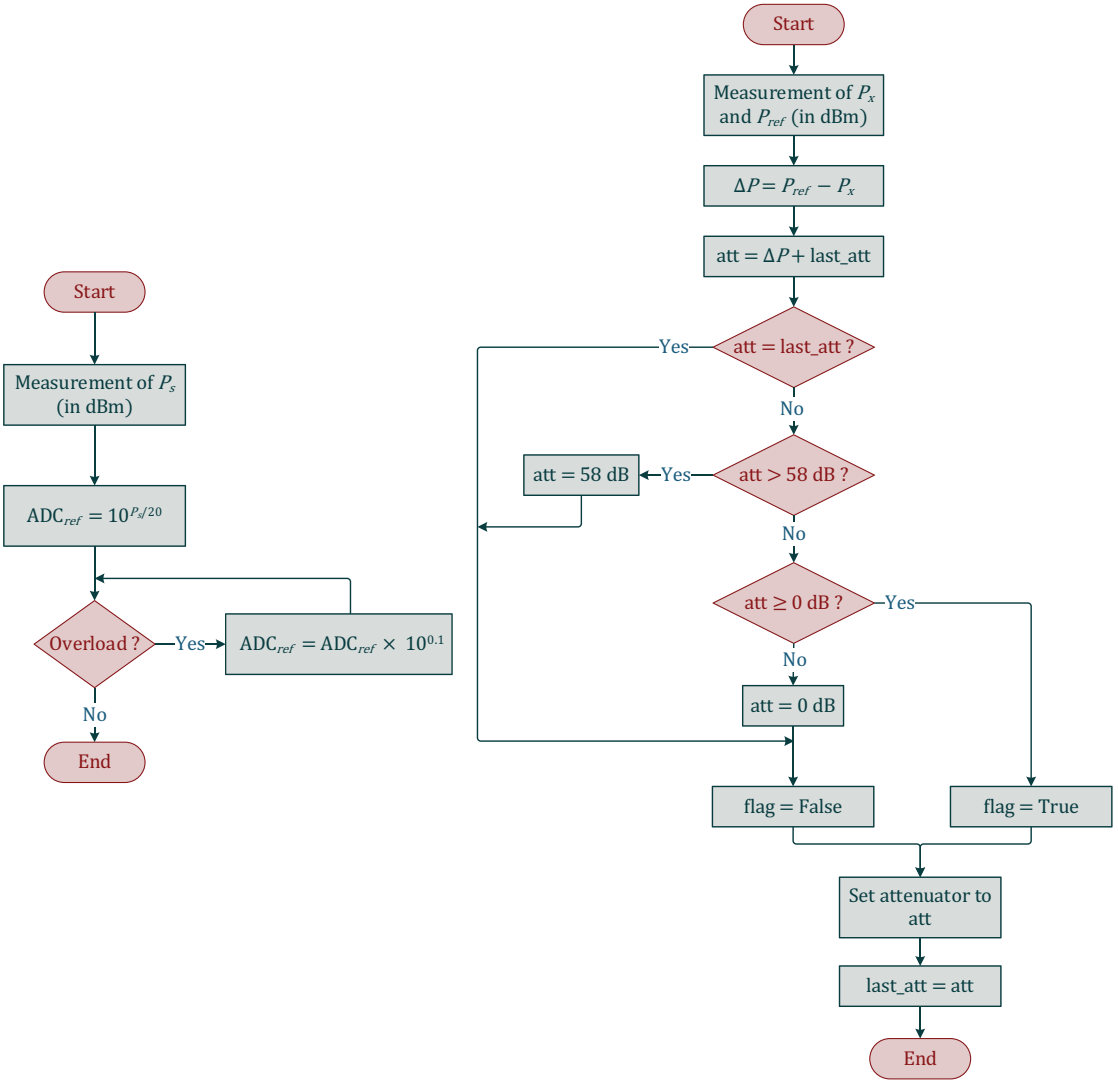


FIGURE 5.9: Flow charts of (a) the ADC reference configuration process and (b) the attenuation configuration process.

shown in Figure 5.9(b). First, the power $P_x$ of the useful reflected signal and the power $P_{ref}$ of the reference signal are measured (in dBm) by the VSA. The total attenuation (in dB) must then be set to the nearest integer to $\Delta P = P_{ref} - P_x$. Note that if an attenuation value "last_att" was set previous to the measurement of $P_x$ and $P_{ref}$, the new total attenuation (in dB) must be set to att $= \Delta P +$ last_att. Validations are made in order to ensure that the total attenuation is always set between 0 and 58 dB according to the specifications of the employed attenuator. However, it has been observed that for targets located at more that 1 m from the antennas, $P_{ref}$ is always greater than $P_x$ for an attenuation of 0 dB and hence, "att" should never take negative values.

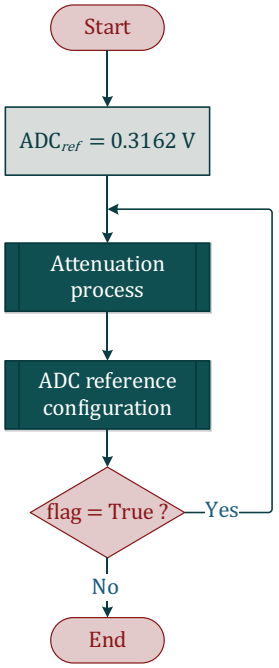


FIGURE 5.10: Flow chart of ADC/attenuation calibration process.

It is important to note that both the ADC reference voltage and the amplitude of the reference signal must be adjusted together. Actually, the powers $P_x$ and $P_{ref}$ might be inaccurately measured if ADC$_{ref}$ had not been properly set. Moreover, once the amplitude of the reference signal has been changed, the reference voltage of the ADC must be readjusted. A "flag" is set to True to inform the system that the attenuation value has been changed and that it must be reverified after readjusting the ADC. The "flag" is set to False when no verification of the attenuation value is needed. As shown in Figure 5.10, a cyclic procedure to optimally set both the reference signal amplitude and the ADC reference voltage has been developed. Note that ADC$_{ref}$ is first set to 0.3162 V, which corresponds to an input signal power of $-10$ dBm, to avoid overloading the system.

Regarding the antennas displacement, the positioning system must be calibrated prior to any measurement process. The antennas are displaced over the rails by a slider which is actuated by a step motor. The rails have sensors at the ends, one of which is used to calibrate the origin of the positioning system. This system is then able to place the antennas to every desired position with a precision of $\pm 0.1$ mm.

## 5.4 Experimental Results

In this section we present some experimental results obtained using the proposed platform. The number of Tx and Rx positions is $L = L_t = L_r = 10$. The set of transmit signals $\{c_i(n)\}_{i=0}^{L_t-1}$ are independent sequences of $N = 512$ QPSK symbols. The same reference signal $s_{ref}(n)$, which is a sequence of $N$ QPSK symbols, is transmitted at every position $i$ of the Tx antenna along with the corresponding useful signal $c_i(n)$. Every transmitted frame $\{s_i(n)\}_{i=0}^{L_t-1}$ is of length $N_s = 2N + 4$ symbols (including the idle symbols). The symbol frequency is set to 64 kHz while the sampling frequency is set to 1.28 MHz. The different positions of the antenna elements are separated by $d = d_t = d_r = \lambda/2$.

Every target is placed using a rotating arm whose rotational axis is in the middle of the rails as shown in Figure 5.11. The actual target DOA is calculated from the measured lengths of the lines $b_1$ and $b_2$ where $b_2$ is a chord of a circle of diameter $b_1$ (i.e. the length of the rails):

$$\theta = \arcsin\left[2\left(\frac{b_2}{b_1}\right)^2 - 1\right]. \tag{5.5}$$

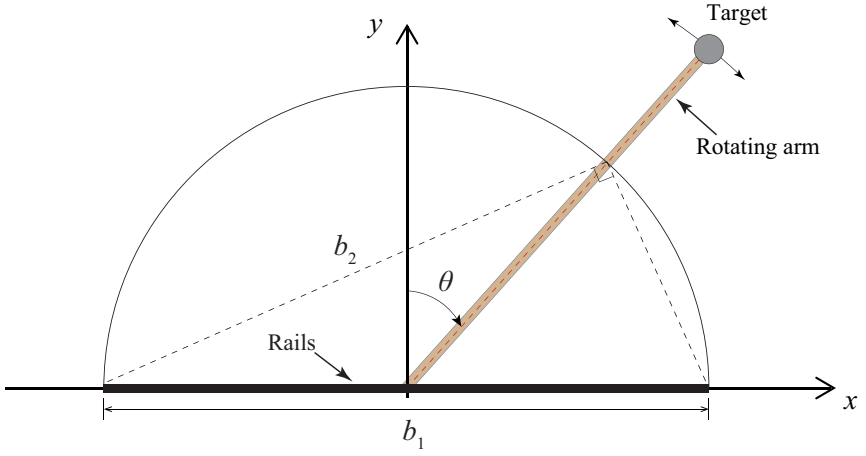


FIGURE 5.11: Target positioning scheme.

### 5.4.1 Repeatability Test

A repeatability test of the experimental platform has been performed using 70 successive trials for one target located at $-6.5°$ and at a distance of 1.8 m of the center of the rails. Figure 5.12 shows the DOA estimated by Capon and MUSIC as a function of the trial index.

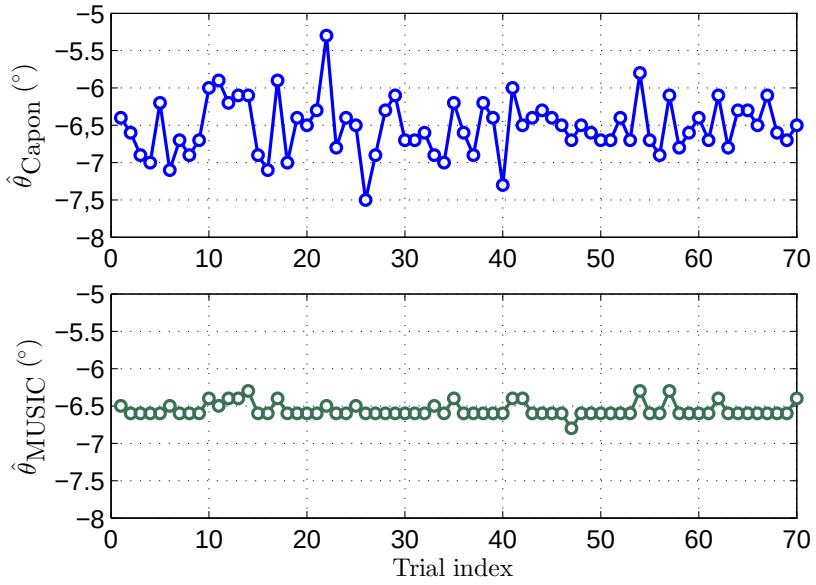


FIGURE 5.12: Repeatability test of the DOA estimation using Capon and MUSIC (one target at $[\theta, R] = [-6.5°, 1.8 \text{ m}]$).

We observe a maximum fluctuation of about $\pm 1°$ on the DOA estimated by Capon around the true target DOA which does not represent a high variation. As for MUSIC, we obtain even better results with a fluctuation of about $\pm 0.4°$. The small fluctuations can be due to noise, to nonlinearities of the circuits, and to residual calibration errors.

### 5.4.2 Narrowband Detection

In a first measurement process, we place two targets at $\theta_1 = -15°$ and $\theta_2 = 18°$ both at a distance of 1.7 m from the center of the rails. The tested targets are two metallic cylinders of diameter of 6 cm and height of 1.5 m. As presented in Chapter 2, the plane-wave condition for a MIMO radar of $L = 10$ transmitting and receiving elements is $R > 5\Delta^2/\lambda$ (with $\Delta = (L-1)d$), which gives $R > 5.17$ m. Our targets are then in the spherical-wave region and hence the spherical-wave steering vectors must be used to compute the spatial spectra.

Once the whole measurement process is finished, the narrowband Capon, MUSIC and GLRT spectra are computed using a grid of angles $\theta \in [-90°, 90°]$ with a mesh grid size of $0.1°$ and a grid of distances $R \in [1 \text{ m}, 2.5 \text{ m}]$ with a step of 0.01 m. The results are shown in Figure 5.13. As we can see, the Capon and MUSIC spectra show two lobes close to the target DOAs (the estimated DOAs are $[\hat{\theta}_1, \hat{\theta}_2]_{\text{Capon}} = [-15.3°, 18.5°]$ and $[\hat{\theta}_1, \hat{\theta}_2]_{\text{MUSIC}} = [-15.2°, 18.5°]$). In contrast, we are unable to detect the targets by using the GLRT since several secondary lobes appear around the target DOAs. The secondary lobes can be seen more clearly by plotting the component of the spectra at

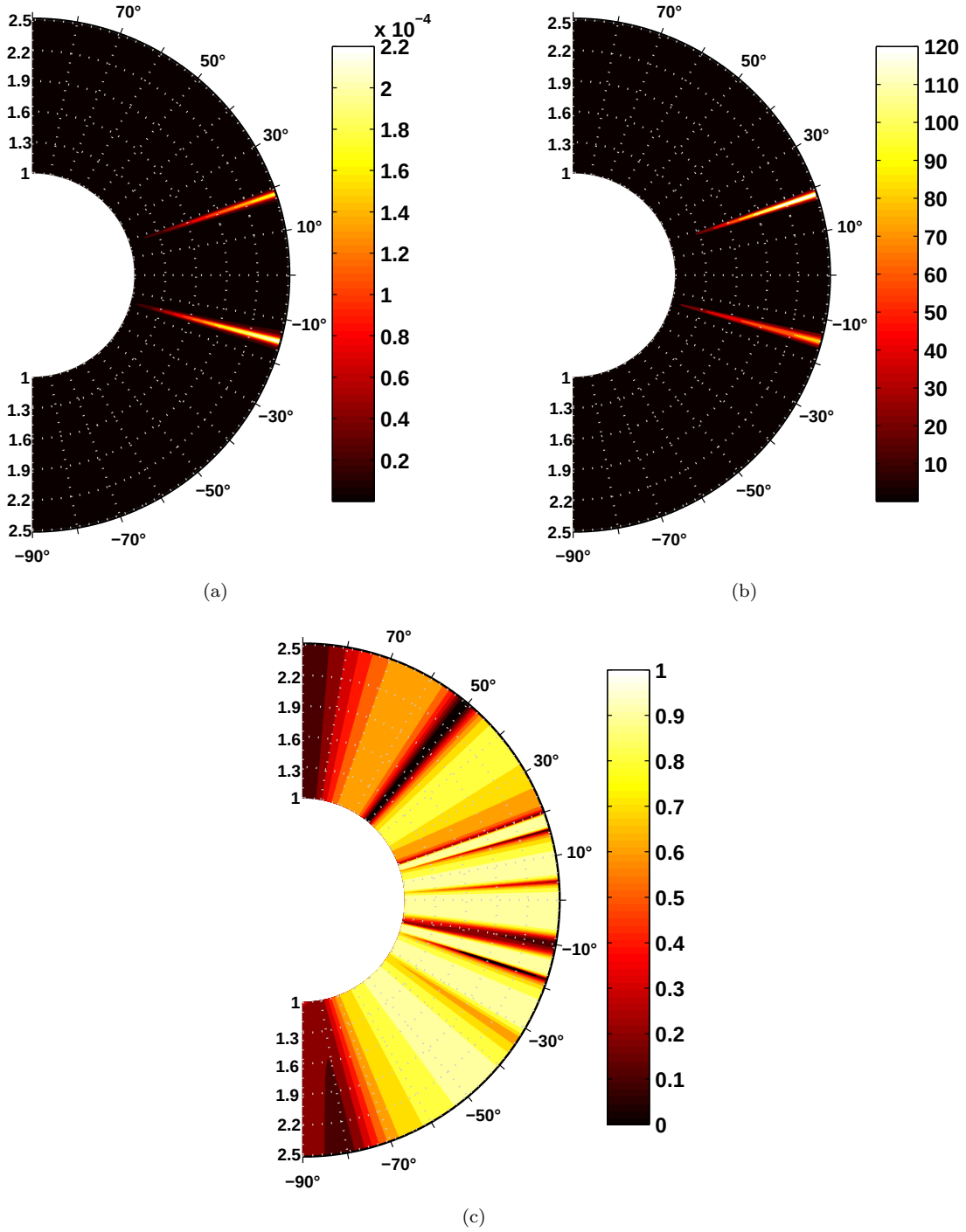


FIGURE 5.13: (a) Capon, (b) MUSIC, and (c) GLRT spectra (experimental measurements with two targets at $[\theta_1, R_1] = [-15°, 1.7 \text{ m}]$ and $[\theta_2, R_2] = [18°, 1.7 \text{ m}]$).

distance $R = 1.7$ m as shown in Figure 5.14. The secondary lobes can be caused by several factors. Even though we have filled the space separating the transmitter and the receiver with an absorbent material, a residual crosstalk level might still affect the GLRT detection technique and produce high secondary lobes around the target DOAs, as shown in Chapter 4. Moreover, the characteristics of the actual noise, which are

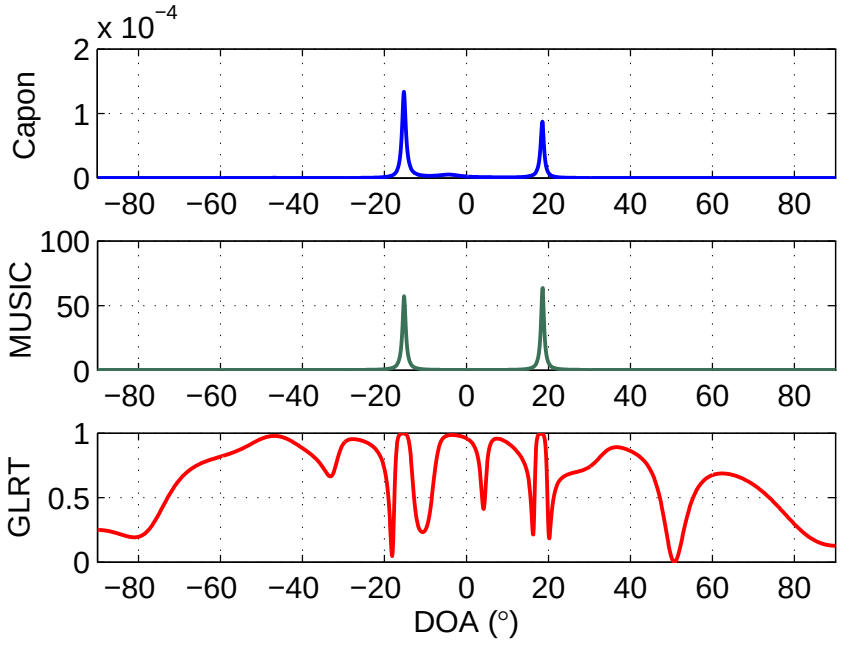


FIGURE 5.14: Component of the Capon, MUSIC, and GLRT spectra at $R = 1.7$ m (experimental measurements with two targets at $[\theta_1, R_1] = [-15°, 1.7 \text{ m}]$ and $[\theta_2, R_2] = [18°, 1.7 \text{ m}]$).

usually unknown, might also deteriorate the GLRT detection performance either if the noise level is too low (leading to ill-conditioning issues) or if the noise is not Gaussian.

### 5.4.3 Crosstalk Reduction

The negative effects of crosstalk can be overcome by using the crosstalk reduction technique proposed in Chapter 4. First, the crosstalk matrix $\mathbf{M}$ must be estimated in a first measurement process in the environment without any target. Then, the crosstalk term is subtracted from the received signals.

#### 5.4.3.1 Estimation of the Crosstalk Matrix

In order to test the reliability of the estimation of the crosstalk matrix, the measurement process in the target-free environment has been performed 100 times, using a different set of transmitted signals at each time. In each case, a different estimated matrix $\hat{\mathbf{M}}$ has been obtained.

The standard deviations of the coefficients of $\hat{\mathbf{M}}$ are shown in amplitude and phase in Figure 5.15. As we can see, the relative standard deviations of $|\hat{m}_{l,i}|$ are lower than 3.5% and the circular standard deviations [73] of $\arg\{\hat{m}_{l,i}\}$ are lower than 0.035 which

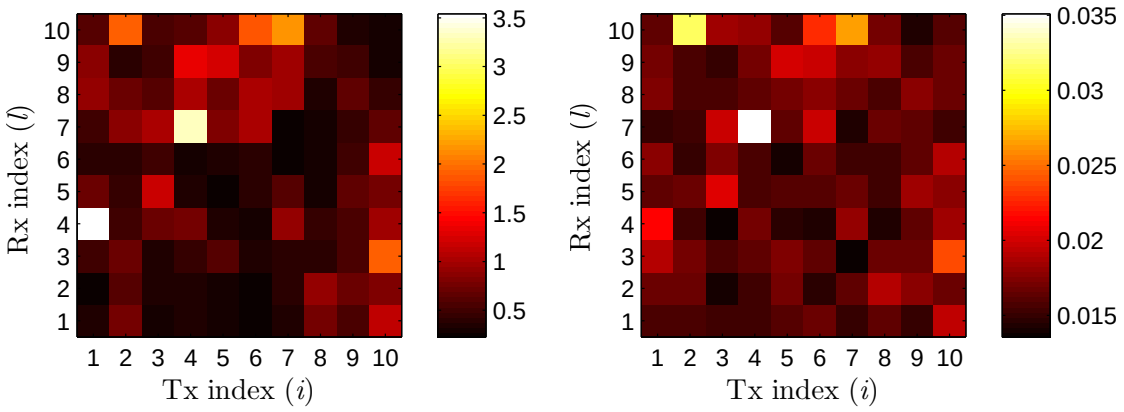


(a) (b)

FIGURE 5.15: (a) Relative standard deviation of the magnitude of the coefficients of $\hat{\mathbf{M}}$ (in %) and (b) circular standard deviation of the phase of the coefficients of $\hat{\mathbf{M}}$.

indicates that the estimates of the coefficients of $\hat{\mathbf{M}}$ are reliable. We must also note that the use of different sets of transmit signals does not influence the estimation of $\mathbf{M}$ in a significant way.

#### 5.4.3.2 Subtraction of the Crosstalk Term

Let us consider the previous configuration of two targets at $[\theta_1, R_1] = [-15°, 1.7 \text{ m}]$ and $[\theta_2, R_2] = [18°, 1.7 \text{ m}]$. We can now reduce the crosstalk term $\hat{\mathbf{M}}\mathbf{c}(n)$ from the received signals by computing

$$\mathbf{x}_{sc}(n) = \mathbf{x}(n) - \hat{\mathbf{M}}\mathbf{c}(n). \tag{5.6}$$

In this particular case, we use as crosstalk matrix the average of $\hat{\mathbf{M}}$ over the 100 trials. Then the Capon, MUSIC, and GLRT spectra are computed again from the signals $\mathbf{x}_{sc}(n)$. As shown in Figures 5.16 and 5.17, the resolution of Capon and MUSIC seems to be improved since their corresponding spectra exhibit sharper lobes after the crosstalk reduction (the estimated DOAs are now $[\hat{\theta}_1, \hat{\theta}_2]_{\text{Capon}} = [-15.5°, 18°]$ and $[\hat{\theta}_1, \hat{\theta}_2]_{\text{MUSIC}} = [-15.3°, 18.1°]$). However, only a few secondary lobes are attenuated in the GLRT spectrum after the crosstalk reduction, and we are still unable to estimate the target DOAs from this spectrum. The remaining secondary lobes may be due to the characteristics of the actual noise present in our measurement system and environment. Indeed, the GLRT technique was developed assuming the presence of white Gaussian noise (see Appendix A). However, the characteristics of the actual noise present in the anechoic chamber and the RF architecture might differ from the Gaussian assumption which might deteriorate the detection performance. Moreover, the noise level might also be very low which would lead to ill-conditioning problems.

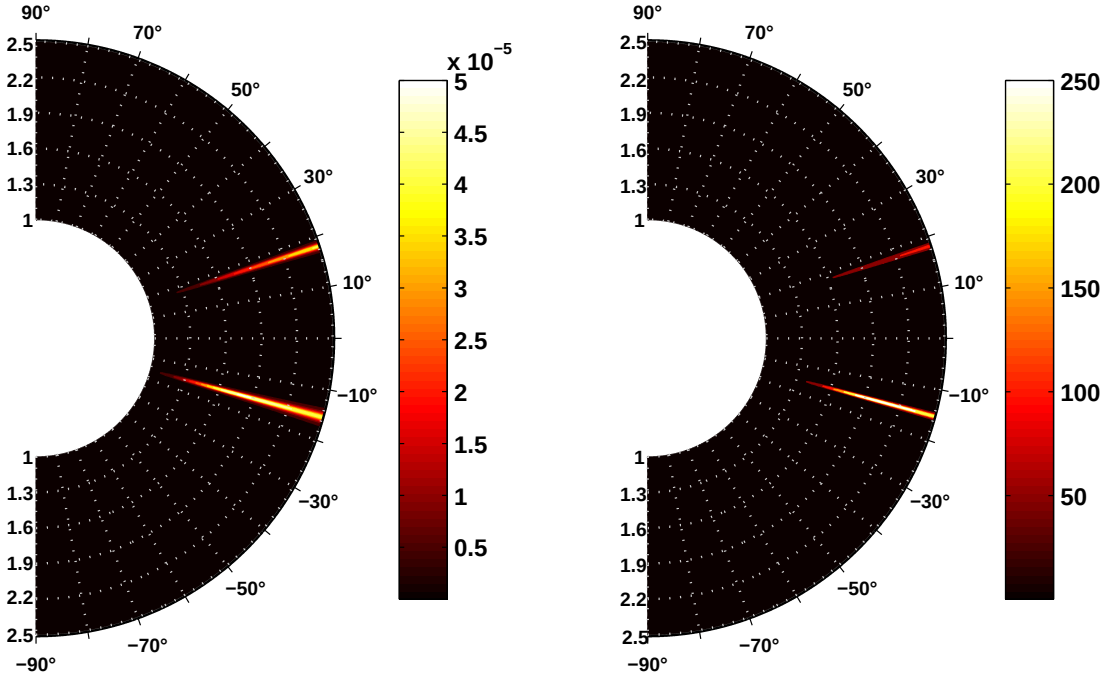


(a) (b)

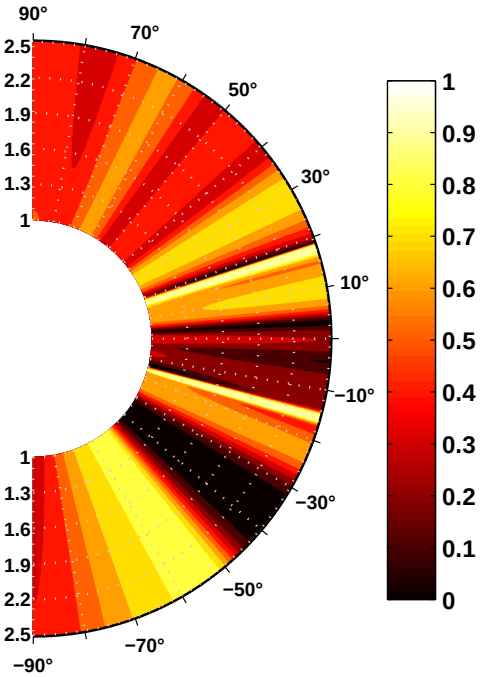


(c)

FIGURE 5.16: (a) Capon, (b) MUSIC, and (c) GLRT spectra after crosstalk reduction (experimental measurements with two targets at $[\theta_1, R_1] = [-15°, 1.7 \text{ m}]$ and $[\theta_2, R_2] = [18°, 1.7 \text{ m}]$).

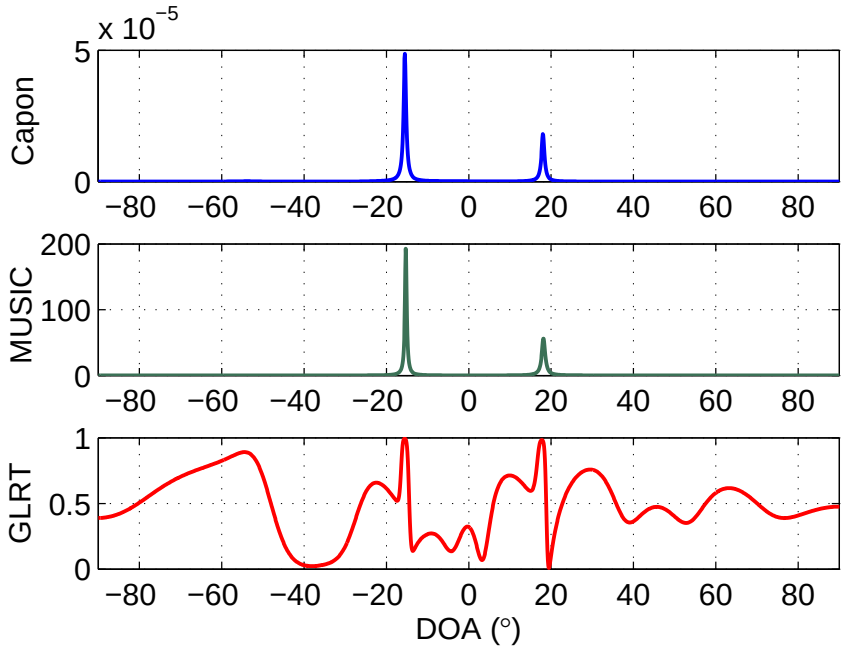


FIGURE 5.17: Component of the Capon, MUSIC, and GLRT spectra at $R = 1.7$ m after crosstalk reduction (experimental measurements with two targets at $[\theta_1, R_1] = [-15°, 1.7 \text{ m}]$ and $[\theta_2, R_2] = [18°, 1.7 \text{ m}]$).

### 5.4.4 Addition of White Gaussian Noise and Crosstalk Reduction

To observe the influence of noise on the performance of GLRT, let us add white Gaussian noise to the received signals $\mathbf{x}(n)$ before crosstalk reduction (without subtracting the crosstalk term $\hat{\mathbf{M}}\mathbf{c}(n)$) as

$$\begin{aligned} \mathbf{x}_{+noise}(n) &= \mathbf{x}(n) + \tilde{\mathbf{z}}(n) \\ n &= 0, \ldots, N-1, \end{aligned} \tag{5.7}$$

where the $\{\tilde{\mathbf{z}}(n)\}_{n=0}^{N-1}$ are complex Gaussian random vectors with zero mean. The power of this additive noise is chosen to be of 70 dB below the received signals power (the latter being of $-36$ dBm).

The GLRT is then computed from the signals $\{\mathbf{x}_{+noise}(n)\}_{n=0}^{N-1}$ and is shown in Figures 5.18 and 5.19. As we can see, several secondary lobes are significantly attenuated by the addition of white Gaussian noise only. However, some secondary lobes are still present around the target DOAs because of crosstalk.

Let us now reduce the crosstalk term from $\mathbf{x}_{+noise}(n)$ by computing

$$\mathbf{x}_{sc+noise}(n) = \mathbf{x}_{+noise}(n) - \hat{\mathbf{M}}\mathbf{c}(n) \tag{5.8}$$

and compute again the GLRT from $\mathbf{x}_{sc+noise}(n)$. As shown in Figures 5.20 and 5.21, all the secondary lobes are greatly reduced after the addition of white Gaussian noise and

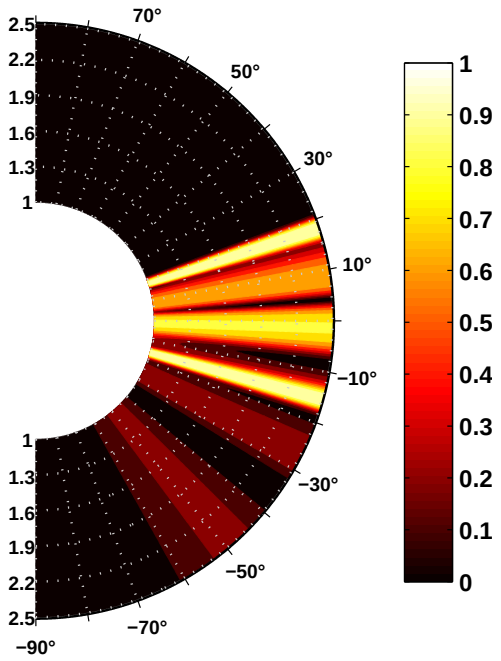


FIGURE 5.18: GLRT spectrum after the addition of white Gaussian noise and before crosstalk reduction (experimental measurements with two targets at $[\theta_1, R_1] = [-15°, 1.7 \text{ m}]$ and $[\theta_2, R_2] = [18°, 1.7 \text{ m}]$).

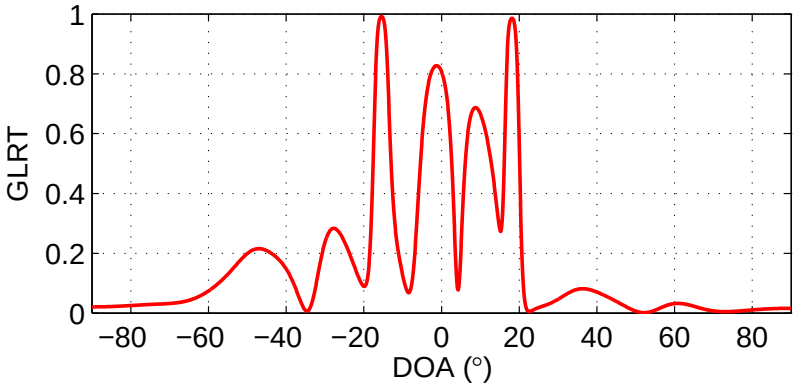


FIGURE 5.19: Component of the GLRT spectrum at $R = 1.7$ m after the addition of white Gaussian noise and before crosstalk reduction (experimental measurements with two targets at $[\theta_1, R_1] = [-15°, 1.7 \text{ m}]$ and $[\theta_2, R_2] = [18°, 1.7 \text{ m}]$).

crosstalk reduction, which allows us to clearly identify the target directions.

## 5.5 Summary

We developed an experimental measurement platform of MIMO radar with colocated antennas using a single Tx/Rx RF architecture. The proposed platform is much less complex and expensive than a real MIMO system. It is also reconfigurable since the

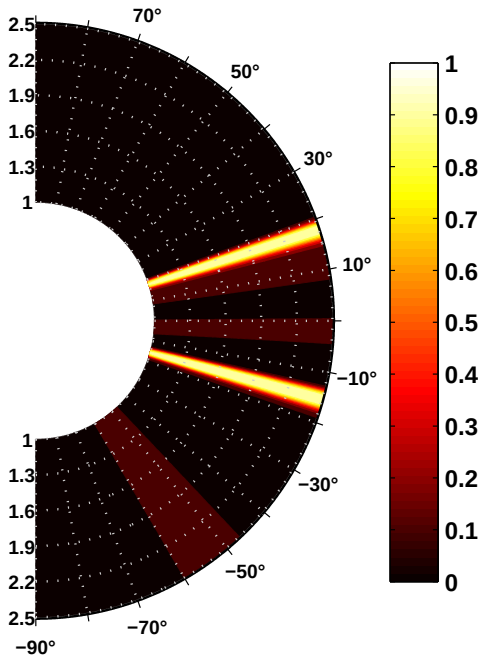


FIGURE 5.20: GLRT spectrum after the addition of white Gaussian noise and after crosstalk reduction (experimental measurements with two targets at $[\theta_1, R_1] = [-15°, 1.7 \text{ m}]$ and $[\theta_2, R_2] = [18°, 1.7 \text{ m}]$).

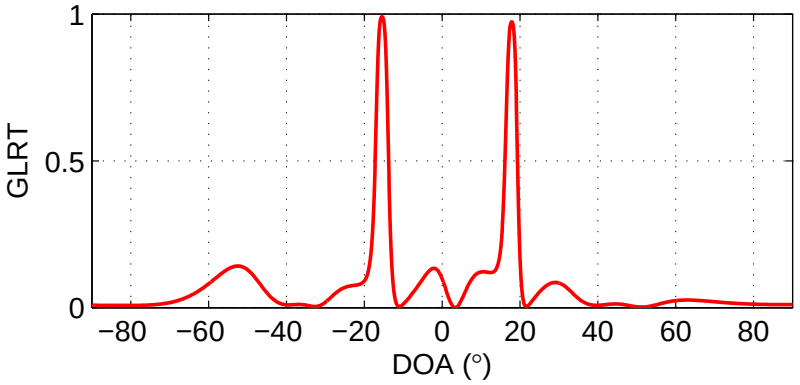


FIGURE 5.21: Component of the GLRT spectrum at $R = 1.7$ m after the addition of white Gaussian noise and after crosstalk reduction (experimental measurements with two targets at $[\theta_1, R_1] = [-15°, 1.7 \text{ m}]$ and $[\theta_2, R_2] = [18°, 1.7 \text{ m}]$).

inter-element spacings and the number of antenna elements can be easily modified, which allows performing different kinds of test.

The repeatability test showed fluctuations in the estimated DOAs of maximum $\pm 1°$ around the true DOA, which proves that the platform is reliable.

The obtained measurements allowed us to validate some detection techniques usually studied from a theoretical point of view. The results showed that the performance of the GLRT is highly affected by the noise characteristics. We remedied this matter by adding white Gaussian post-processing noise on the received signals. We also demonstrated the

effectiveness of the crosstalk reduction technique in reducing the secondary lobes from the GLRT spectrum.

Our contributions presented in this chapter are the development of a reconfigurable experimental platform for narrowband MIMO radar with colocated antennas, and the investigation of the narrowband DOA estimation and crosstalk reduction techniques from an experimental point of view.

# Chapter 6

# Conclusions and Perspectives

The signal model of narrowband MIMO radar with colocated antennas was presented in Chapter 2 followed by the description of the Capon, MUSIC, and GLRT methods as DOA estimation techniques of non-moving targets. The simulations showed that MUSIC offers the best angular resolution followed by Capon and GLRT. Because of its high resolution, MUSIC is able to resolve closely spaced targets. As for the GLRT, even though it has the lowest angular resolution, it is the most robust against noise and the less sensitive to the target reflection coefficients among the three techniques. Moreover, the GLRT has the capability of rejecting strong interference or jammers which are uncorrelated with the transmitted signals.

Additionally, we showed that particular attention must be paid while using the plane-wave assumption. Actually, the plane-wave condition which must be considered from a signal processing point of view differs from the far-field condition $R > 2\Delta^2/\lambda$ established in antenna theory. Indeed, considering the wavefront as plane for $R > 2\Delta^2/\lambda$ may introduce additional errors in the DOA estimation. We found that for antenna arrays of 5, 10, and 15 elements, the condition $R > 5\Delta^2/\lambda$ is more appropriate and the error introduced by the plane-wave approximation can be neglected.

In Chapter 3, we extended the signal model to the case of wideband signals. Next, we investigated and compared two recently proposed wideband waveform design techniques, the WBFIT and the SFBT. The WBFIT is an iterative technique which can synthesize low PAPR sequences with transmitted beampatterns usually smoother than those obtained with the SBFT. However, the performance of WBFIT is poor for relatively large bandwidth, such as $F_s = f_c/2$, leading to deformed beampatterns. On the other hand, the SFBT works well even in the case of relatively large bandwidths and is at least 2000 times faster to compute than the WBFIT. However, the sequences synthesized by the SFBT usually have high PAPR. Based on those two techniques, we

proposed a modified version of SFBT, called M-SFBT, which meets a PAPR constraint and allows transmitting the power directly to the targets while allocating a different non-overlapping frequency band to each one. The use of multiband beampatterns is advantageous since it allows receiving uncorrelated signals from the targets, which makes possible the adaptation of wideband array processing techniques (such as TOPS) to the context of wideband MIMO radar. Note that, although the simulations presented in Chapter 3 allowed us to obtain relevant information on the performance of the waveform design techniques, they were done assuming ideal conditions, i.e. omitting the radiation patterns of the antennas' elements and neglecting mutual coupling. In fact, the actual beampatterns of real antenna arrays may differ from those shown in the simulation results. Such characteristics should be taken into account in further research in order to investigate the performance of the wideband waveform design techniques under more realistic conditions.

We also presented some wideband DOA estimation techniques based on the existing wideband array processing techniques. We first introduced the incoherent methods for wideband MIMO radar, which consist in applying narrowband DOA estimation techniques (such as Capon, MUSIC and GLRT) at several narrowband frequency components and averaging the results to obtain a general spatial spectrum. The performance tests showed that the incoherent Capon, MUSIC, and GLRT techniques have similar performance after transmitting an omnidirectional pattern; however, the GLRT gives the minimum MSE on the DOA. After transmitting a beampattern synthesized by SFBT, the performance of the three techniques is improved and MUSIC outperforms Capon and GLRT at low noise levels ($-10\log_{10}\sigma^2 > 10$).

Also, we proposed an adaptation of TOPS to the context of wideband MIMO radar. TOPS was originally developed to estimate the DOAs of uncorrelated sources and cannot be successfully applied if the signals reflected by the targets are correlated. We then proposed an adaptation of TOPS to the context of MIMO radar. When used along with a multiband beampattern (generated for instance by M-SFBT), we showed that the targets can be properly detected.

In Chapter 4, we took into account the electromagnetic interactions between the different antenna elements in order to introduce a more realistic signal model. By combining electromagnetic simulations with signal processing, we were able to evaluate the performance of the narrowband DOA estimation techniques in the presence of mutual coupling. We showed that the existence of mutual coupling introduces distortions in the radiation patterns which degrade the DOA estimation performance of Capon, MUSIC, and GLRT. We then showed that taking into account the different radiation patterns in the expressions of the steering vectors allows improving the DOA

estimation performance. Given that some techniques might present regrowth at the spectrum edges (e.g. Capon and MUSIC) caused by low magnitudes of the radiation patterns, we can alternatively omit the magnitudes and use only the phase of the radiation patterns without introducing any significant error. On the other hand, the weak amplitudes of the radiation patterns at large angles (in absolute value) make targets located at angles close to $-90°$ or $90°$ difficult to detect. A new challenge involving antenna and waveform designs is then to improve the DOA estimation of targets located at absolute large angles.

Another consequence of mutual coupling is crosstalk, which can significantly degrade the DOA estimation performance: We observed that the resolution of Capon and MUSIC is highly decreased and the GLRT spectrum presents several secondary lobes which do not allow the estimation of the target DOAs. In order to overcome this problem, we proposed a crosstalk reduction technique based on a signal processing approach: The crosstalk matrix is first estimated (by solving a minimum MSE criterion) from a first transmission in an environment without any target, and the crosstalk term is then subtracted from the received signals when targets are present.

From an experimental point of view, we developed a platform for narrowband MIMO radar with colocated antennas, as presented in Chapter 5. Since a large MIMO system is particularly expensive and complex to develop, the proposed platform employs only one transmitter and one receiver RF architectures. An automated mechanism places both the transmitter and the receiver elements in every position of a ULA, and the received signal matrix is constructed by applying the superposition principle. This platform is not only easier to calibrate and synchronize than a real MIMO system would be, but it is also reconfigurable since the number of antenna elements and the inter-element spacings can be easily changed.

The experimental results allowed us to validate some narrowband DOA estimation techniques, which are usually studied from a theoretical point of view. We observed that the performance of the GLRT is affected by the noise characteristics and can be improved by adding white Gaussian post-processing noise. We also demonstrated the validity of the proposed crosstalk reduction technique.

Suggestions for future work are presented below:

1. The performance of the wideband waveform design techniques (WBFIT, SFBT, and M-SFBT) has to be investigated and compared considering the radiation pattern of every transmitter antenna element. From a theoretical point of view, this can be done by simulating wideband antenna arrays to obtain the radiation patterns at every frequency component of interest. Then, the so-obtained

radiation patterns could be included in the wideband steering vectors to simulate more realistic transmit beampatterns.

2. The effects of mutual coupling have to be investigated in the case of wideband signals by combining electromagnetic simulations with signal processing, similarly to the narrowband case. The different radiation patterns obtained at different frequency components have to be included in the transmit and receive steering vectors to evaluate the influence of the pattern distortion on the wideband DOA estimation performance. Additionally, crosstalk has to be investigated also in the case of wideband signals, and new methods of crosstalk reduction have to be explored. One method may rely on the estimation of a different crosstalk matrix at every frequency component via a signal processing approach. The crosstalk matrices might also be obtained by measuring the transmission S-parameters between the transmitter and the receiver elements.

3. The possibility of improving DOA estimation of targets located close to $-90°$ or $90°$ has to be explored. This problem might be addressed by exploiting the antenna pattern diversity and/or the waveform diversity.

4. The possibilities of improving the DOA estimation performance by exploiting the wave polarization diversity could be explored. Indeed, different kinds of targets may produce different types of reflections depending on the polarization of the impinging waves as it is often seen in polarimetric and weather-type radars [74]-[76].

5. In the future, the experimental platform should allow taking the whole effects of mutual coupling into account. This can be done by using real transmitter and receiver arrays, instead of single mobile Tx and Rx elements. The low complexity and cost of the actual platform can be maintained by using two RF switches (one for each array), so that only one transmitter and one receiver elements are active at each time, while the other elements are terminated with matched impedances.

6. The platform needs to evolve in the future so that it can deal with wideband signals. This will require replacing the actual narrowband RF architecture (which includes the antennas, the power amplifiers, the signal generator, and the signal analyzer) with a wideband one.

7. Finally, the ambiguity functions in the case of wideband MIMO radar could be investigated in order to estimate Doppler and range parameters of moving targets. The feasibility of an experimental implementation has to be explored.

# APPENDICES

# Appendix A

# Narrowband Derivations

Consider a narrowband MIMO radar system with $L_t$ transmitting antennas and $L_r$ receiving antennas. According to the signal model (2.29), the received signal due to the reflection from one target located in the plane-wave region is given by

$$\mathbf{X} = \beta \mathbf{a}_r^*(\theta)\mathbf{a}_t^H(\theta)\mathbf{C} + \mathbf{Z} \tag{A.1}$$

where $\mathbf{C}$ and $\mathbf{X}$ are the matrices of the transmitted and the received signals respectively, and $\mathbf{Z}$ is a residual term which includes the unmodelled noise and interference. Each row of $\mathbf{C}$, $\mathbf{X}$, and $\mathbf{Z}$ contains $N$ temporal samples. $\mathbf{a}_t(\theta)$ is the $L_t \times 1$ plane-wave transmit steering vector, $\mathbf{a}_r(\theta)$ is the $L_r \times 1$ plane-wave receive steering vector and $\beta$ is the complex reflection coefficient of the target.

The mathematical developments of the narrowband Capon and GLRT techniques are described thereafter.

## A.1 The Capon Beamformer

The Capon minimization is

$$\begin{aligned} &\min_{\mathbf{w}} \mathbf{w}^H \mathbf{R}_x \mathbf{w} \\ &\text{s.t. } \mathbf{w}^H \mathbf{a}_r^*(\theta) = 1. \end{aligned} \tag{A.2}$$

Let $f = \mathbf{w}^H \mathbf{R}_x \mathbf{w}$ and $g = \mathbf{w}^H \mathbf{a}_r^*(\theta) - 1$. Then

$$\frac{\partial f}{\partial \mathbf{w}} = 2\mathbf{R}_x \mathbf{w} \quad \text{and} \quad \frac{\partial g}{\partial \mathbf{w}} = 2\mathbf{a}_r^*(\theta), \tag{A.3}$$

where the derivatives $\frac{\partial f}{\partial \mathbf{w}}$ and $\frac{\partial g}{\partial \mathbf{w}}$ are obtained using the following derivative rule:

Given a complex variable $w = w_R + jw_I$, the complex derivative of $w$ is

$$\frac{\partial}{\partial w} = \frac{\partial}{\partial w_R} + j\frac{\partial}{\partial w_I}.$$

As a consequence

$$\begin{aligned} \frac{\partial w}{\partial w} &= 1 + j^2 = 0 \\ \frac{\partial w^*}{\partial w} &= 1 + j(-j) = 2. \end{aligned} \tag{A.4}$$

Using the method of Lagrange multipliers to optimize gives

$$\begin{aligned} \frac{\partial f}{\partial \mathbf{w}} - \lambda\frac{\partial g}{\partial \mathbf{w}} &= 0 \\ 2\mathbf{R}_x\mathbf{w} - 2\lambda\mathbf{a}_r^*(\theta) &= 0 \\ \mathbf{w} &= \lambda\mathbf{R}_x^{-1}\mathbf{a}_r^*(\theta). \end{aligned} \tag{A.5}$$

Then, applying the constraint

$$\begin{aligned} \mathbf{w}^H\mathbf{a}_r^*(\theta) &= 1 \\ \lambda\mathbf{a}_r^T(\theta)\mathbf{R}_x^{-1}\mathbf{a}_r^*(\theta) &= 1 \\ \lambda &= \frac{1}{\mathbf{a}_r^T(\theta)\mathbf{R}_x^{-1}\mathbf{a}_r^*(\theta)}. \end{aligned} \tag{A.6}$$

Therefore, the Capon weights are

$$\overset{\triangle}{\mathbf{w}}(\theta) = \frac{\mathbf{R}_x^{-1}\mathbf{a}_r^*(\theta)}{\mathbf{a}_r^T(\theta)\mathbf{R}_x^{-1}\mathbf{a}_r^*(\theta)}. \tag{A.7}$$

## A.2 The GLRT

This section details the derivation of the GLRT presented in [32].

For the derivation of the GLRT it is assumed that the columns of the residual term $\mathbf{Z}$ in (A.1) are i.i.d circularly symmetric complex Gaussian random vectors. All the columns are assumed to have zero mean and unknown but equal covariance matrix $\mathbf{R}_z$.

Before defining the GLRT, the Probability Density Function (PDF) of the residual term, $\mathbf{Z}$ will be defined. The PDF for $\mathbf{Z}_i$, the $i^{\text{th}}$ complex Gaussian random column of $\mathbf{Z}$, is

$$f(\mathbf{Z}_i) = \frac{1}{\pi^{L_r}\left|\mathbf{R}_z\right|}e^{-\left[\mathbf{Z}_i^H\mathbf{R}_z^{-1}\mathbf{Z}_i\right]}. \tag{A.8}$$

But then, since $\mathbf{Z}_1, \ldots, \mathbf{Z}_N$ are all independent from each other,

$$\begin{aligned} f(\mathbf{Z}) &= \prod_{i=1}^{N} f(\mathbf{Z}_i) \\ &= \prod_{i=1}^{N} \frac{1}{\pi^{L_r} |\mathbf{R}_z|} e^{-\left[\mathbf{Z}_i^H \mathbf{R}_z^{-1} \mathbf{Z}_i\right]} \\ &= (\pi)^{-NL_r} |\mathbf{R}_z|^{-N} e^{-\left[\sum_{i=1}^{N} \mathbf{Z}_i^H \mathbf{R}_z^{-1} \mathbf{Z}_i\right]} \\ &= (\pi)^{-NL_r} |\mathbf{R}_z|^{-N} e^{-\operatorname{tr}\left[\mathbf{Z}^H \mathbf{R}_z^{-1} \mathbf{Z}\right]} \\ &= (\pi)^{-NL_r} |\mathbf{R}_z|^{-N} e^{-\operatorname{tr}\left[\mathbf{R}_z^{-1} \mathbf{Z}\mathbf{Z}^H\right]} \end{aligned} \tag{A.9}$$

---

The GLR is defined as [33]

$$\rho(\theta) = 1 - \left[\frac{\max_{\mathbf{R}_z} f(\mathbf{X}|\beta = 0, \mathbf{R}_z)}{\max_{\beta, \mathbf{R}_z} f(\mathbf{X}|\beta, \mathbf{R}_z)}\right]^{\frac{1}{N}}, \tag{A.10}$$

where

$$f(\mathbf{X} \mid \beta, \mathbf{R}_z) = \pi^{-NL_r} |\mathbf{R}_z|^{-N} e^{-\operatorname{tr}[\mathbf{R}_z^{-1}(\mathbf{X} - \beta \mathbf{a}_r^*(\theta)\mathbf{a}_t^H(\theta)\mathbf{C})(\mathbf{X} - \beta \mathbf{a}_r^*(\theta)\mathbf{a}_t^H(\theta)\mathbf{C})^H]} \tag{A.11}$$

is the PDF of the received signal matrix $\mathbf{X}$, given parameters $\beta$ and $\mathbf{R}_z$ (which is equivalent to the PDF of the residual term $\mathbf{Z} = \mathbf{X} - \beta \mathbf{a}_r^*(\theta)\mathbf{a}_t^H(\theta)\mathbf{C}$) as derived in (A.9).

Therefore, the GLR exploits the difference in the PDF when there is no target and the PDF when a target with complex coefficient $\beta$ is present. When a target is present, the denominator $\max_{\beta, \mathbf{R}_z} f(\mathbf{X}|\beta, \mathbf{R}_z)$ will be much greater than $\max_{\mathbf{R}_z} f(\mathbf{X}|\beta = 0, \mathbf{R}_z)$ and then the value of $\rho(\theta)$ will be close to one. When there is no target, the value of $\rho(\theta)$ will approach zero.

Consider the maximization in the numerator of the second term of the GLR. This optimization is

$$\max_{\mathbf{R}_z} f(\mathbf{X} \mid \beta = 0, \mathbf{R}_z) = \max_{\mathbf{R}_z} \pi^{-NL_r} |\mathbf{R}_z|^{-N} e^{-\operatorname{tr}[\mathbf{R}_z^{-1} \mathbf{X}\mathbf{X}^H]}. \tag{A.12}$$

Given that $\hat{\mathbf{R}}_x = \frac{1}{N}\mathbf{X}\mathbf{X}^H$, and using the properties of the trace this becomes

$$\begin{aligned} &\max_{\mathbf{R}_z} \pi^{-NL_r} |\mathbf{R}_z|^{-N} e^{-\operatorname{tr}[\mathbf{R}_z^{-1} N \hat{\mathbf{R}}_x]} \\ &= \max_{\mathbf{R}_z} \pi^{-NL_r} |\mathbf{R}_z|^{-N} e^{-N \operatorname{tr}[\mathbf{R}_z^{-1} \hat{\mathbf{R}}_x]} \\ &= \max_{\mathbf{R}_z} \left(\pi^{L_r} |\mathbf{R}_z| e^{\operatorname{tr}[\mathbf{R}_z^{-1} \hat{\mathbf{R}}_x]}\right)^{-N} \\ &= \left(\min_{\mathbf{R}_z} \pi^{L_r} |\mathbf{R}_z| e^{\operatorname{tr}[\mathbf{R}_z^{-1} \hat{\mathbf{R}}_x]}\right)^{-N}. \end{aligned} \tag{A.13}$$

Now, replace $\mathbf{R}_z$ with the equivalent expression $\hat{\mathbf{R}}_x\hat{\mathbf{R}}_x^{-1}\mathbf{R}_z$. Then, ignoring the factor $\pi^{L_r}$, the objective of the minimization in (A.13) is

$$|\mathbf{R}_z|\, e^{\mathrm{tr}[\mathbf{R}_z^{-1}\hat{\mathbf{R}}_x]} = \left|\hat{\mathbf{R}}_x\right| \left|\hat{\mathbf{R}}_x^{-1}\mathbf{R}_z\right| e^{\mathrm{tr}[\mathbf{R}_z^{-1}\hat{\mathbf{R}}_x]}. \tag{A.14}$$

Then, let $\mathbf{A} = \mathbf{R}_z^{-1}\hat{\mathbf{R}}_x$. Also, diagonalize $\mathbf{A}$ so that $\mathbf{A} = \mathbf{P}\mathbf{\Lambda}\mathbf{P}^{-1}$ with $\mathbf{\Lambda} = \mathrm{diag}(\lambda_i)_{i=1,\ldots,L_r}$, where $\lambda_i$ are the eigenvalues of $\mathbf{A}$ such that

$$\begin{aligned} \mathbf{R}_z^{-1}\hat{\mathbf{R}}_x\mathbf{u}_i &= \lambda_i\mathbf{u}_i \\ i &= 1,\ldots,L_r, \end{aligned} \tag{A.15}$$

where $\mathbf{u}_i$ are the eigenvectors of $\mathbf{A}$. It should be noted that $|\mathbf{A}| = |\mathbf{\Lambda}|$, $\left|\mathbf{A}^{-1}\right| = \left|\mathbf{\Lambda}^{-1}\right|$ and also that $\mathrm{tr}[\mathbf{A}] = \mathrm{tr}[\mathbf{\Lambda}]$.

Note that $\mathbf{R}_z$ is a covariance matrix and therefore positive semidefinite. Then, $\mathbf{R}_z^{-1}$ is also positive semidefinite, which allows to write

$$\left(\mathbf{u}_i^H\hat{\mathbf{R}}_x\right)\mathbf{R}_z^{-1}\left(\hat{\mathbf{R}}_x\mathbf{u}_i\right) \geq 0. \tag{A.16}$$

Substituting Equation (A.15) into Equation (A.16) gives

$$\lambda_i\mathbf{u}_i^H\hat{\mathbf{R}}_x\mathbf{u}_i \geq 0. \tag{A.17}$$

Then, given that $\hat{\mathbf{R}}_x$ is positive semidefinite, it follows that $\mathbf{u}_i^H\hat{\mathbf{R}}_x\mathbf{u}_i \geq 0$ and therefore the eigenvalues $\lambda_i$ are all positive.

Now, from Equation (A.14) we have

$$\begin{aligned} \left|\hat{\mathbf{R}}_x\right| \left|\hat{\mathbf{R}}_x^{-1}\mathbf{R}_z\right| e^{\mathrm{tr}[\mathbf{R}_z^{-1}\hat{\mathbf{R}}_x]} &= \left|\hat{\mathbf{R}}_x\right| \left|\mathbf{A}^{-1}\right| e^{\mathrm{tr}[\mathbf{A}]} \\ &= \left|\hat{\mathbf{R}}_x\right| \left|\mathbf{\Lambda}^{-1}\right| e^{\mathrm{tr}[\mathbf{\Lambda}]} \\ &= \left|\hat{\mathbf{R}}_x\right| \left(\prod_{i=1}^{L_r}\lambda_i^{-1}\right) e^{\sum_{i=1}^{L_r}\lambda_i} \\ &= \left|\hat{\mathbf{R}}_x\right| \prod_{i=1}^{L_r}\left(\frac{e^{\lambda_i}}{\lambda_i}\right). \end{aligned} \tag{A.18}$$

However, it can be shown that $\frac{e^x}{x} \geq e^1$ when $x$ is positive. Therefore, since the eigenvalues $\lambda_i$ are positive, it follows that

$$\frac{e^{\lambda_i}}{\lambda_i} \geq e. \tag{A.19}$$

Thus

$$\prod_{i=1}^{L_r}\frac{e^{\lambda_i}}{\lambda_i} \geq e^{L_r}. \tag{A.20}$$

The lower bound of this inequality will be reached when $\lambda_i = 1$ for $i = 1, \ldots, L_r$. In this case, $\mathbf{\Lambda} = \mathbf{I}$ and therefore, $\mathbf{A} = \mathbf{P}\mathbf{P}^{-1} = \mathbf{I}$, where $\mathbf{I}$ denotes the $L_r \times L_r$ identity matrix. For this to be true, it is required that $\mathbf{R}_z^{-1}\hat{\mathbf{R}}_x = \mathbf{I}$ so $\mathbf{R}_z = \hat{\mathbf{R}}_x$. Finally, substituting (A.20) into (A.13) gives

$$\begin{aligned} \max_{\mathbf{R}_z} f(\mathbf{X} \mid \beta = 0, \mathbf{R}_z) &= \left( \min \pi^{L_r} \left|\hat{\mathbf{R}}_x\right| \prod_{i=1}^{L_r} \frac{e^{\lambda_i}}{\lambda_i} \right)^{-N} \\ &= \left( \pi^{L_r} \left|\hat{\mathbf{R}}_x\right| e^{L_r} \right)^{-N} \\ &= (\pi e)^{-NL_r} \left|\hat{\mathbf{R}}_x\right|^{-N}. \end{aligned} \tag{A.21}$$

Similarly, the maximum value of the denominator of the second term in the GLR can be found:

$$\max_{\beta, \mathbf{R}_z} f(\mathbf{X} \mid \beta, \mathbf{R}_z) = \max_{\beta, \mathbf{R}_z} \pi^{-NL_r} |\mathbf{R}_z|^{-N} e^{-\operatorname{tr}[\mathbf{R}_z^{-1}(\mathbf{X} - \beta \mathbf{a}_r^*(\theta)\mathbf{a}_t^H(\theta)\mathbf{C})(\mathbf{X} - \beta \mathbf{a}_r^*(\theta)\mathbf{a}_t^H(\theta)\mathbf{C})^H]}. \tag{A.22}$$

Let $\mathbf{B} = \mathbf{X} - \beta \mathbf{a}_r^*(\theta)\mathbf{a}_t^H(\theta)\mathbf{C}$. Then, the maximization (A.22) becomes

$$\max_{\beta, \mathbf{R}_z} f(\mathbf{X} \mid \beta, \mathbf{R}_z) = \max_{\beta, \mathbf{R}_z} \pi^{-NL_r} |\mathbf{R}_z|^{-N} e^{-\operatorname{tr}[\mathbf{R}_z^{-1}\mathbf{B}\mathbf{B}^H]} \tag{A.23}$$

which is of the same form as (A.12). Thus, this maximum can be shown to be

$$\max_{\beta, \mathbf{R}_z} f(\mathbf{X} \mid \beta, \mathbf{R}_z) = (\pi e)^{-NL_r} \left( \min_{\beta} \left| \frac{1}{N} (\mathbf{X} - \beta \mathbf{a}_r^*(\theta)\mathbf{a}_t^H(\theta)\mathbf{C})(\mathbf{X} - \beta \mathbf{a}_r^*(\theta)\mathbf{a}_t^H(\theta)\mathbf{C})^H \right| \right)^{-N}. \tag{A.24}$$

It is now necessary to analyze the minimization in (A.24). Let $\hat{\mathbf{Q}}$ be defined as

$$\hat{\mathbf{Q}} = \frac{1}{N}\mathbf{X}\mathbf{X}^H - \frac{\mathbf{X}\mathbf{C}^H\mathbf{a}_t(\theta)\mathbf{a}_t^H(\theta)\mathbf{C}\mathbf{X}^H}{N^2\mathbf{a}_t^H(\theta)\hat{\mathbf{R}}_c\mathbf{a}_t(\theta)}, \tag{A.25}$$

where $\hat{\mathbf{R}}_c = \frac{1}{N}\mathbf{C}\mathbf{C}^H$. Then, it can be shown that

$$\begin{aligned} &\left| \frac{1}{N} (\mathbf{X} - \beta \mathbf{a}_r^*(\theta)\mathbf{a}_t^H(\theta)\mathbf{C})(\mathbf{X} - \beta \mathbf{a}_r^*(\theta)\mathbf{a}_t^H(\theta)\mathbf{C})^H \right| \\ &= \left| \hat{\mathbf{Q}} + (\mathbf{a}_t^H(\theta)\hat{\mathbf{R}}_c\mathbf{a}_t(\theta)) \left( \beta \mathbf{a}_r^*(\theta) - \frac{\mathbf{X}\mathbf{C}^H\mathbf{a}_t(\theta)}{N(\mathbf{a}_t^H(\theta)\hat{\mathbf{R}}_c\mathbf{a}_t(\theta))} \right) \left( \beta \mathbf{a}_r^*(\theta) - \frac{\mathbf{X}\mathbf{C}^H\mathbf{a}_t(\theta)}{N(\mathbf{a}_t^H(\theta)\hat{\mathbf{R}}_c\mathbf{a}_t(\theta))} \right)^H \right|. \end{aligned} \tag{A.26}$$

Now, let $\mu = (\mathbf{a}_t^H(\theta)\hat{\mathbf{R}}_c\mathbf{a}_t(\theta))$ and move $\hat{\mathbf{Q}}$ out of the determinant so the equation becomes

$$\left|\hat{\mathbf{Q}}\right| \left| \mathbf{I} + \mu\hat{\mathbf{Q}}^{-1} \left( \beta \mathbf{a}_r^*(\theta) - \frac{\mathbf{X}\mathbf{C}^H\mathbf{a}_t(\theta)}{N\mu} \right) \left( \beta \mathbf{a}_r^*(\theta) - \frac{\mathbf{X}\mathbf{C}^H\mathbf{a}_t(\theta)}{N\mu} \right)^H \right|. \tag{A.27}$$

Consider the property on matrix determinants given by

$$|\mathbf{I} + \mathbf{AB}| = |\mathbf{I} + \mathbf{BA}|\,. \tag{A.28}$$

Note that this property allows the dimensions of the matrix whose determinant is being evaluated to change.

Therefore, letting $\mathbf{Y} = \beta\mathbf{a}_r^*(\theta) - \frac{\mathbf{X}\mathbf{C}^H\mathbf{a}_t(\theta)}{N\mu}$, (A.27) can be written as

$$\left|\hat{\mathbf{Q}}\right|\left|\mathbf{I} + \mu\hat{\mathbf{Q}}^{-1}\mathbf{Y}\mathbf{Y}^H\right| = \left|\hat{\mathbf{Q}}\right|\left[1 + \mu\mathbf{Y}^H\hat{\mathbf{Q}}^{-1}\mathbf{Y}\right]. \tag{A.29}$$

Therefore, the matrix argument of the second determinant has been transformed to a scalar.

Let define the scalars

$$\begin{aligned}\sigma &= \mathbf{a}_r^T(\theta)\hat{\mathbf{Q}}^{-1}\mathbf{a}_r^*(\theta)\\ \eta &= \mathbf{a}_r^T(\theta)\hat{\mathbf{Q}}^{-1}\mathbf{X}\mathbf{C}^H\mathbf{a}_t(\theta).\end{aligned}$$

Note that $\mu$ and $\sigma$ are real and positive because $\hat{\mathbf{R}}_c$ and $\hat{\mathbf{Q}}$ are Hermitian positive semidefinite.

Considering that

$$\frac{1}{N^2\mu\sigma}\left|\eta - N\mu\sigma\beta\right|^2 \geq 0, \tag{A.30}$$

we have

$$\mu\sigma\left|\beta\right|^2 - \frac{\beta^*\eta}{N} - \frac{\beta\eta^*}{N} \geq -\frac{|\eta|^2}{N^2\mu\sigma}. \tag{A.31}$$

Note that the equality holds for $\beta = \frac{\eta}{N\mu\sigma}$.

Then, taking into account that $|\hat{\mathbf{Q}}| \geq 0$ ($|\hat{\mathbf{Q}}|$ being Hermitian positive semidefinite), it follows that

$$\begin{aligned}&\left|\hat{\mathbf{Q}}\right|\left(1 + \frac{\mathbf{a}_t^H(\theta)\mathbf{C}\mathbf{X}^H\hat{\mathbf{Q}}^{-1}\mathbf{X}\mathbf{C}^H\mathbf{a}_t(\theta)}{N^2\mu} + \mu\sigma\left|\beta\right|^2 - \frac{\beta^*\eta}{N} - \frac{\beta\eta^*}{N}\right)\\ &\geq \left|\hat{\mathbf{Q}}\right|\left(1 + \frac{\mathbf{a}_t^H(\theta)\mathbf{C}\mathbf{X}^H\hat{\mathbf{Q}}^{-1}\mathbf{X}\mathbf{C}^H\mathbf{a}_t(\theta)}{N^2\mu} - \frac{|\eta|^2}{N^2\mu\sigma}\right),\end{aligned} \tag{A.32}$$

which can be rewritten as

$$\begin{aligned}&\left|\hat{\mathbf{Q}}\right|\left[1 + \mu\left(\beta\mathbf{a}_r^*(\theta) - \frac{\mathbf{X}\mathbf{C}^H\mathbf{a}_t(\theta)}{N\mu}\right)^H\hat{\mathbf{Q}}^{-1}\left(\beta\mathbf{a}_r^*(\theta) - \frac{\mathbf{X}\mathbf{C}^H\mathbf{a}_t(\theta)}{N\mu}\right)\right]\\ &\geq \left|\hat{\mathbf{Q}}\right|\left[1 + \frac{\mathbf{a}_t^H(\theta)\mathbf{C}\mathbf{X}^H}{N^2\mu}\hat{\mathbf{Q}}^{-1}\left(\mathbf{I} - \frac{\mathbf{a}_r^*(\theta)\mathbf{a}_r^T(\theta)\hat{\mathbf{Q}}^{-1}}{\mathbf{a}_r^T(\theta)\hat{\mathbf{Q}}^{-1}\mathbf{a}_r^*(\theta)}\right)\mathbf{X}\mathbf{C}^H\mathbf{a}_t(\theta)\right].\end{aligned} \tag{A.33}$$

Note that the left-hand side of this inequality corresponds to (A.29), and that inequality (A.33) can achieve equality for

$$\beta = \frac{\mathbf{a}_r^T(\theta)\hat{\mathbf{Q}}^{-1}\mathbf{X}\mathbf{C}^H\mathbf{a}_t(\theta)}{N(\mathbf{a}_t^H(\theta)\hat{\mathbf{R}}_c\mathbf{a}_t(\theta))(\mathbf{a}_r^T(\theta)\hat{\mathbf{Q}}^{-1}\mathbf{a}_r^*(\theta))}. \tag{A.34}$$

Now using the identity given in (A.28) to rewrite the right-hand side of inequality (A.33) gives

$$\begin{aligned}&\left|\hat{\mathbf{Q}} + \hat{\mathbf{Q}}\hat{\mathbf{Q}}^{-1}\left(\mathbf{I} - \frac{\mathbf{a}_r^*(\theta)\mathbf{a}_r^T(\theta)\hat{\mathbf{Q}}^{-1}}{\mathbf{a}_r^T(\theta)\hat{\mathbf{Q}}^{-1}\mathbf{a}_r^*(\theta)}\right)\mathbf{X}\mathbf{C}^H\mathbf{a}_t(\theta)\left(\frac{\mathbf{a}_t^H(\theta)\mathbf{C}\mathbf{X}^H}{N^2\mu}\right)\right| \\ &= \left|\hat{\mathbf{Q}} + \frac{1}{N^2\mu}\mathbf{X}\mathbf{C}^H\mathbf{a}_t(\theta)\mathbf{a}_t^H(\theta)\mathbf{C}\mathbf{X}^H - \frac{\mathbf{a}_r^*(\theta)\mathbf{a}_r^T(\theta)\hat{\mathbf{Q}}^{-1}\mathbf{X}\mathbf{C}^H\mathbf{a}_t(\theta)\mathbf{a}_t^H(\theta)\mathbf{C}\mathbf{X}^H}{N^2\mu\left(\mathbf{a}_r^T(\theta)\hat{\mathbf{Q}}^{-1}\mathbf{a}_r^*(\theta)\right)}\right|.\end{aligned} \tag{A.35}$$

Replacing $\mu$ and $\hat{\mathbf{Q}}$ with their expressions in the equation gives

$$\left|\hat{\mathbf{R}}_x - \frac{\mathbf{a}_r^*(\theta)\mathbf{a}_r^T(\theta)\hat{\mathbf{Q}}^{-1}\mathbf{X}\mathbf{C}^H\mathbf{a}_t(\theta)\mathbf{a}_t^H(\theta)\mathbf{C}\mathbf{X}^H}{N^2\left(\mathbf{a}_t^H(\theta)\hat{\mathbf{R}}_c\mathbf{a}_t(\theta)\right)\left(\mathbf{a}_r^T(\theta)\hat{\mathbf{Q}}^{-1}\mathbf{a}_r^*(\theta)\right)}\right|. \tag{A.36}$$

$\hat{\mathbf{R}}_x$ is then moved out of the equation giving

$$\left|\hat{\mathbf{R}}_x\right|\left|\mathbf{I} - \frac{\hat{\mathbf{R}}_x^{-1}\mathbf{a}_r^*(\theta)\mathbf{a}_r^T(\theta)\hat{\mathbf{Q}}^{-1}\mathbf{X}\mathbf{C}^H\mathbf{a}_t(\theta)\mathbf{a}_t^H(\theta)\mathbf{C}\mathbf{X}^H}{N^2\left(\mathbf{a}_t^H(\theta)\hat{\mathbf{R}}_c\mathbf{a}_t(\theta)\right)\left(\mathbf{a}_r^T(\theta)\hat{\mathbf{Q}}^{-1}\mathbf{a}_r^*(\theta)\right)}\right|. \tag{A.37}$$

Once again, the matrix whose determinant is being calculated is reshaped by the identity (A.28), by moving the matrix $\hat{\mathbf{R}}_x^{-1}\mathbf{a}_r^*(\theta)$ to the back, to give

$$\left|\hat{\mathbf{R}}_x\right|\left[1 - \frac{\mathbf{a}_r^T(\theta)\hat{\mathbf{Q}}^{-1}\mathbf{X}\mathbf{C}^H\mathbf{a}_t(\theta)\mathbf{a}_t^H(\theta)\mathbf{C}\mathbf{X}^H\hat{\mathbf{R}}_x^{-1}\mathbf{a}_r^*(\theta)}{N^2\left(\mathbf{a}_t^H(\theta)\hat{\mathbf{R}}_c\mathbf{a}_t(\theta)\right)\left(\mathbf{a}_r^T(\theta)\hat{\mathbf{Q}}^{-1}\mathbf{a}_r^*(\theta)\right)}\right]. \tag{A.38}$$

It is noted that

$$\frac{\mathbf{X}\mathbf{C}^H\mathbf{a}_t(\theta)\mathbf{a}_t^H(\theta)\mathbf{C}\mathbf{X}^H}{N^2\mathbf{a}_t^H(\theta)\hat{\mathbf{R}}_c\mathbf{a}_t(\theta)} = \hat{\mathbf{R}}_x - \hat{\mathbf{Q}}$$

and therefore (A.38) becomes

$$\begin{aligned}&\left|\hat{\mathbf{R}}_x\right|\left[1 - \frac{\mathbf{a}_r^T(\theta)\hat{\mathbf{Q}}^{-1}(\hat{\mathbf{R}}_x - \hat{\mathbf{Q}})\hat{\mathbf{R}}_x^{-1}\mathbf{a}_r^*(\theta)}{\mathbf{a}_r^T(\theta)\hat{\mathbf{Q}}^{-1}\mathbf{a}_r^*(\theta)}\right] \\ &= \left|\hat{\mathbf{R}}_x\right|\frac{\mathbf{a}_r^T(\theta)\hat{\mathbf{R}}_x^{-1}\mathbf{a}_r^*(\theta)}{\mathbf{a}_r^T(\theta)\hat{\mathbf{Q}}^{-1}\mathbf{a}_r^*(\theta)}.\end{aligned} \tag{A.39}$$

So, the maximization in (A.24) evaluates to

$$\max_{\beta,\mathbf{R}_z} f(\mathbf{X} \mid \beta, \mathbf{R}_z) = (\pi e)^{-NL_r} \left|\hat{\mathbf{R}}_x\right|^{-N} \left(\frac{\mathbf{a}_r^T(\theta)\hat{\mathbf{R}}_x^{-1}\mathbf{a}_r^*(\theta)}{\mathbf{a}_r^T(\theta)\hat{\mathbf{Q}}^{-1}\mathbf{a}_r^*(\theta)}\right)^{-N}. \tag{A.40}$$

Thus, substituting (A.21) and (A.40) into (A.10) gives

$$\rho(\theta) = 1 - \left[\frac{(\pi e)^{-NL_r} \left|\hat{\mathbf{R}}_x\right|^{-N}}{(\pi e)^{-NL_r} \left|\hat{\mathbf{R}}_x\right|^{-N} \left(\frac{\mathbf{a}_r^T(\theta)\hat{\mathbf{R}}_x^{-1}\mathbf{a}_r^*(\theta)}{\mathbf{a}_r^T(\theta)\hat{\mathbf{Q}}^{-1}\mathbf{a}_r^*(\theta)}\right)^{-N}}\right]^{\frac{1}{N}} \tag{A.41}$$

and the GLR is

$$\rho(\theta) = 1 - \frac{\mathbf{a}_r^T(\theta)\hat{\mathbf{R}}_x^{-1}\mathbf{a}_r^*(\theta)}{\mathbf{a}_r^T(\theta)\hat{\mathbf{Q}}^{-1}\mathbf{a}_r^*(\theta)}. \tag{A.42}$$

# Appendix B

# Wideband Derivations

Consider a wideband MIMO radar system with $L_t$ transmitting antennas and $L_r$ receiving antennas. According to the signal model (3.17), the received signals due to the reflection from $K$ targets located in the plane-wave region are given by

$$\begin{aligned}\mathbf{X}(p) \approx \sum_{k=1}^{K} \beta_k \mathbf{a}_r^*(\theta_k, p)\mathbf{a}_t^H(\theta_k, p)\mathbf{C}(p) + \mathbf{Z}(p) \\ p = 0, \ldots, N-1,\end{aligned} \tag{B.1}$$

with

$$\mathbf{a}_t\left(\theta_k, p\right) = \left[e^{j2\pi(f_c+f_p)(\frac{L_t-1}{2}-i)\frac{d_t \sin\theta_k}{v}}\right]_{i=0,\ldots,L_t-1} \tag{B.2}$$

and

$$\mathbf{a}_r\left(\theta_k, p\right) = \left[e^{j2\pi(f_c+f_p)(\frac{L_r-1}{2}-l)\frac{d_r \sin\theta_k}{v}}\right]_{l=0,\ldots,L_r-1}, \tag{B.3}$$

where

$$f_p = \frac{pF_s}{N} - \frac{F_s}{2}, \tag{B.4}$$

$F_s$ is the sampling frequency, and $\mathbf{X}(p) = \begin{bmatrix} X_0(p) & \cdots & X_{L_r-1}(p)\end{bmatrix}^T$, $\mathbf{C}(p) = \begin{bmatrix} C_0(p) & \cdots & C_{L_t-1}(p)\end{bmatrix}^T$, and $\mathbf{Z}(p) = \begin{bmatrix} Z_0(p) & \cdots & Z_{L_r-1}(p)\end{bmatrix}^T$ are the DFT (element-wise) of $\mathbf{x}(n)$, $\mathbf{c}(n)$, and $\mathbf{z}(n)$ respectively.

## B.1 The WBFIT Algorithm

The Wideband Beampattern Formation via Iterative Techniques (WBFIT) algorithm was proposed in [43] to design low PAPR sequences for transmit beampattern synthesis in wideband MIMO systems. The waveform design problem is formulated with the goal of designing a set of signals $\{\mathbf{c}(n)\}_{n=0}^{N-1}$ such that the power distribution (3.25) matches

a desired beampattern. Letting $\delta(\theta_h, p)$ denote the desired beampattern, where $\{\theta_h\}_{h=1}^{H}$ represents a grid of angles covering the interval $[-90°, 90°]$, the beampattern matching problem can be formulated as

$$\begin{aligned} \min_{\{\mathbf{c}(n)\}} \sum_{h=1}^{H} \sum_{p=0}^{N-1} \left[\delta(\theta_h, p) - \left|\mathbf{a}_t^H(\theta_h, p)\mathbf{C}(p)\right|\right]^2 \\ \text{s.t. PAPR}\left(\{c_i(n)\}_{n=0}^{N-1}\right) \leq \varrho, \\ i = 0, \ldots, L_t - 1, \end{aligned} \tag{B.5}$$

where the PAPR of the $i^{\text{th}}$ signal $\{c_i(n)\}_{n=0}^{N-1}$ is defined as

$$\text{PAPR}\left(\{c_i(n)\}_{n=0}^{N-1}\right) = \frac{\max_n |c_i(n)|^2}{\frac{1}{N}\sum_{n=0}^{N-1} |c_i(n)|^2}, \tag{B.6}$$

and $\varrho \geq 1$ is a predefined threshold.

In order to solve the optimization problem (B.5), the authors propose in [43] a two-stage design approach, which is recalled thereafter.

**Stage 1**

Let consider the following optimization problem:

$$\begin{aligned} \min_{\phi_{hp}} |\delta(\theta_h, p)e^{j\phi_{hp}} - \mathbf{a}_t^H(\theta_h, p)\mathbf{C}(p)|^2 = \min_{\phi_{hp}} \Big\{ \delta^2(\theta_h, p) + \left|\mathbf{a}_t^H(\theta_h, p)\mathbf{C}(p)\right|^2 \\ -2\text{Re}\left[\delta(\theta_h, p)\left|\mathbf{a}_t^H(\theta_h, p)\mathbf{C}(p)\right| e^{j(\arg\{\mathbf{a}_t^H(\theta_h, p)\mathbf{C}(p)\} - \phi_{hp})}\right] \Big\}. \end{aligned} \tag{B.7}$$

Since $\delta(\theta_h, p) \geq 0$, it can be seen that the minimum is obtained for $\phi_{hp} = \arg\{\mathbf{a}_t^H(\theta, p)\mathbf{C}(p)\}$ and that

$$\min_{\phi_{hp}} \left|\delta(\theta_h, p)e^{j\phi_{hp}} - \mathbf{a}_t^H(\theta_h, p)\mathbf{C}(p)\right|^2 = \left[\delta(\theta_h, p) - \left|\mathbf{a}_t^H(\theta_h, p)\mathbf{C}(p)\right|\right]^2. \tag{B.8}$$

Therefore, we can obtain the signals $\{\mathbf{c}(n)\}_{n=0}^{N-1}$ minimizing (B.5) from the $\{\mathbf{C}(p)\}_{p=0}^{N-1}$ which minimize the following criterion:

$$\sum_{h=1}^{H} \sum_{p=0}^{N-1} |\delta(\theta_h, p)e^{j\phi_{hp}} - \mathbf{a}_t^H(\theta_h, p)\mathbf{C}(p)|^2. \tag{B.9}$$

The criterion (B.9) can be minimized with respect to $\{\mathbf{C}(p)\}_{p=0}^{N-1}$ and $\{\phi_{hp}\}$ using the following cyclic algorithm:

Step 0: Given initial arbitrary values of $\{\phi_{hp}\}$ in $[0, 2\pi]$, repeat steps 1 and 2 until convergence.

Step 1: For $\{\phi_{hp}\}$ at their last values, denoted as $\{\hat{\phi}_{hp}\}$, let

$$\begin{aligned} \mathbf{A}(p) &= \begin{bmatrix} \mathbf{a}_t^H(\theta_1, p) \\ \vdots \\ \mathbf{a}_t^H(\theta_H, p) \end{bmatrix}, \\ \mathbf{b}(p) &= \begin{bmatrix} \delta(\theta_1, p) e^{j\hat{\phi}_{1p}} \\ \vdots \\ \delta(\theta_H, p) e^{j\hat{\phi}_{Hp}} \end{bmatrix}. \end{aligned} \tag{B.10}$$

Then, the criterion (B.9) can be written as

$$\sum_{h=1}^{H} \sum_{p=0}^{N-1} |\delta(\theta_h, p) e^{j\phi_{hp}} - \mathbf{a}_t^H(\theta_h, p)\mathbf{C}(p)|^2 = \sum_{p=0}^{N-1} \|\mathbf{b}(p) - \mathbf{A}(p)\mathbf{C}(p)\|^2 . \tag{B.11}$$

The minimizer $\{\mathbf{C}(p)\}_{p=0}^{N-1}$ is given by the least-squares estimate:

$$\hat{\mathbf{C}}(p) = (\mathbf{A}^H(p)\mathbf{A}(p))^{-1}\mathbf{A}^H(p)\mathbf{b}(p). \tag{B.12}$$

Step 2: For $\{\mathbf{C}(p)\}_{p=0}^{N-1}$ set at their last values, the minimizer $\{\phi_{hp}\}$ of the criterion (B.9) is given by

$$\hat{\phi}_{hp} = \arg\{\mathbf{a}_t^H(\theta_h, p)\hat{\mathbf{C}}(p)\}. \tag{B.13}$$

**Stage 2**

In stage 2, a set of signals $\{\mathbf{c}(n)\}_{n=0}^{N-1}$ is synthesized (under the PAPR constraint), so that its DFT approximates the $\{\hat{\mathbf{C}}(p)\}_{p=0}^{N-1}$ obtained in stage 1.

It can be noted that the $\{\mathbf{C}(p)\}_{p=0}^{N-1}$ solving the beampattern matching problem stated in (B.5) have a phase ambiguity, i.e. $\mathbf{C}(p)$ and $\mathbf{C}(p)e^{j\psi_p}$ lead to the same value of (B.5) for any $\psi_p$. To exploit this phase ambiguity, let introduce the auxiliary variables $\{\psi_p\}_{p=0}^{N-1}$. Then, the signals $\{\mathbf{c}(n)\}_{n=0}^{N-1}$ whose DFT approximate the previously obtained $\{\hat{\mathbf{C}}(p)\}_{p=0}^{N-1}$ can be found by solving the following optimization problem:

$$\min_{\{\mathbf{c}(n)\},\{\psi_p\}} \sum_{p=0}^{N-1} \left\| \hat{\mathbf{C}}^T(p) e^{j\psi_p} - \begin{bmatrix} 1 & e^{-j2\pi\frac{1}{N}\left(p-\frac{N}{2}\right)} & \dots & e^{-j2\pi\frac{(N-1)}{N}\left(p-\frac{N}{2}\right)} \end{bmatrix} \mathbf{C}^T \right\|^2, \tag{B.14}$$

where

$$\mathbf{C} = \begin{bmatrix} c_0(0) & \cdots & c_0(N-1) \\ c_1(0) & \cdots & c_1(N-1) \\ \vdots & & \vdots \\ c_{L_t-1}(0) & \cdots & c_{L_t-1}(N-1) \end{bmatrix}. \tag{B.15}$$

By defining

$$\begin{aligned} \mathbf{e}_p^H &= \begin{bmatrix} 1 & e^{-j2\pi\frac{1}{N}\left(p-\frac{N}{2}\right)} & \cdots & e^{-j2\pi\frac{(N-1)}{N}\left(p-\frac{N}{2}\right)} \end{bmatrix}, \\ \mathbf{F}^H &= \begin{bmatrix} \mathbf{e}_0^H \\ \vdots \\ \mathbf{e}_{N-1}^H \end{bmatrix}, \\ \mathbf{G}^T &= \begin{bmatrix} \hat{\mathbf{C}}^T(0)e^{-j\psi_0} \\ \vdots \\ \hat{\mathbf{C}}^T(N-1)e^{-j\psi_{N-1}} \end{bmatrix}, \end{aligned} \tag{B.16}$$

Equation (B.14) can be written as

$$\min_{\{\mathbf{c}(n)\},\{\psi_p\}} \left\| \mathbf{G}^T - \mathbf{F}^H\mathbf{C}^T \right\|^2. \tag{B.17}$$

Given that $(1/\sqrt{N})\mathbf{F}$ is a unitary matrix, the optimization problem can finally be written as

$$\min_{\{\mathbf{c}(n)\},\{\psi_p\}} N \left\| \frac{1}{N}\mathbf{F}\mathbf{G}^T - \mathbf{C}^T \right\|^2. \tag{B.18}$$

The problem can be solved using the following cyclic algorithm:

Step 0: Given arbitrary initial values for $\{\psi_p\}_{p=0}^{N-1}$ and the $\{\hat{\mathbf{C}}(p)\}_{p=0}^{N-1}$ obtained from stage 1, repeat steps 1 and 2 until convergence.

Step 1: For $\{\psi_p\}_{p=0}^{N-1}$ set at their last values, the minimization (B.18) with respect to $\{\mathbf{c}(n)\}_{n=0}^{N-1}$ depends on the PAPR constraint. The resolution of (B.18) can be done by solving $L_t$ separate optimization problems (i.e. for $i = 0, \ldots, L_t - 1$):

$$\begin{aligned} \min_{\{c_i(n)\}_{n=0}^{N-1}} & \left\| \mathbf{v}_i - \begin{bmatrix} c_i(0) & \cdots & c_i(N-1) \end{bmatrix}^T \right\|^2 \\ \text{s.t. } & \text{PAPR}\left(\{c_i(n)\}_{n=0}^{N-1}\right) \leq \varrho, \end{aligned} \tag{B.19}$$

where $\mathbf{v}_i$ denotes the $i^{\text{th}}$ column of $\frac{1}{N}\mathbf{F}\mathbf{G}^T$. This problem can be solved using the "nearest-vector" algorithm proposed in [46] and recalled in Appendix B.2.

Step 2: For $\{\mathbf{c}(n)\}_{n=0}^{N-1}$ set at their latest values, the minimizer $\{\psi_p\}_{p=0}^{N-1}$ in (B.18) is given by

$$\begin{aligned} \hat{\psi_p} &= \arg\{\hat{\mathbf{C}}^H(p)\mathbf{q}_p\} \\ p &= 0, \ldots, N-1, \end{aligned} \tag{B.20}$$

where $\mathbf{q}_p^T$ is the $(p+1)^{\text{th}}$ row of $\mathbf{F}^H\mathbf{C}^T$.

## B.2 The Nearest-Vector Algorithm

The nearest-vector algorithm was proposed in [46], and recalled in [77], to design sequences of low PAPR. Given an initial sequence $\mathbf{y} = \begin{bmatrix} y(0) & \cdots & y(N-1) \end{bmatrix}$, the sequence $\mathbf{y}'$ which meets a PAPR constraint and is closest to $\mathbf{y}$ can be found by solving the following optimization problem

$$\begin{aligned} &\min_{\mathbf{y}'} \left\|\mathbf{y}' - \mathbf{y}\right\|^2 \\ &\text{s.t. PAPR}\left(\mathbf{y}'\right) \leq \varrho, \end{aligned} \tag{B.21}$$

where $\varrho \geq 1$ is a predefined threshold. Additionally, we impose the following energy constraint

$$\left\|\mathbf{y}'\right\|^2 = \sum_{n=0}^{N-1} \left|y'(n)\right|^2 = N. \tag{B.22}$$

Note that, without the PAPR constraint, the solution to (B.21) is $\mathbf{y}'_0 = \sqrt{N}\mathbf{y}/\|\mathbf{y}\|$.

Given the definition of the PAPR in (B.6), it can be seen that the PAPR constraint in (B.21) is equivalent to

$$\max_n |y'(n)| \leq \sqrt{\varrho}. \tag{B.23}$$

Hence, if the magnitude of every sample in $\mathbf{y}'_0$ is less or equal to $\sqrt{\varrho}$, then $\mathbf{y}'_0$ is a solution to (B.21); otherwise, the following recursive procedure is applied: The element in $\mathbf{y}'$ corresponding to the element $y_\alpha$ of largest magnitude in $\mathbf{y}$ is given by $\sqrt{\varrho}e^{j\arg\{y_\alpha\}}$. The other $N-1$ elements in $\mathbf{y}'$ are obtained by solving the same optimization problem (B.21), except that the energy constraint is now $\left\|\mathbf{y}'\right\|^2 = N - \varrho$.

## B.3 Estimation of the Covariance Matrices

In order to estimate the covariance matrices at every frequency component, the discrete-time signals are divided into $M$ blocks of $N_f$ samples, where two consecutive blocks are

overlapped with $\frac{3}{4}N_f$ samples. The covariance matrices are then estimated as

$$\begin{aligned}
\hat{\mathbf{R}}_x(f_{p'}) &= \frac{1}{M}\sum_{m=1}^{M}\mathbf{X}_m(p')\mathbf{X}_m^H(p') \\
\hat{\mathbf{R}}_c(f_{p'}) &= \frac{1}{M}\sum_{m=1}^{M}\mathbf{C}_m(p')\mathbf{C}_m^H(p') \\
\hat{\mathbf{R}}_{xc}(f_{p'}) &= \frac{1}{M}\sum_{m=1}^{M}\mathbf{X}_m(p')\mathbf{C}_m^H(p') \\
p' &= 0,\ldots,N_f-1,
\end{aligned} \tag{B.24}$$

where $\mathbf{X}_m(p')$ and $\mathbf{C}_m(p')$ denote respectively the received and the transmitted sequences at frequency $f_{p'}$ for the $m^{\text{th}}$ block ($m = 1,\ldots,M$), i.e.

$$\begin{aligned}
\mathbf{X}_m(p') &= \sum_{n=0}^{N_f-1}\mathbf{x}\left(n+\frac{m-1}{4}N_f\right)e^{-j2\pi\frac{n}{N_f}\left(p'-\frac{N_f}{2}\right)} \\
\mathbf{C}_m(p') &= \sum_{n=0}^{N_f-1}\mathbf{c}\left(n+\frac{m-1}{4}N_f\right)e^{-j2\pi\frac{n}{N_f}\left(p'-\frac{N_f}{2}\right)}.
\end{aligned} \tag{B.25}$$

# Appendix C

# Résumé long

Un radar MIMO (Multiple Input Multiple Output) est un système radar qui utilise plusieurs antennes émettrices et réceptrices, dans lequel les formes d'ondes émises peuvent être indépendantes. Par rapport aux radars utilisant des antennes en réseaux phasés, les radars MIMO offrent davantage de degrés de liberté, ce qui permet d'améliorer les performances du système en termes de détection et localisation. La technique MIMO offre également la possibilité de synthétiser un diagramme de rayonnement désiré par une définition judicieuse des formes d'ondes émises. Dans la mesure où les paramètres des cibles (positions, vitesses, directions d'arrivée (DOA), ...) sont estimés à partir des échos des signaux émis, on comprend aisément que les formes d'ondes employées jouent un rôle clé dans les performances du système.

Cette thèse porte sur l'estimation de DOA et sur la conception des formes d'ondes pour un radar MIMO. Le cadre d'étude est restreint au cas où les antennes sont colocalisées et les cibles sont immobiles et supposées ponctuelles. La plupart des travaux antérieurs (au commencement de la thèse) portaient sur le radar MIMO bande étroite et faisaient l'hypothèse d'émetteurs-récepteurs idéaux et indépendants. Cette thèse contribue à élargir le cadre d'étude en s'intéressant d'une part au passage en large bande et d'autre part à la modélisation et à la prise en compte de la non-indépendance des émetteurs-récepteurs et d'autres imperfections. Dans la mesure où le recours à des signaux large bande est nécessaire lorsqu'une résolution importante est souhaitée, nous nous sommes attachés dans cette thèse à adapter le modèle d'un système de radar MIMO au cas large bande et à proposer de nouvelles techniques visant à améliorer les performances d'estimation de DOA dans le cas de signaux large bande. Cette thèse analyse également l'influence de conditions non idéales comme l'impact des phénomènes de couplage électromagnétique sur les diagrammes de rayonnement dans un réseau d'antennes. Cette étude est menée dans le cas bande

étroite. En particulier, nous étudions l'influence du couplage direct entre les réseaux d'antennes d'émission et de réception (appelé "crosstalk") sur les performances des techniques proposées. Nous établissons un modèle du signal permettant de prendre en compte ce phénomène et proposons une technique de réduction du "crosstalk" qui permet une estimation efficace des DOA des cibles. Nous montrons par ailleurs comment améliorer les performances d'estimation de DOA en présence de diagrammes de rayonnement incluant le couplage entre antennes. Le dernier apport principal de cette thèse est la conception et réalisation d'une plateforme expérimentale comportant une seule architecture d'émetteur-récepteur, qui permet de simuler un système MIMO utilisant des antennes colocalisées en appliquant le principe de superposition. Cette plateforme nous a permis d'évaluer et valider les performances des techniques proposées dans des conditions plus réalistes.

## C.1 Radar MIMO bande étroite

### C.1.1 Modèle du signal

On considère un système MIMO dont les $L_t$ antennes d'émission et les $L_r$ antennes de réception sont colocalisées. Sous l'hypothèse d'avoir $K$ cibles localisées en champ lointain aux angles $\{\theta_k\}_{k=1}^{K}$, le signal bande étroite reçu par le réseau de réception s'écrit en bande de base (voir chapitre 2)

$$\mathbf{x}(n) = \sum_{k=1}^{K} \beta_k \mathbf{a}_r^*(\theta_k, R_k)\mathbf{a}_t^H(\theta_k, R_k)\mathbf{c}(n) + \mathbf{z}(n), \tag{C.1}$$

où

$$\mathbf{a}_t(\theta, R) = \begin{bmatrix} g_{t,0}^*(\theta)\frac{1}{\|\mathbf{r}_0\|}e^{j\frac{2\pi}{\lambda}\|\mathbf{r}_0\|} \\ \vdots \\ g_{t,L_t-1}^*(\theta)\frac{1}{\|\mathbf{r}_{L_t-1}\|}e^{j\frac{2\pi}{\lambda}\|\mathbf{r}_{L_t-1}\|} \end{bmatrix} \tag{C.2}$$

et

$$\mathbf{a}_r(\theta, R) = \begin{bmatrix} g_{r,0}^*(\theta)\frac{1}{\|\mathbf{r}_0\|}e^{j\frac{2\pi}{\lambda}\|\mathbf{r}_0\|} \\ \vdots \\ g_{r,L_r-1}^*(\theta)\frac{1}{\|\mathbf{r}_{L_r-1}\|}e^{j\frac{2\pi}{\lambda}\|\mathbf{r}_{L_r-1}\|} \end{bmatrix} \tag{C.3}$$

sont respectivement les vecteurs directionnels d'émission et de réception dans le cas d'ondes sphériques, $\mathbf{x}(n) = \begin{bmatrix} x_0(n) & \cdots & x_{L_r}(n) \end{bmatrix}^T$ est l'ensemble des signaux reçus à temps discret[1], $\mathbf{c}(n) = \begin{bmatrix} c_0(n) & \cdots & c_{L_t}(n) \end{bmatrix}^T$ est l'ensemble d'enveloppes complexes

[1]Les signaux $\{x_l(n)\}_{l=0}^{L_r-1}$ sont obtenus en échantillonant les signaux reçus $\{x_l(t)\}_{l=0}^{L_r-1}$ à la fréquence symbole $F_s$, i.e. $x_l(n) \triangleq x_l\left(t = \frac{n}{F_s}\right)$ pour $n = 0, \ldots, N-1$ et $l = 0, \ldots, L_r - 1$.

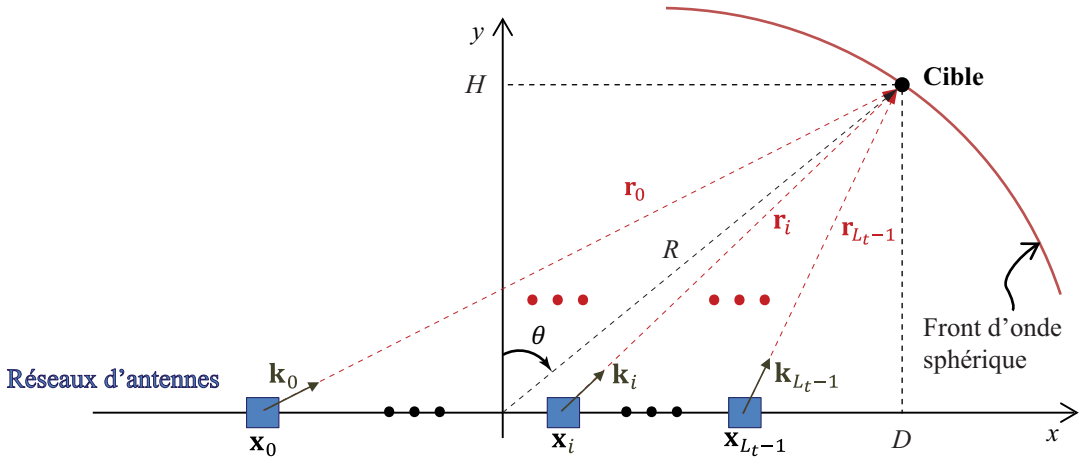


FIGURE C.1: réseau d'antennes linéaire et uniforme.

des signaux émis, $\mathbf{z}(n) = \begin{bmatrix} x_0(n) & \cdots & z_{L_r}(n) \end{bmatrix}^T$ représente le bruit et les interférences additives, $\lambda$ est la longueur d'onde, les $\{g_{t,i}(\theta)\}_{i=0}^{L_t-1}$ et les $\{g_{r,l}(\theta)\}_{l=0}^{L_r-1}$ désignent respectivement les diagrammes de rayonnement des éléments émetteurs et récepteurs, et $\beta_k$ désigne le coefficient de réflexion complexe de la $k^{\text{ième}}$ cible. A noter que la position de chaque cible est donnée par la direction d'arrivée $\theta_k$ et la distance $R_k$ entre l'origine du système cartésien et la position de la $k^{\text{ième}}$ cible (voir figure C.1).

Le modèle (C.2) peut être simplifié en faisant l'approximation d'ondes planes. En effet, il existe une région dans le champ lointain dans laquelle les fronts d'onde peuvent être considérés comme plans et où ce modèle simplifié peut être utilisé. Dans ce cas, le produit scalaire entre les vecteurs d'onde $\mathbf{k}_i$ et les vecteurs $\mathbf{r}_i$ s'exprime comme suit :

$$\mathbf{k}_i^T \mathbf{r}_i = \frac{2\pi}{\lambda}\left(D - \left(i - \frac{L_t-1}{2}\right) d_t\right)\sin\theta + \frac{2\pi}{\lambda} H\cos\theta \qquad i = 0, \ldots, L_t - 1. \tag{C.4}$$

Cette écriture nous permet d'obtenir des vecteurs directionnels qui ne dépendent que des directions d'arrivée $\theta$. On parle alors des vecteurs directionnels d'émission et de réception d'ondes planes

$$\mathbf{a}_t(\theta) = \left[g_{t,i}^*(\theta) e^{j\frac{2\pi}{\lambda}\left(\frac{L_t-1}{2}-i\right)d_t \sin\theta}\right]_{i=0,\ldots,L_t-1} \tag{C.5}$$

et

$$\mathbf{a}_r(\theta) = \left[g_{r,l}^*(\theta) e^{j\frac{2\pi}{\lambda}\left(\frac{L_r-1}{2}-i\right)d_r \sin\theta}\right]_{i=0,\ldots,L_r-1}, \tag{C.6}$$

où $d_t$ et $d_r$ désignent respectivement la distance séparant les élements émetteurs et la distance séparant les éléments récepteurs. Le modèle du signal dans le cas d'ondes planes

est alors donné par

$$\mathbf{x}(n) = \sum_{k=1}^{K} \beta_k \mathbf{a}_r^*(\theta_k)\mathbf{a}_t^H(\theta_k)\mathbf{c}(n) + \mathbf{z}(n). \tag{C.7}$$

En notation matricielle, ce modèle s'écrit

$$\mathbf{X} = \sum_{k=1}^{K} \beta_k \mathbf{a}_r^*(\theta_k)\mathbf{a}_t^H(\theta_k)\mathbf{C} + \mathbf{Z}, \tag{C.8}$$

avec

$$\mathbf{X} = \begin{bmatrix} \mathbf{x}(0) & \cdots & \mathbf{x}(N-1) \end{bmatrix},$$
$$\mathbf{C} = \begin{bmatrix} \mathbf{c}(0) & \cdots & \mathbf{c}(N-1) \end{bmatrix},$$
$$\mathbf{Z} = \begin{bmatrix} \mathbf{z}(0) & \cdots & \mathbf{z}(N-1) \end{bmatrix},$$

où $N$ est le nombre de symboles.

### C.1.2 Techniques d'estimation de DOA

Dans cette section, trois techniques d'estimation de DOA existant dans la littérature sont brièvement décrites.

Elles sont rappelées ci-dessous en utilisant les vecteurs directionnels d'ondes planes (C.5) et (C.6). On parlera alors de traitement d'ondes planes.

Ces techniques peuvent également être appliquées en utilisant les vecteurs directionnels d'ondes sphériques (C.2) et (C.3). Dans ce cas, on parlera de traitement d'ondes sphériques.

#### C.1.2.1 Formation de voies par la méthode de Capon

La formation de voies par la méthode de Capon est une technique de traitement d'antennes qui minimise la puissance reçue dans les directions autres que la direction utile. Le spectre spatial de Capon est donné par

$$P_{cap}(\theta) = \frac{1}{\mathbf{a}_r^T(\theta)\mathbf{R}_x^{-1}\mathbf{a}_r^*(\theta)}, \tag{C.9}$$

où $\mathbf{R}_x$ est la matrice de covariance des signaux reçus. Etant donné que dans le cas du radar MIMO les directions utiles sont les directions des cibles, le spectre spatial de Capon présentera des pics dans les DOA des cibles.

#### C.1.2.2 MUSIC

L'algorithme MUSIC est une technique de traitement d'antennes basée sur l'orthogonalité entre le sous-espace signal et le sous-espace bruit. Le spectre spatial de MUSIC est donné par

$$P_{MUSIC}(\theta) = \frac{1}{\mathbf{a}_r^T(\theta)\mathbf{U}_n\mathbf{U}_n^H\mathbf{a}_r^*(\theta)}, \tag{C.10}$$

où $\mathbf{U}_n$ est une matrice contenant les vecteurs propres du sous-espace bruit. Etant donné que le vecteur directionnel $\mathbf{a}_r(\theta)$ est orthogonal aux vecteurs propres du sous-espace bruit, le spectre spatial de MUSIC présentera des pics dans les directions des cibles.

#### C.1.2.3 GLRT

Le test du rapport de vraisemblance généralisé ou GLRT (Generalized Likelihood Ratio Test) a été proposé dans [32] pour l'estimation de DOA dans le contexte du radar MIMO bande étroite. Le rapport de vraisemblance se fait sous deux hypothèses, la première en supposant l'absence de cible dans la direction $\theta$ ($\beta = 0$), et la deuxième en supposant qu'une cible est bien présente dans la direction $\theta$. Le GLRT est alors défini comme

$$\rho(\theta) = 1 - \left[\frac{\max_{\mathbf{R}_z} f(\mathbf{X}|\beta = 0, \mathbf{R}_z)}{\max_{\beta,\mathbf{R}_z} f(\mathbf{X}|\beta, \mathbf{R}_z)}\right]^{\frac{1}{N}}, \tag{C.11}$$

où $\mathbf{R}_z$ est la matrice de covariance du bruit et $f(\mathbf{X}|\beta, \mathbf{R}_z)$ est la densité de probabilité des signaux reçus connaissant $\beta$ et $\mathbf{R}_z$.

En supposant que les colonnes du terme de bruit $\mathbf{Z}$ sont des vecteurs indépendants et identiquement distribués, Gaussiens, complexes, circulairement symétriques, de moyenne nulle, et tous de même matrice de covariance, le GLRT est donné par [32]

$$\rho(\theta) = 1 - \frac{\mathbf{a}_r^T(\theta)\hat{\mathbf{R}}_x^{-1}\mathbf{a}_r^*(\theta)}{\mathbf{a}_r^T(\theta)\hat{\mathbf{Q}}^{-1}\mathbf{a}_r^*(\theta)}, \tag{C.12}$$

où

$$\hat{\mathbf{Q}} = \hat{\mathbf{R}}_x - \frac{\hat{\mathbf{R}}_{xc}\mathbf{a}_t(\theta)\mathbf{a}_t^H(\theta)\hat{\mathbf{R}}_{xc}^H}{\mathbf{a}_t^H(\theta)\hat{\mathbf{R}}_c\mathbf{a}_t(\theta)}, \tag{C.13}$$

$\hat{\mathbf{R}}_c$ est une estimée de la matrice de covariance des signaux émis et $\hat{\mathbf{R}}_{xc}$ est une estimée de la matrice covariance croisée entre les signaux reçus et les signaux émis.

De façon similaire aux spectres de Capon et de MUSIC, le spectre spatial du GLRT présentera des pics dans les directions des cibles.

### C.1.3 Simulations bande étroite

On considère un radar MIMO dont les réseaux d'émission et de réception sont deux antennes linéaires uniformes (ULA) colocalisées de $L_t = L_r = L = 10$ éléments. La fréquence porteuse est $f_c = 5.8$ GHz et l'espacement entre les éléments des réseaux est $d_t = d_r = d = \lambda/2$. Les signaux émis $\{c_i(n)\}_{i=0}^{L_t-1}$ sont des séquences indépendantes de $N = 512$ symboles QPSK et le bruit additif est blanc Gaussien.

#### C.1.3.1 Détection dans la région d'ondes planes

On considère $K = 3$ cibles situées à $\theta_1 = -60°$, $\theta_2 = 0°$ et $\theta_3 = 40°$, avec des coefficients de réflexion $\beta_1 = \beta_2 = \beta_3 = 1$. On considère également la présence d'un brouilleur situé à 20° émettant un signal QPSK d'une puissance de 70 dB au-dessus de celle des signaux émis. La figure C.2 montre les spectres spatiaux de Capon, MUSIC et GLRT obtenus dans le cas d'un rapport signal sur bruit (SNR) de 10 dB (voir la définition du SNR dans la section 2.3). On peut constater que les trois spectres spatiaux présentent bien des pics dans les directions des cibles ; le spectre de MUSIC présente les lobes les plus étroits, suivi par Capon, tandis que le spectre du GLRT présente les lobes les plus larges. D'autre part, on peut voir qu'un pic important est présent dans les spectres de Capon et MUSIC autour de 20°, ce qui correspond à la position du brouilleur et qui pourrait donner lieu à la détection d'une fausse cible. Le GLRT, en revanche, rejette totalement

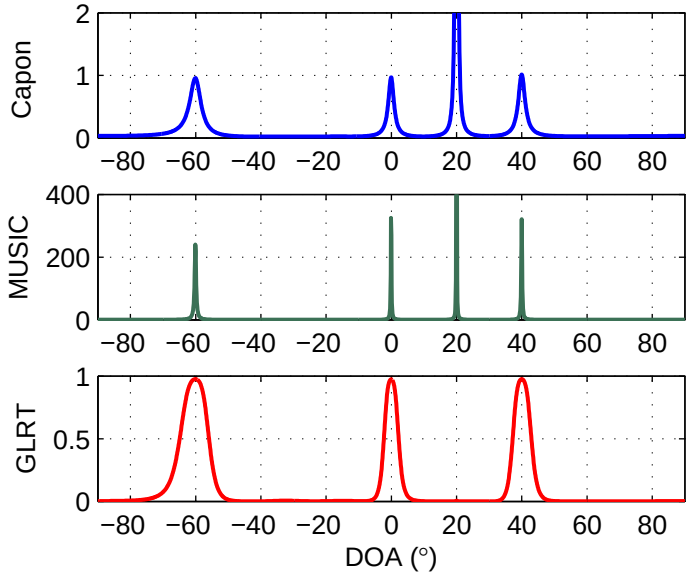


FIGURE C.2: spectres spatiaux de Capon, MUSIC et GLRT en présence d'un brouilleur à 20°.

le brouilleur et le spectre associé ne présente que les lobes correspondants aux cibles. L'intérêt d'utiliser le GLRT réside alors dans sa robustesse face aux interférences qui sont décorrélées des signaux émis.

#### C.1.3.2 Détection dans la région d'ondes sphériques

On considère $K = 3$ cibles situées à $[\theta_1, R_1] = [-65°, 0.35 \text{ m}]$, $[\theta_2, R_2] = [5°, 0.45 \text{ m}]$ et $[\theta_3, R_3] = [45°, 0.55 \text{ m}]$, avec des coefficients de réflexion $\beta_1 = \beta_2 = \beta_3 = \beta = 1$. Les spectres spatiaux de Capon, MUSIC et GLRT obtenus après un traitement d'ondes sphériques et dans le cas d'un SNR de 10 dB sont présentés figure C.3. On peut voir que le spectre de MUSIC présente des lobes très étroits permettant d'estimer les paramètres $\theta_k$ et $R_k$ des cibles. Le spectre du GLRT, quant à lui, présente des lobes qui sont beaucoup plus larges mais qui permettent de trouver numériquement des maxima proches des positions $[\theta_k, R_k]$ des cibles. En revanche, le spectre de Capon présente des lobes qui ne cessent de croître radialement et qui ne permettent pas l'estimation des paramètres $R_k$ des cibles mais seulement leur DOA.

#### C.1.3.3 Limite entre les régions d'ondes sphériques et d'ondes planes

Le traitement d'ondes sphériques permet, en utilisant MUSIC et/ou GLRT, la localisation de cibles en $R$ et en $\theta$. Cependant, ce traitement est beaucoup plus lourd que celui d'ondes planes car une recherche exhaustive doit être effectuée en $R$ et en $\theta$. Ce traitement est d'autant plus lourd que la distance entre les cibles et les antennes augmente car la zone de recherche doit également être augmentée. La question est alors de déterminer quand une cible se trouve dans la région d'ondes sphériques ou dans la région d'ondes planes.

Pour évaluer la limite entre les régions d'ondes sphériques et d'ondes planes, on considère une cible située à $\theta_1 = 60°$, à une distance allant de 0.2 m à 10 m par pas de 0.05 m. Pour chaque distance, l'erreur quadratique moyenne (MSE : Mean Square Error) de la DOA estimée est calculée en effectuant 100 essais de Monte Carlo. Le modèle du signal simulé correspond au cas d'ondes sphériques (C.1) mais les spectres de Capon, MUSIC et GLRT sont calculés en utilisant les vecteurs directionnels d'ondes planes $\mathbf{a}_t(\theta)$ et $\mathbf{a}_r(\theta)$.

Les MSE calculées pour trois SNR différents ($-10$, 0 et 10 dB) sont montrées figure C.4. On peut voir que les MSE ont des fortes valeurs pour des faibles distances $R$, puis décroissent pour se stabiliser à partir d'une certaine distance, ce qui signifie que l'approximation d'ondes planes n'introduit plus aucune erreur dans l'estimation des DOA. On constate que la condition de champ lointain $R > 2\Delta^2/\lambda$ (où $\Delta$ est la plus

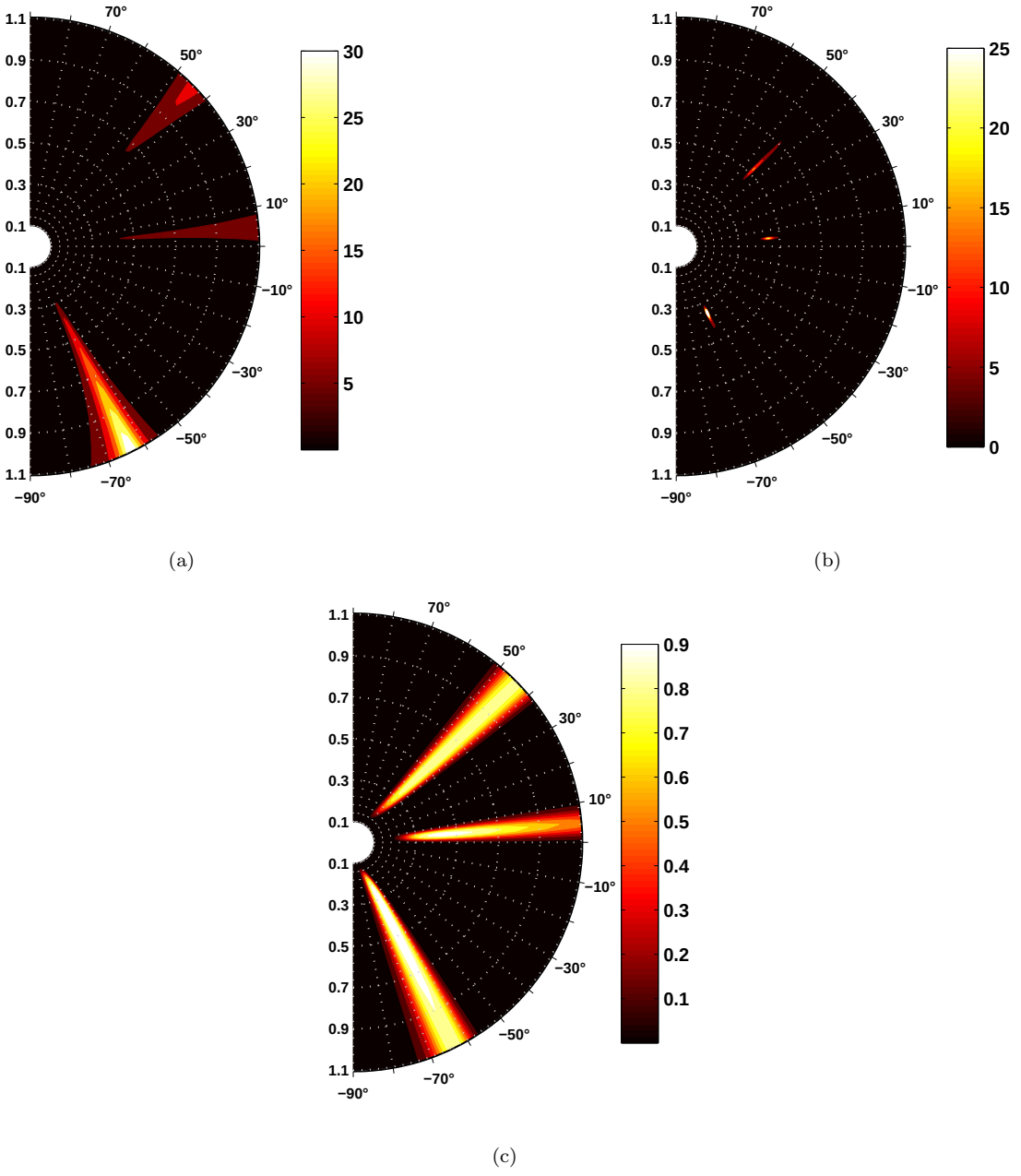


(a) (b)

(c)

FIGURE C.3: spectres de (a) Capon, (b) MUSIC et (c) GLRT (cibles situées dans la région d'ondes sphériques à $[\theta_1, R_1] = [-65°, 0.35 \text{ m}]$, $[\theta_2, R_2] = [5°, 0.45 \text{ m}]$ et $[\theta_3, R_3] = [45°, 0.55 \text{ m}]$).

grande dimension de l'antenne) est valable en tant que condition d'ondes planes pour des faibles SNR ($-10$ dB par exemple), mais cette condition n'est pas valable pour des SNR plus importants (10 dB par exemple). A partir des résultats de simulation, nous avons établi que la condition d'ondes planes $R > 5\Delta^2/\lambda$ est valable pour les trois SNR utilisés et pour les trois techniques de détection étudiées : Capon, MUSIC et GLRT.

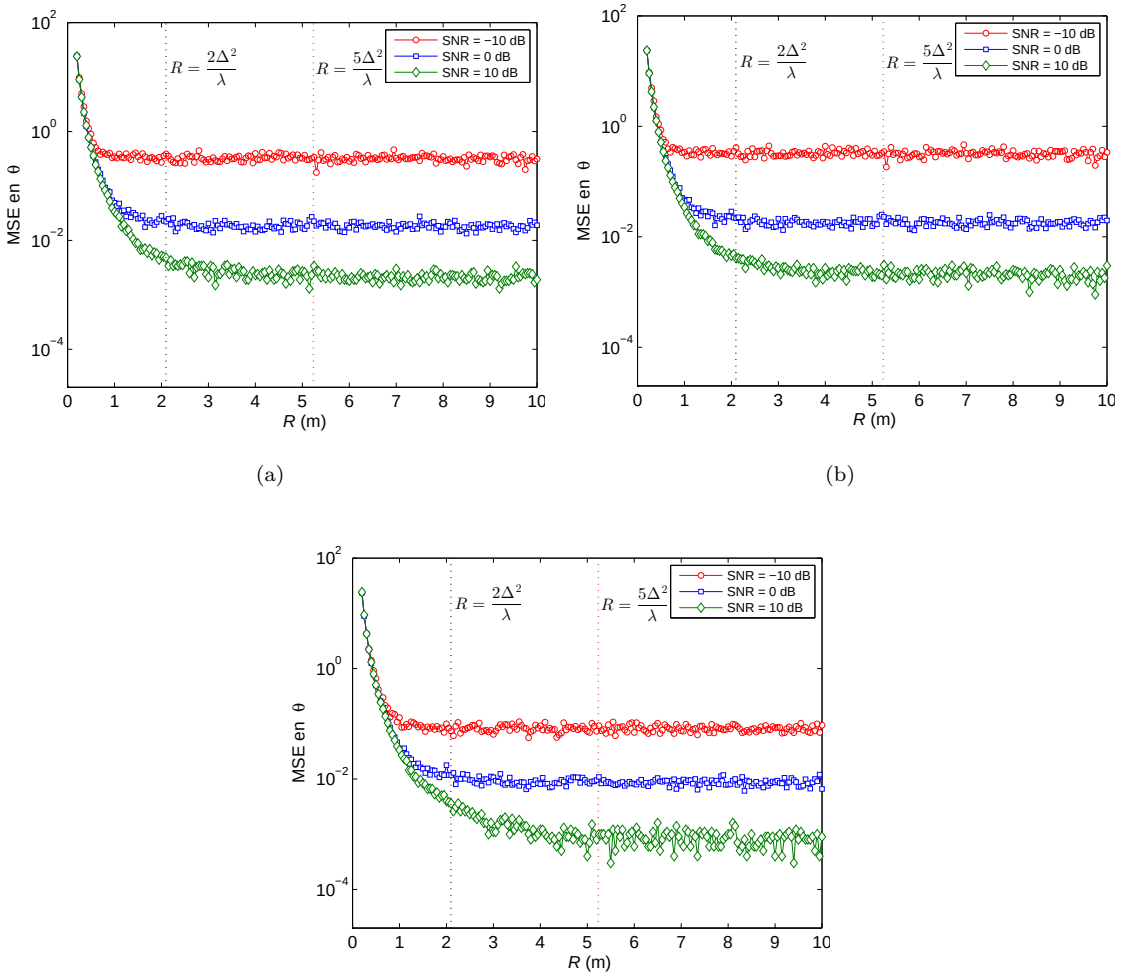


(a) (b)

(c)

FIGURE C.4: MSE en $\theta$ de la DOA estimée par (a) Capon, (b) MUSIC et (c) GLRT, pour différents SNR (traitement d'ondes planes).

## C.2 Radar MIMO large bande

### C.2.1 Modèle du signal

Dans la région d'ondes planes, le modèle du signal large bande s'écrit à fréquence discrète (voir chapitre 3)

$$\mathbf{X}(p) \approx \sum_{k=1}^{K} \beta_k \mathbf{a}_r^*(\theta_k, p)\mathbf{a}_t^H(\theta_k, p)\mathbf{C}(p) + \mathbf{Z}(p) \qquad p = 0, \ldots, N-1, \tag{C.14}$$

où

$$\mathbf{a}_t(\theta_k, p) = \left[ e^{j2\pi(f_c+f_p)(\frac{L_t-1}{2}-i)\frac{d_t \sin\theta_k}{v}} \right]_{i=0,\ldots,L_t-1} \tag{C.15}$$

et

$$\mathbf{a}_r\left(\theta_k, p\right) = \left[e^{j2\pi(f_c+f_p)(\frac{L_r-1}{2}-l)\frac{d_r \sin\theta_k}{v}}\right]_{l=0,\ldots,L_r-1} \tag{C.16}$$

sont les vecteurs directionnels d'ondes planes large bande, l'indice $p$ correspond à la fréquence discrète $f_p$ telle que

$$f_p = \frac{pF_s}{N} - \frac{F_s}{2}, \tag{C.17}$$

$F_s$ est la fréquence symbole, $\mathbf{X}(p) = \begin{bmatrix} X_0(p) & \cdots & X_{L_r-1}(p) \end{bmatrix}^T$, $\mathbf{C}(p) = \begin{bmatrix} C_0(p) & \cdots & C_{L_t-1}(p) \end{bmatrix}^T$ et $\mathbf{Z}(p) = \begin{bmatrix} Z_0(p) & \cdots & Z_{L_r-1}(p) \end{bmatrix}^T$ sont respectivement l'ensemble des signaux reçus, l'ensemble des signaux émis et l'ensemble des termes de bruit à la fréquence $f_p$.

### C.2.2 Techniques existantes de conception de formes d'ondes

Dans cette section, deux techniques de conception de formes d'ondes large bande existant dans la littérature sont brièvement décrites. Ces techniques nécessitent de disposer de premières estimées des DOA des cibles.

#### C.2.2.1 WBFIT (Wideband Beampattern Fromation via Iterative Techniques)

WBFIT est une technique qui permet, par une méthode itérative, la conception de formes d'ondes respectant un diagramme de rayonnement désiré et une contrainte de PAPR (Peak to Average Power Ratio) [43].

WBFIT se déroule en deux étapes : dans la première, les signaux dans le domaine fréquentiel $\{\mathbf{C}(p)\}_{p=0}^{0-1}$ sont conçus de façon à approximer un diagramme de rayonnement désiré $\delta(\theta_h, p)$; dans la deuxième étape, les signaux dans le domaine temporel $\{\mathbf{c}(n)\}_{n=0}^{N-1}$ sont calculés à partir des $\{\mathbf{C}(p)\}_{p=0}^{0-1}$ tout en respectant une contrainte de PAPR.

Les signaux à émettre $\{\mathbf{c}(n)\}_{n=0}^{N-1}$ sont alors la solution du problème d'optimisation

$$\begin{aligned} \min_{\{\mathbf{c}(n)\}} \sum_{h=1}^{H}\sum_{p=0}^{N-1} \left[\delta(\theta_h, p) - \left|\mathbf{a}_t^H(\theta_h, p)\mathbf{C}(p)\right|\right]^2 \\ \text{s.c. PAPR}\left(\{c_i(n)\}_{n=0}^{N-1}\right) \leq \varrho, \\ i = 0, \ldots, L_t - 1, \end{aligned} \tag{C.18}$$

où

$$\text{PAPR}\left(\{c_i(n)\}_{n=0}^{N-1}\right) = \frac{\max_n |c_i(n)|^2}{\frac{1}{N}\sum_{n=0}^{N-1}|c_i(n)|^2}, \tag{C.19}$$

$\varrho \geq 1$ est la limite supérieure de PAPR prédéfinie, et $\{\theta_h\}_{h=1}^{H}$ est une grille d'angles couvrant l'intervalle $[-90°, 90°]$.

#### C.2.2.2 SFBT (Spectral density Focusing Beampattern synthesis Technique)

SFBT est une technique de conception de formes d'ondes proposée dans [44], dans laquelle la puissance est envoyée directement dans les directions des cibles dans toute la bande de fréquences. Les formes d'ondes dans le domaine fréquentiel $\{\mathbf{C}(p)\}_{p=0}^{N-1}$ sont données par

$$\begin{aligned} \mathbf{C}(p) &= \sum_{k=1}^{K} \mathbf{a}_t(\hat{\theta}_k, p) e^{j\phi_k(p)} \\ p &= 0, \ldots, N-1, \end{aligned} \tag{C.20}$$

où $\{\phi_k(p)\}$ est une phase aléatoire dans l'intervalle $[0, 2\pi]$ et les $\{\hat{\theta}_k\}_{k=1}^{K}$ sont des premières estimées des DOA des cibles.

Les signaux à émettre dans le domaine temporel $\{c_i(n)\}_{n=0}^{N-1}$ $(i = 0, \ldots, L_t - 1)$ sont trouvés en calculant les transformées de Fourier discrètes inverses (IDFT) des $\{C_i(p)\}_{p=0}^{N-1}$.

#### C.2.2.3 Comparaison entre WBFIT et SFBT

Pour comparer WBFIT avec SFBT on considère qu'on dispose d'une première estimée $\hat{\theta}_1 = 40°$ de la DOA d'une cible $(K = 1)$ située dans la région d'ondes planes. WBFIT et SFBT sont alors utilisés pour synthétiser des ensembles de signaux $\{\mathbf{c}(n)\}_{n=0}^{N-1}$ tels que la puissance soit directement émise vers la cible. Pour WBFIT, on se fixe une limite de PAPR $\varrho = 2$ et un diagramme de rayonnement désiré

$$\begin{aligned} \delta(\theta, p) &= \begin{cases} 1, & \theta = \hat{\theta} \\ 0, & \text{ailleurs} \end{cases} \\ p &= 0, \ldots, N-1. \end{aligned} \tag{C.21}$$

Les diagrammes de rayonnement synthétisés par WBFIT et SFBT sont montrés figures C.5 et C.6 respectivement. On peut constater que dans les deux diagrammes de rayonnement, un maximum de puissance est bien émis dans la direction de la cible dans toute la bande de fréquence. Les diagrammes de WBFIT et de SFBT sont très similaires, cependant, le lobe du diagramme de SFBT est un peu plus large que celui de WBFIT pour les basses fréquences.

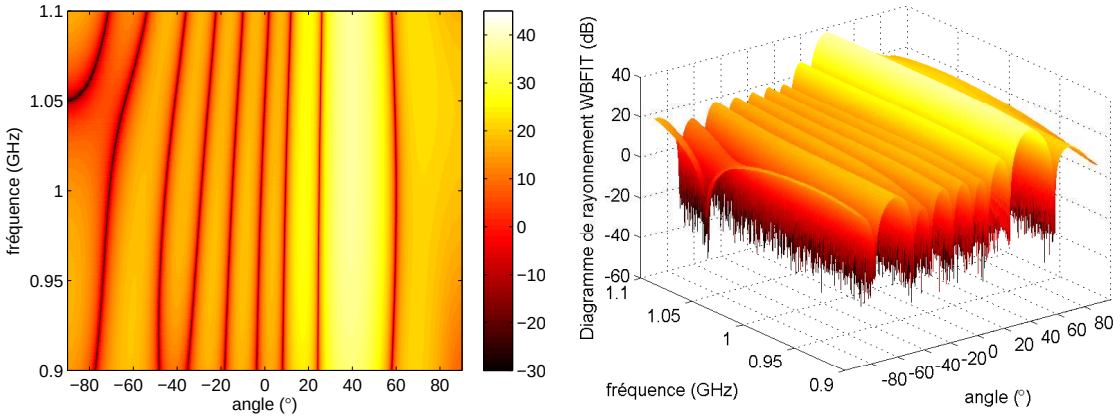


(a) (b)

FIGURE C.5: diagramme de rayonnement WBFIT en dB avec $\varrho = 2$, $F_s = f_c/5 = 200$ MHz (1 cible à $\hat{\theta} = 40°$). (a) Tracé en 2D, (b) tracé en 3D.

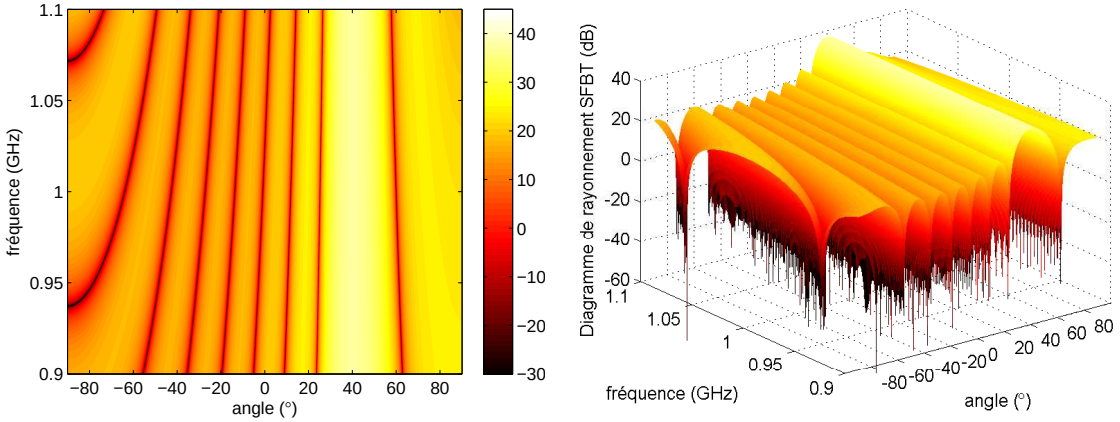


(a) (b)

FIGURE C.6: diagramme de rayonnement SFBT en dB avec $F_s = f_c/5 = 200$ MHz (1 cible à $\hat{\theta} = 40°$). (a) Tracé en 2D, (b) tracé en 3D.

Néanmoins, les signaux synthétisés par ces deux techniques présentent de grandes différences en termes de PAPR, comme on peut le voir dans la figure C.7, qui montre le PAPR de chaque signal émis. En effet, les signaux synthétisés par WBFIT respectent parfaitement la limite de PAPR $\varrho = 2$ tandis que les signaux synthétisés par SFBT ont des valeurs de PAPR qui sont relativement élevées et non maîtrisées. Une autre grande différence entre WBFIT et SFBT réside dans le temps de calcul nécessaire pour ces techniques : dans toutes les simulations réalisées, SFBT a été au moins 2000 fois plus rapide que WBFIT.

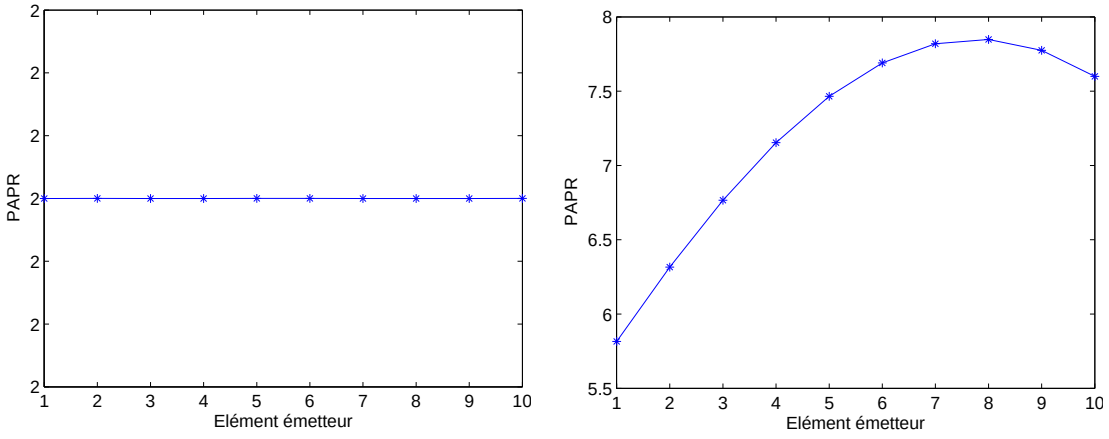


(a) (b)

FIGURE C.7: PAPR de chaque $\{c_i(n)\}_{n=0}^{N-1}$ synthétisé par (a) WBFIT ($\varrho = 2$) et (b) SFBT.

### C.2.3 Proposition d'une nouvelle technique de conception de formes d'ondes : M-SFBT

En nous inspirant des deux techniques précédentes, WBFIT et SFBT, nous avons proposé une nouvelle technique de conception de formes d'ondes que nous avons appelée Multiband Spectral density Focusing Beampattern synthesis Technique (M-SFBT). Cette technique permet d'envoyer la puissance dans les directions des cibles dans des bandes de fréquences distinctes, de façon à décorréler les signaux réfléchis par les cibles. Les formes d'ondes dans le domaine fréquentiel $\{\mathbf{C}(p)\}_{p=0}^{N-1}$ sont données par

$$\begin{aligned} \mathbf{C}(p) &= \sum_{k=1}^{K} \mathbf{a}_t(\hat{\theta}_k, p)\delta_k(p)e^{j\phi_k(p)} \\ & p = 0, \ldots, N-1, \end{aligned} \tag{C.22}$$

où $\delta_k(p)$ désigne l'allocation de puissance désirée en fonction de la fréquence. Les signaux dans le domaine temporel $\{\mathbf{c}(n)\}_{n=0}^{N-1}$ sont alors trouvés en calculant la IDFT de $\{\mathbf{C}(p)\}_{p=0}^{N-1}$.

Comme on l'a vu précédemment, le PAPR des signaux issus de SBFT n'est pas maîtrisé, c'est pourquoi nous avons décidé d'ajouter une contrainte de PAPR. Il s'agit de trouver les signaux $\{\mathbf{c}'(n)\}_{n=0}^{N-1}$ qui s'approchent le plus des signaux $\{\mathbf{c}(n)\}_{n=0}^{N-1}$ tout en ayant un PAPR inférieur ou égal à une constante $\varrho$. Les signaux $\{\mathbf{c}'(n)\}_{n=0}^{N-1}$ sont la solution du

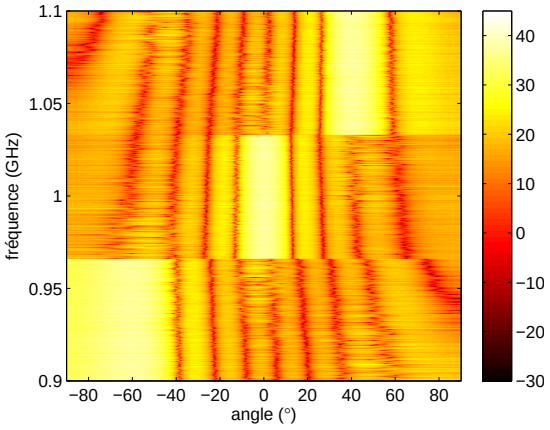


FIGURE C.8: diagramme de rayonnement M-SFBT en dB avec $\varrho = 2$, $F_s = f_c/5 = 200$ MHz ($\hat{\theta}_1 = -60°$, $\hat{\theta}_2 = 0°$, $\hat{\theta}_3 = 40°$).

problème

$$\begin{aligned} &\min_{\{c_i'(n)\}_{n=0}^{N-1}} \left\| c_i'(n) - c_i(n) \right\|^2 \\ &\text{s.c. PAPR}\left( \{c_i'(n)\}_{n=0}^{N-1} \right) \leq \varrho \\ &i = 0, \ldots, L_t - 1. \end{aligned} \tag{C.23}$$

Un exemple de diagramme de rayonnement synthétisé par M-SFBT est présenté figure C.8. Dans ce cas, nous avons décidé d'envoyer la puissance dans les directions de $K = 3$ cibles dont les premières estimées sont $\hat{\theta}_1 = -60°$, $\hat{\theta}_2 = 0°$ et $\hat{\theta}_3 = 40°$, tout en utilisant des bandes de fréquence distinctes suivant l'allocation de puissance désirée

$$\begin{aligned} \delta_k(p) = \begin{cases} 1 & \text{pour } (k-1)\left\lfloor \frac{N}{K} \right\rfloor \leq p \leq k \left\lfloor \frac{N}{K} \right\rfloor - 1 \\ 0 & \text{ailleurs} \end{cases} \\ p = 0, \ldots, N-1 \\ k = 1, \ldots, K, \end{aligned} \tag{C.24}$$

et respectant une limite de PAPR $\varrho = 2$. On peut voir que la puissance est bien envoyée dans les directions des cibles dans des bandes distinctes conformément à l'allocation $\delta_k(p)$. De plus, les signaux synthétisés respectent parfaitement la limite de PAPR $\varrho = 2$ comme le montre la figure C.9.

### C.2.4 Techniques d'estimation de DOA large bande

Dans cette section, nous présentons l'adaptation des techniques d'estimation de DOA bande étroite (Capon, MUSIC et GLRT) au cas large bande, ainsi que l'adaptation d'une technique de traitement d'antennes large bande (TOPS) au contexte du radar MIMO large bande.

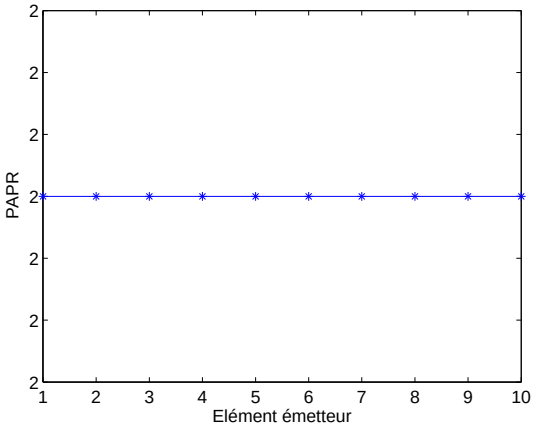


FIGURE C.9: PAPR de chaque $\{c_i(n)\}_{n=0}^{N-1}$ synthétisé par M-SFBT avec $\varrho = 2$.

#### C.2.4.1 Adaptation des techniques d'estimation de DOA bande étroite au cas large bande (méthodes incohérentes)

Etant donné que notre modèle du signal large bande (C.14) est un modèle à fréquence discrète, il est possible d'appliquer les techniques bande étroite Capon, MUSIC et GLRT, à chaque fréquence $f_p$. La question est de savoir combiner convenablement les résultats obtenus à des fréquences distinctes, de façon à obtenir un spectre spatial général permettant de localiser les cibles. Une méthode simple consiste à calculer une moyenne des résultats obtenus sur l'ensemble des fréquences. Ces techniques sont appelées méthodes incohérentes.

Ainsi, le spectre général de Capon $\bar{P}_{cap}(\theta)$ est obtenu en calculant la moyenne arithmétique des spectres obtenus à chaque fréquence

$$\bar{P}_{cap}(\theta) = \frac{1}{N} \sum_{p=0}^{N-1} P_{cap}(\theta, f_p), \tag{C.25}$$

où $P_{cap}(\theta, f_p)$ est le spectre de Capon obtenu à la fréquence $f_p$.

Quant à MUSIC, la moyenne est plutôt effectuée sur le test d'orthogonalité entre les sous-espaces signal et les sous-espaces bruit. Le spectre général de MUSIC est alors donné par

$$\bar{P}_{MUSIC}(\theta) = \frac{1}{\sum_{p=0}^{N-1} \mathbf{a}_r^T(\theta, p)\mathbf{U}_n(f_p)\mathbf{U}_n^H(f_p)\mathbf{a}_r^*(\theta, p)}, \tag{C.26}$$

où $\mathbf{U}_n(f_p)$ est une matrice contenant les vecteurs propres du sous-espace bruit à la fréquence $f_p$.

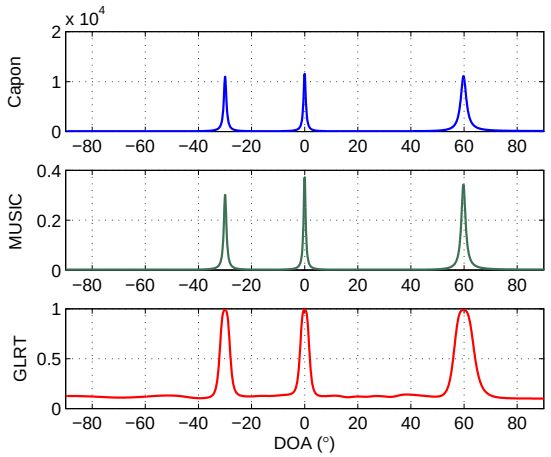


FIGURE C.10: spectres spatiaux incohérents de (a) Capon, (b) MUSIC et (c) GLRT ($\theta_1 = -30°$, $\theta_2 = 0°$, $\theta_3 = 60°$, $F_s = f_c/5 = 200$ MHz).

De façon similaire à Capon, le spectre général du GLRT $\bar{\rho}(\theta)$ est obtenu en calculant la moyenne arithmétique de l'ensemble de spectres obtenus à chaque fréquence

$$\bar{\rho}(\theta) = \frac{1}{N} \sum_{p=0}^{N-1} \rho(\theta, f_p), \tag{C.27}$$

où $\rho(\theta, f_p)$ est le spectre du GLRT obtenu à la fréquence $f_p$.

A titre d'exemple, on considère $K = 3$ cibles situées dans la région d'ondes planes à $\theta_1 = -30°$, $\theta_2 = 0°$, et $\theta_3 = 60°$, toutes avec des coefficients de réflexion égaux à 1. La détection se fait après l'émission de séquences indépendantes $\{\mathbf{c}(n)\}_{n=0}^{N-1}$ de $N = 512$ symboles QPSK, avec pour fréquence symbole $F_s = f_c/5 = 200$ MHz. Les spectres généraux de Capon, MUSIC et GLRT sont montrés figure C.10. On peut voir que les spectres incohérents sont très similaires aux spectres bande étroite et qu'il est bien possible d'estimer les DOA des cibles tout en utilisant des signaux large bande. Ces techniques fonctionnent bien lorsque le SNR est constant dans toute la bande de travail, en revanche, si le SNR est variable, les résultats obtenus à certaines fréquences pourraient être très mauvais ce qui donnerait également de mauvaises moyennes.

#### C.2.4.2 Proposition d'une adaptation de TOPS au contexte du radar MIMO large bande : M-TOPS

Le test d'orthogonalité de sous-espaces projetés (TOPS) est une technique de traitement d'antennes qui a été développée pour estimer les DOA de sources large bande non corrélées. Dans cette technique, la matrice de covariance $\hat{\mathbf{R}}_x(f_p)$ estimée à chaque fréquence est décomposée en un sous-espace signal $\mathbf{U}_s(f_p)$ et un sous-espace bruit $\mathbf{U}_n(f_p)$.

Le sous-espace signal $\mathbf{U}_s(f_{ref})$ à la fréquence de référence $f_{ref}$ est ramené à chaque fréquence $f_p$ en utilisant une matrice de transformation $\mathbf{\Phi}(\Delta f_p, \theta)$ :

$$\mathbf{\Phi}(\Delta f_p, \theta) = \text{diag}\left(\left[e^{j2\pi(f_c+\Delta f_p)(\frac{L_r-1}{2}-l)\frac{d_r \sin\theta}{v}}\right]_{l=0,\ldots,L_r-1}\right), \tag{C.28}$$

où

$$\Delta f_p = f_p - f_{ref}. \tag{C.29}$$

Les sous-espaces signal transformés $\mathbf{F}_s(f_p)$ sont alors donnés par

$$\begin{aligned} \mathbf{F}_s(f_p) &= \mathbf{\Phi}(\Delta f_p, \theta)\mathbf{U}_s(f_{ref}) \\ p &= 0, \ldots, N-1. \end{aligned} \tag{C.30}$$

Les sous-espaces signal transformés sont ensuite projetés dans l'espace vectoriel engendré par les $\mathbf{a}_r(\theta, p)$ en utilisant une matrice de projection $\mathbf{P}(\theta, f_p)$, de façon à éliminer quelques termes d'erreur introduits dans l'estimation des matrices de covariance. Les sous-espaces projetés sont donnés par

$$\begin{aligned} \mathbf{F}'_s(\theta, f_p) &= \mathbf{P}(\theta, f_p)\mathbf{F}_s(f_p) \\ p &= 0, \ldots, N-1, \end{aligned} \tag{C.31}$$

où

$$\mathbf{P}(\theta, f_p) = \mathbf{I} - \left(\mathbf{a}_r^T(\theta, p)\mathbf{a}_r^*(\theta, p)\right)^{-1}\mathbf{a}_r^*(\theta, p)\mathbf{a}_r^T(\theta, p). \tag{C.32}$$

Finalement, un test d'orthogonalité entre les sous-espaces bruit et les sous-espaces signal projetés est effectué pour tous les angles $\theta$ dans une grille $[-90°, 90°]$. Le test d'orthogonalité se fait en définissant une matrice $\mathbf{D}(\theta)$

$$\mathbf{D}(\theta) = \left[\mathbf{F}_s'^H(\theta, f_0)\mathbf{U}_n(f_0) \quad \cdots \quad \mathbf{F}_s'^H(\theta, f_{N-1})\mathbf{U}_n(f_{N-1})\right]. \tag{C.33}$$

Il faut noter que lorsque l'angle $\theta$ correspondra à la DOA d'une cible, la matrice $\mathbf{D}(\theta)$ présentera une déficience de rang. On peut alors obtenir le spectre spatial de TOPS en calculant

$$P_{\text{TOPS}}(\theta) = \frac{1}{\sigma_{\min}(\theta)}, \tag{C.34}$$

où $\sigma_{\min}(\theta)$ désigne la plus petite valeur singulière de $\mathbf{D}(\theta)$.

A titre d'exemple, on considère $K = 3$ cibles situées dans la région d'ondes planes à $\theta_1 = -30°$, $\theta_2 = 0°$ et $\theta_3 = 60°$, toutes avec des coefficients de réflexion égaux à 1. La détection se fait après l'émission de séquences indépendantes $\{\mathbf{c}(n)\}_{n=0}^{N-1}$ de $N = 512$ symboles QPSK, avec pour fréquence symbole $F_s = f_c/5 = 200$ MHz. La figure C.11

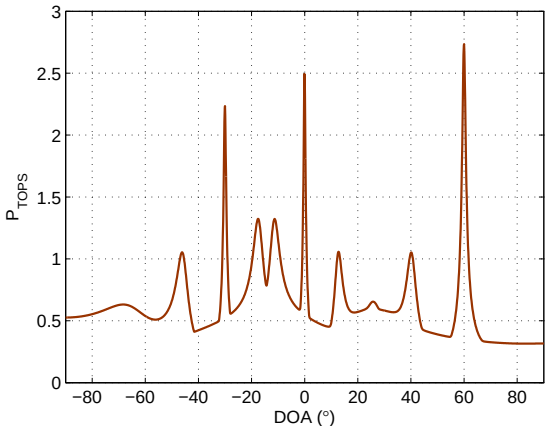


FIGURE C.11: spectre de TOPS après utilisation d'un diagramme de rayonnement omnidirectionnel ($\theta_1 = -30°$, $\theta_2 = 0°$, $\theta_3 = 60°$, $F_s = f_c/5 = 200$ MHz).

montre le spectre de TOPS obtenu en calculant (C.34). On peut voir que le spectre présente les trois pics correspondants aux cibles, cependant, plusieurs pics parasites apparaissent dans d'autres directions, ce qui pourrait donner lieu à la détection de fausses cibles. Ce problème vient du caractère corrélé des signaux réfléchis par les cibles alors que TOPS a été développé pour la détection de sources non corrélées.

Nous avons proposé une adaptation de TOPS au contexte du radar MIMO large bande. La méthode choisie consiste à allouer une bande de fréquences distincte à chaque cible en utilisant M-SFBT, de façon à décorréler les signaux réfléchis. TOPS est alors appliqué dans chaque sous-bande : le sous-espace signal $\mathbf{U}_s(f_{ck})$ à la fréquence centrale de chaque sous-bande $f_{ck}$ est ramené aux autres fréquences de la même sous-bande selon la transformation

$$\begin{aligned} \mathbf{F}_{s_k}(f_p) &= \mathbf{\Phi}(\Delta f_{p_k}, \theta)\mathbf{U}_s(f_{ck}) \\ p &= 0, \ldots, N-1, \end{aligned} \tag{C.35}$$

où

$$\Delta f_{p_k} = f_p - f_{ck}. \tag{C.36}$$

Les sous-espaces signal projetés de chaque sous-bande sont alors donnés par

$$\begin{aligned} \mathbf{F}'_{s_k}(\theta, f_p) &= \mathbf{P}(\theta, f_p)\mathbf{F}_{s_k}(f_p) \\ p &= 0, \ldots, N-1. \end{aligned} \tag{C.37}$$

Un test d'orthogonalité est ensuite effectué dans chaque sous-bande en définissant des matrices $\mathbf{D}_k(\theta)$ :

$$\mathbf{D}_k(\theta) = \left[\mathbf{F}'^H_{s_k}(\theta, f_0)\mathbf{U}_n(f_0) \quad \cdots \quad \mathbf{F}'^H_{s_k}(\theta, f_{N-1})\mathbf{U}_n(f_{N-1})\right]. \tag{C.38}$$

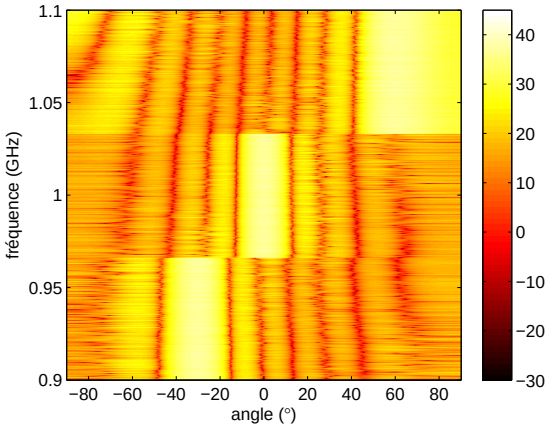


FIGURE C.12: diagramme de rayonnement M-SFBT en dB avec $\varrho = 2$, $F_s = f_c/5 = 200$ MHz ($\theta_1 = -30°$, $\theta_2 = 0°$ et $\theta_3 = 60°$).

A noter que chaque matrice $\mathbf{D}_k(\theta)$ aura une déficience de rang quand $\theta$ correspondra à la DOA d'une cible. Les DOA des cibles peuvent alors être estimées en cherchant les maxima du spectre de M-TOPS

$$P_{M-TOPS}(\theta) = \max \left\{ \frac{1}{\sigma_k(\theta)} \right\}_{k=1}^{K}, \tag{C.39}$$

où $\sigma_k(\theta)$ est la plus petite valeur singulière de $\mathbf{D}_k(\theta)$.

A titre d'exemple, on considère $K = 3$ cibles situées dans la région d'ondes planes à $\theta_1 = -30°$, $\theta_2 = 0°$ et $\theta_3 = 60°$, toutes avec des coefficients de réflexion égaux à 1. Les signaux émis sont synthétisés par M-SFBT à partir des premières estimées obtenues en utilisant la technique GLRT incohérente (après l'émission de symboles QPSK indépendants). Une bande de fréquence distincte est allouée à chaque cible comme le montre la figure C.12 et la limite de PAPR est fixée à $\varrho = 2$.

La figure C.13 montre le spectre spatial M-TOPS obtenu en calculant (C.39). On peut voir que tous les pics parasites ont totalement disparu et que seuls les pics correspondant aux cibles sont présents, car les signaux réfléchis par les cibles sont maintenant décorrélés.

## C.3 Effets du couplage mutuel sur les performances du radar MIMO bande étroite

Les différents diagrammes de rayonnement des éléments des réseaux d'émission et de réception ont précédemment été supposés identiques, de gain unitaire et indépendants de $\theta$. Cependant, en réalité, les ondes électromagnétiques émises ou reçues par chaque

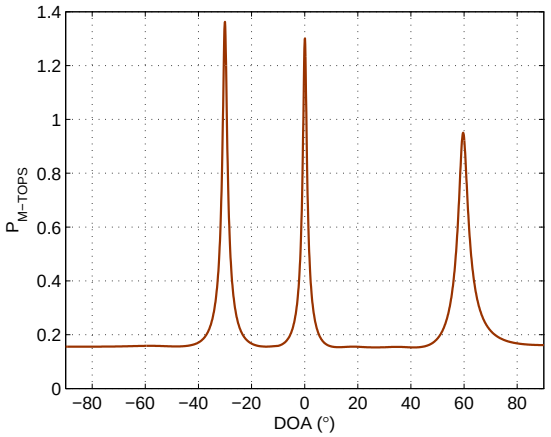


FIGURE C.13: spectre de TOPS après utilisation du diagramme de rayonnement multi-bandes généré par M-SFBT ($\theta_1 = -30°$, $\theta_2 = 0°$, $\theta_3 = 60°$, $F_s = f_c/5 = 200$ MHz).

élément interagissent avec les éléments environnants, changeant leurs caractéristiques électriques et électromagnétiques telles que leur impédance d'entrée et leur diagramme de rayonnement. Ce phénomène est connu sous le nom de couplage mutuel.

Une autre conséquence du couplage mutuel est l'existence du phénomène de "crosstalk" ou diaphonie lorsqu'une partie des signaux émis est directement transmise entre le réseau d'émission et le réseau de réception. L'existence du crosstalk dégrade fortement les performances d'estimation de DOA.

Dans cette section, nous étudions les effets du couplage mutuel sur les performances du radar MIMO bande étroite. En particulier, nous montrons comment améliorer les performances d'estimation des DOA en présence de diagrammes de rayonnement incluant le couplage entre antennes et nous proposons une technique de réduction du "crosstalk".

### C.3.1 Prise en compte des diagrammes de rayonnement

Pour observer l'influence du couplage mutuel sur les diagrammes de rayonnement de chaque élément des antennes, nous avons simulé le réseau de 6x2 éléments montré figure C.14 sous le logiciel CST Microwave Studio. Les diagrammes de rayonnements obtenus pour le réseau de réception et pour le réseau d'émission sont montrés figures C.15 et C.16 respectivement. Les résultats montrent que les diagrammes de rayonnement sont tous déformés et différents les uns des autres, en raison du couplage mutuel. Toutefois, il existe une certaine symétrie due à la géométrie du réseau d'antennes.

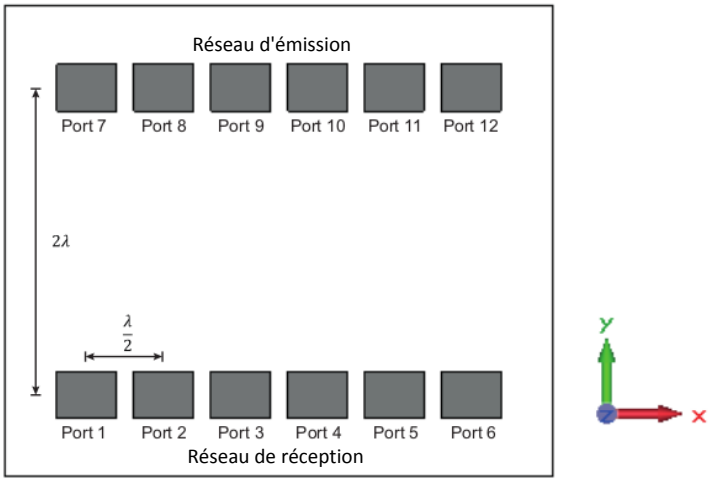


FIGURE C.14: réseaux d'émission et de réception d'antennes patch ($L = L_t = L_r = 6$).

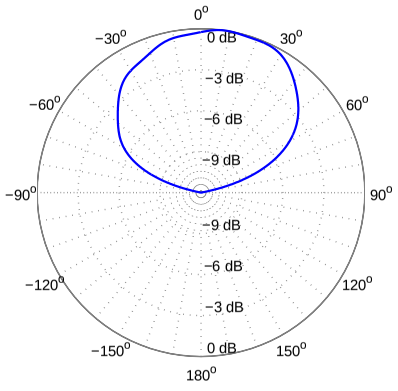


(a) Port 7

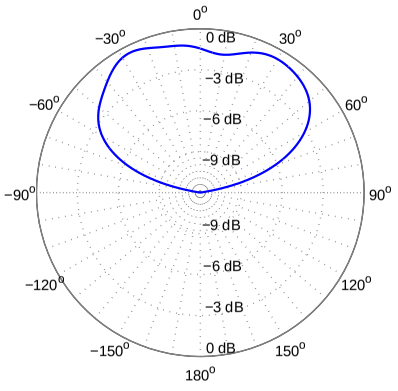


(b) Port 8

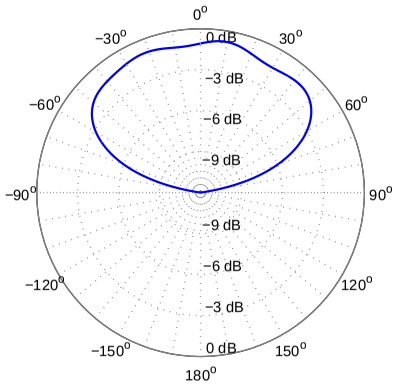


(c) Port 9

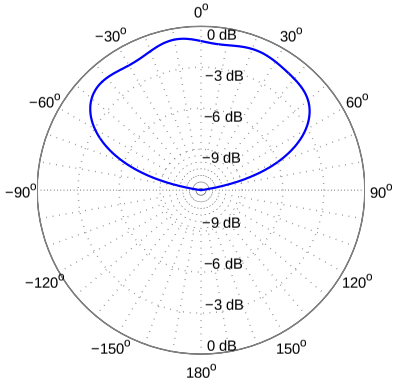


(d) Port 10

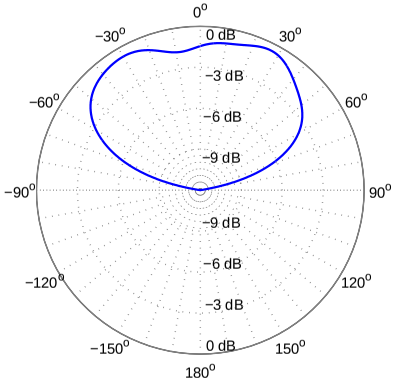


(e) Port 11

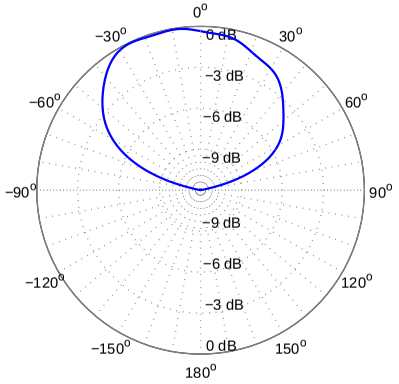


(f) Port 12

FIGURE C.15: diagrammes de rayonnement normalisés (en amplitude) des éléments récepteurs à 5.8 GHz (ports 1 à 6).

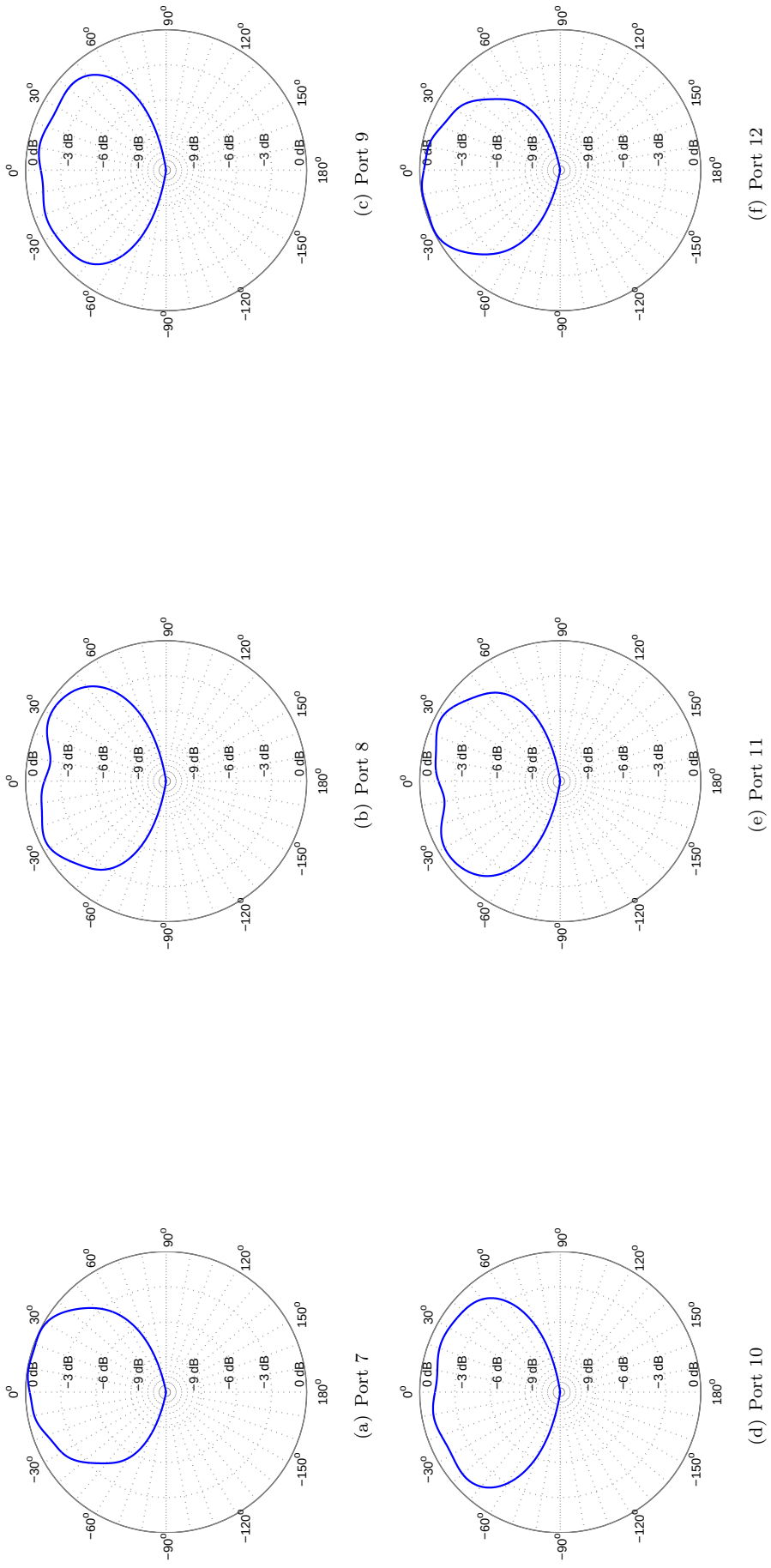


(a) Port 7 (b) Port 8 (c) Port 9

(d) Port 10 (e) Port 11 (f) Port 12

FIGURE C.16: diagrammes de rayonnement normalisés (en amplitude) des éléments émetteurs à 5.8 GHz (ports 7 à 12).

Il paraît maintenant évident que les vecteurs directionnels classiques $\mathbf{a}_t(\theta)$ et $\mathbf{a}_r(\theta)$, faisant abstraction des diagrammes de rayonnement, ne devraient pas être utilisés. Le traitement devrait alors se faire en utilisant les vecteurs directionnels généraux

$$\tilde{\mathbf{a}}_t(\theta) = \left[ g_{t,i}^*(\theta) e^{j\frac{2\pi}{\lambda}(\frac{L_t-1}{2}-i)d_t \sin\theta} \right]_{i=0,\dots,L_t-1} \tag{C.40}$$

et

$$\tilde{\mathbf{a}}_r(\theta) = \left[ g_{r,l}^*(\theta) e^{j\frac{2\pi}{\lambda}(\frac{L_r-1}{2}-l)d_r \sin\theta} \right]_{l=0,\dots,L_r-1} \tag{C.41}$$

qui eux prennent bien en compte les différents diagrammes de rayonnement.

Pour observer l'influence des diagrammes de rayonnement sur la détection, considérons $K = 3$ cibles situées dans la région d'ondes planes à $\theta_1 = -40°$, $\theta_2 = -5°$ et $\theta_3 = 5°$ avec des coefficients de réflexion $\beta_1 = \beta_2 = \beta_3 = \beta = 1$. Le modèle du signal simulé

$$\mathbf{x}(n) = \sum_{k=1}^{K} \beta_k \tilde{\mathbf{a}}_r^*(\theta_k) \tilde{\mathbf{a}}_t^H(\theta_k) \mathbf{c}(n) + \mathbf{z}(n), \tag{C.42}$$

utilise les vecteurs directionnels généraux.

La figure C.17 montre les spectres spatiaux de Capon, MUSIC et GLRT obtenus en utilisant les vecteurs directionnels classiques $\mathbf{a}_t(\theta)$ et $\mathbf{a}_r(\theta)$, c'est-à-dire sans prendre en compte les différents diagrammes de rayonnement. On peut voir que, dans les trois spectres, le lobe qui devrait être à $-40°$ est un peu décalé. De plus, les cibles situées à $-5°$ et $5°$ sont difficilement détectables car un seul lobe est présent.

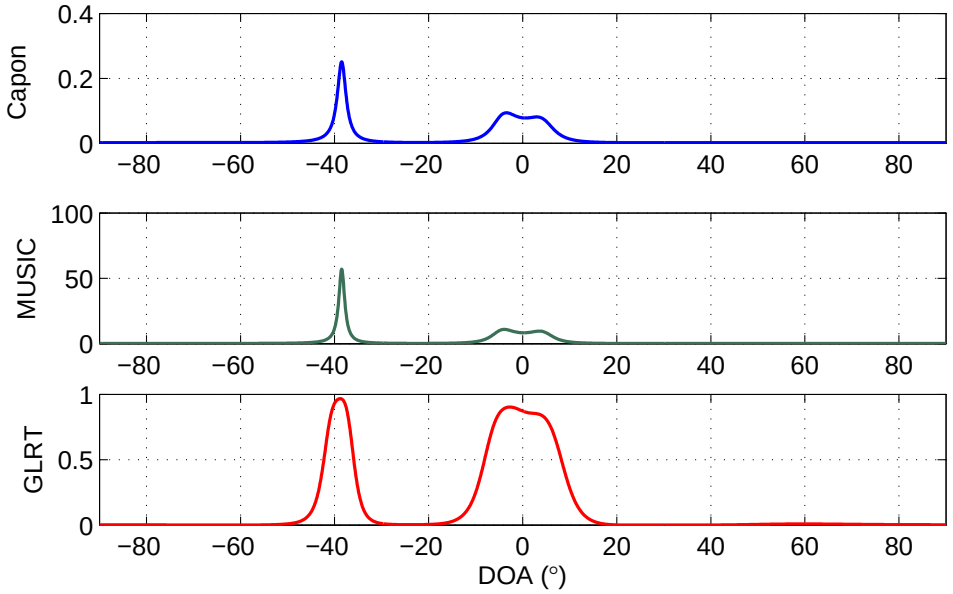


FIGURE C.17: spectres de Capon, MUSIC et GLRT dans le cas de trois cibles à $\theta_1 = -40°$, $\theta_2 = -5°$ et $\theta_3 = 5°$, sans prise en compte des diagrammes de rayonnement ($-10\log_{10}\sigma^2 = 20$).

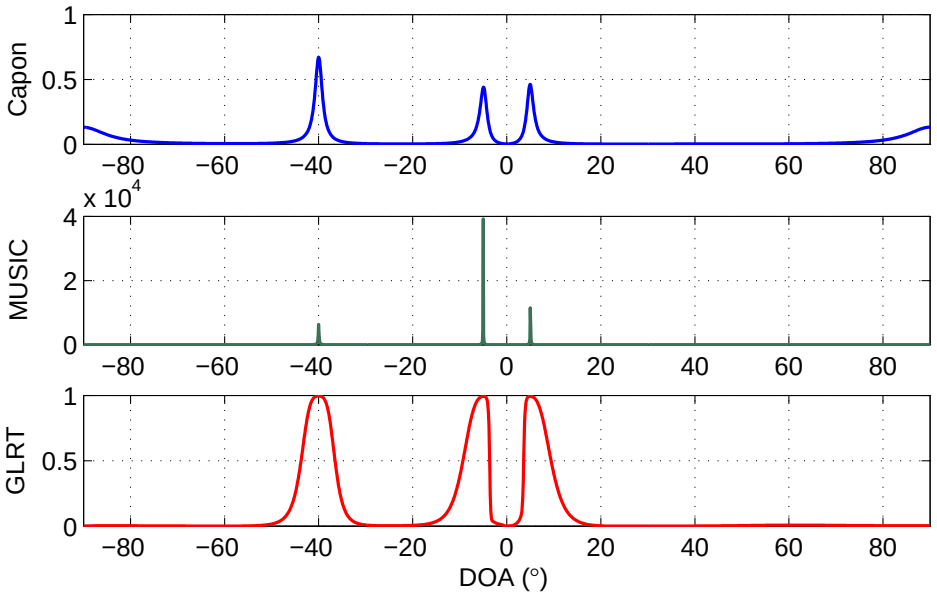


FIGURE C.18: spectres de Capon, MUSIC et GLRT dans le cas de trois cibles à $\theta_1 = -40°$, $\theta_2 = -5°$ et $\theta_3 = 5°$, avec prise en compte des diagrammes de rayonnement ($-10\log_{10}\sigma^2 = 20$).

Si maintenant on utilise les vecteurs directionnels généraux $\tilde{\mathbf{a}}_t(\theta)$ et $\tilde{\mathbf{a}}_r(\theta)$ pour recalculer les spectres de Capon, MUSIC et GLRT, on obtient les résultats montrés par la figure C.18. On voit que les lobes sont maintenant recentrés dans les directions des cibles ce qui permet une meilleure estimation des DOA par rapport au cas précédent. De plus, on obtient une nette amélioration de la résolution et les cibles à $-5°$ et $5°$ sont parfaitement détectables. Cependant, on peut voir qu'une remontée survient dans le spectre de Capon pour des angles proches de $-90°$ et $90°$ à cause de la faible amplitude des diagrammes de rayonnement à ces angles. Cette remontée est d'autant plus importante que le niveau de bruit est élevé et affecte également MUSIC (voir chapitre 4). Pour résoudre ce problème nous proposons d'utiliser les vecteurs directionnels généraux (phase uniquement)

$$\boldsymbol{\alpha}_t(\theta) = \left[e^{-j\arg\{g_{t,i}(\theta)\}} e^{j\frac{2\pi}{\lambda}\left(\frac{L_t-1}{2}-i\right)d_t\sin\theta}\right]_{i=0,\ldots,L_t-1} \tag{C.43}$$

et

$$\boldsymbol{\alpha}_r(\theta) = \left[e^{-j\arg\{g_{r,l}(\theta)\}} e^{j\frac{2\pi}{\lambda}\left(\frac{L_r-1}{2}-l\right)d_r\sin\theta}\right]_{l=0,\ldots,L_r-1}, \tag{C.44}$$

qui ne prennent en compte que la phase des diagrammes de rayonnement.

Pour évaluer l'impact des différents vecteurs directionnels sur les performances d'estimation des DOA, nous avons calculé les MSE de la DOA estimée par Capon, MUSIC et GLRT, dans le cas d'une cible unique à $-40°$ ($\beta = 1$), en effectuant 500 essais de Monte Carlo. Les MSE ont été calculées dans quatre cas différents :

- **Cas idéal** : la propagation des signaux est simulée sans inclure les diagrammes de rayonnement dans le modèle du signal $\mathbf{x}(n) = \beta \mathbf{a}_r^*(\theta_1)\mathbf{a}_t^H(\theta_1)\mathbf{c}(n) + \mathbf{z}(n)$, et les spectres de Capon, MUSIC et GLRT sont calculés en utilisant les vecteurs directionnels classiques $\mathbf{a}_r(\theta)$ et $\mathbf{a}_t(\theta)$.

- **Cas du traitement classique** : la propagation des signaux est simulée en incluant les diagrammes de rayonnement dans le modèle du signal $\mathbf{x}(n) = \beta \tilde{\mathbf{a}}_r^*(\theta_1)\tilde{\mathbf{a}}_t^H(\theta_1)\mathbf{c}(n) + \mathbf{z}(n)$, mais les spectres de Capon, MUSIC et GLRT sont calculés en utilisant les vecteurs directionnels classiques $\mathbf{a}_r(\theta)$ et $\mathbf{a}_t(\theta)$.

- **Cas du traitement basé sur le couplage mutuel (CM)** : la propagation des signaux est simulée en incluant les diagrammes de rayonnement dans le modèle du signal $\mathbf{x}(n) = \beta \tilde{\mathbf{a}}_r^*(\theta_1)\tilde{\mathbf{a}}_t^H(\theta_1)\mathbf{c}(n) + \mathbf{z}(n)$, et les spectres de Capon, MUSIC et GLRT sont calculés en utilisant les vecteurs directionnels généraux $\tilde{\mathbf{a}}_r(\theta)$ et $\tilde{\mathbf{a}}_t(\theta)$.

- **Cas du traitement basé sur le couplage mutuel (CM) utilisant la phase uniquement** : la propagation des signaux est simulée en incluant les diagrammes de rayonnement dans le modèle du signal $\mathbf{x}(n) = \beta \tilde{\mathbf{a}}_r^*(\theta_1)\tilde{\mathbf{a}}_t^H(\theta_1)\mathbf{c}(n) + \mathbf{z}(n)$, et les spectres de Capon, MUSIC et GLRT sont calculés en utilisant les vecteurs directionnels généraux (phase uniquement) $\boldsymbol{\alpha}_r(\theta)$ et $\boldsymbol{\alpha}_t(\theta)$.

Les résultats sont présentés figure C.19. On peut constater que le cas de simulation idéal donne les meilleurs résultats, cependant il s'agit d'un cas non réaliste. En revanche, le cas du traitement classique donne des erreurs importantes (fortes valeurs de la MSE pour tous les niveaux de bruit) car les diagrammes de rayonnement incluant les effets du couplage mutuel ne sont pas pris en compte pour calculer les spectres spatiaux. D'autre part, les résultats obtenus pour Capon montrent que dans le cas du traitement basé sur le couplage mutuel, la MSE a de fortes valeurs quand le niveau du bruit est élevé ($-10\log_{10}\sigma^2 \leq -5$), conséquence de la remontée spectrale observée pour des angles proches de $-90°$ et $90°$. Lorsque les vecteurs directionnels incluant uniquement la phase des diagrammes de rayonnement sont utilisés, la MSE diminue et on obtient les résultats qui s'approchent le plus des résultats du cas idéal.

Quant à MUSIC et au GLRT, les deux traitements basés sur le couplage mutuel donnent des résultats similaires : les courbes des MSE sont superposées, ce qui indique que le fait d'utiliser seulement la phase des diagrammes de rayonnement n'introduit pas d'erreurs importantes dans l'estimation de la DOA.

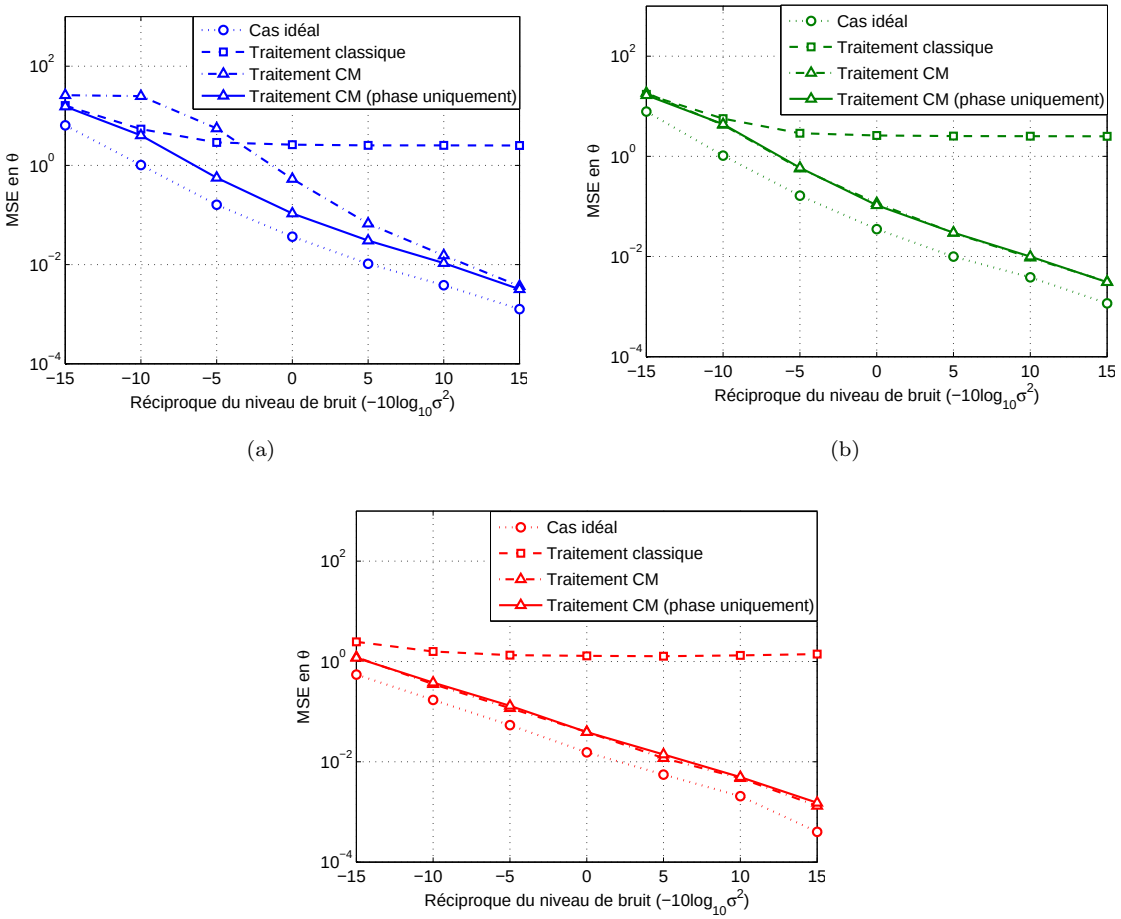


FIGURE C.19: MSE en $\theta$ de la DOA estimée par (a) Capon, (b) MUSIC et (c) GLRT, pour une cible à $-40°$.

### C.3.2 Prise en compte du "crosstalk" ou diaphonie

#### C.3.2.1 Modélisation

Les signaux directement transmis des émetteurs aux récepteurs sont modélisés comme un mélange de l'ensemble des signaux émis. Le modèle du signal prenant en compte à la fois les diagrammes de rayonnement et le crosstalk s'écrit

$$\mathbf{x}(n) = \sum_{k=1}^{K} \beta_k \tilde{\mathbf{a}}_r^*(\theta_k)\tilde{\mathbf{a}}_t^H(\theta_k)\mathbf{c}(n) + \mathbf{M}\mathbf{c}(n) + \mathbf{z}(n), \tag{C.45}$$

où

$$\mathbf{M} = \begin{bmatrix} m_{0,0} & \cdots & m_{0,L_t-1} \\ \vdots & \ddots & \vdots \\ m_{L_r-1,0} & \cdots & m_{L_r-1,L_t-1} \end{bmatrix} \tag{C.46}$$

est la matrice de crosstalk composée de coefficients de transmission complexes.

#### C.3.2.2 Proposition d'une technique de réduction du "crosstalk"

La matrice de crosstalk peut être estimée à partir d'une première transmission dans un environnement sans cible. Dans ce cas, le modèle du signal est

$$\tilde{\mathbf{x}}(n) = \mathbf{M}\mathbf{c}(n) + \mathbf{z}(n). \tag{C.47}$$

On cherche la matrice de crosstalk $\mathbf{M}$ qui minimise le critère MSE

$$J = E\left[\|\tilde{\mathbf{x}}(n) - \mathbf{M}\mathbf{c}(n)\|^2\right]. \tag{C.48}$$

Ce critère d'optimisation peut être décomposé en $L_r$ problèmes de filtrage de Wiener classique (voir chapitre 4). Après un simple développement mathématique, la matrice $\mathbf{M}$ qui minimise (C.48) s'écrit

$$\tilde{\mathbf{M}} = \mathbf{R}_{\tilde{x}c}\mathbf{R}_c^{-1}, \tag{C.49}$$

où $\mathbf{R}_{\tilde{x}c} = E\left[\tilde{\mathbf{x}}(n)\mathbf{c}^H(n)\right]$.

Le terme de crosstalk peut alors être soustrait des signaux reçus dans un cas de fonctionnement normal du radar en calculant

$$\mathbf{x}_{sc}(n) = \mathbf{x}(n) - \hat{\mathbf{M}}\mathbf{c}(n), \tag{C.50}$$

où $\hat{\mathbf{M}}$ est une estimée de $\tilde{\mathbf{M}}$, obtenue à partir de versions estimées de $\mathbf{R}_{\tilde{x}c}$ et $\mathbf{R}_c$.

#### C.3.2.3 Simulation

On considère un radar MIMO de $L = L_t = L_r = 6$ éléments, $K = 2$ cibles situées dans la région d'ondes planes à $\theta_1 = -20°$ et $\theta_2 = 20°$ et un réciproque du niveau de bruit de $-10\log_{10}\sigma^2 = 20$. On utilise une matrice de crosstalk dont les parties réelles et imaginaires des coefficients sont aléatoirement générées et uniformément distribuées dans l'intervalle ouvert $]-1/\sqrt{2}\,,1/\sqrt{2}[$.

Les spectres de Capon, MUSIC et GLRT calculés avant réduction du crosstalk sont montrés figure C.20. On observe que les deux cibles sont détectables en utilisant Capon et MUSIC mais les lobes ne sont pas centrés autour des directions des cibles. Dans le cas du GLRT, plusieurs lobes secondaires apparaissent dans tout le spectre, ne permettant pas la localisation des cibles.

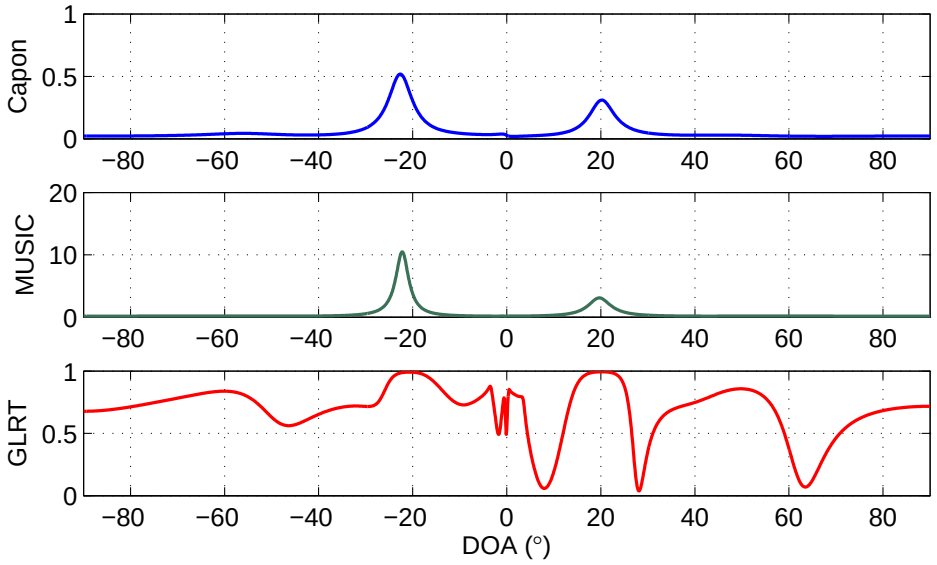


FIGURE C.20: spectres de Capon, MUSIC et GLRT dans le cas de deux cibles à $\theta_1 = -20°$ et $\theta_2 = 20°$ avant réduction du crosstalk.

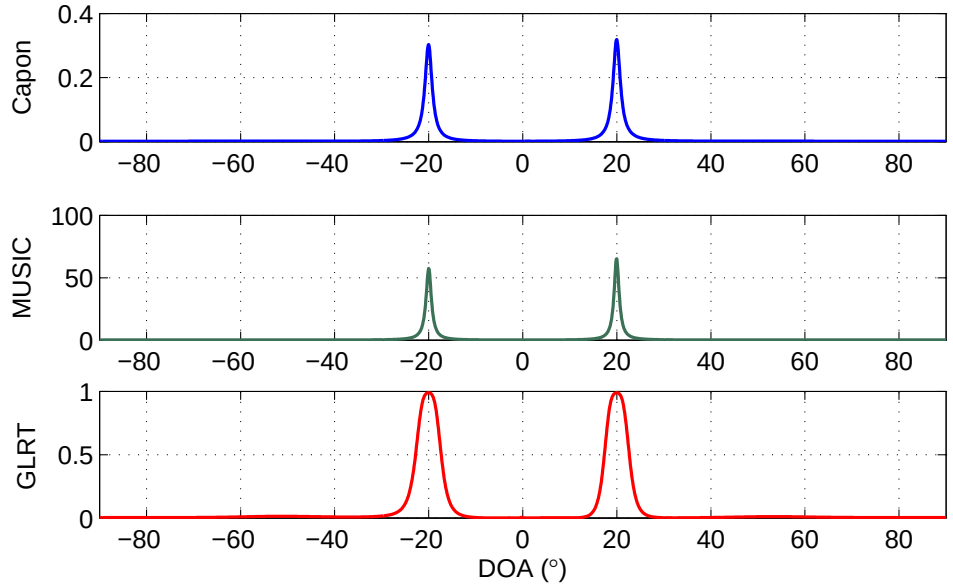


FIGURE C.21: spectres de Capon, MUSIC et GLRT dans le cas de deux cibles à $\theta_1 = -20°$ et $\theta_2 = 20°$ après réduction du crosstalk.

Les spectres spatiaux sont maintenant recalculés après réduction du crosstalk à partir des signaux $\mathbf{x}_{sc}(n)$. Comme le montre la figure C.21, les lobes présents dans les spectres de Capon et MUSIC sont maintenant plus étroits et recentrés autour des directions des cibles. De plus, tous les lobes secondaires ont disparu du spectre du GLRT, ce qui permet une très bonne estimation des DOA des cibles.

## C.4 Développement d'une plateforme expérimentale de radar MIMO bande étroite

### C.4.1 Description de la plateforme

Dans un véritable système MIMO, les formes d'ondes sont transmises simultanément; chaque antenne doit donc disposer de sa propre architecture d'émission (Tx) ou de réception (Rx) RF. Afin de réduire la complexité d'un tel système, la plateforme proposée ici ne comporte qu'un seul émetteur et un seul récepteur mobiles. L'émetteur et le récepteur sont constitués d'une antenne et de l'architecture RF associée. Un système mécanique automatisé comportant deux rails –un pour chaque antenne– déplace indépendamment l'émetteur et le récepteur sur un ensemble de positions pré-définies de façon à reconstituer un système MIMO composé de $L_t$ éléments d'émission et de $L_r$ éléments de réception linéairement espacés. Ainsi, pour chacune des $L_t$ positions de l'émetteur, le récepteur parcourt successivement $L_r$ positions. En appliquant le principe de superposition, la matrice $\mathbf{X}$ des signaux reçus du système MIMO sous-jacent peut être construite.

Pour garantir la stationnarité du canal, les mesures sont faites dans une chambre anéchoïde (voir Figure C.22). Afin de réduire le couplage mutuel entre les antennes, l'espace séparant l'émetteur et le récepteur a été comblé par des panneaux absorbants.

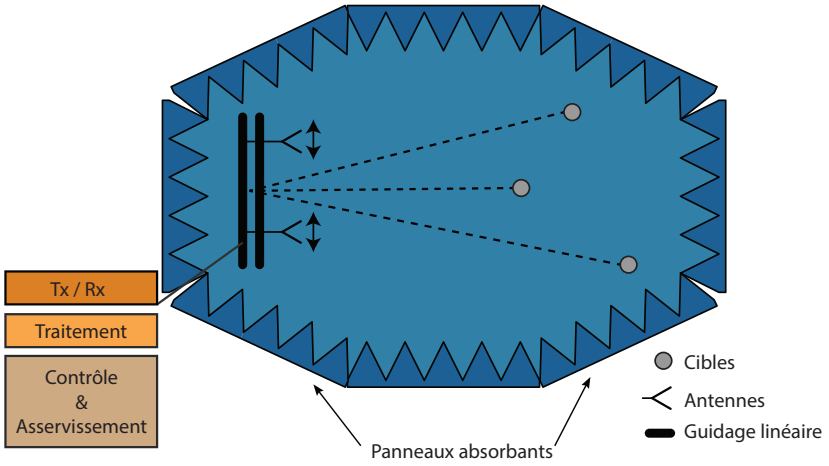


FIGURE C.22: configuration de la plateforme.

La Figure C.23 représente le schéma fonctionnel de l'architecture d'émetteur-récepteur RF. Les signaux sont générés par un générateur arbitraire de signaux (AWG) et l'acquisition des signaux reçus est effectuée par un analyseur vectoriel de signaux (VSA). L'AWG et le VSA sont contrôlés par un ordinateur externe (PC) en utilisant une interface GPIB et une communication par protocole TCP. Le PC synthétise les

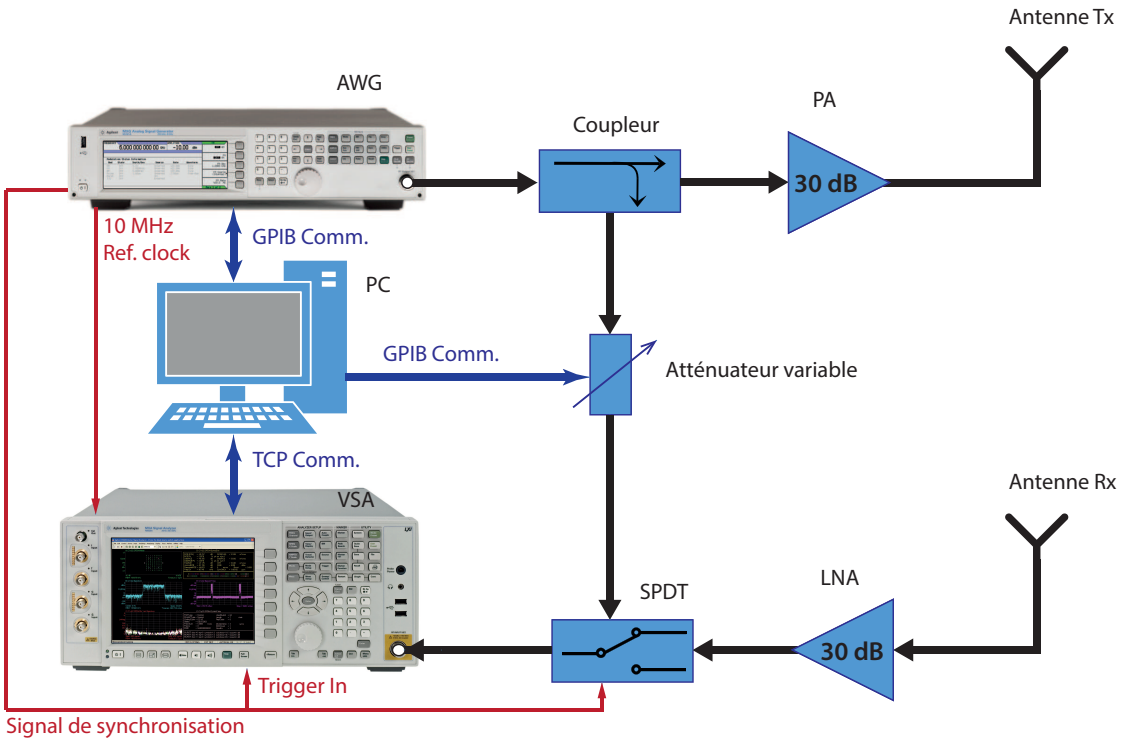


FIGURE C.23: schéma-bloc fonctionnel du système.

formes d'onde émises par l'intermédiaire d'une application Matlab et transmet ces signaux à l'AWG. Il contrôle le système des rails guidés afin d'asservir le déplacement des antennes.

La synchronisation entre l'émetteur et le récepteur est réalisée en utilisant un signal de référence transmis de l'AWG au VSA par le biais d'un coupleur directionnel. Un atténuateur variable ajuste le niveau du signal de référence à celui des signaux reçus, ce qui permet d'utiliser la dynamique du convertisseur analogique-numérique de façon optimale. Un SPDT (Single Pole Double Throw) permet de commuter des signaux réfléchis par les cibles au signal de référence.

Les signaux sont transmis dans une bande passante de 1.28 MHz autour d'une fréquence porteuse de 5.88 GHz. La puissance de sortie de l'AWG est fixée à $-5$ dBm. Un amplificateur de puissance 30 dB est utilisé pour atteindre une puissance en sortie de 25 dBm au niveau de l'antenne Tx. Les deux antennes sont des antennes patch alimentées par câble coaxial. Les différentes positions des éléments de l'antenne sont uniformément espacées d'une demi-longueur d'onde. Les cibles testées sont des cylindres métalliques de 6 cm de diamètre.

### C.4.2 Résultats expérimentaux

Après avoir testé la répétabilité de la plateforme, nous avons réalisé une campagne de mesure pour détecter $K = 2$ cibles situées à $\theta_1 = -15°$ et $\theta_2 = 18°$. Le nombre de positions de l'émetteur et du récepteur a été fixé à $L = L_t = L_r = 10$. Les signaux émis sont des séquences indépendantes de $N = 512$ symboles QPSK ayant une fréquence symbole de 64 kHz.

La Figure C.24 présente les spectres spatiaux de Capon, MUSIC et GLRT ainsi obtenus. Comme on peut le voir, les spectres de Capon et MUSIC présentent deux pics correspondant aux directions des cibles. Dans le cas du GLRT, plusieurs lobes secondaires apparaissent autour des directions des cibles, ce qui pourrait conduire à des détections erronées. En réalité, le comportement du GLRT observé ici peut s'expliquer par l'existence du crosstalk entre émetteur et récepteur dû à leur proximité, ainsi que par la nature du bruit présent dans la chambre anéchoïde et dans l'électronique. En effet, le GLRT a été développé sous l'hypothèse d'un bruit blanc Gaussien, et l'existence d'un bruit de caractéristiques différentes pourrait détériorer les performances.

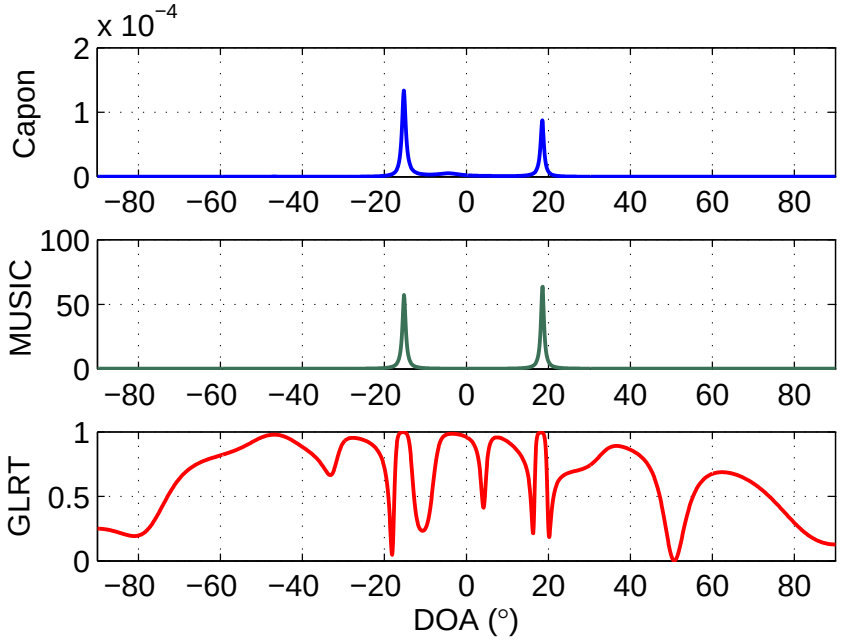


FIGURE C.24: spectres de Capon, MUSIC et GLRT avant réduction du crosstalk (mesures expérimentales avec deux cibles à $\theta_1 = -15°$ et $\theta_2 = 18°$).

Dans un deuxième temps, le terme de crosstalk peut être déduit des signaux reçus en utilisant la technique de réduction de crosstalk que nous avons proposée précédemment. La matrice de crosstalk est déterminée à partir de (C.49) après une transmission en l'absence de cible et le terme de crosstalk est soustrait des signaux reçus selon (C.50).

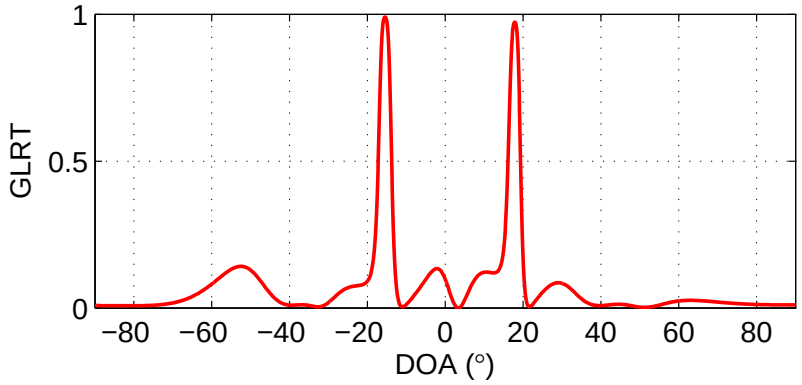


FIGURE C.25: spectre du GLRT après ajout d'un bruit blanc Gaussien et réduction du crosstalk (mesures expérimentales avec deux cibles à $\theta_1 = -15°$ et $\theta_2 = 18°$).

Afin de travailler avec un modèle adapté au GLRT, un bruit blanc Gaussien est ajouté aux signaux $\mathbf{x}_{sc}(n)$ obtenus précédemment. La puissance de ce bruit additif est prise inférieure de 70 dB à la puissance des signaux reçus (elle-même égale à -36 dBm).

La Figure C.25 montre l'impact de cette technique de réduction du couplage Tx-Rx sur le GLRT : on observe que les lobes secondaires dus au couplage sont désormais fortement atténués, ce qui permet d'identifier clairement les directions des cibles.

## C.5 Conclusions

Nous avons étudié les conditions de validité de l'approximation d'ondes planes en fonction de la distance de la cible. Nous avons établi la condition d'ondes planes $R > 5\Delta^2/\lambda$.

Dans le cas large bande, nous avons proposé une technique de conception de formes d'ondes (M-SFBT) qui permet de décorréler les signaux réfléchis par les cibles. De plus, nous avons proposé des techniques d'estimation de DOA dans le cas large bande : des techniques basées sur l'adaptation des techniques bande étroite au cas large bande (méthodes incohérentes), et une technique reposant sur l'adaptation d'une technique de traitement d'antennes (TOPS) au contexte du radar MIMO large bande.

De plus, nous avons étudié les performances du système MIMO sous des conditions non idéales, en utilisant un modèle du signal plus réaliste qui permet de prendre en compte le phénomène de couplage mutuel. Nous avons par ailleurs montré que l'inclusion des diagrammes de rayonnement dans les vecteurs directionnels permet d'améliorer les performance d'estimation des DOA, et nous avons également proposé une technique de réduction du crosstalk.

En ce qui concerne la partie expérimentale, nous avons développé une plateforme expérimentale de radar MIMO bande étroite comportant une seule architecture d'émetteur-récepteur. Cette plateforme nous a permis de valider les techniques bande bande étroite Capon, MUSIC et GLRT, ainsi que notre technique de réduction du crosstalk.

# Bibliography


[1] H. Krim and M. Viberg. Two decades of array signal processing research: The parametric approach. *IEEE Signal Processing Magazine*, 13(4):67–94, 1996. ISSN 1053-5888. doi: 10.1109/79.526899.

[2] B. D. Van Veen and K. M. Buckley. Beamforming: A versatile approach to spatial filtering. *IEEE ASSP Magazine*, 5(2):4–24, April 1988. ISSN 0740-7467. doi: 10.1109/53.665.

[3] T. W. Jeffrey. *Phased-Array Radar Design: Application of Radar Fundamentals*. Institution of Engineering and Technology, 2009. ISBN 9781891121692.

[4] J. Li and P. Stoica. MIMO radar with colocated antennas. *IEEE Signal Processing Magazine*, 24(5):106–114, 2007. ISSN 1053-5888. doi: 10.1109/MSP.2007.904812.

[5] D. W. Bliss and K. W. Forsythe. Multiple-input multiple-output (MIMO) radar and imaging: Degrees of freedom and resolution. In *Conference Record of the Thirty-Seventh Asilomar Conference on Signals, Systems and Computers, 2004*, volume 1, pages 54–59, Nov 2003. doi: 10.1109/ACSSC.2003.1291865.

[6] I. Bekkerman and J. Tabrikian. Target detection and localization using MIMO radars and sonars. *IEEE Transactions on Signal Processing*, 54(10):3873–3883, 2006. ISSN 1053-587X. doi: 10.1109/TSP.2006.879267.

[7] Y. Qu, G. S. Liao, S. Q. Zhu, X. Y. Liu, and H. Jiao. Performance comparisons of MIMO and phased-array radar. In *17th International Conference on Microwaves, Radar and Wireless Communications, MIKON 2008*, pages 1–4, May 2008.

[8] A. M. Haimovich, R. S. Blum, and L. J. Cimini. MIMO radar with widely separated antennas. *IEEE Signal Processing Magazine*, 25(1):116–129, 2008. ISSN 1053-5888. doi: 10.1109/MSP.2008.4408448.

[9] E. Fishler, A. Haimovich, R. S. Blum, L. J. Cimini, D. Chizhik, and R. A. Valenzuela. Spatial diversity in radars-Models and detection performance. *IEEE Transactions on Signal Processing*, 54(3):823–838, March 2006. ISSN 1053-587X. doi: 10.1109/TSP.2005.862813.

[10] H. Yan, J. Li, and G. Liao. Multitarget identification and localization using bistatic MIMO radar systems. *EURASIP Journal on Advances in Signal Process*, 2008: 48:1–48:8, January 2008. ISSN 1110-8657. doi: 10.1155/2008/283483.

[11] X. F. Ma, W. X. Sheng, and F. Huang. Mono-static MIMO radar array design for interferences suppressing. In *2009 IEEE Asia-Pacific Microwave Conference (APMC)*, pages 2683–2686, Dec 2009. doi: 10.1109/APMC.2009.5384120.

[12] W. Wiesbeck. The radar of the future. In *2013 European Radar Conference (EuRAD)*, pages 137–140, Oct. 2013.

[13] M. Lesturgie. Some relevant applications of MIMO to radar. In *2011 Proceedings International Radar Symposium (IRS)*, pages 714–721, 2011.

[14] A. Martinez-Vazquez and J. Fortuny-Guasch. UWB MIMO radar arrays for small area surveillance applications. In *The Second European Conference on Antennas and Propagation EuCAP 2007*, pages 1–6, 2007.

[15] S. Lutz, K. Baur, and T. Walter. 77 GHz lens-based multistatic MIMO radar with colocated antennas for automotive applications. In *2012 IEEE MTT-S International Microwave Symposium Digest (MTT)*, pages 1–3, 2012. doi: 10.1109/MWSYM.2012.6259526.

[16] K. Schuler, M. Younis, R. Lenz, and W. Wiesbeck. Array design for automotive digital beamforming radar system. In *2005 IEEE International Radar Conference*, pages 435–440, 2005. doi: 10.1109/RADAR.2005.1435864.

[17] J. H. Kim, A. Ossowska, and W. Wiesbeck. Investigation of MIMO SAR for interferometry. In *2007 European Radar Conference EuRAD 2007*, pages 51–54, 2007. doi: 10.1109/EURAD.2007.4404934.

[18] C. Fischer, A. Herschlein, M. Younis, and W. Wiesbeck. Detection of antipersonnel mines by using the factorization method on multistatic ground-penetrating radar measurements. *IEEE Transactions on Geoscience and Remote Sensing*, 45(1):85–92, 2007. ISSN 0196-2892. doi: 10.1109/TGRS.2006.883464.

[19] A. Dzvonkovskaya, K. W. Gurgel, T. Pohlmann, T. Schlick, and J. Xu. Simulation of tsunami signatures in ocean surface current maps measured by HF radar. In *OCEANS 2009 - EUROPE*, pages 1–6, May 2009. doi: 10.1109/OCEANSE.2009.5278315.

[20] S. J. Anderson and W. C. Anderson. A MIMO technique for enhanced clutter selectivity in a multiple scattering environment: Application to HF surface wave radar. In *2010 International Conference on Electromagnetics in Advanced*

*Applications (ICEAA)*, pages 133–136, Sept 2010. doi: 10.1109/ICEAA.2010.5652215.

[21] X. P. Masbernat, M. G. Amin, F. Ahmad, and C. Ioana. An MIMO-MTI approach for through-the-wall radar imaging applications. In *2010 International Waveform Diversity and Design Conference (WDD)*, pages 000188–000192, 2010. doi: 10.1109/WDD.2010.5592466.

[22] J. Li and P. Stoica. *MIMO Radar Signal Processing*. John Wiley & Sons, 2009. ISBN 9780470391433.

[23] E. Pancera, T. Zwick, and W. Wiesbeck. Ultra wideband radar imaging: An approach to monitor the water accumulation in the human body. In *2010 IEEE International Conference on Wireless Information Technology and Systems (ICWITS)*, pages 1–4, 2010. doi: 10.1109/ICWITS.2010.5611899.

[24] C. A. Balanis. *Advanced Engineering Electromagnetics*. Wiley, 1989. ISBN 0471621943.

[25] A. Shlivinski, E. Heyman, and R. Kastner. Antenna characterization in the time domain. *IEEE Transactions on Antennas and Propagation*, 45(7):1140–1149, Jul 1997. ISSN 0018-926X. doi: 10.1109/8.596907.

[26] J. G. Proakis and D. G. Manolakis. *Digital Signal Processing: Principles, Algorithms, and Applications*. Prentice-Hall International editions. Prentice Hall, 1996. ISBN 9780133737622.

[27] P. P. Vaidyanathan, P. Pal, and C. Y. Chen. MIMO radar with broadband waveforms: Smearing filter banks and 2d virtual arrays. In *2008 42nd Asilomar Conference on Signals, Systems and Computers*, pages 188–192, 2008. doi: 10.1109/ACSSC.2008.5074389.

[28] S. Licul and William A. Davis. Unified frequency and time-domain antenna modeling and characterization. *IEEE Transactions on Antennas and Propagation*, 53(9):2882–2888, Sept 2005. ISSN 0018-926X. doi: 10.1109/TAP.2005.854533.

[29] I. Ziskind and M. Wax. Maximum likelihood localization of multiple sources by alternating projection. *IEEE Transactions on Acoustics, Speech and Signal Processing*, 36(10):1553–1560, 1988. ISSN 0096-3518. doi: 10.1109/29.7543.

[30] J. Capon. High-resolution frequency-wavenumber spectrum analysis. *Proceedings of the IEEE*, 57(8):1408–1418, 1969. ISSN 0018-9219. doi: 10.1109/PROC.1969.7278.

[31] R. O. Schmidt. Multiple emitter location and signal parameter estimation. *IEEE Transactions on Antennas and Propagation*, 34(3):276–280, 1986. ISSN 0018-926X. doi: 10.1109/TAP.1986.1143830.

[32] L. Xu, J. Li, and P. Stoica. Radar imaging via adaptive MIMO techniques. In *Proceedings of the 14th European Signal Processing Conference (EUSIPCO'06)*, 2006.

[33] E. J. Kelly. An adaptive detection algorithm. *IEEE Transactions on Aerospace and Electronic Systems*, AES-22(2):115–127, 1986. ISSN 0018-9251. doi: 10.1109/TAES.1986.310745.

[34] M. N. Cohen. An overview of high range resolution radar techniques. In *National Telesystems Conference, 1991. Proceedings. Vol.1., NTC '91*, pages 107–115, 1991. doi: 10.1109/NTC.1991.147997.

[35] F. Dai, P. Wang, H. Liu, and S. Wu. Detection performance comparison for wideband and narrowband radar in noise. In *2010 IEEE Radar Conference*, pages 794–798, 2010. doi: 10.1109/RADAR.2010.5494514.

[36] H. Sun, Y. Lu, and G. Liu. Ultra-wideband technology and random signal radar: An ideal combination. *IEEE Aerospace and Electronic Systems Magazine*, 18(11): 3–7, 2003. ISSN 0885-8985. doi: 10.1109/MAES.2003.1246580.

[37] Y. D. Shirman, S. P. Leshchenko, and Y. M. Orlenko. Wideband radar (advantages and problems). In *2004 Second International Workshop on Ultrawideband and Ultrashort Impulse Signals*, pages 71–76, 2004. doi: 10.1109/UWBUS.2004.1388051.

[38] A. S. Mudukutore, V. Chandrasekar, and R. J. Keeler. Pulse compression for weather radars. *IEEE Transactions on Geoscience and Remote Sensing*, 36(1): 125–142, 1998. ISSN 0196-2892. doi: 10.1109/36.655323.

[39] G. S. Liu, H. Gu, W. Su, H. B. Sun, and J. H. Zhang. Random signal radar - A winner in both the military and civilian operating environments. *IEEE Transactions on Aerospace and Electronic Systems*, 39(2):489–498, 2003. ISSN 0018-9251. doi: 10.1109/TAES.2003.1207261.

[40] C. Y. Chen and P. P. Vaidyanathan. MIMO radar ambiguity properties and optimization using frequency-hopping waveforms. *IEEE Transactions on Signal Processing*, 56(12):5926–5936, 2008. ISSN 1053-587X. doi: 10.1109/TSP.2008.929658.

[41] B. Friedlander. Waveform design for MIMO radars. *IEEE Transactions on Aerospace and Electronic Systems*, 43(3):1227–1238, 2007. ISSN 0018-9251. doi: 10.1109/TAES.2007.4383615.

[42] P. Stoica, J. Li, and Y. Xie. On probing signal design for MIMO radar. *IEEE Transactions on Signal Processing*, 55(8):4151–4161, 2007. ISSN 1053-587X. doi: 10.1109/TSP.2007.894398.

[43] H. He, P. Stoica, and J. Li. Wideband MIMO systems: Signal design for transmit beampattern synthesis. *IEEE Transactions on Signal Processing*, 59(2):618–628, 2011. ISSN 1053-587X. doi: 10.1109/TSP.2010.2091410.

[44] P. Jardin, F. Nadal, and S. Middleton. On wideband MIMO radar: Extended signal model and spectral beampattern design. In *2010 European Radar Conference (EuRAD)*, pages 392–395, 2010.

[45] O. Gómez, P. Jardin, F. Nadal, B. Poussot, and G. Baudoin. Multiband waveform synthesis and detection for a wideband MIMO radar. In *2011 IEEE International Conference on Microwaves, Communications, Antennas and Electronics Systems (COMCAS)*, pages 1–5, 2011. doi: 10.1109/COMCAS.2011.6105884.

[46] J. A. Tropp, I. S. Dhillon, R. W. Heath, and T. Strohmer. Designing structured tight frames via an alternating projection method. *IEEE Transactions on Information Theory*, 51(1):188–209, 2005. ISSN 0018-9448. doi: 10.1109/TIT.2004.839492.

[47] M. Wax, T. J. Shan, and T. Kailath. Spatio-temporal spectral analysis by eigenstructure methods. *IEEE Transactions on Acoustics, Speech and Signal Processing*, 32(4):817–827, 1984. ISSN 0096-3518. doi: 10.1109/TASSP.1984.1164400.

[48] T. Pham and B. M. Sadler. Adaptive wideband aeroacoustic array processing. In *Proceedings of the 8th IEEE Signal Processing Workshop on Statistical Signal and Array Processing*, pages 295–298, 1996. doi: 10.1109/SSAP.1996.534875.

[49] H. Wang and M. Kaveh. Coherent signal-subspace processing for the detection and estimation of angles of arrival of multiple wide-band sources. *IEEE Transactions on Acoustics, Speech and Signal Processing*, 33(4):823–831, 1985. ISSN 0096-3518. doi: 10.1109/TASSP.1985.1164667.

[50] S. Valaee and P. Kabal. The optimal focusing subspace for coherent signal subspace processing. *IEEE Transactions on Signal Processing*, 44(3):752–756, 1996. ISSN 1053-587X. doi: 10.1109/78.489056.

[51] H. Hung and M. Kaveh. Focussing matrices for coherent signal-subspace processing. *IEEE Transactions on Acoustics, Speech and Signal Processing*, 36(8):1272–1281, 1988. ISSN 0096-3518. doi: 10.1109/29.1655.

[52] R. A. Horn and C. R. Johnson. *Matrix Analysis*. Cambridge University Press, 1990. ISBN 9780521386326.

[53] D. N. Swingler and J. Krolik. Source location bias in the coherently focused high-resolution broad-band beamformer. *IEEE Transactions on Acoustics, Speech and Signal Processing*, 37(1):143–145, 1989. ISSN 0096-3518. doi: 10.1109/29.17516.

[54] Y. S. Yoon, L. M. Kaplan, and J. H. McClellan. TOPS: New DOA estimator for wideband signals. *IEEE Transactions on Signal Processing*, 54(6):1977–1989, 2006. ISSN 1053-587X. doi: 10.1109/TSP.2006.872581.

[55] O. Gómez, F. Nadal, P. Jardin, G. Baudoin, and B. Poussot. On wideband MIMO radar: Detection techniques based on a DFT signal model and performance comparison. In *2012 IEEE Radar Conference (RADAR)*, pages 0608–0612, 2012. doi: 10.1109/RADAR.2012.6212212.

[56] J. L. Allen and B. L. Diamond. *Mutual Coupling in Array Antennas*. Technical report (Lincoln Laboratory, M.I.T.). Defense Technical Information Center, 1966.

[57] D. F. Kelley and W. L. Stutzman. Array antenna pattern modeling methods that include mutual coupling effects. *IEEE Transactions on Antennas and Propagation*, 41(12):1625–1632, 1993. ISSN 0018-926X. doi: 10.1109/8.273305.

[58] I. J. Gupta and A. A. Ksienski. Effect of mutual coupling on the performance of adaptive arrays. *IEEE Transactions on Antennas and Propagation*, 31(5):785–791, 1983. ISSN 0018-926X. doi: 10.1109/TAP.1983.1143128.

[59] C. K. E. Lau, R. S. Adve, and T. K. Sarkar. Minimum norm mutual coupling compensation with applications in direction of arrival estimation. *IEEE Transactions on Antennas and Propagation*, 52(8):2034–2041, 2004. ISSN 0018-926X. doi: 10.1109/TAP.2004.832511.

[60] A. J. Weiss and B. Friedlander. Direction finding in the presence of mutual coupling. In *Twenty-Second Asilomar Conference on Signals, Systems and Computers, 1988*, volume 2, pages 598–602, 1988. doi: 10.1109/ACSSC.1988.754613.

[61] D. Segovia Vargas, R. Martín Cuerdo, and M. Sierra Pérez. Mutual coupling effects correction in microstrip arrays for direction-of-arrival (DOA) estimation. *IEE Proceedings Microwaves, Antennas and Propagation*, 149(2):113–118, 2002. ISSN 1350-2417. doi: 10.1049/ip-map:20020232.

[62] H. Wang, D. G. Fang, and P. Ge. Mutual coupling reduction between two conformal microstrip patch antennas. In *5th Asia-Pacific Conference on Environmental*

*Electromagnetics, CEEM 2009*, pages 176–179, 2009. doi: 10.1109/CEEM.2009.5304778.

[63] A. Habashi, J. Nourinia, and C. Ghobadi. Mutual coupling reduction between very closely spaced patch antennas using low-profile folded split-ring resonators (FSRRs). *IEEE Antennas and Wireless Propagation Letters*, 10:862–865, 2011. ISSN 1536-1225. doi: 10.1109/LAWP.2011.2165931.

[64] K. S. Min, D. J. Kim, and Y. M. Moon. Improved MIMO antenna by mutual coupling suppression between elements. In *The European Conference on Wireless Technology*, pages 125–128, 2005. doi: 10.1109/ECWT.2005.1617671.

[65] J. Ouyang, F. Yang, and Z. M. Wang. Reducing mutual coupling of closely spaced microstrip MIMO antennas for WLAN application. *IEEE Antennas and Wireless Propagation Letters*, 10:310–313, 2011. ISSN 1536-1225. doi: 10.1109/LAWP.2011.2140310.

[66] J. Itoh, N. Michishita, and H. Morishita. A study on mutual coupling reduction between two inverted-F antennas using mushroom-type EBG structures. In *IEEE Antennas and Propagation Society International Symposium, AP-S 2008*, pages 1–4, 2008. doi: 10.1109/APS.2008.4619710.

[67] L. Chiu, Q. Xue, and C. H. Chan. Radiating patches with low mutual coupling for antenna arrays. In *2007 IEEE Antennas and Propagation Society International Symposium*, pages 3620–3623, 2007. doi: 10.1109/APS.2007.4396322.

[68] S. Farsi, H. Aliakbarian, D. Schreurs, B. Nauwelaers, and G. A. E. Vandenbosch. Mutual coupling reduction between planar antennas by using a simple microstrip U-section. *Antennas and Wireless Propagation Letters, IEEE*, 11:1501–1503, 2012. ISSN 1536-1225. doi: 10.1109/LAWP.2012.2232274.

[69] C. H. Niow, Y. T. Yu, and H. T. Hui. Compensate for the coupled radiation patterns of compact transmitting antenna arrays. *IET Microwaves, Antennas Propagation*, 5(6):699–704, 2011. ISSN 1751-8725. doi: 10.1049/iet-map.2010.0487.

[70] J. W. Wallace and M. A. Jensen. Mutual coupling in MIMO wireless systems: A rigorous network theory analysis. *IEEE Transactions on Wireless Communications*, 3(4):1317–1325, 2004. ISSN 1536-1276. doi: 10.1109/TWC.2004.830854.

[71] Y. Qun, C. Xiang-yu, Y. Yi, and Y. Xu. Analysis of DOA and adaptive beam forming including mutual coupling. In *2011 IEEE International Conference on Signal Processing, Communications and Computing (ICSPCC)*, pages 1–4, 2011. doi: 10.1109/ICSPCC.2011.6061685.

[72] D. M. Pozar. The active element pattern. *IEEE Transactions on Antennas and Propagation*, 42(8):1176–1178, 1994. ISSN 0018-926X. doi: 10.1109/8.310010.

[73] N. I. Fisher. *Statistical Analysis of Circular Data*. Cambridge University Press, 1995. ISBN 9780521568906.

[74] L. M. Carter, D. B. Campbell, and B. A. Campbell. Geologic studies of planetary surfaces using radar polarimetric imaging. *Proceedings of the IEEE*, 99(5):770–782, May 2011. ISSN 0018-9219. doi: 10.1109/JPROC.2010.2099090.

[75] E. Hanle. Choice of optimum polarization bases for different radar applications with limited system capabilities. In *Radar 97 (Conf. Publ. No. 449)*, pages 828–832, 1997. doi: 10.1049/cp:19971793.

[76] M. Galletti, D. S. Zrnic, V. M. Melnikov, and R. J. Doviak. Degree of polarization at horizontal transmit: Theory and applications for weather radar. *IEEE Transactions on Geoscience and Remote Sensing*, 50(4):1291–1301, April 2012. ISSN 0196-2892. doi: 10.1109/TGRS.2011.2167516.

[77] H. He, P. Stoica, and J. Li. On aperiodic-correlation bounds. *IEEE Signal Processing Letters*, 17(3):253–256, 2010. ISSN 1070-9908. doi: 10.1109/LSP.2009.2038108.